Università degli Studi di Padova

Sede amministrativa: Padova
Dipartimento di Fisica "G. Galilei"

Scuola di Dottorato di Ricerca
in Fisica

Ciclo XXIII

Tesi di Dottorato:

A Level 1 Tracking Trigger for the CMS Experiment at the LHC Phase 2 Luminosity Upgrade

Direttore della Scuola

prof. Attilio Stella

Supervisori

prof. Dario Bisello

dott. Marcello Mannelli

Dottorando

Nicola Pozzobon

Abstract

The second decade of Large Hadron Collider operations, from about 2020 onwards, envisages a remarkable increase in collider instantaneous luminosity, one order of magnitude above the project one. This luminosity increase presents several challenges to the LHC experiments. The present Tracker of the Compact Muon Solenoid experiment must be replaced with a system providing excellent tracking quality at higher luminosities, as well as Tracking Trigger inputs to the existing "Level 0" CMS Trigger system at the full 40 MHz bunch-crossing rate. The minimal requirements for a Tracking Trigger would be the capability to confirm the presence of high-p_T tracks associated with Calorimeter and/or Muon Level 0 Triggers. The ability to provide effective isolation criteria may also be required, and would in any case substantially improve the Trigger performance.

Maintaining the data rates generated by Tracking Trigger inputs within a manageable bandwidth requires sensor modules able to locally sparsify the data. Measuring at detector module level the track direction in the transverse plane, and hence deriving its transverse momentum, is the most promising solution to provide such a detector-embedded data reduction feature. These so-called "p_T-modules" would only transmit to the Level 1 Trigger "stubs", pairs of correlated hits in two closely separated sensors, derived by tracks with p_T above a given threshold. To exemplify, a 2 GeV/c threshold would cut data rate of more than a factor 10, hence providing a data rate well within the capabilities of present data links.

The p_T-modules design discussed in this work consists of two, closely spaced segmented silicon sensors, featuring both pattern hit correlation across the module and a single hit position resolution high enough to compute stubs with the required accuracy to resolve track directions despite a lever arm of about only 1 mm. A concept Tracker layout, the so-called "Long Barrel", consisting in an Outer Tracker completely built out of p_T-modules, has been proposed. The Long Barrel Tracker is particularly flexible in simulation studies of Tracking Trigger as it allows for information from several layers of the Tracker to be combined in a projective geometry. For this reason, it is meant as a testing ground to compare the performance of different designs and configurations. The Long Barrel layout also allows the generation of even more structured Trigger Objects

such as “tracklets”, consisting of pairs of stubs in opportunely paired layers, which can in turn be used as seeds to generate “Level 1 tracks”, including even more stubs.

The choice of stacked sensors for p_T-modules has been recently strengthened by test beam results obtained with novel prototypes of Monolithic Active Pixel Sensors and reported in this thesis. The developement of Tracking Trigger simulations is also presented as a major step towards the design of a realistic Trigger capable Tracker upgrade. A particular challenge for the Trigger system is given by τ leptons produced in many rare processes searched at the LHC. The performance of a Tracking Trigger on final states with τ leptons will be crucial at very high luminosities and is presented at the and of this document as the natural step forward in the work on the subject.

Riassunto

Durante il secondo decennio di operazioni al Large Hadron Collider, a partire dall'anno 2020, è previsto un notevole aumento della luminosità istantanea del collisionatore, di un ordine di grandezza superiore rispetto a quella di progetto. Questa luminosità presenta numeose sfide per gli esperimenti a LHC. Il Tracciatore attualmente impiegato nell'esperimento Compact Muon Solenoid dovrà essere rimpiazzato con un sistema in grado di garantire una tracciatura di qualità eccellente ad alte luminosità e, allo stesso tempo, fornire informazioni utili per l'attuale "Livello 0" del sistema di Trigger a CMS, alla frequenza di collisioni di 40 MHz. Le richieste minime per un Trigger basato sul Tracciatore sono la capacità di confermare la presenza di tracce ad alto p_T associate a Trigger di Livello 0 ottenuti con i Calorimetri o i rivelatori di muoni. La capacità di fornire criteri efficaci di isolazione può essere ulteriormente richiesa e in ogni caso migliorerebbe significativamente le prestazioni del Trigger.

Il rateo dei dati associati con la generazione nel Tracciatore di informazione di Trigger può essere mantenuto in una larghezza di banda sufficientemente maneggevole richiedendo che i moduli sensitivi siano in grado di ridurre localmente i dati. I principali candidati per una simile riduzione locale del rateo i dati sono caratterizzati dalla capacità di fornire la direzione della traccia nel piano trasverso, oltre alla sua posizione, da cui poter dedurre la quantità di moto della traccia stessa. Questi "p_T-modules" trasmetterebbero di conseguenza al Trigger di primo livello degli abbozzi di traccia ("stub") generati da particelle con p_T al di sopra di 2 GeV/c. La scelta di una simile soglia permetterebbe la riduzione dei dati di un fattore superiore a 10, consentendo quindi un rateo facilmente tollerabile.

I moduli di Trigger possono essere realizzati con due sensori di silicio paralleli leggermente separati, caratterizzati da una risoluzione sulla misura del singolo punto d'impatto tale che gli stub, ottenuti tramite correlazione tra i punti misurati nel modulo, possano fornire un'adeguata misura della direzione della traccia, nonostante il braccio di leva sia dell'ordine del millimetro. Un'ipotetica configurazione per il Tracciatore, composto da "lunghi barili", che prevede un Tracciatore esterno realizzato totalmente con moduli di Trigger, è stata proposta. Essa è particolarmente flessibile negli studi di simulazione

per il Trigger realizzato con il Tracciatore giacché consente di combinare tra loro, tramite proiezioni geometriche, le informazioni provenienti da diversi strati del Tracciatore. Pertanto è un campo di prova per confrontare le prestazioni di diverse concezioni e diverse configurazioni. Il Tracciatore proposto permette anche la generazione di oggetti più articolati degli stub per il Trigger, come ad esempio le "tracklet", che consistono in coppie di stub opportunamente associate tra loro, le quali possono a loro volta essere usate come punto di partenza per la costruzione di Tracce di Primo Livello.

La scelta di moduli di Trigger realizzati con sensori accoppiati è rafforzata da risultati recenti ottenuti con dei prototipi innovativi di rivelatori a Pixel Monolitici durante dei test sotto fascio riportati in questa tesi. Lo sviluppo di simulazioni per un Trigger con il Tracciatore è anch'esso presentato come un significativo progresso verso la progettazione di un nuovo Tracciatore realistico e capace di fornire informazioni utili per il Trigger. Particolarmente impegnativo è lo sforzo per un Trigger che selezioni i leptoni τ prodotti in numerosi processi rari di interesse per gli esperimenti a LHC. Le prestazioni di un Trigger con il Tracciatore su stati finali contenenti leptoni τ saranno fondamentali a luminosità molto elevate e sono illustrate alla fine di questo documento, come naturale prosecuzione del lavoro descritto.

Table of Contents

Introduction

This thesis presents the development of a Level 1 Tracking Trigger for the Compact Muon Solenoid (CMS) experiment at the CERN Large Hadron Collider (LHC) in view of a luminosity upgrade of the *pp* collider. The challenging physics programme of the Large Hadron Collider requires cutting-edge performances to the experiments collecting its data, such as CMS. The current Triggers, based on Calorimetry and Muon identification Primitives, are foreseen to be saturated at higher luminosities, similar to those aimed by LHC after an upgrade of the accelerator chain delivering protons. For this reason, an even more challenging effort is going on: the design of a new Tracker is needed in order to add further Trigger capabilities to the CMS experiment and collect rare events in a larger background environment.

To better understand the needs of a challenging experiment, such as CMS, a deep awareness of the measurements it is designed to achieve is needed, as well as the background environment it is expected to operate within. This Chapter presents a review of the major results in experimental particle physics together with the open points the scientific community is aiming to clarify with the LHC. The final constraints on the design of the CMS experiment are presented on a qualitative basis, together with a summary of the work presented herein.

Physics at the LHC and Constraints on the Design of the CMS Experiment

Most experimental data in particle physics can be explained to an impressively high precision by the so-called Standard Model (SM) of fundamental interactions. All known matter is built, according to the SM, from spin-$\frac{1}{2}$ fermions, six leptons and six quarks,

associated to their antiparticles, carrying opposite quantum numbers. The known matter is capable of experiencing four kinds of fundamental interactions: gravitational, electromagnetic, weak and strong. The SM is a gauge theory including electromagnetic, weak and strong interactions, also called "gauge forces"[(1)], while incorporating gravity is still an open problem. The gauge interactions of fermions are described by the SM in terms of exchanges of spin-1 gauge bosons. The EW interaction is propagated by a massless photon γ and by three massive bosons W^+, W^- and Z^0. The strong interaction between quarks is carried by eight massless colored gluons g. The SM is completed by a scalar field, the Higgs field, which permeates the physical vacuum breaking the symmetry of the theory and giving masses to fundamental bosons and fermions.

In a gauge theory as the SM, the fundamental particles are described by quantized fields ψ and their interactions are expressed by the Lagrangian density $\mathcal{L}$. In this formalism, the EM interaction, referred to as quantum-electro-dynamic (QED) is written as

$$\mathcal{L}_{QED} = \bar{\psi}(i\partial\!\!\!/ - m)\psi - \frac{1}{4}F^{\mu\nu}F_{\mu\nu} + eA^{\mu}\bar{\psi}\gamma_{\mu}\psi \tag{1}$$

where the three terms respectively describe the free particle, the photon field and the interaction of a charge density with the field itself[(2)]. QED processes can be perturbatively calculated according to the Feynman's rules, often shown in graphic representations of the processes called Feynman diagrams. The strength of the interaction depends on the constant associated to each fermion-fermion-boson vertex in Feynman diagrams, called coupling constant. QED equation of motion are invariant under the U(1) local gauge transformations.

The observed weak interaction phenomena are consistent with the fermions being organized into doublets of weak isospin $\chi = (\psi_u, \psi_d)$. To account for this nature of the weak interaction and to include QED into this description, a SU(2) $\otimes$ U(1) gauge theory was proposed and set up by Glashow, Salam and Weinberg (GSW) [1, 2, 3, 4]. The result is the SM EW Lagrangian whose interaction term is written by making use of the weak fields B_μ and $\mathbf{W}_\mu = (W^1_\mu, W^2_\mu, W^3_\mu)$:

$$\mathcal{L}_{EW} = g\mathbf{J}_\mu \cdot \mathbf{W}^\mu + \frac{g'}{2}J^Y_\mu B^\mu \tag{2}$$

(1) Electromagnetic and weak interactions are described by a single interaction, named electroweak (EW).

(2) In the used formalism one has thet $\partial\!\!\!/ = \gamma^\mu\partial_\mu$, the γ^μ are the Dirac matrices, the EM field $F^{\mu\nu}$ is built from the EM scalar and vector potential A^μ as $F^{\mu\nu} = \partial^\mu A^\nu - \partial^\nu A^\mu$ and e is the charge of the particle.

The novelty with respect to QED is the introduction of three currents, linked to the positively and negatively charged current interactions and to the neutral current interaction: $J^i_\mu(x) = \bar{\chi}\gamma_\mu \frac{\sigma^i}{2}\chi$ [3]. The definition of the weak current is consistent with the observation that it couples only to left handed (LH) fermions if χ, in the case of leptons, is replaced by $\chi_L = (\nu_\ell, \ell^-)_L$. In the original GSW SM, neutrinos are massless[4] and therefore the right handed (RH) fields are weak isospin singlets ℓ_R. The LH quark field expression must take into account the observation of flavor changing charged currents coupled to it $\chi_L = \left(u_i, d'_i\right)_L$ where the index i runs on the quark families. The d'_i are the fields expressed in terms of the Cabibbo-Kobayashi-Maskawa quark mixing matrix

$$d' = V_{CKM} d = \begin{pmatrix} V_{ud} & V_{us} & V_{ub} \\ V_{cd} & V_{cs} & V_{cb} \\ V_{td} & V_{ts} & V_{tb} \end{pmatrix} \begin{pmatrix} d \\ s \\ b \end{pmatrix} \tag{3}$$

which is requested to be unitary. Quark mixing is related to the violation of the charge conjugation-parity symmetry (CP) in weak interactions: in fact, as the CKM matrix is complex instead of being real, probabilities of particular decays are different between particle and antiparticle. Since the EM interaction is experienced by RH fermions too, the EM current is expressed in function of the weak one as $J^{EM}_\mu = J^3_\mu + \frac{1}{2}J^Y_\mu$, where $J^Y_\mu = \bar{\psi}\gamma_\mu Y \psi$ and ψ is the fermion field including both leptons and quarks. If the fermion weak isospin is T^3, the charge e is related to it via the hypercharge $Y = 2\cdot(e - T^3)$. Left handed fermions have $T^3 = \frac{1}{2}$ while right handed have $T^3 = 0$.

As the physical carriers of the weak charged current interaction are $W^\pm = \frac{1}{\sqrt{2}}\left(W^1 \pm iW^2\right)$, one can decouple the EM current from the weak neutral current by mixing W^3_μ and B_μ and making the photon field and the neutral carrier of weak interactions arise:

$$A_\mu = \frac{g' W^3_\mu + g B_\mu}{\sqrt{g^2 + g'^2}} = W^3_\mu \sin\theta_W + B_\mu \cos\theta_W \tag{4}$$

$$Z^0_\mu = \frac{g W^3_\mu - g' B_\mu}{\sqrt{g^2 + g'^2}} = W^3_\mu \cos\theta_W - B_\mu \sin\theta_W \tag{5}$$

The angle θ_W is called weak mixing angle, while the request of consistency between

[3] Here σ_i are the Pauli matrices, J_3 is the neutral current, while J_1 and J_2 are linear combinations of the charged ones. g and g' are the weak and EM couplings which, in principle, can be different.

[4] This picture has been modified by the discovery made in the Nineties that neutrinos have a tiny but non-zero mass.

the different forms of writing the QED Lagrangian leads to $e = g \sin\theta_W = g' \cos\theta_W$ for particles of unit charge. The sectors of the Lagrangian density introduced so far leak of the interactions among the EW gauge bosons.

The symmetry of the Lagrangian density described so far must be broken in order to allow for non-zero physical masses of the particles. This is done by introducing additional scalar fields that interact with both the fundamental fermions and the gauge bosons. Since the EW interactions are local and the masses of the particles are different from zero also when non interacting, the scalar field must be always locally present and is then usually said to have a non vanishing vacuum expectation value. This mechanism is called Higgs mechanism, after the name of the scientist who proposed it [5, 6, 7]. The additional terms of the Lagrangian density describing the scalar field interaction with the gauge bosons and with itself can be written as

$$\mathcal{L}_H = \left(\left(i\partial^\mu - gT_i W^{i\mu} - g'\frac{Y}{2}B^\mu\right)\phi\right)^\dagger \left(\left(i\partial_\mu - gT_i W^i_\mu - g'\frac{Y}{2}B_\mu\right)\phi\right) - \mu^2\phi^\dagger\phi + \lambda(\phi^\dagger\phi)^2 \quad (6)$$

keeping only monomials up to dimension 4 in order to preserve the renormalizability of the theory. The choice fell on a SU(2) doublet of complex (charged) scalars with $Y = 1$: $\phi = \left(\phi^+, \phi^0\right)$. The symmetry is broken if the minimum of the potential $V(\phi) = \mu^2\phi^\dagger\phi + \lambda(\phi^\dagger\phi)^2$ occurs at $\langle\phi^\dagger\phi\rangle = v^2/2 \neq 0$, or, in other terms, if $\mu^2 = -\lambda v^2 < 0$. The gauge freedom allows to choose the scalar field in its ground state: $\phi = \left(0, v/\sqrt{2}\right)$. After this, a mass term for the weak bosons emerges in $\mathcal{L}_H$ with $m_W^\pm = \frac{gv}{2}$, $m_Z = \frac{v}{2}\sqrt{g^2 + g'^2}$ while the photon field A remains without mass term as the symmetry is still unbroken. An useful parameterization of the scalar field is the one in which the Higgs boson H appears after appropriate transformations of the fields, $\phi(x) \rightarrow \frac{1}{\sqrt{2}}(0, v + H(x))$, whose mass depends on the parameters describing the Higgs potential: $m_H = 2v\sqrt{\lambda} = \mu\sqrt{2}$. A similar approach describes the way fermions get their masses.

The remaining sector of SM, the Quantum-Chromo-Dynamics (QCD), deals with the strong interaction binding quarks into hadrons. Since the charge associated to the strong interaction is the color which occurrs into three different states (named "red", "blue" and "green"), the structure of the interaction term is dependent on 8 gauge bosons A_a, whose physical states are called gluons g:

$$\mathcal{L}_{QCD} = \bar{\psi}(i\partial\!\!\!/ - m)\psi - \frac{1}{4}G^{\mu\nu}_a G^a_{\mu\nu} - g_S\bar{\psi}\gamma_\mu T^a_S\psi A^\mu_a \quad (7)$$

where the index a runs on the 8 bosons and, to satisfy gauge invariance, the $G^a_{\mu\nu}$ tensor is defined as $G^a_{\mu\nu} = \partial_\mu A^a_\nu - \partial_\nu A^a_\mu - g_S f_{abc} A^b_\mu A^{c\,(5)}_\nu$. The final gauge structure of SM is then $\mathrm{SU}(3)_C \otimes \mathrm{SU}(2)_L \otimes \mathrm{U}(1)_Y$.

The SM has been experimentally tested to a high degree of accuracy by many predictions supported by a wide set of measurements, including

- observation of neutral currents at the Gargamelle detector in 1973 [8]
- observation of the W and Z electroweak gauge bosons at the UA1 [9, 10] and UA2 [11, 12] experiments at CERN in 1983, in $\bar{p}p$ collisions
- precise measurement of the W boson mass at CERN LEP [13] and Fermilab Tevatron [14] colliders
- precise measurement of the muon anomalous magnetic moment [15]
- precise measurements of Z pole observables in e^+e^- collisions at the CERN LEP [16]
- observation of the top quark at the CDF [17] and D0 [18] experiments at Fermilab in 1995, in $\bar{p}p$ collisions
- precise measurement of the top quark mass at the Fermilab Tevatron collider [19]

An experimental confirmation of the Higgs mechanism, such as the observation of the Higgs boson, is the major missing element to support the SM. The Higgs boson couples directly to the W and Z, controlling the high energy divergences predicted in WW scattering providing the Higgs mass is lower than the TeV scale [20, 21]. The Higgs also interacts with the fermionic fields with a coupling strength proportional to the fermion mass. This is why the search for Higgs boson is carried on looking at final states with t and b quarks or τ leptons. Figure 1 shows a comparison of different production and decay modes of the SM Higgs boson as a function of its mass.

Even if the Higgs mass cannot be directly predicted by the SM, it affects many phenomena which can be studied with precise EW measurements. Calculations of radiative corrections to m_W from loops involving H and t constrain the SM Higgs mass to $m_H = 89^{+35}_{-26}$ GeV/c^2, where experimental uncertainties at 68% CL are derived from a global fit to all Z pole data, m_t, m_W andd Γ_W [23]. Combining these results with direct searches at LEP and

(5) Here the f_{abc} are the structure constants of the SU(3) group: $[T^a_S,\ T^b_S] = i2 f_{abc} T^c_S$.

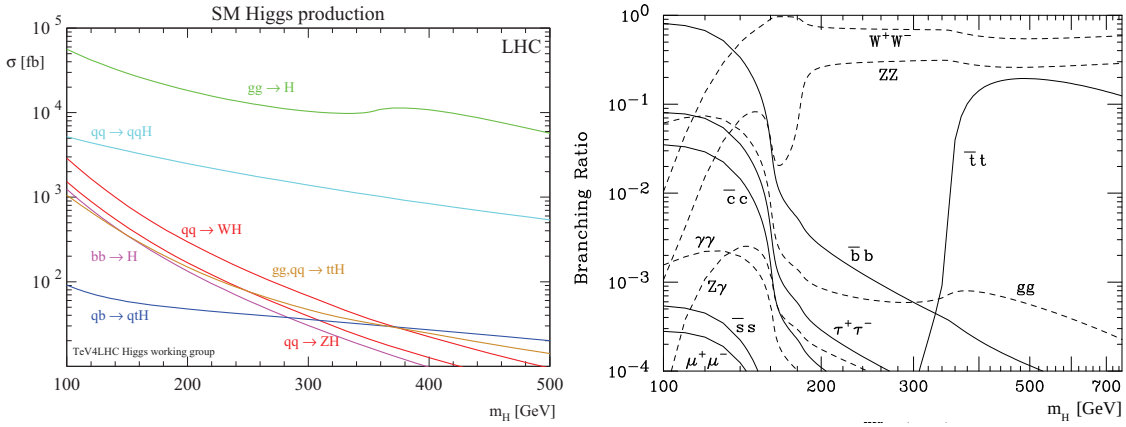

Figure 1: SM Higgs boson production cross sections for $\bar{p}p$ collisions at $\sqrt{s} = 14$ TeV (LEFT) and branching ratios for the main decays of the SM Higgs boson (RIGHT), as calculated as a function of Higgs boson mass [22].

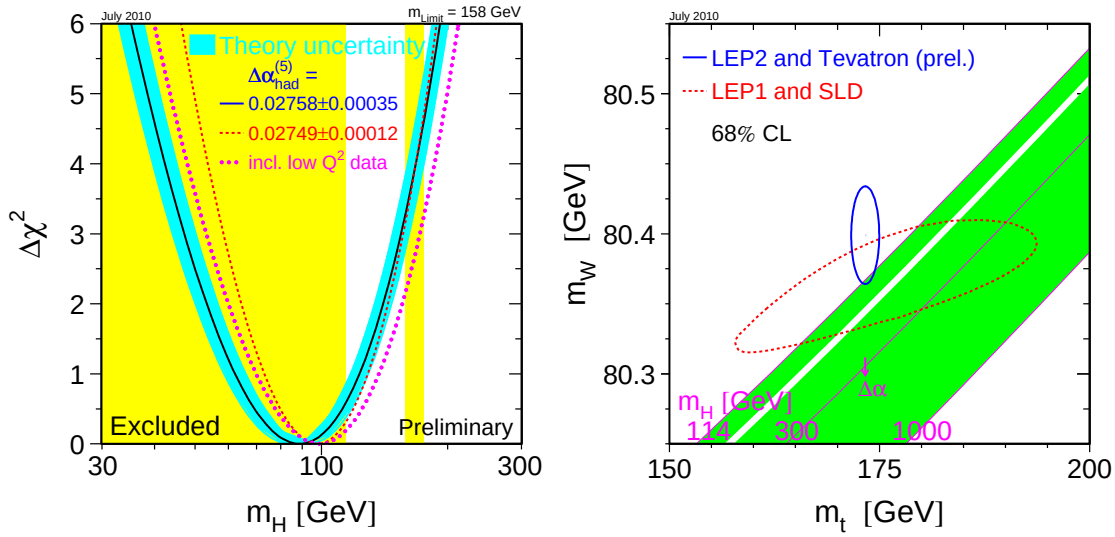

Figure 2: Limits to SM Higgs boson mass from a global fit to precise electroweak measurements. LEFT side shows the deviation of the χ^2 used in the global fit from its minimum, as a function of the Higgs boson mass, using all high-Q^2 data; the band represents an estimate of the theoretical error due to missing higher order corrections; vertical bands show the 95% CL exclusion limits from direct searches at LEP-II and Tevatron; dashed and dotted lines are obtained using different input data. RIGHT side shows the comparison of the indirect constraints on m_W and m_t based on LEP-I/SLD data (dashed contour) and the direct measurements from the LEP-II/Tevatron experiments (solid contour); in both cases the 68% CL contours are plotted; also shown is the SM relationship for the masses as a function of the Higgs mass in the region favoured by theory (below 1000 GeV) and not excluded by direct searches [23].

Tevatron, all studies carried on so far have lower and upper limits to m_H at 114.4 GeV/c^2 and 185 GeV/c^2, respectively, with 95% CL. Figure 2 displays the results of the global fit to precise electroweak measurements with the exclusions from direct searches.

Despite being a very successful model, our current theoretical understanding of the universe cannot be a fundamental description of particle physics. The SM fails in many points:

- it contains at least 18 free parameters (EW and strong couplings, m_Z, m_H, the masses of quarks and leptons and the CKM matrix parameters)
- it cannot predict the spectrum of fermion masses and the Higgs boson mass
- it assumes massless neutrinos, which was proven to be false after the discovery of neutrino oscillations [24, 25]
- it is not a true unification of the three gauge forces as the QCD coupling cannot be related to the EW ones
- it does not include gravitation as a quantum theory
- the Higgs boson mass diverges quadratically when single loop calculations are attempted
- it cannot explain the origin of the large amount of cold dark matter in the universe estimated from astrophysical measurements [26]

In particular, in order to get rid of the divergence of m_H, one must either finely tune the SM parameters to an extremely precise degree either reduce the SM scale to the order of $\sim$ 1 TeV. There are many "beyond SM" theories which try to explain the failures of the SM. One of these extensions would be the introduction of Supersymmetries (SUSY), which require every fermionic field to have a bosonic superpartner and vice-versa. Even in its minimal form, the Minimal Supersymmetric Standard Model (MSSM), a whole spectrum of undiscovered supersymmetric particles, usually called "sparticles", is predicted together with five different Higgs bosons. The single particle states of a SUSY theory fall into irreducible representations of the SUSY algebra called supermultiplets. The simplest ones consist in a two-component Weyl spinor associated to a complex scalar field, called *chiral* or *matter* supermultiplet, or a massless spin-1 gauge boson associated to a massless

spin-$\frac{1}{2}$ partner, called *gauge* or *vector* supermultiplet[(6)]. Quarks and leptons fit into chiral supermultiplet and their partners are called *squarks* and *sleptons*. Also the Higgs scalar boson must reside in a chiral supermultiplet since it has spin 0. To avoid anomalies in the theory, two Higgs supermultiplets are needed. Higgs fermionic superpartners are called *higgsinos*. Analogously, EW gauge bosons reside in gauge supermultiplets together with their superpartners called gauginos. All these particles would have been easy to detect long time ago if the supersymmetry were an unbroken symmetry in the vacuum state chosen by Nature. For this reason they are expected do have very large masses.

The first benefit of SUSY is the cancellation of radiative corrections to m_H without fine-tuning [27], which comes as a necessary consequence. As an additional benefit, the introduction of SUSY seems to allow the convergence of the gauge coupling constants at an energy scale of 10^{16} GeV. The introduction of SUSY allows also the inclusion of gravity in the theory as the supersymmetric algebra can include also spin-2 bosons such as the mediator of the gravitational interaction. Moreover SUSY comes with an additional discrete symmetry, called *R*-parity. If it is satisfied, le lightest SUSY particle is stable and massive but does not couple to ordinary matter, being a natural candidate for dark matter.

At present, all searches do refer to a specific model as it is needed to translate results into constraints on physically relevant quantities such as the masses of SUSY particles. Direct searches of SUSY at LEP and Tevatron aimed at the observation of the lightest supersymmetric particles. In particular, colored particles such as squarks and gluinos are expected to be produced at hadron colliders in larger amount but in the MSSM scenario they will suffer a large background. For this reason, SUSY searches are often carried on in multileptonic final states that may arise from chargino or neutralino decays[(7)].

The baseline for CMS detector performance is strongly constrained by the measurements it is aimed to [28, 29], such as finding evidence of the Higgs boson(s) or Supersymmetries, and that can be briefly summarized as:

- search for low mass $m_H < 150$ GeV/c^2 SM Higgs boson decaying to photon pairs

[(6)] The massless vector boson has two helicity states and therefore can be paired to a Weyl fermion into a supermultiplet. Moreover the masslessness of the vector boson is not a limit to the theory before the gauge symmetry is spontaneously broken.

[(7)] Charginos and neutralinos are the mass eigenstates that are expected to arise after the superimposition of the fields of gauginos and higgsinos. In particular, charginos are linear combinations of $W^{\pm}$ charged superpartner, called *wino*, and one charged higgsino. On the other side, neutralinos are combinations of γ and Z^0 neutral superpartners, called *photino* and *zino*, and one neutral higgsino.

- search for large mass $m_H > 130$ GeV/c^2 SM Higgs boson decaying to pairs of Z bosons, one of which may be virtual, turning out into two pairs of leptons: $H \to ZZ^* \to \ell^+\ell^-\ell^+\ell^-$; the four charged leptons may be either 4 electrons, 4 muons or one $\mu^+\mu^-$ pair jontly with a e^+e^- pair
- search for large mass $m_H > 130$ GeV/c^2 SM Higgs boson decaying to pairs of W bosons, one of which may be virtual, turning out into two opposite-sign muons and two neutrinos: $H \to WW^* \to \mu^+\nu\mu^-\bar{\nu}$
- search for additional heavy neutral gauge bosons predicted in many superstring-inspired theories or Great Unification theories, decaying to muon pairs: $Z' \to \mu^+\mu^-$
- search for new physics in dijet events
- search for SUSY at low masses in multijet plus large $\not{E}_T$ events[(8)]:
  - gluinos decaying to a quark-scalar quark pair
  - scalar quarks decaying to a quark plus chargino/neutralino pair
  - charginos and neutralinos decaying to leptons and scalar leptons
- study of the violation of the CP symmetry in the decay of the B_s^0 meson into $J/\psi\phi \to \mu^+\mu^+K^+K^-$
- search for a very large mass MSSM Higgs boson produced in association to b quark pairs and decaying into τ lepton pairs: $b\bar{b}H \to b\bar{b}\tau^+\tau^-$
- search for low mass $m_H < 135$ GeV/c^2 SM Higgs boson produced in association to t quark pairs and decaying into b quark pairs: $t\bar{t}H \to bW^+\bar{b}W^-b\bar{b}$
- study of QCD and jet physics at the TeV scale
- study of top quark physics
- study of EW physics

The final states of the processes to be studied at LHC need the CMS experiment meet the following requirements:

1. good muon identification and momentum resolution over a wide range of momenta

[(8)] Missing transverse energy $\not{E}_T$ is the vector in the transverse plane needed to set back to zero the vector sum of all the measured transverse momenta.

2. good dimuon mass resolution – 1% at 100 GeV
3. ability to determine without ambiguities the charge of muons with $p_T < 1$ TeV/c
4. good charged particle momentum resolution and reconstruction efficiency in the tracking volume
5. efficient triggering and offline tagging of τ leptons and b jets
6. good electromagnetic energy resolution
7. good diphoton and dielectron mass resolution – 1% at 100 GeV
8. measurement of the direction of photons, rejection of $\pi^0 \rightarrow \gamma\gamma$
9. efficient vertex localization and isolation of leptons and photons at high luminosities
10. good missing transverse energy $\not\!\!E_T$ and dijet mass resolution

Thesis Overview

This thesis presents some aspects of the great effort to meet the previous requirements also in the scenario of an upgraded LHC with a luminosity pushed higher than the designed one. This increase in luminosity is justified by the need to collect a large number of rare events to explore physics at the TeV scale, no matter if some important discoveries made in the next years or it they need even more data. In particular, if the luminosity is increased by about one order of magnitude than the design one, CMS will suffer large inefficiencies in the online data selection, whose first step is currently based on calorimeters and muon detectors and requires both data processing at 40 MHz rate and decision making in few microseconds. One possible approach is to include into the first level of data selection and rejection also other subdetectors, such as the Tracker, which are not currently used for this scope. The state of the art in the development of a new Tracker is reported and completed by measurements on prototypes of innovative Monolithic Arrays of Pixel Sensors. A possible scenario is chosen and used to study a Level 1 Tracking Trigger for the CMS experiment which is then tested on final states involving τ leptons.

The current status of the Large Hadron Collider and of the CMS Experiment are presented in Chapter 1, followed by a summary of the luminosity upgrades planned for the next decade and by the plans of the CMS Collaboration to meet new requirements.

Chapter 2 presents the need for a Tracker upgrade. The topic is split according to the two main phases of LHC luminosity upgrades and the replacement of the Pixel detector, coping with the first one, is described. Evolution of Triggering capabilities of the CMS detector at higher luminosities introduces the upgrades foreseen for the second phase.

One possible approach to select Tracker hits from large transverse momentum tracks is described in Chapter 3. This approach is based on the identification of wide charge deposits in silicon detectors which occurr at large impact angles of a charged particle. Results from a test beam in September 2010, performed on new Pixel detector prototypes, are used to state the feasability of a Tracking Trigger based on cluster width. A different approach, based on pattern hit correlations between to closely placed sensors, is presented in Chapter 4. The idea of Trigger Modules and its inclusion in a Tracker for Phase 2 upgrades are described.

Chapter 5 describes the simulation studies that have been carried on so far to understand the Trigger Primitives that can be built starting from pattern hit correlation. The work presented in this thesis is part of this study line and improvements to existing tools are deeply analysed. Chapter 6 describes the first attempt to extend the portfolio of Trigger Primitives described in Chapter 5, in order to have a global object out of the whole Tracker, called Level 1 track. The definition and the analysis of this object are described in detail together with its main limitations. Chapter 7 presents a possible application of Level 1 Tracking Trigger to final states with τ leptons, inspired to the current High Level Trigger selection, which is capable of remarkable improvements in background rejection if compared to a standalone Level 1 Calorimeter Trigger.

Relevant simulation tools are described within the text and in Appendix A. Appendix B describes one possible hardware implementation of the Level 1 Tracking Trigger objects used in the simulation studies presented in this thesis, showing common features and differences due to the pursuit of keeping their production simple and fast.

1. The CERN Large Hadron Collider and the Compact Muon Solenoid Experiment

After reviewing those topics in experimental particle physics involved in the goals of the LHC scientific programme, the experimental apparatus is described in this Chapter. The Large Hadron Collider and the Compact Muon Solenoid experiment are presented with particular emphasis on the subjects of major interest for the work described herein: collider luminosity, charged particle tracking system and Trigger. The Chapter ends with the description of the plans for LHC luminosity upgrades and the consequent changes to be implemented on the CMS detector.

1.1 The Large Hadron Collider

The CERN Large Hadron Collider is the most recent particle accelerator designed and built for frontier research in fundamental interactions [30]. It is a double superconducting proton storage ring operated in collider mode. It is installed in the 26.7 km tunnel which formerly hosted the LEP electron-positron collider. The LHC is connected to the CERN accelerator chain which provides proton injection to the LHC.

As the antiproton production process has very low efficiency, the LHC was designed as a *pp* collider [31, 32]. In fact, the high luminosity required to search for new physics, at center of mass energy $\sqrt{s} \sim 10$ TeV, would make the production and storage of intense antiproton beams unpractical and costly. This decision required two paired rings and special magnet design, twin-bore magnets, to allow same-charge particles rotate in opposite directions inside the pipes. The large momentum of protons circulating in the LHC requires a proper bending by dipole magnets. These superconducting magnets, shown in Figure 1.1, are made of NbTi cables cooled down to 1.9 K, differently from

other superconducting proton storage rings, such as the Tevatron, whose temperature is slightly higher than 4.2 K. The heat capacity of the superconducting cable is reduced by an order of magnitude allowing currents providing a bending field larger than 8 T. The twin-bore design allows the housing of magnets inside a common cold mass cooled down by common services. The main drawback is the magnetical and mechanical coupling of magnets to each other.

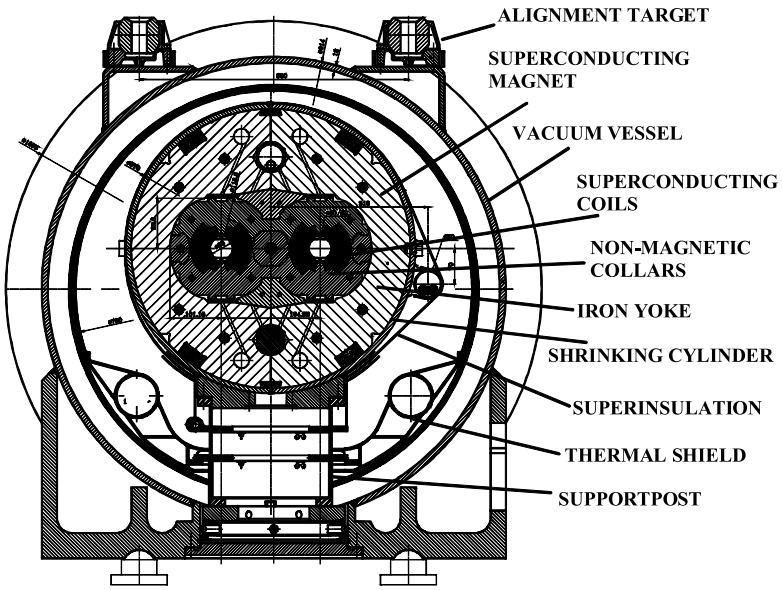

Figure 1.1: Cross section of a LHC superconducting dipole [33].

The design goal for LHC is to provide $\sqrt{s} = 14$ TeV pp collisions at a luminosity $\mathcal{L} = 10^{34}$ cm^{-2}s^{-1} with nominal bunch spacing of $T_{\rm b} = 25$ ns and a bunch fill ratio[(1)] $\simeq 0.8$. The total inelastic cross section, extrapolated from measurements at lower energies, is $\sigma_T = 80$ mb [34, 35], leading to approximately

$$N_{\rm ev} = \mathcal{L} \times \sigma_T \times T_{\rm b} \times \frac{N_{\rm b}^{\rm tot}}{N_{\rm b}^{\rm fill}} \simeq 25 \tag{1.1}$$

superimposed events per bunch crossing, also called pile-up events (PU), in each of the high-luminosity collision points where the ATLAS [36] and CMS [37] experiments are

[(1)]The bunch fill ratio is the ratio between the number of filled buckets at $T_{\rm b} = 25$ ns, $N_{\rm b}^{\rm fill} = 2808$, and the available ones, $N_{\rm b}^{\rm tot} = 3564$.

housed. Lower luminosities, 2 to 5 orders of magnitude lower than those delivered to ATLAS and CMS, are provided at different collision points for experiments dedicated to studies of CP violation in the b sector, LHCb [38], or pp cross section measurements, TOTEM [39] and LHCf [40]. In addition to the pp collider mode, the LHC can be operated as a heavy ion collider, providing data to both ATLAS and CMS and to a dedicated experiment: ALICE [41].

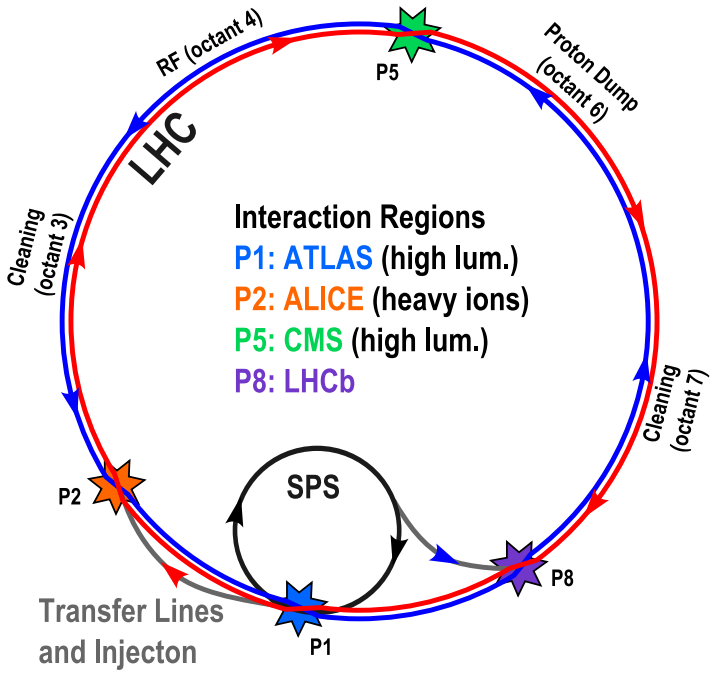

Figure 1.2: Layout of the CERN Large Hadron Collider, showing the interaction regions of the four main LHC experiments and the twin-ring design of the collider. The CMS experiment cave is located beyond access point 5, in Cessy (France).

The layout of the LHC is constrained by the cost-saving choice of exploiting the existing LEP tunnel. The high-luminosity intersections are located on opposite sides of the tunnel while ALICE and LHCb are housed in proximity of the injection points. In each of the four interaction regions the beam crosses the magnet passing from one bore to the other one, as depicted in Figure 1.2. Insertions at points 3 and 7 contain beam collimators, insertion at point 4 contains two independent RF systems (one per beam) and the beam is dumped in insertion at point 6. Both injection and extraction are done out of the storage ring plane.

The proton beams colliding in the LHC are accelerated and injected in stages [42]. Each proton beam is produced from gaseous hydrogen which is injected into the "duoplasmatron", a cavity where a strong electric field breaks them up into protons and electrons. Protons are collected and accelerated up to 100 keV to a a RF quadrupole which provides the first foccusing and a further kick up to 750 keV. This beam is sent to a linear accelerator, Linac 2, a multichamber resonant cavity tuned to provide 50 MeV beam. The first transfer line drives the beam to the Proton Synchrotron (PS) booster, a small four-ring synchrotron with 25 m radius. The PS Booster is used to raise the proton energy up to 1.4 GeV, which is actually a value higher than the 1.0 GeV reached in earlier operations of the PS. The 1.4 GeV beam is then accelerated up to 25 GeV by the PS, a 100 m radius synchrotron, the oldest proton accelerator used for frontier physics research at CERN. It is in the PS that the final bunch structure of LHC beams is obtained: 81 bunches with 25 ns time spacing between each other are extracted at the end of each cycle. Triplets of 81 bunches are transferred to the Super Proton Synchrotron (SPS), a 1 km radius proton synchrotron which was operated in a $p\bar{p}$ collider mode in the early eighties, allowing the discovery of the $W^{\pm}$ and Z^0 bosons, one of the milestones in elementary particle physics. Besides being connected to several secondary lines, the SPS is capable, after important upgrades, to bring protons up to an energy of 450 GeV, which is the one they enter the LHC. The whole injection chain is shown in Figure 1.3.

The major improvements to the existing accelerator complex can be summarized as follows [42]:

- new transfer lines to fill the LHC rings with both clockwise and anticlockwise rotating beams
- upgraded ejection system to extract the beams from the SPS
- reduction of coupling impedances in the SPS to achieve stability in LHC bunches
- 40 MHz and 80 MHz cavities in the PS to impress on the LHC bunch spacing of 25 ns, and bunch length of 4 ns
- increase the PS booster energy from 1.0 to 1.4 GeV to reduce space-charge effects in the PS
- new RF system in the PS booster to operate with one single beam end enabling two-batch filling

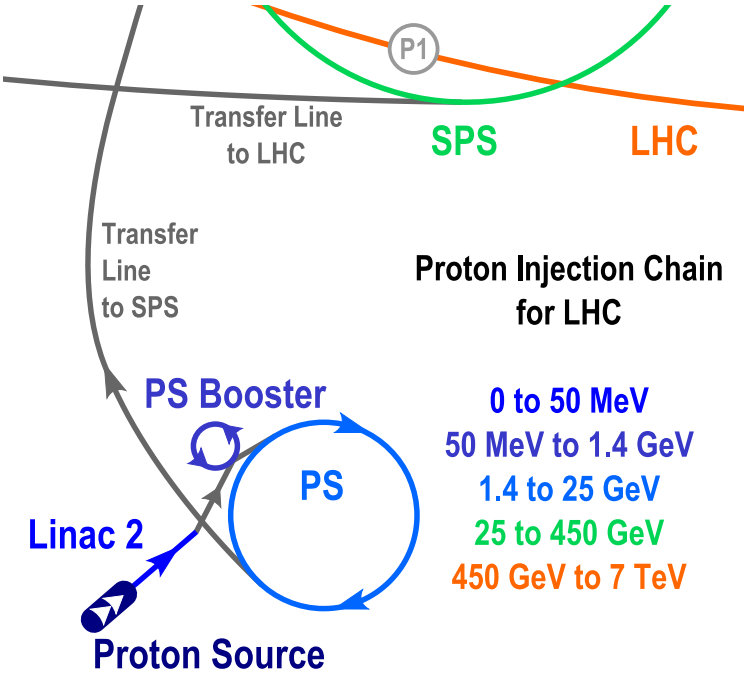

Figure 1.3: Layout of the CERN Large Hadron Collider Injection chain, showing the accelerators involved from proton source to the delivery of 7 TeV beams. All accelerators belonging to the CERN complex that are dedicated to other purposes are omitted.

- transverse fast dampers in the PS, SPS and LHC to reduce emittance blow-up due to mis-steering at injection

- new beam profile monitors with improved precision and resolution to cope with LHC beam brightness

The beam is injected into the two rings of the LHC by kickers in octants 2 and 8, close to the ALICE and LHCb interaction points.After the chosen amount of bunches is inside the LHC, the energy is raised by RF cavities from 450 GeV up to 3.5 TeV. This value is the one currently used after the beginning of the LHC scientific programme[(2)] and is planned to be doubled by 2011-2012 to reach the design center of mass energy for proton-proton collisions at 14 TeV.

[(2)] Also the bunch spacing and the fill ratio are lower than the design ones.

1.2 The CMS Experiment

The Compact Muon Solenoid [37] is a general purpose detector housed at interaction region 5 of the CERN Large Hadron Collider. It is designed around a 4 T solenoidal magnetic field provided by the largest superconducting solenoid ever built. The structure of CMS is shown in Figure 1.4, with particular emphasis to the volumes of the different subsystems: the Silicon Pixel Detector, the Silicon Strip Tracker, the Electromagnetic and Hadronic Calorimetry and Muon Detectors.

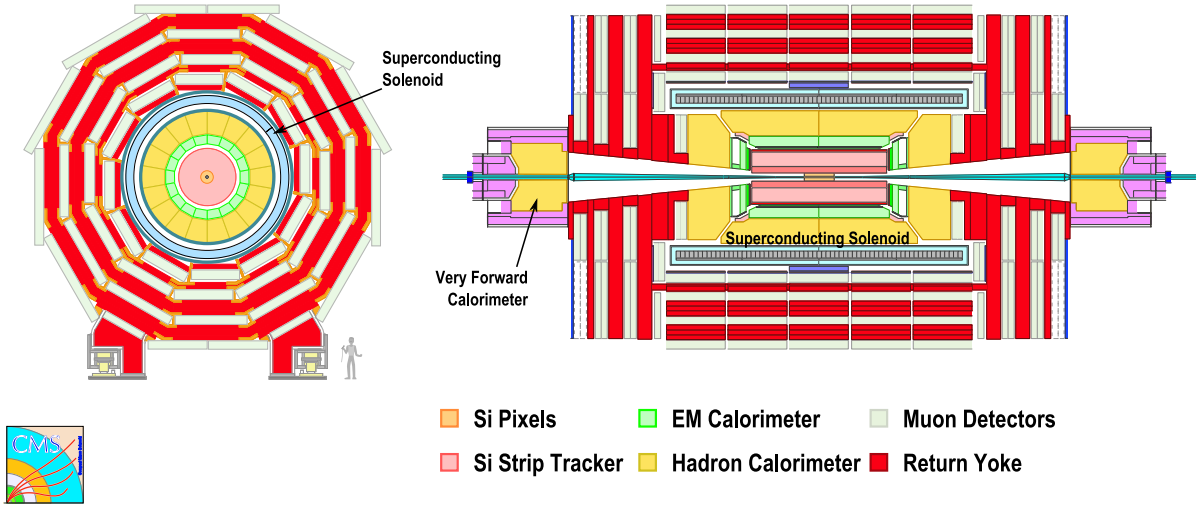

Figure 1.4: Transverse (LEFT) and longitudinal (RIGHT) cross sections of the Compact Muon Solenoid detector showing the volumes of the different detector subsystems. The transverse cross section is drawn for the central barrel, coaxial with the beam line, while complementary end-caps are shown in the longitudinal one.

The large number of collisions is source of a harsh radiation environment which imposed several constraints on the technologies used in the construction of CMS subdetectors. Both the sensitive elements and the readout electronics must withstand the high particle fluences in order to extend the detector lifetime and keep the detector performances robust against total dose radiation damage and single event upsets. Radiation tolerance will be an even more challenging issue if the LHC luminosity is increased up to $\sim 10^{35}$ cm^{-2}s^{-1} as currently planned in the forthcoming decade.

The reference frame used to describe the CMS detector and the collected events has

its origin in the geometrical center of the solenoid. It is embedded with different types of global coordinates measured with respect to the origin[(3)]:

- Cartesian coordinate system – $\hat{x}$ axis points towards the center of the LHC, $\hat{y}$ points upwards, perpendicular to the LHC plane, while $\hat{z}$ completes the right-handed reference pointing along the beamline towards the Jura mountains
- polar coordinate system – directions are defined with an azimuthal angle $\tan\phi = y/x$ and a polar angle $\tan\theta = r_\perp/z$
- from polar angle the pseudorapidity η is obtained, in analogy with the rapidity y measuring the same angle for massless particles

$$\eta = -\ln\left(\tan\frac{\theta}{2}\right) = \lim_{m\to 0} y(\mathbf{p}, m) = \lim_{m\to 0}\frac{1}{2}\ln\left(\frac{E+p_z}{E-p_z}\right) \tag{1.2}$$

1.2.1 The Magnet

The whole CMS detector is designed around a $\sim$ 4 T superconducting solenoid [43] 12.5 m long and with inner radius of 3 m. To reach the necessary current of 41.7 MA-turn, the 220 t solenoid cold mass is composed of a 4-layer of NbTi wires co-extruded and mechanically reinforced with Al. The solenoid thickness is 3.9 radiation lengths and it can store up to 2.6 GJ of energy.

The field is closed by a 10,000 t iron return yoke made of five barrels and two end-caps, composed of three layers each. The yoke is instrumented with four layers of muon stations. The coil is cooled down to 4.8 K by a helium refrigeration plant, while insulation is given by two pumping stations providing vacuum on the 40 m^3 of the cryostat volume.

The magnet was designed in order to reach precise measurement of muon momenta. A high magnetic field is required to keep a compact spectrometer without stringent demands on the spatial resolution and the alignment of muon chambers. The solenoidal field was chosen because it keeps the bending in the transverse plane, where an accuracy better than 20 μm is acheved in vertex position measurements. Such a strong bending facilitates Triggers based on track extrapolation to the vertex. The size of the solenoid

[(3)] Global coordinates are measured in the CMS reference frame while local coordinates are measured in the reference frame of a specific subdetector or sensitive element.

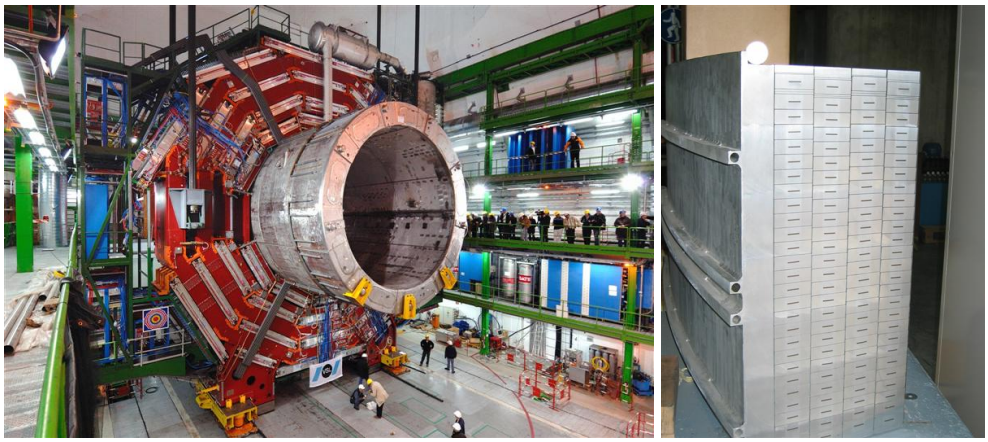

Figure 1.5: (LEFT) CMS superconducting solenoid during assembly: the barrel return yokes are painted red. Muon detectors are already mounted and visible between return yoke layers. (RIGHT) Cross section of the CMS magnet cables [44].

allows efficient muon detection and measurement up to a pseudorapidity of 2.4. This way the spectrometer can be built with only one magnet, simplifying the overall detector design. The inner radius is large enough to accommodate the silicon tracker and the calorimeters.

A high magnetic field let the detector layout be compact and enables an efficient first level Triggering on muons, which is one of the goals of CMS. This property mus be optimized without compromising the performance of other parts of the detector. The goal is to achieve sharp Trigger thresholds in order to keep first level Trigger rate low. At a muon p_T threshold of 20 GeV/c the muon Trigger rate almost doubles going up from 6 kHz to about 10 kHz when the magnetic field goes down from 4 T to 3 T. The magnet is currently operated at 3.8 T.

1.2.2 Muon Detectors

Detection of muons at CMS exploits different technologies and can be thought as a "muon system" rather than a single detector [45]. While electromagnetic and hadronic backgrounds are mainly contained inside the calorimeters, muons are able to travel through the solenoid with minimal energy loss inside the detector. Muons can provide strong indication of a signal event and are natural candidates for Triggering purposes. The CMS muon system was designed to cope with three major functions: robust and

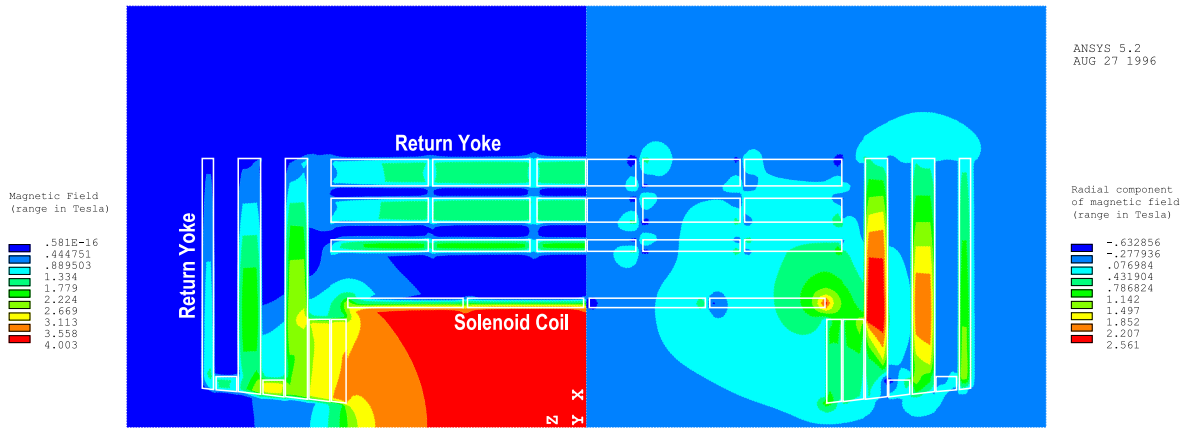

Figure 1.6: Simulations of the CMS solenoid magnetic field tuned at 4 T: (LEFT) magnitude of the field and (RIGHT) radial component of the field [43].

fast identification of muons, good resolution of momentum measurement and Triggering.

The muon system is composed of three types of gaseous detectors, located inside the empty volumes of the iron yoke and therefore arranged in barrel and end-cap sections. The coverage of muon system is shown in Figure 1.7.

In the barrel region the neutron-induced background is small and the muon rate is low; moreover, the field, as shown in Figure 1.6, is uniform and contained in the yoke. For these reasons, standard drift chambers with rectangular cells are used. The barrel drift tubes (DT) cover the $|\eta| < 1.2$ region and are organized in four stations housed among the yoke layers. The first three stations contain 12 chambers, arranged in two layers providing measurement in the transverse plane and one layer measuring along z, each of them containing four chambers. The fourth station provides measurement only in the transverse plane. To eliminate dead spots in the efficiency, cells in consecutive layers are shifted by half of their width. Both the muon rates and backgrounds are high in the forward region, where the magnetic field is large and non uniform. The choice for muon detectors fell upon cathode strip chambers (CSC) because of their fast response time, fine segmentation and radiation tolerance. Each end-cap is equipped with four stations of CSCs. The CSCs cover the $0.9 < |\eta| < 2.4$ pseudorapidity range. The cathode strips are oriented radially and provide precise measurement in the bending plane, the anode wires run approximately perpendicular to the strips and are read out to measure the pseudorapidity and the beam-crossing time of a muon. The muon reconstruction efficiency is typically 95-99% except for the regions between two barrel DT wheels or at

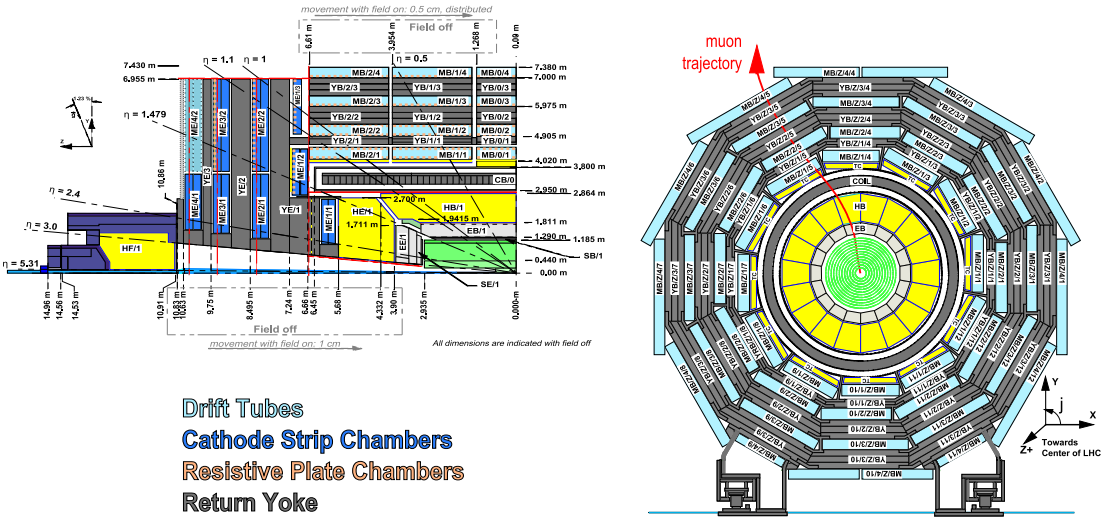

Figure 1.7: Transverse and longitudinal cross sections of the CMS detector showing the muon system with particular emphasis on the different technologies used for detectors; the ME/4/2 CSC layers in the end-cap were included in the design but are not currently installed.

the transition between DTs and CSCs, where the efficiency drops.

Both the DTs and CSCs can Trigger on muons with a Level 1 p_T resolution of 15% and 25% respectively. Additional Trigger-dedicated muon detectors were added to help in measuring the correct beam-crossing time. These are Resistive Plate Chambers (RPC), gaseous detector operated in the avalanche mode, which can provide independent and fast Trigger with high segmentation and sharp p_T threshold over a large portion of the pseudorapidity range. The overall p_T resolution on muons is shown in Figure 1.8, with emphasis on the different contribution from the Muon System and the Silicon Tracker

1.2.3 Calorimetry

Identification of electrons, photons and hadrons relies on accurate calorimetry, which is a destructive measurement of the energy of a particle. As in most of the particle physics experiments, a distinction is made between electromagnetic calorimetry and hadron calorimetry. EM calorimetry is based on the production of EM showers inside an absorber while hadron calorimetry measures the effects of inelastic scattering of hadrons, including production of photons from neutral pions and muons and neutrinos from weak decays. Calorimetry must be precise and hermetic also to measure any unbalancement

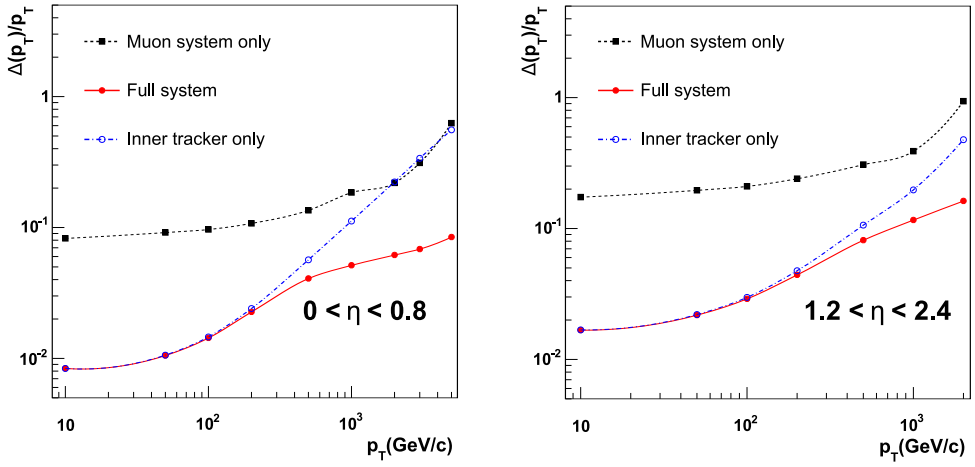

Figure 1.8: Resolution on p_T measurement of muons with the Muon System, the Silicon Tracker or both, in the barrel (LEFT) and end-caps (RIGHT) [37].

of momenta in the transverse plane which can signal the presence of undetected particles such as large p_T neutrinos.

The electromagnetic calorimeter of CMS (ECAL, [46]) is a homogeneous calorimeter, where the absorber and the sensitive material are the same. ECAL is composed of 61,200 lead tungstate ($PbWO_4$) cristals in the barrel region and 7,324 ones in the endcaps, as shown in Figures 1.9 and 1.10. Endcaps are equipped with a preshower detector. $PbWO_4$ was chosen because of its high density, 8.28 g/cm^3, short radiation length, 0.89 cm, small Molière radius, 2.2 cm. The calorimeter can be kept compact with fine granularity while scintillation and optical properties of $PbWO_4$ make it fast and radiation tolerant. Signal transmission exploits total internal reflection. Scintillation light detection relies on two different technologies. Avalanche photodiodes are used in the barrel region, mounted in pairs on each crystals, while vacuum phototriodes are used in the endcaps. The preshower detector is a sampling calorimeter composed of lead radiators and silicon strips detectors and it is used to identify neutral pions in the forward region. The energy resolution measured with electron beams having momenta between 20 and 250 GeV/c is

$$\left(\frac{\sigma_E}{E}\right)^2 = \left(\frac{2.8\%}{\sqrt{E}}\right)^2 + \left(\frac{0.12}{E}\right)^2 + (0.30\%)^2 \tag{1.3}$$

where the different contributions can be read as:

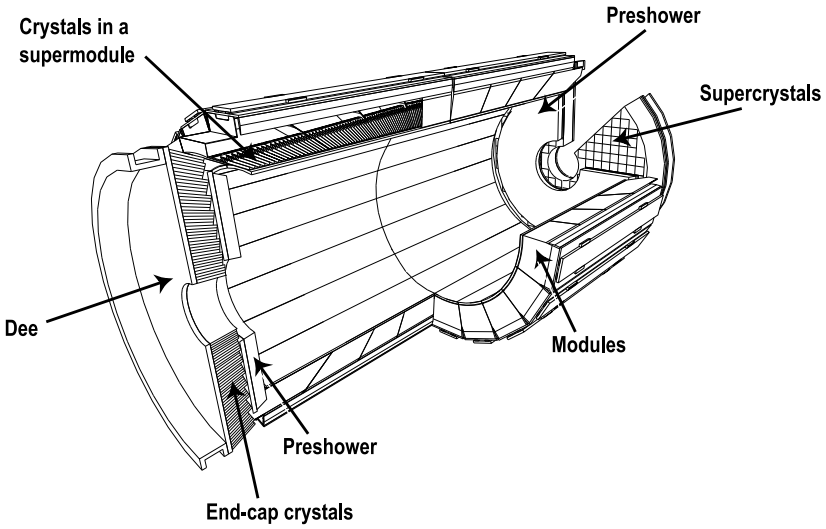

Figure 1.9: Cut-away view of the CMS ECAL showing the hierarchical structure of crystals arranged in supercystals and modules and the orientation of crystals whose major axis is always directed to the origin of the reference frame.

- the first term is the stochastic one, due to fluctuations in the lateral shower containment and in the energy released in the reshower
- the second term is the noise one, due to electronics, digitization and pileup
- the third term is the constant one, due to intercalibration errors, energy leakage from the back of the crystal and non-uniformity in light collection.

The hadron calorimeter of CMS (HCAL, [47]) is a sampling calorimeter crucial in measuring hadron jets and neutrinos or exotic particles resulting in apparent missing transverse energy. A longitudinal view of HCAL is shown in Figure 1.11. The hadron calorimeter size is limited in the barrel region, $|\eta| < 1.3$, by the maximum radius of ECAL and the inner radius of the solenoid coil. Because of this, the total amount of the absorber material is limited and an outer calorimeter layer is located outside of the solenoid to collect the tail of the showers. The pseudorapidity coverage is extended in the $3 < |\eta| < 5.2$ by forward Cherenkov-based calorimeters. The barrel part, HB, consists of 36 wedges, segmented into 4 azimuthal sectors each and made out of flat brass absorber layers, enclosed between two steel plates and bolted together without any dead material on the full radial extent. Additional segmentation in pseudorapidity of plastic scintillator provide an overall segmentation with $\Delta\phi \times \Delta\eta = 0.087 \times 0.087$. The same segmentation is mantained in endcap calorimeters, HE, up to $|\eta| < 1.6$, while becoming two times

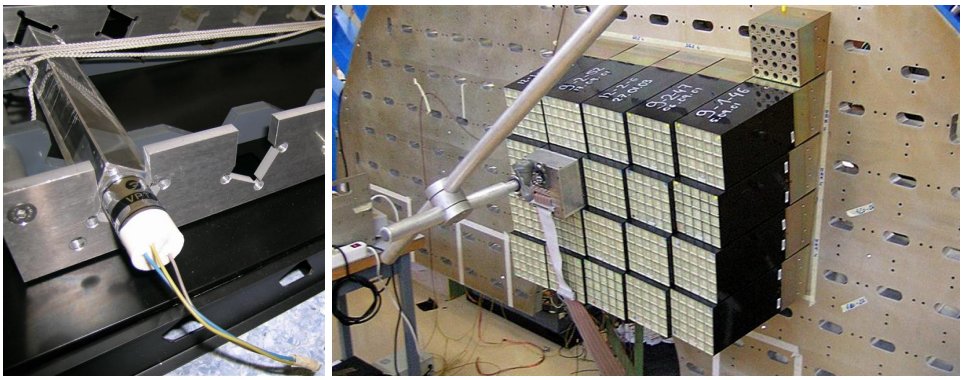

Figure 1.10: (LEFT) ECAL endcap crystal coupled to the readout VPT and supercrystal assembly (RIGHT) [44].

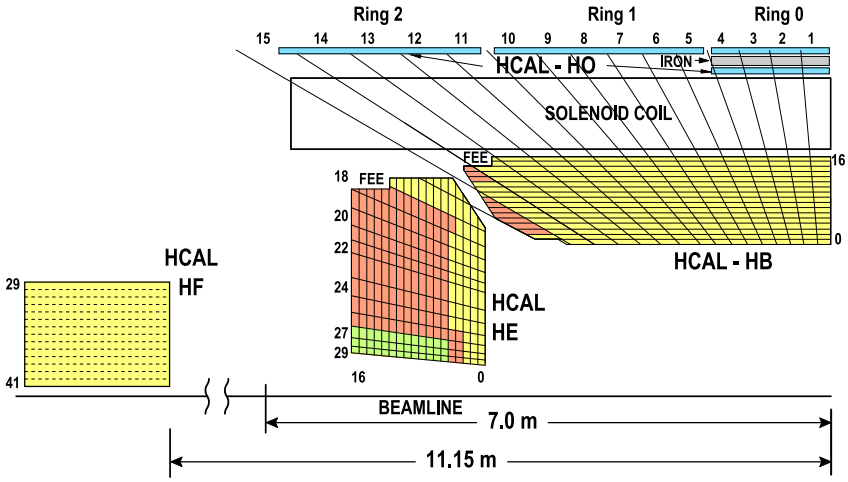

Figure 1.11: Cross section of the CMS HCAL showing the tower segmentation.

larger at larger pseudorapidities. The maximum material amount in both HB and HE corresponds to approximately 10 interaction lengths λ_I. The energy resolution on single electron and hadron jets is shown in Figure 1.12.

1.2.4 Silicon Tracker

The core of CMS is a tracker [48, 49] designed to provide a precise and efficient measurement of the trajectories of charged particles emerging from LHC collisions and reconstruction of secondary vertices. The tracker, with its 2.5 m diameter and 5.8 m length, surrounds the interaction region and is fully immersed in the 4 T magnetic field

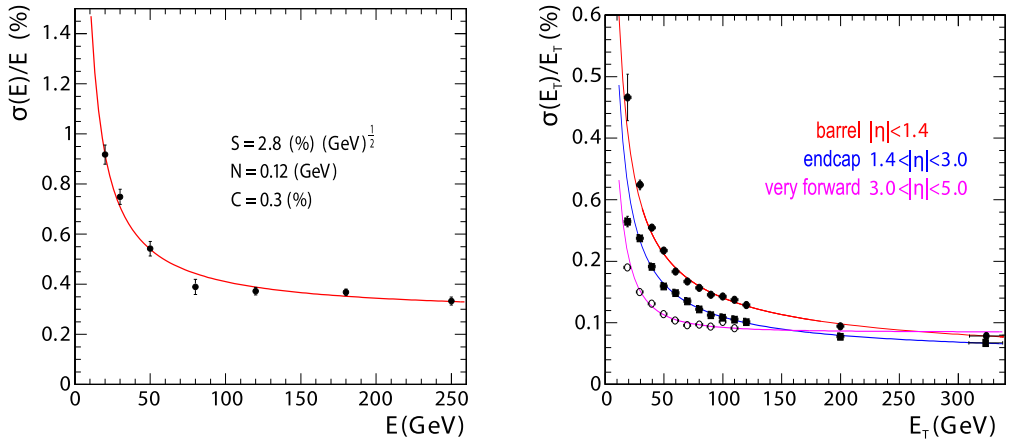

Figure 1.12: (LEFT) ECAL energy resolution as a function of the electron energy as measured from a beam test. The energy was measured in a 3×3 crystals array with the electron impacting the central one. The stochastic, noise and constant terms are given. (RIGHT) The jet transverse energy resolution as a function of the transverse energy for barrel jets, end-cap jets and very forward jets reconstructed with an iterative cone algorithm with cone radius $R = 0.5$ [37].

produced by the CMS superconducting solenoid. In order to obtain reliable trajectory identification and attribution to the correct bunch crossing, the CMS tracker deserves high granularity and fast response because of the large number of particles, $\sim$ 1000, expected to be produced at full LHC luminosity with more than 20 overlapping interactions per bunch crossing, as in (1.1). To cope with such requirements, a high power of on-detector electronics is required together with an efficient cooling. This conflicts with the need of keeping the material budget as low as possible to limit multiple scattering, bremsstrahlung, photon conversion and nuclear interactions and lead to a compromise. Another relevant aspect of the tracker design is the radiation damage due to intense particle fluxes, particularly in the innermost layers. The chosen design is expected to guarantee a tracker lifetime of $\sim$ 10 years in the harsh LHC environment.

The CMS tracking system is composed of both silicon Pixel and Strip detectors, as shown in Figure 1.13. The Pixel detector consists of 1440 pixel modules arranged in three barrel layers and two disks in each endcap as in Figure 1.16. The Strip detector consists of an inner tracker with four barrel layers and three endcap disks and an outer tracker with six barrel layers and nine endcap disks, housing a total amount of 15,148 Strip modules of both single-sided and double-sided types. Its active silicon surface of about 200 m^2 makes the CMS tracker the largest silicon tracker ever built.

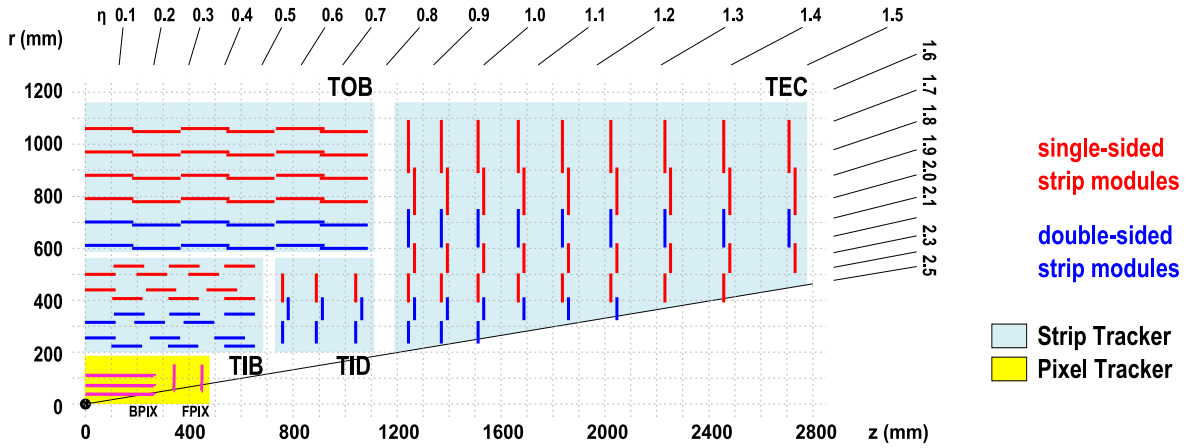

Figure 1.13: Layout of the CMS silicon tracker showing the relative position of hybrid pixels, single-sided strips and double-sided strips.

The LHC physics program requires high reliability, efficiency and precision in reconstructing the trajectories of charged particles with transverse momentum $p_T > 1$ GeV/c in the pseudorapidity range $|\eta| < 2.5$. Heavy quark flavours can be produced in many of the interesting channels and a precise measurement of secondary vertices is therefore needed. The tracker completes the functionalities of ECAL and of the muon system to identify electrons and muons. Also hadronic decays of tau leptons need robust tracking to be identified in both the one-prong and three-prongs topologies. Tracker information is heavily used in the High Level Trigger of CMS to help in reducing the event collection rate from the 40 MHz of bunch crossing to the 100 Hz of mass storage.

The performance of the Silicon Tracker in terms of track reconstruction efficiency and resolution of measurements are shown in Figures 1.14 and 1.15 respectively. The first one, in particular, shows the difference in reconstruction efficiency for muons and pions due to the larger interaction cross section of pions, which cannot be assumed to be minimum-ionising particles and therefore are much more degraded by the amount of material.

Silicon Pixel Detector The large number of particles produced at 25 PU result into a hit rate density of 1 MHz/mm^2 at 4 cm from the beamline decreasing down to 3 kHz/mm^2 at a radius of 115 cm. Pixel detectors are used at radii below 10 cm to keep the occupancy below 1%. The chosen size for Pixels, 0.100×0.150 mm^2 in the transverse and longitudinal directions respectively, leads to an occupancy of the order of 10^{-4}. The layout of the Pixel Detector consists of a barrel region (BPIX), with three barrels at radii

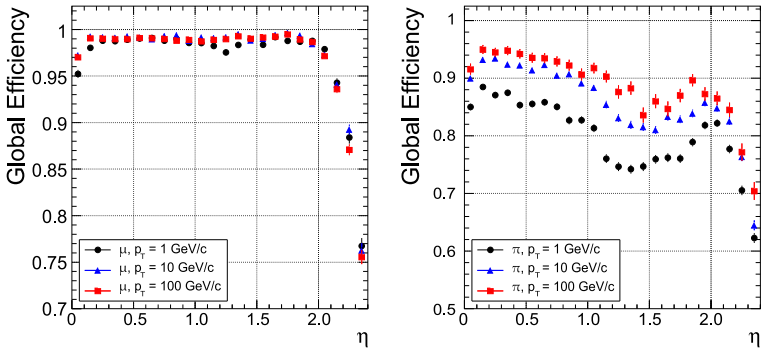

Figure 1.14: Global track reconstruction efficiency as a function of track pseudorapidity for muons (LEFT) and pions (RIGHT) of transverse momenta of 1, 10 and 100 GeV/c [37].

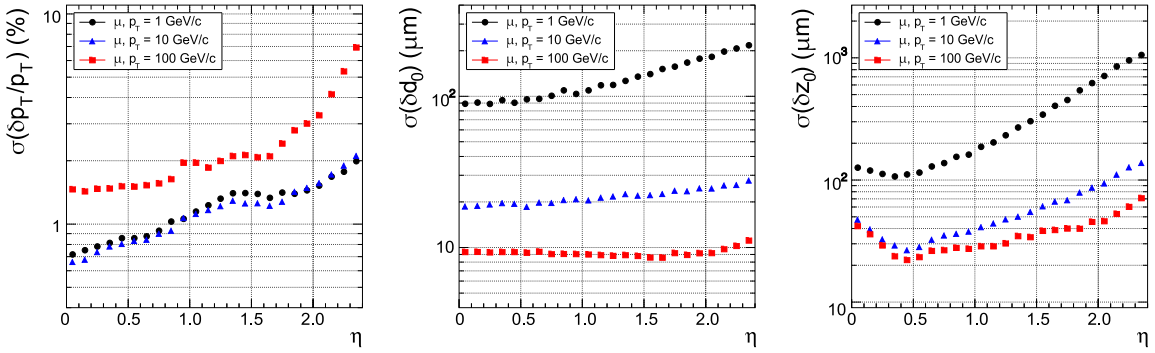

Figure 1.15: Resolution of several track parameters as a function of track pseudorapidity for single muons with transverse momenta of 1, 10 and 100 GeV/c: transverse momentum (LEFT), transverse impact parameter (MIDDLE) and longitudinal impact parameter (RIGHT) [37].

of 4.4, 7.3 and 10.2 cm, complemented by two disks on each side (FPIX), at 34.5 and 46.5 cm from the interaction point. This layout provides about 66 million Pixels covering a total area of about 1 m^2 and measuring three high precision points on each charged particle trajectory up to $|\eta| = 2.5$. Detectors in forward Pixel disks are tilted by 20° in a turbine-like geometry to induce charge sharing and achieve a spatial resolution of about 20 μm.

Pixel sensors are built with the n^+-on-n technology. They consist of high dose n-implants into a high resistivity, 3.7 kΩcm, n substrate. This resistivity leads to a full depletion voltage of 50-60 V of the 0.285 mm thick sensors. A rectifying pn junction is

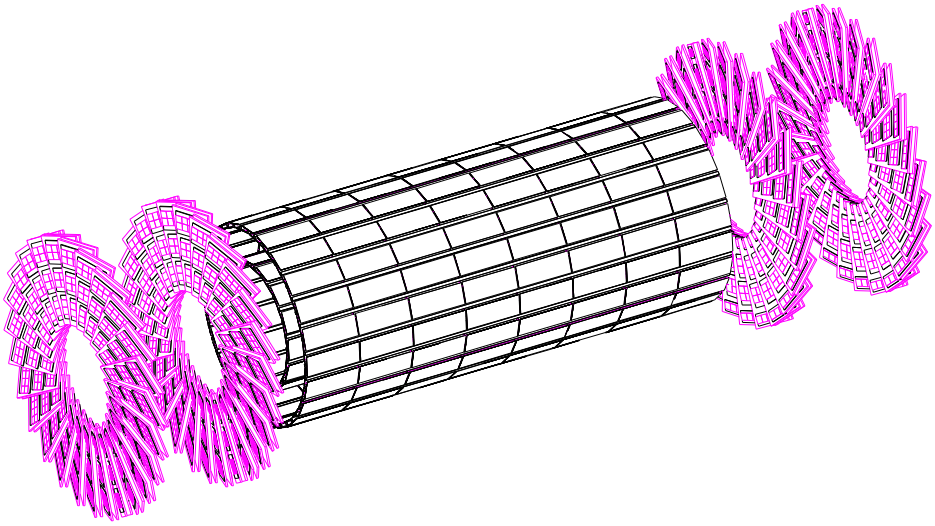

Figure 1.16: Layout of the current CMS Pixel Detector.

placed on the back side and surrounded by a multi-guard ring structure. This approach ensures high collected charge at moderate bias voltages (< 600 V), even after high hadron fluences, and it allows the guard ring scheme to keep all edges grounded. Pixels are isolated from each other by means of *p*-stops in disks and *p*-sprays in barrels. CMS Pixels are *hybrid* Pixels, as their individual read-out is housed in a different wafer than the sensor. Each read-out cell is built on an array with the same scheme as the sensor one and each Pixel is bump-bonded to its individual readout by means of indium microspheres which guarantee electric contact [50]. Indium bumps are roughly 50 μm wide in diameter.

Read-out chips (ROCs) are full custom ASIC fabricated in commercial 0.250 μm CMOS technology which employ enclosed layout transistors. Every ROC pixel cell collects, amplifies and buffers the charge signal from the corresponding bonded sensor Pixel. Signals exceeding the in-cell programmable threshold are considered worth hit and stored in an analog buffer at the ROC periphery, together with the pixel coordinates and a beam-synched timestamp. When a Level 1 Trigger token asks retrieving an event, all stored hit whit matching timestamp are sent to the token manager chip which in turn stitch the data coming from an entire module (16 ROCs) and stream them to the front end DAQ. Non retrieved are discarded to free the buffer. Cell threshold levels are per-pixel, real time adjustable via a 4 bit DAC to account for process variation and tolerances. The data loss dominant mechanism is the overflow of the periphery buffer: for too large hits rate the present size of the buffer is not enough to store all collected hits until the Level 1

Trigger token arrives. Second order data-loss patterns are related to the internal double column structure of the ROC and to the dead period a cell experience after registering a hit, which renders it insensitive for some beam bunches.

Silicon Strip Tracker In the inner Strip Tracker, which is housed between radii of 20 and 55 cm, the reduced particle flux allows a typical cell size of 0.080×100 mm^2, resulting in a 2% occupancy per Strip. In the outer region, the Strip pitch is increased to 0.180×250 mm^2 together with the sensor thickness which scales from 0.320 mm to 0.500 mm. This choice compensates the larger capacitance of the strip and the corresponding larger noise with the possibility to achieve a larger depletion of the sensitive volume and a higher charge signal.

The Tracker Inner Barrel and Disks (TIB and TID) deliver up to 4 r-ϕ measurements on a trajectory using 0.320 mm thick silicon strip sensors with strips parallel to the beam-line. The Strip pitch is 0.080 mm in the first two layers and 0.120 mm in the other two layers, while in the TID the mean pitch varies from 0.100 mm to 0.141 mm. Single point resolution in the TIB is 0.023 mm with the finer pitch and 0.035 mm with the coarser one. The Tracker Outer Barrel (TOB) surrounds the TIB/TID and provides up to 6 r-ϕ measurements on a trajectory using 0.500 mm thick sensors. The Strip pitch varies from 0.183 mm in the four innermost layers to 0.122 mm in the outermost two layers, corresponding to a resolution of 0.053 mm and 0.035 mm respectively. Tracker End-Caps (TEC) enclose the previous subdetectors at 124 cm $< |z| <$ 282 cm with 9 disks carrying 7 rings of microstrips, 4 of them are 0.320 mm thick while the remaining 3 are 0.500 mm thick. TEC strips are radially oriented and their pitch varies from 0.097 mm to 0.184 mm.

As shown in Figure 1.13, the first two layers and rings of TIB, TID and TOB, as well as three out of the TEC rings, carry Strips on both sides with a stereo angle of 100 milliradians to measure the other coordinate: z in barrels and r in rings. This layout ensures 9 hits in the silicon Strip Tracker in the full acceptance range $|\eta| < 2.4$, and at least four of them are two-dimensional. The total area of Strip Tracker is about 198 m^2 read out by 9.3 million channels. The material budget strongly depends on the pseudorapidity as shown in Figure 1.17.

Strip sensors are built with the p^+-on-n technology. Substrate resistivity ranges from 1.55 to 3.25 kΩcm for 0.320 mm thick sensors and from 4 to 8 kΩcm for 0.500 mm thick ones. Differently from Pixel sensors, which are built fabricated a double-side

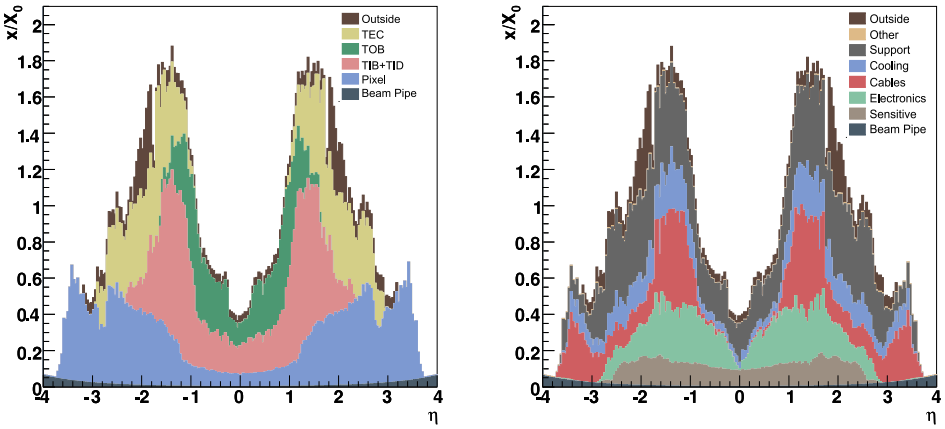

Figure 1.17: Material budget of the current CMS Tracker in units of radiation length X_0 as a function of the pseudorapidity, showing the different contribution of subdetectors (LEFT) and functionalities (RIGHT) [37].

process, Strips are made with single-side process and show a significant bow which is required to be less than 0.100 mm. The *pn* junction can move to the rear side of the sensor after receiving significant dose of radiation, because of substrate type inversion. A compromise between low strip capacitance and good high-voltage behaviour of the sensor is obtained by choosing a width-over-pitch ratio of 0.25, corresponding to a 1.2 pF/m capacitance and bias voltages up to 500 V. Strip sensor are reaf out by a custom ASIC, the APV25, featuring an analogue pipeline capable of storing the full analogue information to be used for accurate pedestal and common mode subtraction as well as data sparsification. All control signals are transmitted by optical links.

Radiation Damage and Power Consumption One major constraint in the design of the Silicon Tracker is the radiation damage introduced by high particle fluxes [28]. The estimates of the radiation suffered by the Tracker are listed in Table 1.1. Despite fluxes are expected to decrease when the distance from the beamline becomes larger, the outer region of the Strip Tracker is subject also to the flow of neutrons generated in hadronic interactions in the $PbWO_4$ crystals of ECAL. The effects taken into account in the evaluation of radiation damage of the Tracker are:

- surface damage created by holes, generated by the passage of charged particles, which are trapped in SiO_2 layers – this is particularly important for front-end electronics where the properties of MOS structures can be altered by this kind of damage

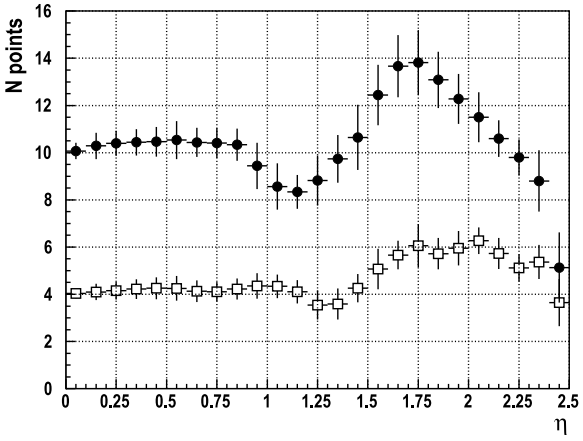

Figure 1.18: Number of measurement points in the Strip Tracker as a function of the pseudo-rapidity. Filled circles show the total number (back-to-back modules count as one) while open squares show the hits in stereo layers.

- bulk damage, which is a change in the Si crystal lattice induced by non-ionising energy losses – this mainly affects the sensitive elements by adding new energy levels in the band gap and increasing the leakage current, further damage results in doping change from *n*- to *p*-type and remarkable changes of the depletion voltage

- transient phenomena such as single event upsets (SEU), due to the generation of charge by ionising particles in the electronic circuitry which result in flipping the state of a memory cell and compromise the output value or the correct functioning of the read-out.

r (cm)	fast hadron fluence (10^{14}cm^{-2})	dose (Mrad)	charged particle flux (cm^{-2}s^{-1})
4	32	84	10^8
11	4.6	19	
22	1.6	7	6×10^6
75	0.3	0.7	
115	0.2	0.18	3×10^5

Table 1.1: Radiation levels within the barrel of CMS Tracker at different radial distances from beamline after 10 years of operation corresponding to 500 fb^{-1} of integrated luminosity [37].

Surface damage scales with the absorbed dose and is reduced using ⟨100⟩ oriented crystals for the Strip sensors, instead of the more common ⟨111⟩, bulk damage scales

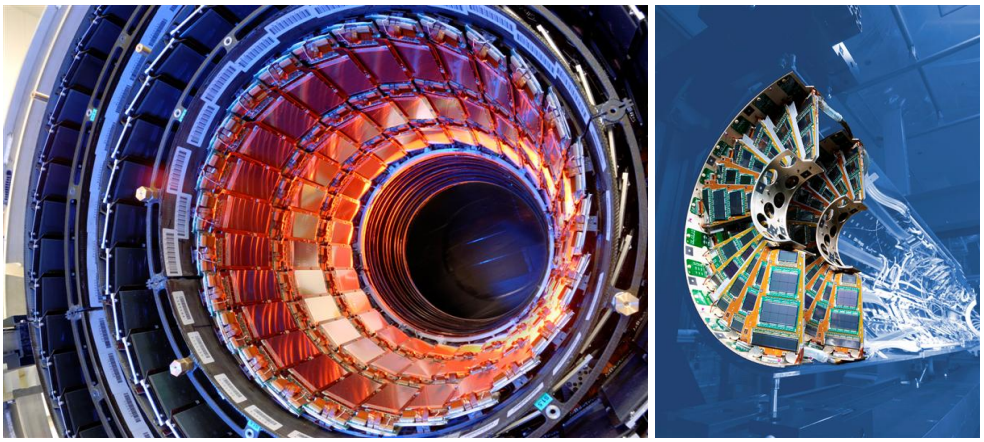

Figure 1.19: (LEFT) TIB during assembly and (RIGHT) FPIX during assembly [44].

approximately with the fast hadron fluence and is expected to create additional trapping centers and therefore reduce the signal by roughly 10% in 10 years. For this reason the signal-to-noise ratio must be guaranteed to be at least 10 to 1 over the full detector lifetime. The increased leakage current can lead to a dangerous self-heating of the silicon sensor, which starts a positive feedback known as thermal runaway. The modules are therefore efficiently coupled to che cooling system which brings the silicon temperature down to $-10\,^{\circ}$C and is capable of extracting ~ 60 kW generated by front-end and read-out electronics. The cooling fluid temperature at the end of the detector lifetime is expected to be even lower: $-27\,^{\circ}$C. All the Tracker structures must be robust against thermal cycles between room temperature and 30 to 50 $^{\circ}$C lower ones. Read-out electronics is fabricated in 250 nm CMOS technology which is radiation hard because of the thin gate oxides and special design rules. The bulk damage of the sensitive volume is therefore the main limit to the detector lifetime and, to ensure charge collection is efficient, depletion voltages must be as high as 500 V after 10 years of LHC running. Pixels need lower depletion voltages, because of the different sensor layout. The power consumption is 55 μW for each Pixel, including 13 μW from the leakage current at final fluences. This adds up to 3.6 kW for the whole Pixel Detector. The power load on aluminum cooling tubes is expected to be 50 W/m. The sensors are refirgerated by a liquid phase C_6F_{14} cooling.

1.2.5 Trigger and Data Aquisition

High bunch crossing rates and design luminosity at LHC correspond to approximately 20-25 superimposed events every 25 ns, for a total of 10^9 events per second. The

large amount of data associated with them is impossible to store and process, therefore a dramatic rate reduction has to be achieved. This is obtained with two steps: the Level 1 Trigger [51] and the High Level Trigger (HLT, [52]).

The Level 1 Trigger is based on custom and programmable electronics[(4)], while HLT is a software system implemented on a $\sim$ 1000 commercial processors farm. The overall Trigger is designed to reduce the rate of at least 106 times. The maximum allowed output rate for Level 1 Trigger is 100 kHz, which should be even kept lower, about 30 kHz, for safe operation. Level 1 Trigger uses rough information from coarse segmentation of Calorimeters and Muon Detectors and holds the high-resolution data in a pipeline until acceptance/rejection decision is made. HLT exploits the full amount of collected data for each bunch crossing accepted by Level 1 Trigger and is capable of complex calculations such as the off-line ones. HLT algorithms are those expected to undergo major changes in time, particularly with increasing luminosity. Configuration and operation of the Trigges components are handled by a software system called Trigger Supervisor.

The Level 1 Trigger relies on local, regional and global components. The Local Triggers, also called Trigger Primitive Generators, are based on energy deposits in calorimeter Trigger towers and track segments or hit patterns in muon chambers, respectively. Regional Triggers combine their information and use pattern logic to determine ranked and sorted Trigger objects such as electron or muon candidates in limited spatial regions. The rank is determined as a function of energy or momentum and quality, which reflects the level of confidence attributed to the L1 parameter measurements, based on detailed knowledge of the detectors and Trigger electronics and on the amount of information available. The Global Calorimeter and Global Muon Triggers determine the highest-rank calorimeter and muon objects across the entire experiment and transfer them to the Global Trigger, the top entity of the Level-1 hierarchy. The latter takes the decision to reject an event or to accept it for further evaluation by the HLT. The total allowed latency time for the Level 1 Trigger is 3.2 μs.

Calorimeter Trigger The input data for the Local Calorimeter Trigger (TPG) come from Trigger Towers. These cover an angle of $\Delta\eta\times\Delta\phi = 0.087\times0.087$ up to $|\eta| = 1.74$ and larger angles for larger pseudorapidities. TPG electronics is integrated with Calorimeter read-

[(4)] For reasons of flexibility, the Level 1 Trigger Hardware mainly consists of Field Programmable Gate Arrays (FPGAs) or custom ASICs and programmable memory lookup tables (LUTs). The latter are widely used where one must comply with the need for speed, density and radiation resistance.

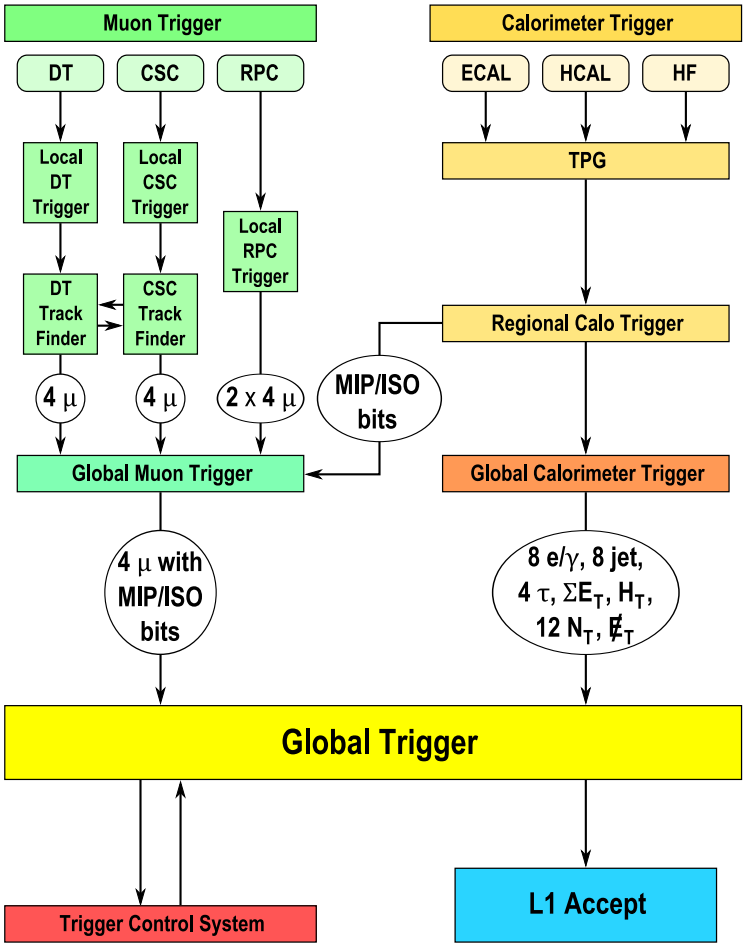

Figure 1.20: Schematic representation of the Level 1 Trigger data flow.

out. Each Trigger tower counts 25 crystals in ECAL. TPG output is transmitted with serial links to the Regional Calorimeter Trigger which builds candidate electrons/photons, the sums of transverse energies (defined as $E_T = E \sin\theta$), τ-veto bits and relevant information about muons being minimum-ionising particles (MIP) and isolated from calorimetric activity (ISO). Regional Calorimeter Trigger works on 4×4 Trigger Towers. In HF each Trigger Tower is a Trigger Region itself. ECAL and HCAL energy deposits are summed in each Tower.

Electron/photon candidates are built around the largest energy deposits in ECAL towers. Isolation of e/γ candidates within $|\eta| \leqslant 2.5$ is determined from shower profiles of both lateral extension, to be smaller than 2×5 crystals, and longitudinal extension, calculated from the ratio between HCAL and ECAL deposits, to be lower than 5%. Iso-

lation is based on vetoes on 8 neighbor Towers. Four isolated and Four non-isolated e/γ candidates are sent to che Global Calorimeter Trigger. The Regional Calorimeter Trigger also sums E_T in a given region of the central Calorimeter, excluding HF, and determines veto bits for 1-prong and 3-prongs decays of τ leptons, which are narrower than ordinary quark/gluon jets. τ-vetoes are set for continuous patterns of Trigger Towers larger than 2×2 within a Trigger Region.

The Global Calorimeter Trigger determines the highest-rank Calorimeter Trigger objects, including e/γ candidates, across the entire detector. It finds and counts jets, calculates the total transverse energy E_T, the missing transverse energy vector $\not{E}_T$, the scalar transverse energy sum of all jets above a chosen threshold (usually identifyed by the symbol H_T). Jets are found with a four-stage clustering technique. Up to four jets and four τ-jets are forwarded to the Global Trigger. The sum of E_T and $\not{E}_T$ are computed in x and y components up to $|\eta| < 5$.

Muon Trigger All Muon Detectors – DT, CSC and RPC – contribute to the Trigger. Barrel DTs provide Local Trigger in the form of track segments in ϕ and hit patterns in η. Endcap CSCs provide 3-dimensional track segments. Both CSCs and DTs provide also timing information to identify the bunch crossing corresponding to candidate muons. The Local DT Trigger is implemented in custom electronics. BTIs, Bunch and Track Identifiers, search for coincidences of aligned hits in the four equidistant planes of staggered drift tubes in each chamber superlayer. From the associated hits, track segments defined by position and angular direction are determined. TRACOs, Track Correlators, attempt to correlate Track segments measured in DT ϕ superlayers, enhancing the angular resolution and producing a quality hierarchy. The requirement of robustness implies redundancy, which introduces, however, a certain amount of noise or duplicate tracks giving rise to false Triggers. Therefore the BTIs, the TRACOs and the different parts of the Local Trigger contain complex noise and ghost reduction mechanisms. The position, transverse momentum and quality of Tracks are coded and transmitted to the DT regional Trigger, called the Drift Tube Trigger Track Finder (DTTF), through high-speed optical links.

The endcap regions are challenging for the Trigger since many particles are present and muons at a given p_T have a higher momentum than in the barrel, which gives rise to more bremsstrahlung photons. In addition, photon conversions in a high-radiation (neutron-induced) environment occur frequently. Therefore the CSCs consist of six lay-

ers equipped with anode wires and cathode strips, which can be correlated. Muon Track segments, consisting of positions, angles and bunch crossing information, are first determined separately in the nearly orthogonal anode and cathode views. They are then correlated in time and in the number of layers hit. The cathode electronics is optimized to measure the ϕ-coordinate, the anode electronics to identify the bunch crossing with high efficiency. The Local CSC Trigger is based on on the center of gravity of the charge induced in cathode Strips by signal collection in anode Wires. As for the cathodes, at least four coincident hits are required, since in contrast to neutron-induced background, a real muon leaves coincident signals in at least four layers with a probability that exceeds 99%. Actually a coincidence of two signals (pre-Trigger) is used to identify the crossing. The track segments from the cathode and anode electronics are finally combined into threedimensional Track segments characterized by the high-precision ϕ-coordinate in the bending plane, the bending angle ϕ_{bend}, a rough η and the bunch crossing number. The best two segments of each chamber are transmitted to the regional CSC Trigger, called the CSC Track Finder (CSCTF), which joins segments to complete tracks.

The RPCs are dedicated Trigger detectors. Their main advantage is their excellent timing resolution of about 1 ns, which ensures an unambiguous bunch crossing identification. The RPC Trigger is based on the spatial and temporal coincidence of hits in several layers. As opposed to the DT/CSC, there is no local processing on a chamber apart from synchronization and cluster reduction. The Pattern Comparator Trigger (PACT) logic compares strip signals of all four muon stations to predefined patterns in order to assign p_T and electric charge, after having established at least three coincident hits in time in four planes. Spatially the PACT algorithm requires a minimum number of hit planes, which varies depending on the Trigger tower and on the p_T of the muon. Either 4/6 (four out of six), 4/5, 3/4 or 3/3 hit layers are minimally required. The outer section of the hadron calorimeter (HO) consists of scintillators placed after the magnet coil up to $|\eta| < 1.24$, which can also be taken into account by the RPC Trigger in order to reduce rates and suppress background. The RPC muon candidates are sorted separately in the barrel and forward regions. The best four barrel and the best four forward muons are sent to the Global Muon Trigger.

The Regional Muon Trigger consists of the DT and CSC Track Finders, which join segments to complete Tracks and assign physical parameters to them. The Track finding principle relies on extrapolation from a source Track segment in one muon station

to a possible target segment in another station according to a pre-calculated trajectory originating at the vertex. If a compatible target segment with respect to location and bending angle is found, it is linked to the source segment. A maximum number of compatible track segments in up to four muon stations is joined to form a complete track, to which parameters are then assigned. DTTF operates only in the transverse plane, coarse assignment of η is nevertheless possible by determining which chambers were crossed by the track. For the regional Trigger the DT chambers are organized in sectors and wedges. Adjustable extrapolation windows are stored in look-up tables. In CSCs, nearly all possible pairwise combinations of track segments are tested for consistency with a single track. In contrast to the DTTF, no data exchange between neighbor processors is performed. Complete tracks are assembled from the extrapolation results and redundant ones canceled, as well as in the DTTF. The best four muons in both DTs and CSCs, according to quality parameters, are sent to the Global Muon Trigger.

The Global Muon Trigger combines the information from DTs, CSCs and RPCs, achieving an improved momentum resolution and efficiency compared to the standalone systems. It also reduces the Trigger rate and suppressess backgrounds by making use of the complementarity and redundancy of the three muon systems. The Global Muon Trigger also exploits MIP/ISO bits from the Regional Calorimeter Trigger. A muon is considered isolated if its energy deposit in the calorimeter region from which it emerged is below a defined threshold. DT and CSC candidates are first matched with barrel and forward RPC candidates based on their spatial coordinates. If a match is possible, the kinematic parameters are merged. Several merging options are possible and can be selected individually for all Track parameters, taking into account the strengths of the individual muon systems. Unmatched candidates are optionally suppressed. Cancel-out units reduce duplication of muons in the overlap region between the barrel and the endcaps. Muons are back-extrapolated through the calorimeter regions to the vertex, in order to retrieve the corresponding MIP and ISO bits, which are then added to the GMT output and can be taken into account by the Global Trigger. Finally, the muons are sorted by transverse momentum and quality to deliver four final candidates to the GT. The Muon Trigger works up to $|\eta| < 2.1$ at LHC startup, while it is designed to cover up to $|\eta| < 2.4$.

Global Trigger The Global Trigger takes the decision to accept or reject an event at Level 1, based on candidate e/γ, muons, jets, as well as global quantities such as $\sum E_T$, $\not{E}_T$, H_T[(5)] and 12 threshold-dependent jet multiplicities. Objects representing particles and jets are ranked and sorted. Up to four objects are available and characterized by their p_T or E_T, direction and quality. Charge, MIP and ISO bits are also available for muons. The Global Trigger has five basic stages implemented in FPGAs: input, logic, decision, distribution and read-out. The core of the GT is the Global Trigger Logic (GTL) stage, in which algorithm calculations are performed. The most basic algorithms consist of applying p_T or E_T thresholds to single objects, or of requiring the jet multiplicities to exceed defined values. Since location and quality information is available, more complex algorithms based on topological conditions can also be programmed into the logic. The results of the algorithm calculations are sent to the Final Decision Logic (FDL) in the form of one bit per algorithm. The number of algorithms that can be executed in parallel is 128. Up to 64 technical Trigger bits may in addition be received directly from dedicated boards. For normal physics data taking a single Trigger mask is applied, and the Level 1 Accept decision is taken accordingly and, if positive, the event is sent to the Data Aquisition stage.

High Level Trigger and Data Aquisition The CMS Trigger and DAQ system is designed to collect and analyse the detector information at the LHC bunch crossing frequency of 40 MHz. The rate of events to be recorded for offline processing and analysis is on the order of a few 10^2 Hz. The first level Trigger is designed to reduce the incoming average data rate to a maximum of 100 kHz, by processing fast Trigger information coming from the calorimeters and the muon chambers, and selecting events with interesting signatures. Therefore, the DAQ system must sustain a maximum input rate of 100 kHz, and must provide enough computing power for a software filter system, the High Level Trigger (HLT), to reduce the rate of stored events by a factor of 1000. In CMS all events that pass the Level 1 Trigger are sent to a computer farm (Event Filter) that performs physics selections, using faster versions of the offline reconstruction software, to filter events and achieve the required output rate. The various sub-detector front-end systems store data continuously in 40-MHz pipelined buffers. Upon arrival of a synchronous L1 Trigger Accept via the Timing, Trigger and Control System, the corresponding data are extracted from the front-end buffers and pushed into the DAQ system by the Front-End Drivers (FEDs). The event builder assembles the event fragments belonging to the same

(5) $H_T = \sum_{\text{jets}} E_T^{\text{jet}}$ for jets above threshold.

Level 1 Trigger from all FEDs into a complete event and transmits it to one Filter Unit (FU) in the Event Filter for further processing. The DAQ system includes back-pressure from the filter farm through the event builder to the FEDs. Back-pressure from the down-stream event-processing, or variations in the size and rate of events, may give rise to buffer overflows in the sub-detectorâs front-end electronics, which would result in data corruption and loss of synchronization. The Trigger-Throttling System (TTS) protects against these buffer overflows. During operation, Trigger thresholds and pre-scales will be optimized in order to fully utilize the available DAQ and HLT throughput capacity.The design of the DAQ system allows for gradual expansion in event building rate and processing.

1.3 Plans for the LHC Luminosity Upgrade

In order to extend the discovery potential of a hadron collider two approaches may be pursued: either the center-of-mass energy either the luminosity may be increased. The first one is unrealistic for the LHC because of both the technical challenge it would bring and the cost. On the other side, a luminosity increase of the LHC could enhance what it does represent for the scientific community as a tool to carry on frontier studies in particle physics at an energy scale never explored so far [53]. The major challenges in LHC operation, such as the extremely high stored beam energy and the large number of circulating bunches, 2808, will become even more relevant with a luminosity upgrade. The luminosity upgrade of the LHC has already been planned and the work to get to the first phase is already ongoing.

One of the factors that limit the luminosity in the LHC is the large crossing angle θ_c between colliding beams, which is kept at a value of $\theta_c = 285$ μrad in order to reduce the number of parasitic beam-beam collisions, 15 on each side of the primary interaction region, due to the large number of circulating beams. The geometric luminosity reduction factor is approximately $R(\phi) \approx 1/\sqrt{1+\phi^2}$, where ϕ is the Piwinski angle defined as:

$$\phi = \frac{\sigma_z \theta_c}{2\sigma^*_{x,y}} \tag{1.4}$$

where σ_z is the RMS bunch lenght and $\sigma^*_{x,y}$ are the transverse RMS beam size. This approximation is valid for round beams with a lenght much shorter than the betatron

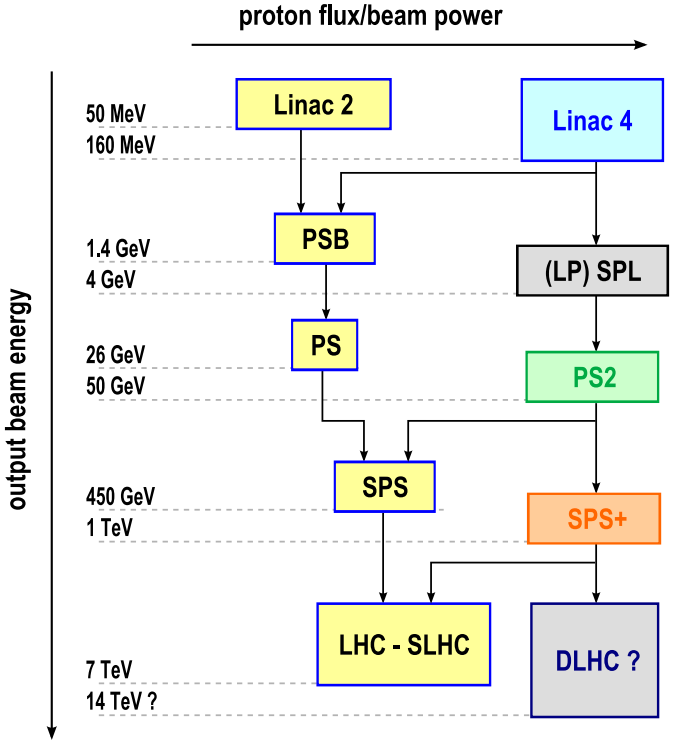

Figure 1.21: CERN accelerator complex upgrade plans, including the hypothesis of a $\sqrt{s}$ = 28 TeV LHC [54].

function at the collision point β^*. LHC operations at nominal conditions feature $R(\phi) \simeq 0.84$. The geometric luminosity reduction factor is expected to decrease for smaller β^* and larger θ_c. The accelerator chain upgrades will increase collider luminosity thanks to the large number of superimposed collisions, the reduction of β^* at collision points, pertinent final-focus quadrupoles, higher beam current from injectors, and an upgrade of collimation system.

The design luminosity of LHC, 10^{34} cm^{-2}s^{-1} is planned to be increased in steps [54]. The Phase 1 upgrade consists of new NbTi triplets with large aperture, new separation dipoles and new front quadrupole absorbers, leading to a β^* decrease from 0.55 m down to 0.25-0.30 m. A new injection is planned, with the construction of the Linac 4 which will deliver an ultimate intensity of 1.7×10^{11} protons per bunch. The Phase 1 upgrade is expected to be completed by 2016. The Phase 2 upgrade, formerly known also as Super-LHC (SLHC), would be realized in 2020. By that time the commissioning of new accelerators at CERN will be completed, including the Superconducting Proton Linac

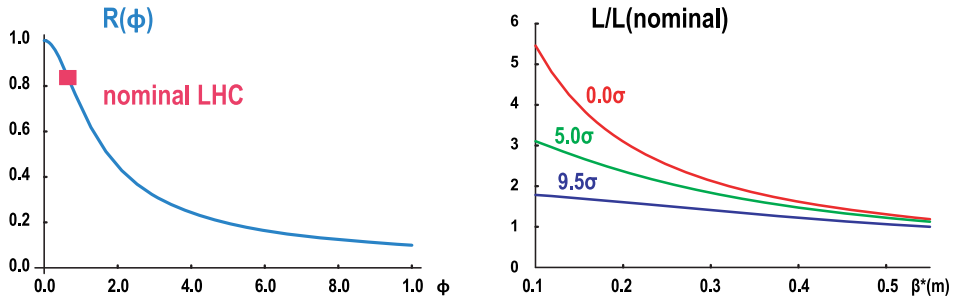

Figure 1.22: (LEFT) Geometric luminosity reduction factor as a function of the Piwinski angle; the nominal LHC operation point is indicated too. (RIGHT) Luminosity with respect to nominal LHC luminosity as a function of β^* for different values of crossing angle in units of RMS beam divergence [54].

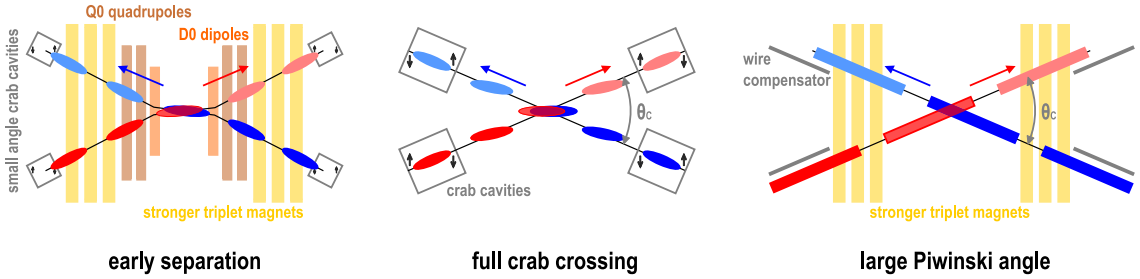

Figure 1.23: Schematic of different interaction region layouts for the Phase 2 LHC luminosity upgrade: (LEFT) early separation scheme with squeezed optics $\beta^* \simeq 8$ cm, (MIDDLE) full crab crossing scheme with very small Piwinski angle $\phi \simeq 0$ and (RIGHT) large Piwinski angle scheme with $\beta^* \simeq 25$ cm and $\phi \gg 1$.

(SPL) and the Proton Synchrotron 2 (PS2) which will replace the PS and its booster, doubling the beam brightness at 25 ns bunch spacing. Also the existing SPS will be modified with the deposition of a new coating with low secondary emission yield on the vacuum chambers to suppress the electron cloud. Interaction regions must be rebuilt with new triplets to bring the betatron function down to 0.15 m or below. Four different Phase 2 upgrade scenarios are under study, and the peak PU at the beginning of each run is expected to vary from 270 to 450 events according to the chosen one. Luminosity levelling (Figure 1.24 and [55]) can reduce the maximum PU in the detectors acting on β^*, θ_c and σ_z. The four scenarios differ from each other as follows:

- *early separation scheme* (ES) – aims at obtaining beam separation not with a large θ_c but with the insertion of dipoles inside detectors

- *full crab crossing scheme* (FCC) – maximizes the overlap of colliding bunches to be equal to the case of head-on collisions while bunch centroids still cross with a non-zero angle and rotation of bunches is achieved with transverse modes in RF cavities
- *low emittanche scheme* (LE) – recovers the luminosity lost with the crossing angle with low transverse emittance
- *large Piwinski angle scheme* (LPA) – bunch charge is increased with the reduction of beam-beam tune shift ΔQ_{bb}

Further details are included in Table 1.2. The current schedule (winter 2010-2011) can be divided into six major periods:

- up to 2011 – $\sqrt{s}$ = 7 TeV operations, commissioning of LHC and its experiments, early physics measurements
- 2012 shutdown – allow LHC operate at $\sqrt{s}$ = 14 TeV and reach design luminosity
- up to 2015 – $\sqrt{s}$ = 14 TeV operations
- 2016 shutdown – improvement of collimation in LHC to reach Phase 1 luminosity, connection of Linac 4 to the accelerator complex, upgrade of the PS Booster, preparation for Phase 2 upgrades
- up to 2020 – $\sqrt{s}$ = 14 TeV operations at Phase 1 luminosity $\simeq 2 \times 10^{34}$ cm^{-2}s^{-2}
- up to 2030 – Phase 2 upgrades and operations

1.4 Overview of CMS Upgrades

As half of the total integrated luminosity of Phase 1 is expected to be delivered at peak luminosities larger than those the detectors were designed to handle, some Phase 1-compliant upgrades of CMS are currently being developed and implemented. The detectors, including the inner tracking system, must be rebuilt to cope with Phase 2 requirements: they must deal with extreme radiation level and process a very large number of events per bunch crossing.

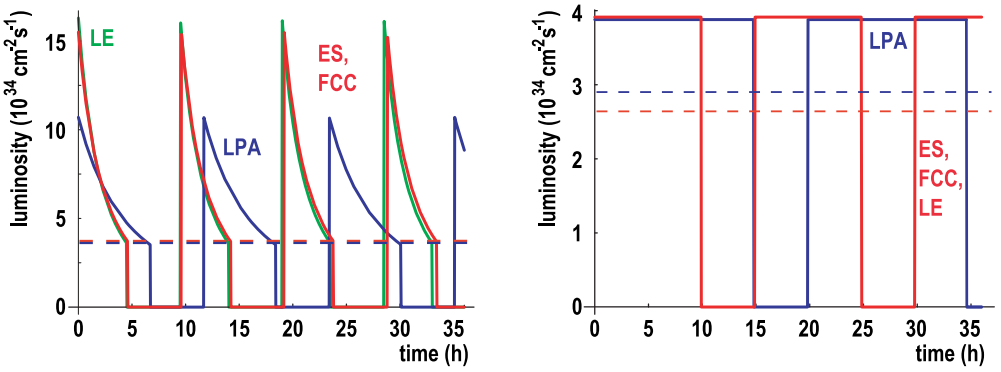

Figure 1.24: (LEFT) Ideal luminosity evolution for the different Phase 2 scenarios in the hypothesis of a $\sim$ 5 hours optimum runtime, dashed lines indicate the corresponding time-averaged luminosity. The same picture is shown in case of luminosity levelling (RIGHT) [54].

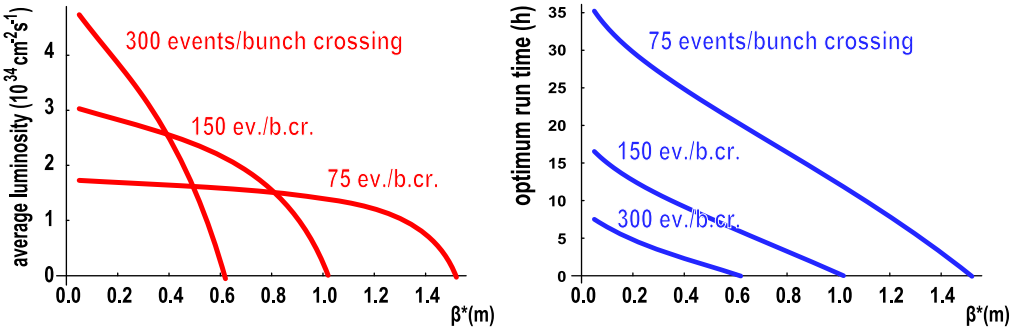

Figure 1.25: Average luminosity (LEFT) and optimum runtime (RIGHT) for LPA Phase 2 upgrade scheme as a function of β^* in one possible case of luminosity levelling [55].

There are several motivations for the detector upgrades [56]. The Trigger and DAQ recognize and preserve for analysis bunch crossings showing interesting signatures among the number of piled-up interactions: high luminosity can confuse the CMS Level 1 Trigger as the small amount of information available at this stage of DAQ is degraded by the increasing number of superimposed interactions. Upgrades to the muon system and the hadron calorimeters aim to provide more and higher quality inputs to the Level 1 Trigger and preserve it. Pileup can also confuse the analysis: interactions are distributed along the collision region over several cm in z and, while Tracking resolution is good enough to associate each charged track to the correct vertex, Calorimeters lack precise directional capability and hence cannot associate neutral particles, which appear as deposits of energy, with vertices. Fortunately, most soft interactions deposit very little

	parameter	LHC	Phase 1	ES/FCC	LE	LPA
N_b (10^{11})	p per bunch	1.15	1.7	1.7	1.7	4.9
Δt_{sep} (ns)	bunch spacing	25	25	25	25	50
I (A)	average current	0.58	0.86	0.86	0.86	1.22
	longitudinal profile	Gaus	Gaus	Gaus	Gaus	Unif
σ_z (cm)	RMS bunch length	7.55	7.55	7.55	7.55	11.8
β^* (m)	beta function at IP	0.55	0.30	0.08	0.10	0.25
θ_c (μrad)	crossing angle	285	410	0	311	381
ϕ	Piwinski angle	0.4	1.26	0	3.2	2.01
$R(\phi)$	geometric reduction	0.84	0.62	0.77	0.30	0.48
$\mathcal{L}_0$ (10^{34} cm^{-2}s^{-1})	peak luminosity	1.0	3.0	14.0	16.3	11.9
	events per bunch crossing	19	57	266	310	452
σ_z^{lumi} (mm)	RMS luminous region	45	33	53	16	53
τ_L (h)	initial luminosity lifetime	22	11	2.2	2.0	4.0
$\langle\mathcal{L}\rangle$ (10^{34} cm^{-2}s^{-1})	average luminosity (5 h)	0.6	1.4	3.4	3.0	3.0

Table 1.2: Comparison of the beam parameters at IP1 and IP5 for the design LHC luminosity, the Phase 1 upgrade and the four scenarios of Phase 2 upgrade [55].

energy in the CMS calorimeters and many of the events of real physics interest deposit large amounts. Discrimination using transverse energy thresholds requires clear separation of high energy deposits in the calorimeters from lower energies in surrounding regions, referred to as "isolation".

Radiation in CMS also damages the detectors, so that over time the signals may decline and the noise levels may rise, compromising the performance by degrading the resolution or efficiency. Detectors may become less effective at detecting real signals and more vulnerable to creating fake ones with obvious consequences for the overall physics capability of CMS. Most CMS detectors can sustain the integrated luminosity of Phase 1 with slight degradation. Only two cases require detector replacement earlier than Phase 2: one is at the inner radius of the Forward Hadron Calorimeter which receives very large doses that will reduce the transmission of the windows of the PMTs, the other one is the inner layer of BPIX which is only 4 cm from the colliding beams.

Other motivation for detector upgrades are the obsolescence of the components which may lack of spare replacements available on the market and the reduction of downtime. Downtime refers to periods when the LHC is producing collisions but CMS is not in a condition to record them. Improvements to the detector and the experiment infrastructure to prevent failures that would cause downtime or help recover from failures more

quickly all contribute to the success of the experiment. The relocation of electronics for the DT Muon Trigger from a high radiation area to a low radiation one is an example of an upgrade to eliminate a potential source of failure. CMS has a requirement to reduce downtime below 10% and eventually as an advanced goal below 5%.

The proposed upgrades for Phase 1 can be listed as follows:

1. Muon System

   - addition of the currently missing fourth layer of CSC (ME4/2) and associated readout and Triggering electronics and services to reduce the accidental Trigger rate and to preserve a low p_T threshold for the Level 1 Muon Trigger at high luminosity
   - upgrade of the ME1/1 electronics with a new CSC "Digital" Front End to read out independently each strip and let ME1/1 continue to contribute to the Muon Trigger at high luminosity
   - replacement of the Theta Trigger Boards by an FPGA-based board (or new ASIC) for the DT Muon Trigger
   - relocation of the Sector Collector boards of the DT Trigger from the periphery of the detector where they are exposed to radiation and high magnetic fields, and where the cooling is marginal to the Underground Control Room where the environment is more congenial
   - addition of a fourth layer of RPCs to extend coverage to $|\eta| = 1.6$ to preserve a low PT threshold for the Level 1 Muon Trigger at high instantaneous luminosity
   - R&D to develop detectors that can extend coverage to the region $1.6 < |\eta| < 2.1$ or higher

2. Hadron Calorimeters

   - replacement of the HPDs in all the Calorimeters inside the Solenoid HB/HE/HO with Silicon Photomultipliers (SiPM) having better quantum efficiency, higher gain, and better immunity to magnetic fields than HPDs; moreover, SiPMs operate at relatively low voltages and do not produce large pulses from high voltage breakdown that mimic energetic showers

- implementation of depth segmentation; this feature, made possible by the use of SiPMs, will help in coping with higher luminosities and will compensate for radiation damage of scintillators
- use of timing to clean up backgrounds, made possible by the extra gain and better signal-to-noise of the SiPMs
- new backend electronics designed to provide enhanced information to the upgraded Regional Calorimeter Trigger (RCT).
- replacement of the PMTs of the Forward Hadron Calorimeter with new ones to reduce the amount of Cherenkov light generated in the glass, improve rejection of spurious signals, improve efficiency and make the HF last longer under irradiation

3. Silicon Pixel Detector (a more detailed description is given in Section 2.2): the present detector was designed to operate with a maximum luminosity of 10^{34} $cm^{-2}s^{-1}$ and it will not sustain Phase 1 conditions because of severe data losses in the ROC

   - replacement of the current 3-layer barrel (BPIX), 2-disk endcap (FPIX) system with a 4-layer barrel, 3-disk endcap system for four hit coverage in order to maintain the present level of tracking performance even in the high occupancy environment of the upgraded LHC and to provide a safety margin in case the first strip layer in TIB degrades faster than expected
   - ultra-lightweight support with CO_2 cooling and displacement of the electronic boards and connections out of the tracking volume
   - new ROC with reduced data loss at higher collision rates
   - development of high bandwidth readout electronics and links as well as DC-DC power converters, which allow reuse of the existing fibers and cables

   The upgraded Pixel Detector will feature reduced mass and material budget, smaller innermost radius, increased lever arm with benefits for tracking, vertexing and *b*-jet tagging.

4. Trigger and DAQ

   - rebuilding the Regional Calorimeter Trigger (RCT) using advanced technologies, to take advantage of the full granularity of the data available from the

Calorimeter front end and to implement more sophisticated clustering and isolation algorithms

- rebuilding the CSC Trigger Track-Finder to accomodate the additional information from ME4/2 and ME1/1, to use more input segments and to combine a greater variety of tracks to enhance performance amidst greater occupancy and backgrounds
- rebuilding the RPC track finder to accomodate the additional plane of RPCs
- modification of the DT track finder to accomodate the move of the Sector Collectors and convert to the new Trigger technology
- implementation of a new Timing and Trigger Control system
- increase the bandwidth of the DAQ by a factor of 2 to 5 to handle the larger data volume produced at Phase 1 lumnosity
- replace the Event Builder and the processors of the HLT

5. Further upgrades are planned for beam monitoring and common facilities, including infrastructures, safety systems, the beampipe, power supplies and cooling.

2. The CMS Tracker Upgrade

The present Chapter focusses on the motivation for a Tracker upgrade, currently planned in two main phases as the LHC upgrades are. More details are given on the Phase 1 upgrades, constisting in a novel Pixel Detector which is described herein. The motivation for Phase 2 upgrades conclude the Chapter.

2.1 Motivation for a New Tracker Design

The CMS Tracker Upgrade is required to cope with the Phase 1 and Phase 2 planned luminosities of the LHC. In particular, the final Tracker performance should not be degraded by the higher particle fluxes, detector occupancies, trigger rates and radiation damage. Tracking performance and radiation damage are the main motivations for the Phase 1 Tracker upgrade, while the requirement of novel strategies for Level 1 Trigger drive the ongoing developement of a Phase 2 Tracker upgrade [56].

The Silicon Pixel Detector, with its $0.100 \times 0.150\ \mathrm{mm}^2$ granularity, provides three high-precision measurements to reconstruct the trajectory of a charged particle. These points are sufficient to give the HLT good enough track information and also to guarantee efficient seeding of the reconstruction of Tracks in the full Tracker volume. The innermost layer, which is only 4.4 cm far from the beamline, allows minimization of the multiple scattering effects and extrapolation uncertainties and makes Pixel information vital for the reconstruction of initial position and direction of charged particles and identification of primary vertices, secondary vertices and secondary tracks, which are essential to identify long lived particles.

The current Silicon Pixel Detector will not be able to sustain the Phase 1 luminosities because of large data losses in the ROC. The long shutdown of 2016 will be the best

opportunity to replace and commission a new Pixel Detector. This Pixel detector must overcome the limitations of the current one:

- the ROC buffer size and readout speed produce a 4% inefficiency at design LHC luminosity and 25 ns bunch spacing, which is expected to increase exponentially with increasing luminosity, getting up to 15% at Phase 1 conditions, leading to a remarkable overall tracking performance

- the three-hit coverage is not hermetic as efficiencies in the $|\eta| < 1.5$ region are 10% to 15%, while the track seeding inefficiency is even larger at larger pseudorapidities, with limitations for the HLT algorithms

- the Pixel Detector lifetime due to radiation damage is expected to correspond to an integrated luminosity lower than the one to be collected at the end of Phase 1, which is expected to be ≈ 350 fb^{-1}

- the support mechanics and the services of the Pixel Detector contain a large amount of passive material that degrades both tracking and calorimetric measurements due to multiple scatterin, photon conversions and nuclear interactions

An upgraded Pixel Detector must therefore mantain a high efficiency at 2×10^{34} cm^{-2}s^{-1} with lower material budget and four hits instead of three over pseudorapidities up to $|\eta| = 2.5$. These goals can be achieved thanks to the progress in cooling, power distribution, mechanical support, CMOS electronics and sensor material that have been made since the design of the current CMS Pixel Detector. However, radiation damage will significantly degrade the performance also of the innermost layers of the upgraded Pixel Detector during the three-years of Phase 1 run. The resolution on position measurement will worsen by about a factor two after experiencing a fluence of 10^{15} n equivalent per square cm. The dynamic inefficiency is expected to be greater during the second half of this run as the luminosity increases. These issues will be considered in the design of replacement parts featuring smaller pixel and a more radiation-resistant sensor technology.

The upgraded Pixel Detector will give benefits to HLT, which makes large use of "Pixel-only tracks", to the overall track reconstruction, because of better quality seeds, to the resolution of track parameters, because of the lower material budget, to primary and secondary vertexing and also to heavy flavour identification.

The design of an upgraded Tracker to replace the current Silicon Strip Tracker is motivated by the problems arising after the Phase 2 upgrades of LHC. At luminosities larger than 2×10^{34} cm^{-2}s^{-1} the current Level 1 Triggers, and those foreseen for the Phase 1 upgrade, will not be capable to comply with the maximum allowed output rate of Level 1 Trigger, which is 100 kHz. These topics will be described in detail in Section 2.3 and Chapter 4.

2.2 Phase 1 Upgrade: Inner Tracker

2.2.1 Pixel Detector Layout

The Phase 1 Tracker upgrade consists of a new Pixel Detector complying with the requirements described in Section 2.1. The current system will be replaced by an ultra-light detector with improved ROCs, four barrel layers and three end-cap disks. Particular care was adopted in designing the layout to optimize coverage with minimal innermost layer radius. The four barrel layers are arranged on cylinders of 3.9, 6.8, 10.9, and 16.0 cm in radius, respectively. End-cap disks range from 4.5 to 16.1 cm in radius and are mounted at 29.1, 39.6 and 51.6 cm from the interaction point along z.

Each module, in the new desing, will be equipped with 16 ROCs and will be mounted on ultra-lightweight support structures integrated with the cooling distribution. To further reduce the material budget, che current single-phase C_6F_{14} cooling will be replaced by a two-phase CO_2 one, with the coolant flowing into thin-walled (0.1 mm) stainless steel pipes. Material is further reduced by using new cables to carry signals to optical hybrid boards out of the tracking volume. Particular care will be put in designing a detector layout allowing an easy replacement of the innermost layers and rings after radiation damage. For FPIX, this requires each halfdisk be divided into an inner and outer ring. Similar to the current detector, the blades in the forward disks are rotated by 20° in a turbine like geometry to induce charge sharing. Orientation and tilting can then be optimized to obtain the best position resolution in both r and ϕ thanks to the separation of the inner and outer sectors of disks, allowing the inner ones to be tilted in a cone-wise way by an angle likely to be 12° towards the interaction point. The major constraints on the design of the Pixel upgrade are the insertion volume and services. In particular, services of the Si Strip Tracker are not being changed for Phase 1.

Another aspect related to the Phase 1 Tracker upgrade involves the beampipe, as the improvement in terms of impact parameter and vertex resolution requires the innermost Pixel layer to be the closest as possible to che beamline. This requirement must also meet safe and efficient operation of the accelerator with minimum background in the experiment, as the last machine element should always be the point of smallest aperture and the minimum diameter is constrained by mechanical stability in vacuum conditions. The current beampipe is segmented into 9 sections, the central one being 6.2 m long and consisting on a cylindrical part with conical ends. The 1.8 m long cylindrical part is made of 0.8 mm thick beryllium and features an inner diameter of 58 mm. As the LHC machine group concluded that a reduction of the diameter down to 50 mm would not affect the beam optics, it is proposed to install a new central beampipe with an inner diameter of 50 mm together with the new Pixel Detector. The smaller beampipe diameter allows bringing the innermost Pixel layer radius from 4.4 cm to about 3.9 cm.

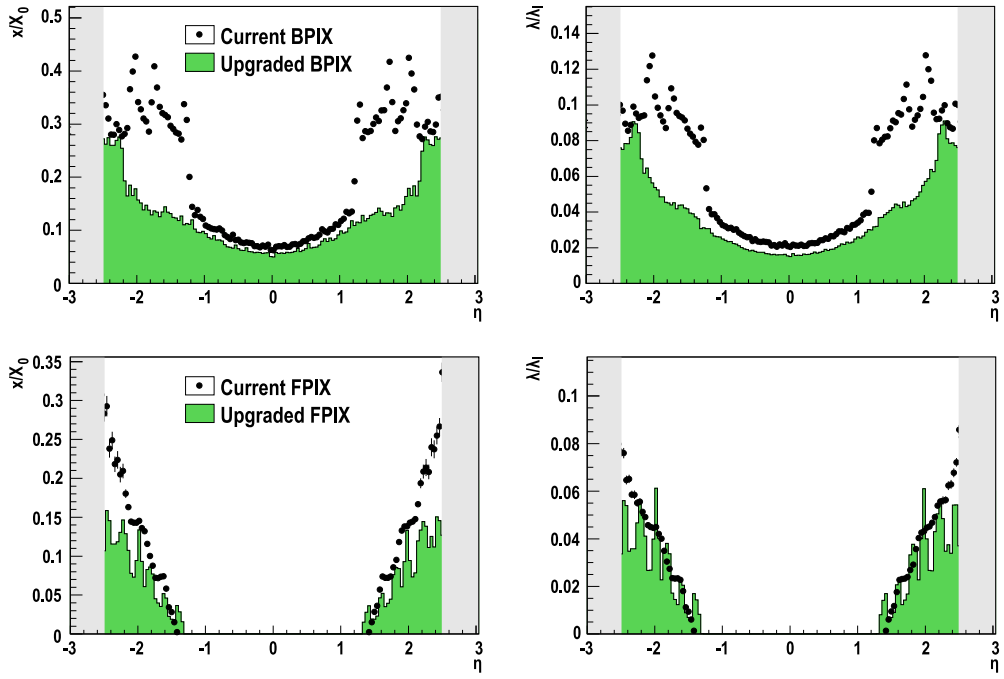

Figure 2.1: Material budget comparison between the current and the proposed Barrel (TOP) and Forward (BOTTOM) Pixel Detector in terms of radiation length (LEFT) and nuclear interaction length (RIGHT). The shaded region shows the material distribution outside the fiducial tracking volume [56].

2.2.2 Sensor and Front-End Electronics

The new Pixel Detector will count, in the barrel region, about 1200 modules instead of the present 770 and the number of Pixels will increase from 48 million to 80 million. Forward disks will count 45 million channels because of the increased module size. Only one type of sensor module will be used in the Pixel Detector, with an active area of 16.2×64.8 mm^2. Pixel size will not be changed, remaining 0.100×0.150 mm^2. The baseline is to use the same n^+-on-n technology as for the current sensors. The sensor is bump-bonded to 16 ROCs which will be thinned down to 75 μm for the two innermost layers while will be 200 μm thick otherwise.

Bump bonding really constrained the current Pixel Detector because of cost and complexity. Since the number of Pixels nearly doubles after the Phase 1 upgrade, particular care was put in choosing the best solution. Industrial procedures for bump bonding with 30 μm diameter bumps and 100 μm Pixel pitch are becoming available to avoid the long operations currently needed to deposit indium micro-spheres on the detector surface.

The current ROC is well understood and robust enough to survive the Phase 1 integrated luminosity, however it is expected to suffer inefficiencies depending on istantaneous luminosity when larger than the LHC design one. Therefore the changes to the ROC will focus on the essential needs in order to keep the ROC core as similar as possible to the current one.

To cope with the increased luminosity, the size of internal data buffers must be increased and an addicional buffer stage on the ROC will hold the Level 1 Trigger hits until a readout token is received. The addition of new buffers, while the CMOS process is still in 0.250 μm technology, will increase the chip periphery size. An additional buffering stage is being designed to reduce dead time related to readout latency and allow for a more efficient use of the output bandwidth. Simulation shows that for the innermost layer at 3.9 cm, the peak inefficiency of this upgraded ROC at Phase 2 luminosity with 25 ns bunch crossing is about 4.7% with an average, over a 10 hours fill, of 2.1%.

A faster readout is needed because of the increased number of modules and the limited amount of optical fibers. The present readout uses an effective bandwidth of 100 Mbps. The clock rate on analogue links cannot be increased because of rise time

limitations, so a digital readout is being developed with an effective bandwidth of 160 Mbps, which can be furtherly doubled with clever multiplexing. Other advantages of digital readout are reduced power consumption and reduced material in cables. The core of the ROC, including the Pixel front end amplifier, threshold comparator with trimming and the column drain architecture remain unchanged. Phase-lock circuits, designed to synchronize the 40 MHz LHC clock to the readout and to ADCs, have already been tested. The full layout for the upgrade ROC is expected to be ready in Summer 2011, with first test submission following shortly. A 50 ns bunch spacing scenario is also being taken uderd consideration for alternative ROC design.

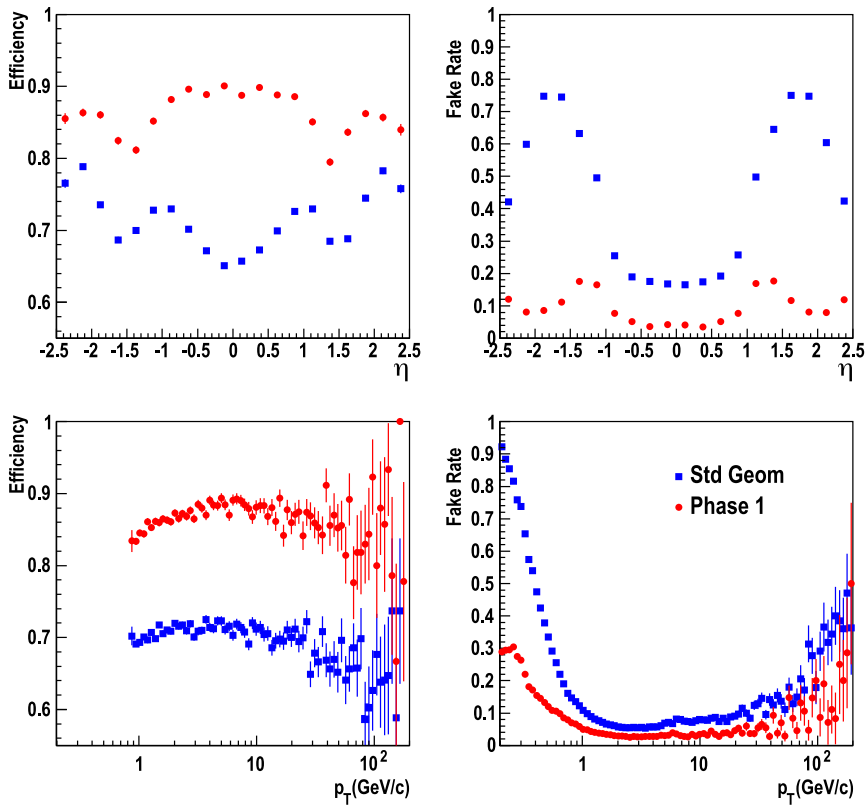

Figure 2.2: Comparison of iterative tracking performance with current and upgraded Pixel Detector at $\mathcal{L} = 2\times10^{34}$ cm^{-2}s^{-1} in simulated high-p_T jets. Efficiency (LEFT) and fake rate (RIGHT) are shown as a function of pseudorapidity (TOP) and p_T (BOTTOM) [56].

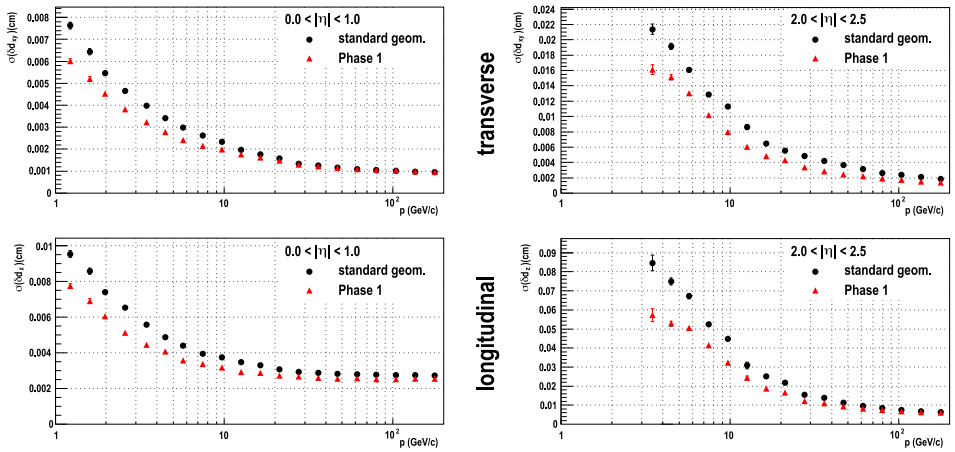

Figure 2.3: Comparison of iterative tracking performance with current and upgraded Pixel Detector at $\mathcal{L} = 2 \times 10^{34}$ cm^{-2}s^{-1} in simulated high-p_T jets. Resolution of impact parameter measurement in xy (TOP) and z (BOTTOM) are shown for tracks in two reference regions: $|\eta| < 1$ (LEFT) and $2.0 < |\eta| < 2.5$ (RIGHT) [56].

2.2.3 Expected Performance

Despite the number of Pixels being roughly twice as much as the current one, the expected reduction of material in the tracking volume is expected to be a factor 2, as shown in Figure 2.1. This important result will be achieved thanks to the use of a different cooling and thanks to the relocation of some services. This will reduce multiple scattering, photon conversions, and nuclear interactions. Such reductions in the amount of passive material will have a large impact on charged particle tracking efficiency as well as electron and photon identification and resolution. For example, the probability for a photon at $|\eta| = 1.5$ to convert into an e^+e^- pair inside the Pixel Detector volume is currently 22% but it would be 11% with the proposed upgrade. All signatures involving photons in final states, such as $H \to \gamma\gamma$ would receive benefits.

Interesting studies to be carried on during Phase 1 are likely to involve the reconstruction of tracks in high-p_T jets. The reliability of tracking with high local hit density is therefore vital. After studies for the heavy ion collision program, it turned out that track seeding with three-hit combinations in the Pixel Detector results in more precise estimate of track parameters, more reliable association of Strip hits and lower fake rates. The new layout provides enough redundancy for three-hit seeds, even when the inner layer performance starts to degrade because of radiation damage. Tracking performance

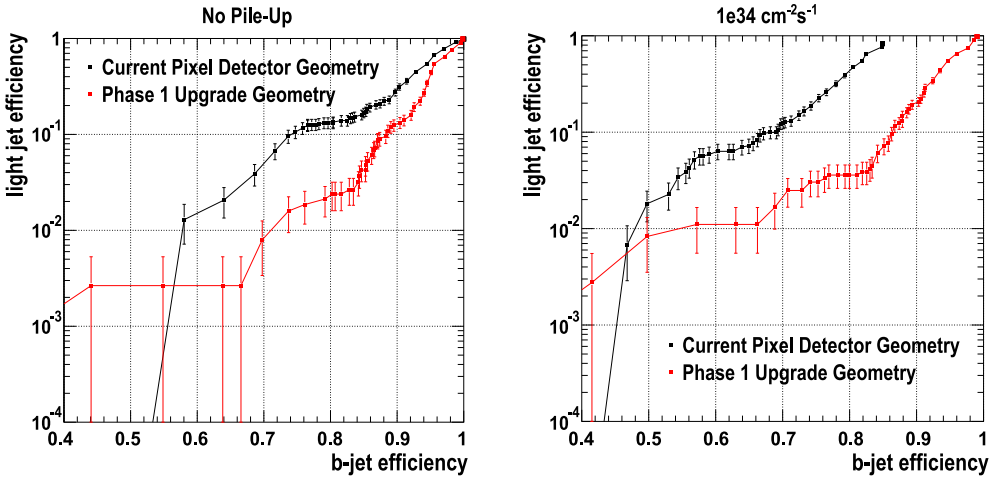

Figure 2.4: Comparison of iterative tracking performance with current and upgraded Pixel Detector in simulated events with high-p_T jets. Light quark jet tagging efficiency is shown as a function of b-tagging efficiency in simulated jets with the current and the proposed Pixel geometries in the no-pileup hypothesis (LEFT) and at design LHC luminosity (RIGHT) [56].

with the standard layout and the upgraded one can be compared with simulated jet and $t\bar{t}$ events, assuming an istantaneous luminosity of 2×10^{34} cm^{-2}s^{-1}. In both cases an iterative tracking algorithm is used starting from triplets of hits in the Pixel Detector. Also quadruplets can be used as seeds in the upgraded geometry. Figure 2.2 shows the effect of reduced material budget and addition of a fourth hit in seeding on track reconstruction efficiency. Fake tracks are caused by the incorrect association of hits and are much more likely in regions with more passive material. They cause significant problems for b-tagging and are much reduced in the upgraded detector.

The Pixel Detector is supposed to make precise measurement of the track direction before degradation of information due to multiple scattering. The impact parameter resolution with the proposed Pixel Detector is compared to the current one in Figure 2.3. The fourth barrel layer increases the measured track length by a factor two, improving the p_T resolution on standalone Pixel tracks by a factor four, with further benefits for the HLT. In consequence of such improvement, also vertexing and b-tagging performance improve: this is crucial to unwrap all the 20 to 40 pileup events per bunch crossing and to search for long lived particles. Overall, the upgrade gives an improvement in the resolution of about 20% on vertex measurement.

2.3 Evolution of Triggers at Higher Luminosity

The main challenge brought by Phase 2 luminosities involves Trigger rates. In fact, the CMS detector must guarantee efficient background rejection in any data taking environement provided by the LHC. Figure 2.5 shows the expected muon Trigger rates at full LHC design luminosity, as well as the rate of electron/photon Level 1 candidates at low LHC luminosity; in particular, the data rate reduction is stronger with the inclusion of tracking information in the HLT.

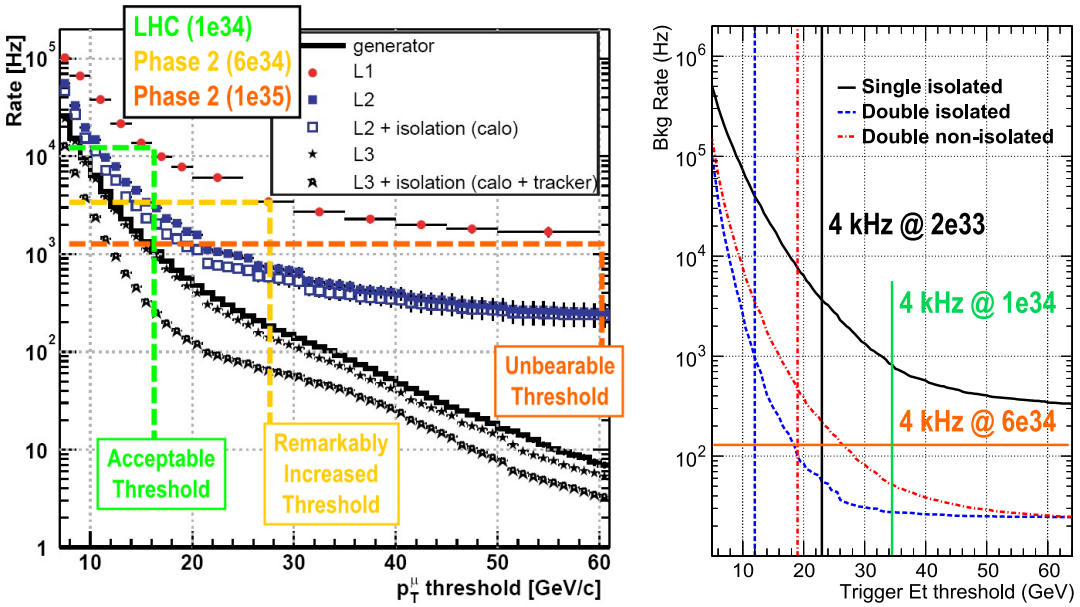

Figure 2.5: (LEFT) Comparison of expected muon Triggers at LHC design luminosity. The increase in muon Trigger rate, due to higher luminosities envisaged for Phase 1 and Phase 2, can be translated into a shift of the rate axis. The maximum allowed Level 1 Muon Trigger bandwidth is marked by dashed coloured lines pointing to the corresponging thresholds: green for LHC design luminosity, yellow for Phase 1 low luminosity, orange for Phase 2 high luminosity. (RIGHT) Expected electron Level 1 Trigger rate at low LHC design luminosity. The increase in electron Trigger rate, due to higher luminosities envisaged for Phase 1 and Phase 2, can be translated into a shift of the rate axis. The maximum allowed Level 1 electron Trigger bandwidth is marked by coloured lines pointing to the corresponging thresholds: black for low LHC design luminosity, green for LHC design luminosity, orange for Phase 2 low luminosity [28].

The effect of the LHC luminosity increase envisaged for Phase 2 can be intuitively understood by shifting the rate axis by roughly one order of magnitude. To cope with the maximum allowed bandwidth for Level 1 Muon Trigger, which is 12.5 kHz, even

using the full muon detector information the threshold to be set would be too high. As the rate increase is due to insufficient p_T resolution allowing high-p_T assignment of low energy muons, the solution would be the inclusion of Tracking information into the Level 1 Trigger, whose improved resolution would allow to keep the data rate within the maximum banwidth and keep low thresholds to have high efficiency. On the other hand, the large number of minimum-bias events will affect the ability of Level 1 Calorimeter Trigger to perform effective isolation cuts, exceeding therefore the maximum allowed bandwidth which is even lower than the muon one (4 to 5 kHz for single isolated electron). Also in this case, increasing the thresholds would reduce the sensitivity to any low-mass phenomena studied at the LHC.

The current CMS Tracker cannot provide inputs to the Level 1 Trigger, therefore a novel design is needed. Chapter 3 introduces an approach to low-p_T track rejection based on the cluster size in high granularity sensors, while the currently foreseen strategy for Tracking Trigger at Phase 2 luminosities is described starting from Chapter 4.

3. Monolithic Pixel Detector Prototypes in SOI Technology for Future Trackers

One of the major problem faced by a Level 1 Tracking Trigger at high luminosity is providing an effective rejection of very-low p_T tracks. One proposed way to achieve the goal relies upon using high granularity Strips or Pixels to recognize the elongated cluster generated by particles passing through the detector at large impact angle, rejecting the associated tracks.

In the framework of an international R&D effort on Monolithic Active Pixel Sensor (MAPS) specifically targeted at particle tracking, valuable experimental data have been recently gathered in a CERN test beam [57]. A brief review of these data and the constrain they put on the cluster shape recognition approach are presented herein.

3.1 Solid State Imaging Technology and Monolithic Arrays of Pixel Sensors

Present solid state technology provides a broad range of pixel detectors employed as imaging devices in virtually any scientific, technological and medical application. In addition to CCDs, which has been the first practical solid state technology able to provide high granularity particle detector, CMOS (Complementary Metal Oxide Semiconductor) is one of the major contemporary technologies employed in building imaging pixel devices [58]. CMOS imagers process into electronic signals the charge released in the sensitive volume by light conversion or by the passage of an ionising particle. Each CMOS pixel embeds its own charge-to-voltage conversion, and the sensor often also includes amplifiers, noise-correction, and other circuits.

With each pixel doing its own conversion, uniformity is usually lower than CCDs. Fill factor, i.e. the actual pixel sensible area, is also lower than in CCD, as hosting the readout transistors in-pixel prevents using all the volume as sensitive element. Anyway both these drawbacks have been greatly reduced in last generation CMOS pixel detectors, making them a viable choice even for the most demanding scientific applications. A key advantage of CMOS technologies over other solid-state processes comes from the fact CMOS is the standard process for the manufacturing of near all commercial electronic ICs. This translates into the lowest cost per unit of area of any silicon pixel detector technology, making it the first candidate for any large area application, as trigger layers are foreseen to be.

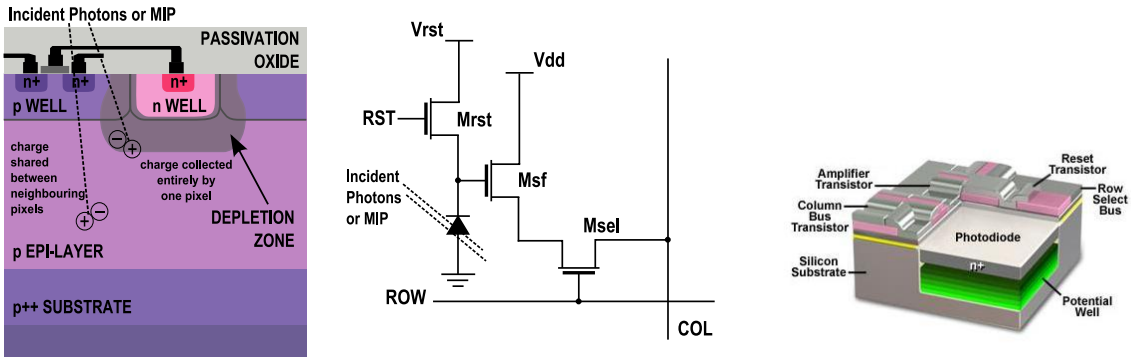

Figure 3.1: Cross section and schematic of a typical 3T pixel cell in CMOS technology.

In the CMOS manufacturing process, thousands of solid state components are embedded and connected into a single chip to address a specific task. In the case of imaging devices, this task is to collect the charge generated by the incoming radiation, or by a traveling MIP, while it interacts with the device itself, and make it available for further processing. All modern technologies employed for CMOS imaging devices are silicon based, the electronic components being created through the definition of different doping regions into the silicon itself: this means that the material the radiation has to interact with to generate the charge signal is, in a monolithic device, the same silicon the electronics is built on.

In scientific applications, each pixel can host its own complex (up to hundreds of transistor) signal processing system. A modern CMOS imager is primary constituted by a one or two dimensional array of pixel cells, each cell being composed by a photodetec-

tor, usually a biased diode, and the basic readout electronic, which in its simpler modern form consists of three transistors: one for amplification, one for selecting the cell and one to reset it (APS configuration) as shown in Figure 3.1. On the same die are included, on the periphery, the decoders and the multiplexers necessary to access the stored pixels signals by addressing each cell in turn, together with the analog circuitry used to amplify and buffer the output analog signal retrieved from the selected pixel.

In the view of future applications as tracking elements at the High Energy Physics colliders, the trend for pixel detectors development pushes towards challenging performance in terms of lower material budget, higher read-out speed, higher radiation tolerance, lower power consumption. Monolithic approaches, where sensor and readout electronics do not require complicated and expensive hybridization, but come as a single entity, have appeared since many years as an answer to these demands [59, 60].

CMOS MAPS are candidates to replace hybrid Pixels in many areas of future Trackers for particle physics experiments. While present CMOS technology cannot provide detectors with the high radiation tolerance (in the order of 100 MRad) necessary to survive the innermost vertex tracking regions, where the only viable technology today available is the hybrid one, it can provide excellent detectors for the outermost layers or for any not such harsh radiation environments.

MAPS detectors have intrinsically lower power consumption when compared to hybrid solutions due the lower capacitance present at the detection node, which is fully internal. The integrated electronic also allows for detector thinning down to some tens of microns without affecting the detection efficiency [61]. These two characteristics both helps in effectively reducing the material budget for a given sensitive area, while the low power consumption alone also gives the opportunity for air or other low material budget cooling systems. Furthermore, the practical major advantage of CMOS MAPS is the low production cost, which translates into an extremely favourable granularity/price ratio for large areas.

3.2 The SOI Technology and the LRDR-SOImager Prototype

Since several years R&D efforts are attempting to develop monolithic pixel sensors for particle detection in technologies different from the standard CMOS MAPS in order to add to its strength the characteristics of hybrid Pixels, such as those used in CMS [62, 50]: hybrid pixels, in fact, are capable of efficient charge collection as they can be fully depleted, while, on the other hand, monolithic pixels would result in a reduced material budget and require lower power to be operated. Silicon-on-Insulator is one of these promising technologies since the pioneering work of Marczewski *et al.* [63] and is currently available through the SOIPIX collaboration, grown up around dedicated MPW runs started by KEK and OKI industries [64].

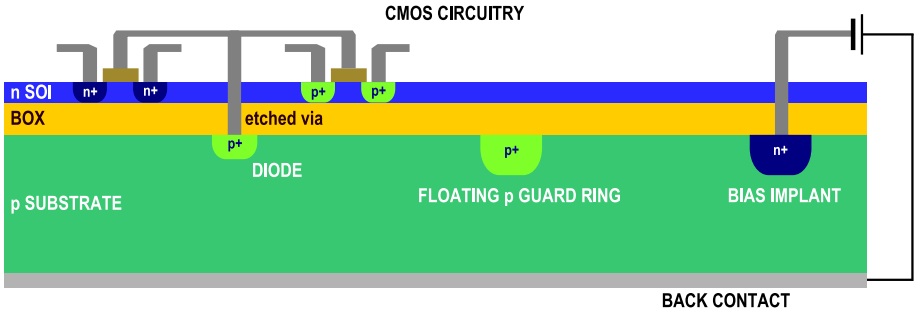

Figure 3.2: Cross section of a typical pixel cell in SOI technology with standard CMOS circuitry.

SOI is a technology developed to build commercial electronics on a compound substrate instead of a purely silicon one [65]. In SOI technology standard CMOS integrated circuitry is built on a thin silicon layer electrically insulated from the bulk silicon by means of a buried oxide (BOX) layer, typically silicon dioxide (SiO_2). The dielectric insulation between electronics and the bulk allows the design of pixel detectors with a full CMOS circuitry integrated in each pixel. The choice of high resistivity bulk substrates allows to apply a reverse bias. Vias etched through the BOX contact the top electronics to the substrate, so that pixel implants can be contacted, as shown in Figure 3.2. Thanks to the electrical field, a larger charge is collected by drift, making monolithic detectors in SOI technology more effective in radiation detection if compared to the standard bulk

CMOS pixel sensors. The *p* implant on the substrate acts as a biased collecting diode: the gathered signal is routed through the oxide by the via to the input of the above buffer transistor, thus allowing the readout of the deposited charge. By limiting the junctions parasitic capacitance thanks to the shallow epitaxial layer, the SOI process shows even lower consumption than standard CMOS technology in switching applications, like the data sparsification and transmission which occur at the detector periphery.

The thickness of the bulk silicon layer, the insulator layer and the SOI layer depend on the applications. There are different industrial procedures to produce SOI wafers. The one chosen for detector R&D is shown in Figure 3.3 and was developed by the French company SOITEC [66]. It consists of a multi-step wafer bonding where the thin silicon substrate is separated from the initial wafer by the implantation of hydrogen ions that allows the formation of bubbles inside the wafer, which is then literaly split by cleavage at the mean ion penetration depth.

The key point in applying the SOI technology to radiation detection is the BOX layer which, by insulating the electronic from the high resistivity substrate, allows its depletion by the mean of an electric potential. Charge pairs generated into the depleted substrate are hence drifted by the electric field before they recombine, allowing the collection at the diode junction of the charge generated along the whole track of the particle trough the substrate. Table 3.1 shows the depletion depth that can be obtained for different bias voltages applied to a a 700 Ω/cm substrate, together with the charge generated by a MIP traveling a distance equal to the depletion depth.

V_{bias} (V)	depletion depth (μm)	collected charge (*eh* pairs)
0	10	800
10	48	3840
50	106	8480
100	149	11920
200	211	16880
500	333	26640

Table 3.1: Depleted thickness for different bias voltages applied to a a 700 Ω/cm substrate. The number of electron-holes pairs generated by a MIP traveling a distance equal to the depletion depth are included too.

A series of test chips have been designed, characterized and tested in the framework

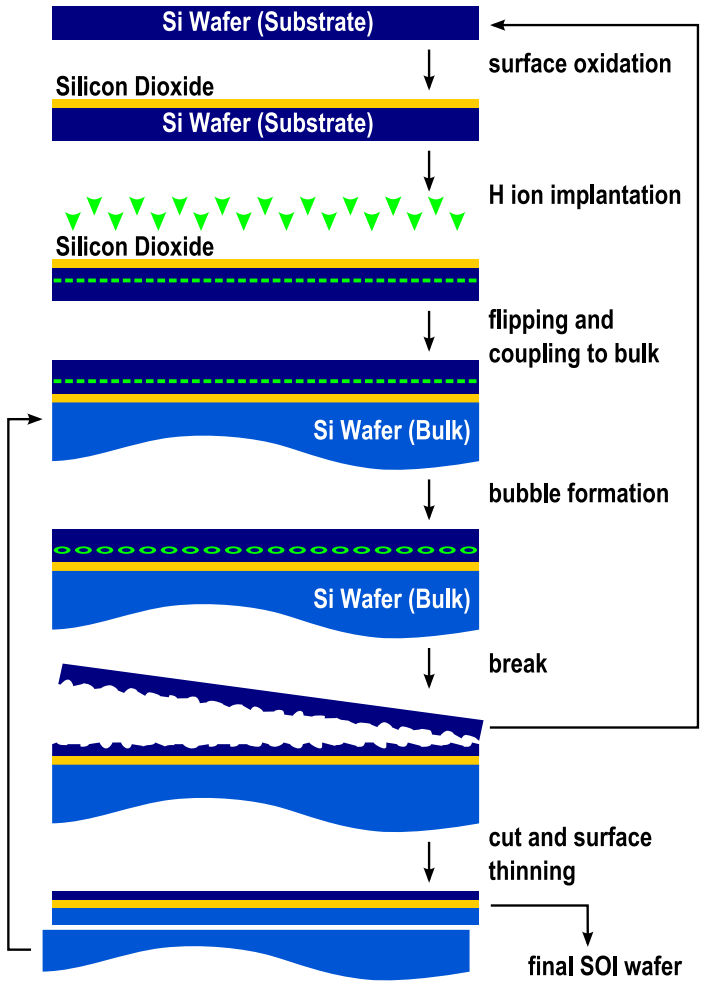

Figure 3.3: SOITEC smart cut procedure.

of a collaboration between Lawrence Berkeley National Laboratories (LBNL), the Physics Department of University of Padova, the National Insitute for Nuclear Physics (INFN) at Padova and, more recently, the University of California at Santa Cruz. Prototype chips with both analogue and digital[(1)] Pixels have been designed in LBNL since 2006. The first prototype, LDRD-SOI-1, produced at the 0.150 μm OKI R&D line, was succesfully tested at the 1.5 GeV/c electron line at the LBNL Advanced Light Source synchroton and was the first SOI Pixel sensor to detect particles from a beam. The second prototype, called LDRD-SOI-2, was processed by OKI in 0.200 μm FD SOI technology. Figure 3.4 shows the potential map in a model of LDRD-SOI-1 prototype simulated with Sentaurus TCAD

[(1)] Analogue Pixels readout is based on the 3T -three transistor- scheme while digital Pixels are equipped with a built-in comparator.

[67]. The depletion volume under collecting diodes is clearly visible, as well as the high potential at the interface between the BOX and the substrate ar the periphery.

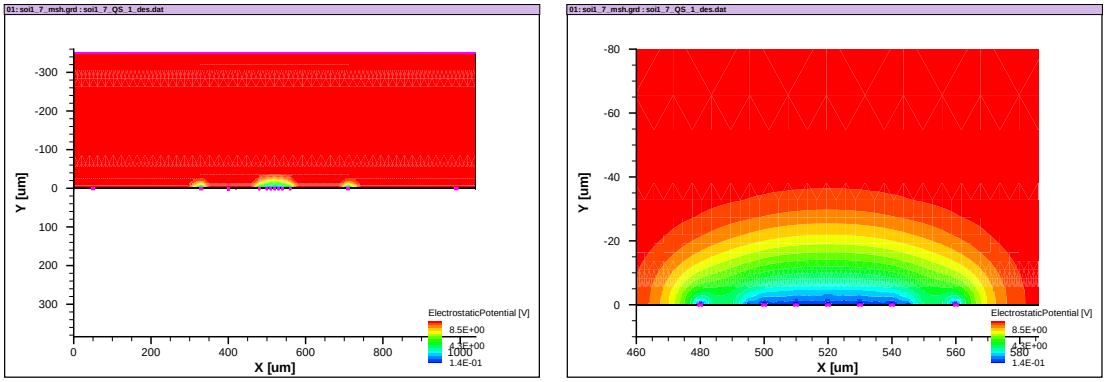

Figure 3.4: Sentaurus TCAD simulations of the LDRD-SOI-1 prototype showing the potential in the overall volume (LEFT) and in the pixel matrix region (RIGHT) after applying a bias voltage of 10 V.

3.2.1 Characterization of SOI Prototypes

One of the main issues to be solved when dealing with SOI MAPS is the so-called back-gating [68]. The reverse bias applied to the bulk to deplete the sensitive volume increases the potential at the Si-BOX interface making the BOX act as a parasitic gate on the CMOS channels, causing a shift on the transistor thresholds depending on the bias voltage V_{bias}. Figure 3.5 shows the threshold shift measured on the n-type transistors test structures embedded in the first chip: for increasing V_{bias} the transistors switch on at lower voltages, actually affecting the device behaviour for bias voltages greater than 15 V. A floating guard-ring was implanted around each pixel, and floating and grounded p-type guard-rings were also implanted around the pixel matrix and around the peripheral I/O electronics to take under control the transistor back-gating effect, as TCAD simulations showed this solution could give benefits in keeping low the field bewteen diode implants.

Results from measurements on analogue Pixels, in tests with IR lasers, were encouraging as the device could be operated up to a depletion voltage $V_{\text{bias}} \simeq 20$ V, while the collected charge q_{coll} depends as expected on V_{bias} up to $V_{\text{bias}} \simeq 15$ V: $q_{\text{coll}} \propto \sqrt{V_{\text{bias}}}$.

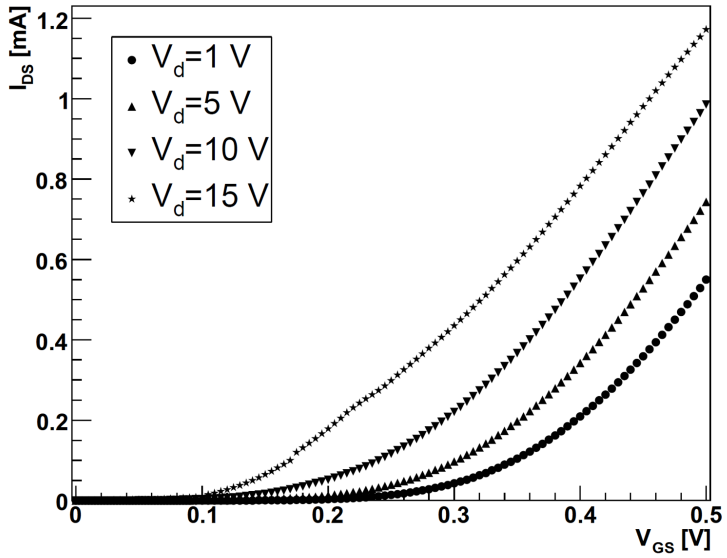

Figure 3.5: Shift of input characteristics vs. substrate bias V_{bias} for 1.0 V n-MOS test transistor with $W/L = 50/0.3$ [68].

At larger depletion voltages, the collected charge saturates between 15 and 20 V and decreases for $V_{\text{bias}} > 20$ V. The depletion volume at $V_{\text{bias}} \simeq 15$ V is only 55 μm deep and at larger applied voltages the back-gating effects manifested itself through a loss of collected charge first and eventually a non-functioning pixel cell. Digital pixels were functional up to 35 V. They have been extensively tested at the Berkeley ALS 1.35 GeV/c electron beam, where despite the back-gating effect it was possible to establish a correlation between the thickness of the depletion zone and the charge collection efficiency. The detector was exposed to a low intensity electron beam together with a reference detector to normalize the beam flux data. At every beam bunch a 10 μs integration time frame was taken. After masking the noisy and bad pixels, the frame was analysed and the number of reconstructed clusters computed. Data showed a maximum of reconstructed clusters for $V_{\text{bias}} = 15$ V, where the convolution between the increased signal due to the collected charge and the deteriorating performance of the in-pixel comparator reaches its maximum.

The performance of the analogue Pixels in the LDRD-SOI-2 prototype motivated the realization of a completely analogue chip, called the LDRD-SOImager, featuring an active area of 3.5×3.5 mm^2 populated with 256×256 equally spaced Pixels of 13.75 μm pitch. Further guard rings were added in the design of the LDRD-SOImager chip, as

previous prototypes showed the output analogue stages were affected by the threshold shift due to back-gating. To increase the speed of the standard rolling shutter readout scheme, the Pixel matrix is divided into 4 parallel arrays of 64 columns each connected to 4 identical parallel output analog stages. Both the pixel cell and the ancillary electronics have been designed and tested to operate up to 50 MHz readout frequency.

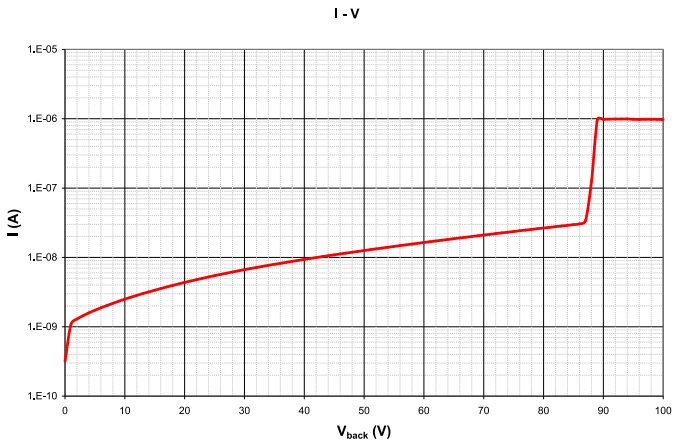

Figure 3.6: Measurement of leakage current in the LDRD-SOImager prototype [69]. Courtesy of S. Mattiazzo, Università degli Studi di Padova and INFN.

The substrate leakage current for different depletion voltages was characterized by mean of *I*-*V* measurements. In the typical working bias voltage interval the leakage current was measured to be few nA with monotonic dependence on V_{bias}, as in Figure 3.6 allowing to perform a reliable measurement of the thickness of the depleted volume by a *C*-*V* measurement by using the pixel guard-ring grid as electrode and assuming the detector area being a single, large diode. During the measurement, the guard-ring structure was kept at ground potential and the chip was depleted applying V_{bias} to the metalized backside. The same measurements were repeated by applying Vbias to the biasing *n*-type guard-ring. The results from the two approaches are shown in Figure 3.7, where the measured depletion voltage is plotted against the substrate V_{bias}. Data well matched the expected curve for the nominal substrate resistivity of 200 Ω/cm.

Within the range of operability, pixels showed a noise of 60 electrons for V_{bias} up to 20 V. As it is possible to see in Figure 3.8, noise does not scale with $\sqrt{V_{\text{bias}}}$, as it should in case of major contribution from the leakage current, hinting this value is representative of the actual pixel cell noise, mainly due to the reset noise and the junction capacitance.

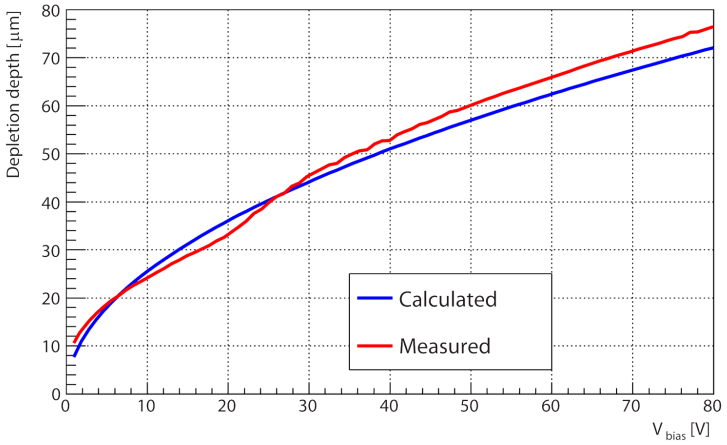

Figure 3.7: Substrate depletion depth in microns for different bias voltages [57].

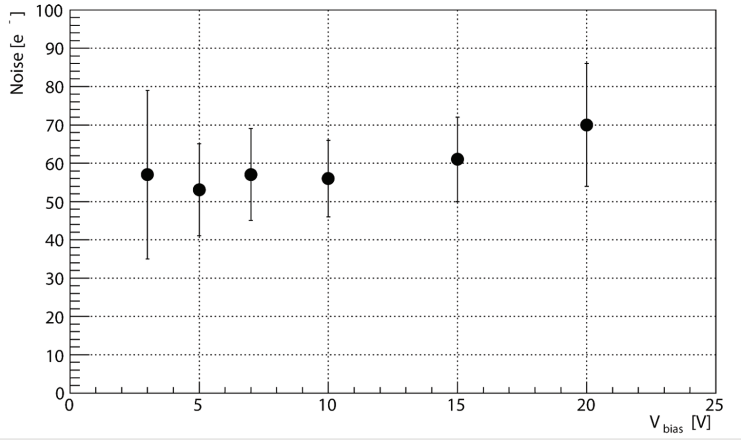

Figure 3.8: Measured noise, in electrons, at room temperature for different bias voltages [57].

In order to optimize the design of the Pixel cell for mitigating the back-gating effect and enhancing the charge collection, a test chip based on the earlier SOImager and implementing pixel cells of different design has been built and processed in the same OKI 0.200 μm FD SOI process (Figure 3.9). The pixel cell keeps the same 3T design and pixel pitch as the previous chip for the whole matrix, but the 256×256 Pixel array has been divided into eight different sectors, each sector implementing a different Pixel layout. Floating and grounded guard rings as well as a lightly *p*-doped layer have been implemented in order to insulate the transistors from the effect of the potential below the BOX. Guard-rings have been also implemented around the Pixel matrix and the

peripheral I/O electronics. The use of a buried *p*-well (BPW), created by light *p*-spray implants under the BOX, to shield the transistors has already been successfully tested on single transistor test structures [64]. The BPW appears to be more effective in shielding the transistors from back-gating effect compared to the guard rings adopted in earlier designs, it is less competitive in charge collecting to the diode and it takes no space in the Pixel cell, allowing more circuital nodes to be implemented per Pixel. The most effective layouts, after chip characterization, have no guard rings and use BPW implants: one features a 5 μm diode with *p*-spray implant only beneath the diode area, while the second has a smaller diode (1.5 μm) with *p*-spray implants filling the full pixel area. Both cells yield comparable results, providing the same charge collection efficiency and successfully withstanding substrate biasing voltages up to 70 V. This voltage limit arises from the substrate leakage current in this batch of chips more than by the back-gating effect.

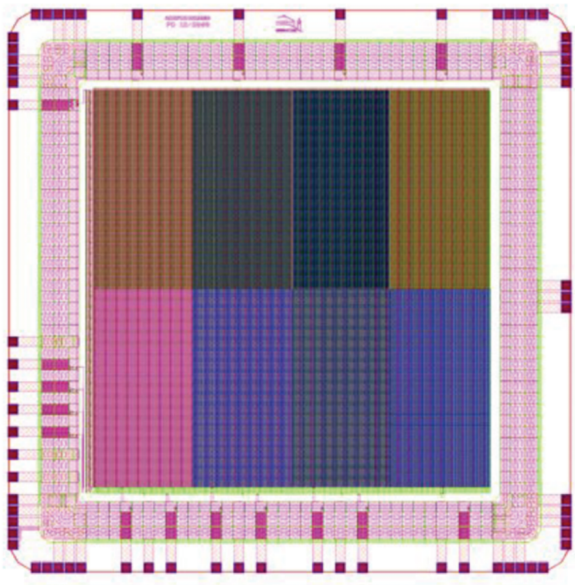

Figure 3.9: Layout of the LDRD-SOImager-2 prototype. It is easy to distinguish the 8 different pixel cell layout. Courtesy of Berkeley Lab Engineering Division, P. Denes.

3.2.2 Radiation Tolerance of SOI Prototypes

The SOI technology is potentially sensitive to the effects of ionizing radiation, due to positive charge trapping in the thick buried oxide. This problem is even more worrying

for depleted detectors built in this technology, as the voltage applied to the substrate increases the charge trapping in the BOX. Total dose effect studies have been already performed on this technology, with a particular emphasis on the effect of different substrate bias conditions during irradiation [70]. Figure 3.10 summarizes the results obtained irradiating with a 10 keV X-Ray source the 0.20 μm OKI SOI process transistor test structures, consisting of both *n*-MOS and *p*-MOS transistors with common sources and separated gates and drains, surrounded by 1 μm *p*-sub ring. Irradiation has been repeated over different structures with different biasing conditions: results clearly show the strong dependence of the radiation tolerance respect to V_{bias}. On the employed test structures no light *p*-spray implant was available, but the *p*-sub biasing ring present around the transistors was kept both floating and grounded during irradiations at V_{bias} = 10 V to check for any shielding effect: grounding the *p*-sub ring actually helps in increasing the radiation tolerance due to its screening effect. Those results are of particular interest when correlated with the effectiveness of the light-*p* doping layer in shielding the buried oxide from the depletion field: in such a condition the radiation tolerance of this technology is hence expected to reach hundreds of krad.

With respect to Single Event Upsets (SEU), instead, SOI devices are traditionally considered more radiation hard than those manufactured in standard bulk CMOS technology, thanks to their smaller charge collection volume (limited to the thin top Si layer). Most recently, new SEU tests on SOI devices with BOX thicknesses less than 200 nm showed unexpectedly high SEU cross-sections [71]. This was a clear indication that the charge induction, at least for some technologies, occurs not only when the carriers move in the top silicon layer but also when they move below the BOX. SEU radiation tolerant designs and a solution to the charge accumulation in the BOX are hence required to develop a sensor able to withstand the doses of interest for tracking and vertexing at future colliders.

3.3 Recent Results: Response to Minimum Ionising Particles and Low-Momentum Track Rejection

The interesting properties SOI MAPS showed in terms of high granularity, high signal-to-noise ratio expected for MIPs (due to high depleted region and low noise) make them

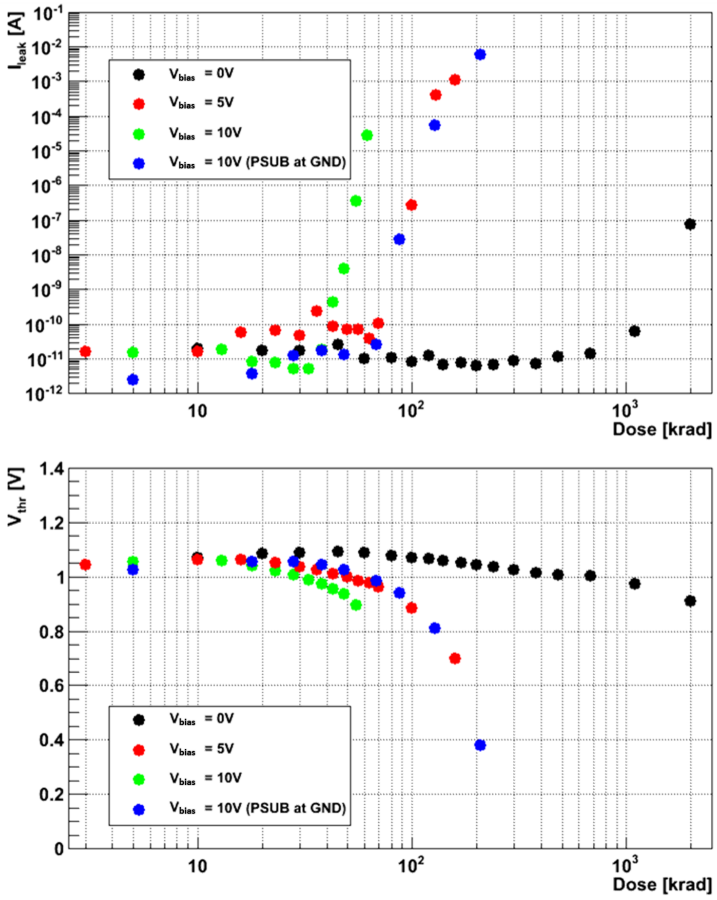

Figure 3.10: Leakage current (TOP) and transistors thresholds shift (BOTTOM) versus total dose for 10 keV X-Ray irradiation. Different colours indicate the different biasing condition of the substrate during the whole irradiation [70].

to be seen as candidates for future Trackers in particle physics experiments, once the radiation tolerance is increased. In particular, looking at CMS Phase 2 upgrades, MAPS technologies could be an interesting alternative to current technologies for tracking elements at large radii, where the radiation environement is less challenging. For this reason, the LDRD-SOImager-2 prototype was tested with a MIP beam.

The response to minimum ionising particles has been studied in a beam test carried out with 200 GeV/c pions on the H4 SPS beam line at CERN [57]. Three chips have been aligned on the beam line to measure, as a function of the applied depletion voltage, the signal output, the pixel multiplicity in the signal clusters, the detection efficiency and the single point resolution. Detectors were operated at 12.5 MHz, corresponding to a rate of about 1500 frames/spill. Data has been collected using a custom DAQ system [73]

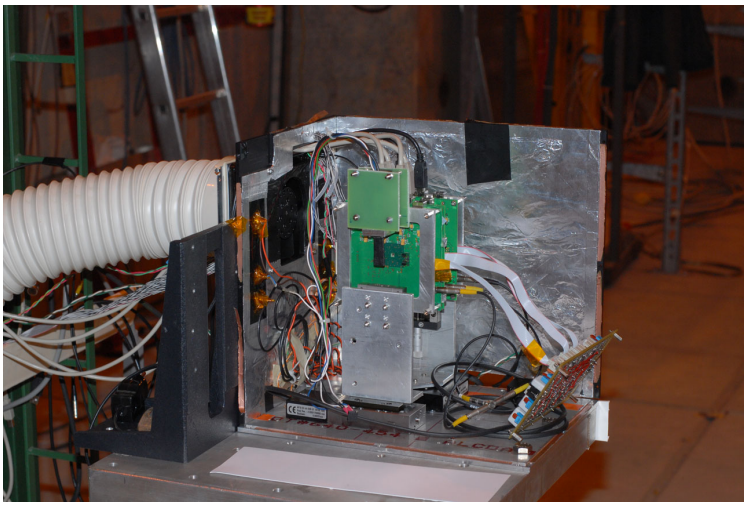

Figure 3.11: Experimental test setup to study the response of the LDRD-SOImager-2 at the H4 SPS beam line at CERN [72]. Courtesy of P. Giubilato, CERN and UCSC.

which allowed real time cluster search and data sparsification. Figure 3.11 shows the experimental setup used for the reported measurements.

Cluster multiplicity shrinks as expected for increasing V_{bias} due to the collection by drift mechanism. The single point resolution has been extracted from the measured residual distribution on the intermediate detector plane. Preliminary results for the measured Gaussian width of the residuals correspond to a single point resolution of $\simeq 1.2$ μm for $V_{\text{bias}} > 40$ V. Both these results are shown in Figure 3.12.

Figure 3.13 illustrates how the information from a test beam can be used to deduce some results for a collider detector geometry. In fact, the surface of the detector prototype under beam can be thought as the surface of a sensitive element in a barrel-like Tracker layout, untilted to keep the analogy simpler. Any track has an impact angle on the detector surface which depends on both the geometry of the layout and the track p_T. This way, using measurements on cluster size obtained with different impact angles, one can get important hints on the capabilities of similar detectors to reject low p_T tracks with measurements within a single layer. One has, from the chord C subtended by the trajectory axis, the trajectory vertex and the impact point on the detector element, that:

$$\cos(\gamma - \alpha) = \cos\gamma\cos\alpha + \sin\gamma\sin\alpha = \frac{C}{2R} \tag{3.1}$$

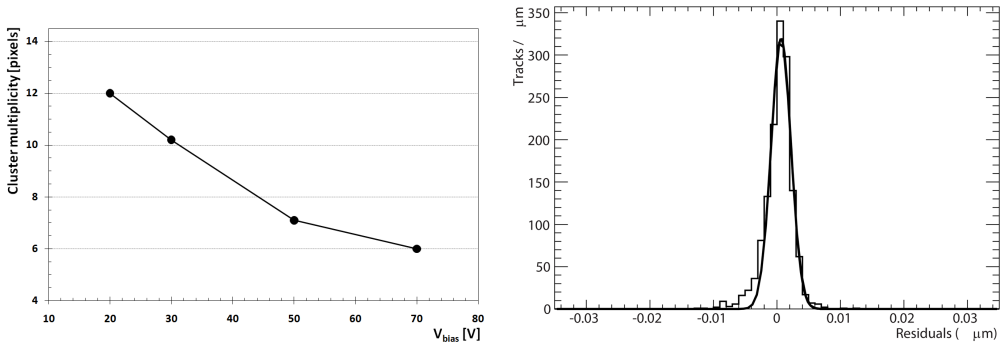

Figure 3.12: Cluster multiplicity distribution for different depletion voltages V_{bias} (LEFT) and tracks residuals distribution on the second plane with V_{bias} = 70 V (RIGHT) in 200 GeV/c pion beam test of the LDRD-SOImager-2 prototype [57].

Then, as $\beta = \frac{\pi}{2} - \gamma$, one can find how the impact angle β depends on the geometry:

$$L \sin\beta + d \cos\beta = \frac{L^2 + d^2}{2R} \tag{3.2}$$

Solving for $\cos\beta$ one gets

$$\cos\beta = \frac{d}{2R} \pm \frac{L}{2R} \sqrt{\frac{4R^2}{L^2 + d^2} - 1} \tag{3.3}$$

The solution with the "minus" sign corresponds to negative values of d, such as for the dashed trajectory in Figure 3.13, and therefore must be corrected for an angle of 180°. The only remaining parameter in (3.3) is the trajectory radius R which depends on the transverse momentum and magnetic field as:

$$p_T = R \cdot c \cdot B \cdot q \cdot 10^{-5} \tag{3.4}$$

where p_T is measured in GeV/c, R in cm, B in T, q in units of elementary charge and $c \simeq 299.792$ mm/ns is the speed of light. For $B = 4$ T one gets that a particle of unit charge with $p_T = 2$ GeV/c draws a trajectory with a radius $R \simeq 167$ cm. One can thus calculate the impact angles for some reference momenta and typical configurations which are summarized in Table 3.2. The choice of reference momenta came from simulations of minimum bias events, which showed that the particle p_T spectrum decreases rapidly, as from Figure 3.14. Figure 3.15 shows that the rejection factor of $\sim 90\%$, or even larger, could be obtained with a p_T threshold at 2 GeV/c.

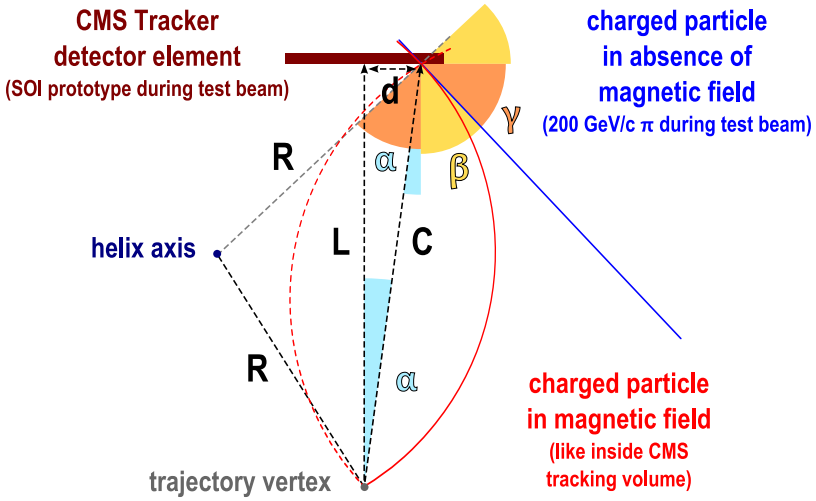

Figure 3.13: The impact angle of a charged particle on a silicon detector flat surface can be thought both as a straight trajectory and a curved trajectory in a magnetic field in which both the geometry and the track momentum contribute to the overall angle as stated in (3.3). Dashed trajectory corresponds to negative values of d.

The SOI detector under beam test was depleted at different voltages, ranging from 10 to 70 V and corresponding approximately to a depleted thickness in the 10 to 130 μm range. The dataset corresponding to a depletion voltage of 50 V was chosen for this purpose because of two main reasons:

- it corresponds to approximately 100 μm of depletion thickness, larger than that can usually be obtained with MAPS in CMOS technology; to minimize the material budget, a 100 μm maximum thickness sensor is foreseen for a trigger layer, so a 100 μm collection depth sets an upper limit on performances about cluster shape discrimination capability in such an application

- the corresponding collected charge, as stated in Table 3.1, is approximately 200 times larger than the measured noise at room temperature, resulting in a preservation of the MIP detection efficiency even after deterioration due to a total dose of 1 MRad

Figure 3.16 shows the variation of the average cluster size with different impact angles of the pion beam on the detector surface. These angles span the whole range of angles calculated in Table 3.2 and therefore data represent what could be seen if the LDRD-SOImager-2 prototype were used to identify low-p_T tracks. The cluster size is

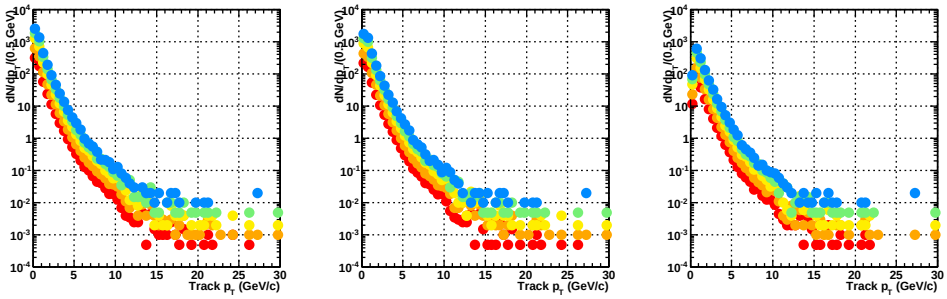

Figure 3.14: Spectrum of charged particles in minimum-bias events with `FastSimulation`, averaged per bunch crossing, leaving at least one hit in sensor layers placed at 32 (LEFT), 48 (MIDDLE) and 98.5 cm from the beamline (RIGHT). Different colours correspond to different pile-up values, ranging from 25 to 200 superimposed events per bunch crossing.

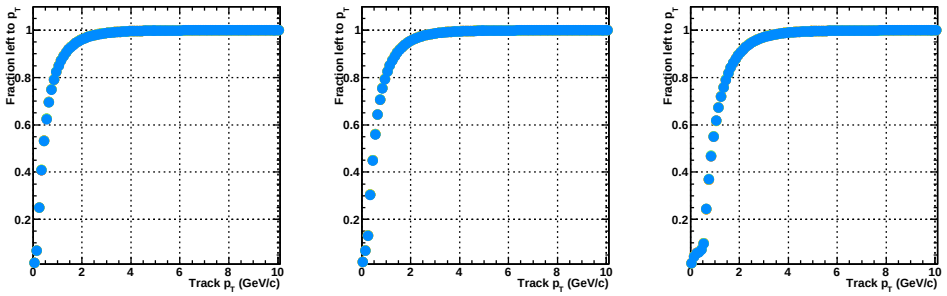

Figure 3.15: Fraction of tracks in minimum-bias events with a transverse momentum lower than the given one, relative to spectra leafing hits in sensor layers at 32 (LEFT), 48 (MIDDLE) and 98.5 cm from the beamline (RIGHT).

reported in terms of the average number of columns and rows that compose the cluster. The setup was mounted to have column index change along the horizontal direction, and high-precision rotations around a vertical axis were obtained with a micrometric rotation stage. For the purpose of low-p_T rejection based on cluster size, only columns are relevant, as one could in principle sum over rows to mimic longer Pixels or even Strips. The striking result is that, even at larger impact angles, the cluster size does not increase more than 40%. The transverse distance traveled by a MIP is, in first approximation, negligible for frontal impact and $\sim 36\%$ of the depletion thickness at $\beta = 20°$.

The experimental conditions, besides being representative of the use of the LRDR-SOImager-2 prototype in a tracking system aimed at rejecting low-p_T tracks, can be defined optimal because of the fine pixel pitch, 13.75 μm, and because of the 100 μm

p_T (GeV/c)	R (cm)	L (cm)	d (cm)	β (degrees)	
2.0	167	30.0	0.0	5.15	5.15
2.0	167	30.0	2.0	1.35	8.98
2.0	167	30.0	5.0	4.24	14.69
2.0	167	60.0	0.0	10.35	10.35
2.0	167	60.0	2.0	8.45	12.26
2.0	167	60.0	5.0	5.62	15.15
2.0	167	90.0	0.0	15.63	15.63
2.0	167	90.0	2.0	14.36	16.91
2.0	167	90.0	5.0	12.48	18.84
5.0	417	30.0	0.0	2.06	2.06
5.0	417	30.0	2.0	1.75	5.88
5.0	417	30.0	5.0	7.37	11.55
5.0	417	60.0	0.0	4.13	4.13
5.0	417	60.0	2.0	2.22	6.04
5.0	417	60.0	5.0	0.62	8.90
5.0	417	90.0	0.0	6.20	6.20
5.0	417	90.0	2.0	4.92	7.47
5.0	417	90.0	5.0	3.02	9.38

Table 3.2: Calculated impact angles for some reference combinations of transverse momentum, detector distance from beamline and impact position on the detector surface.

of depletion depth where charge is collected. In fact, other MAPS usually can be depleted no more than 30 to 50 μm. A very large-p_T track, corresponding to orthogonal impact in the collected data samples, releases charge resulting in an average cluster size of 3.5 pixels, corresponding to 48 μm. The opposite scenario with a low-p_T track, which we matched to the 20° impact angle sample, results in a 4.7 pixels cluster, 65 μm wide. The difference is approximately 20 μm and can be resolved, taking into account some fluctuations, with $\approx$ 10 μm pixel pitch. This is the same resolution as the one of the LRDR-SOImager-2 prototype which is, in fact, able to distinghush them. The pixel pitch-to-depletion depth ratio, to perform a low-p_T track rejection, is therefore roughly 1-to-10. To make a comparison with current CMS Pixels, one must recall these can be fully depleted over their 285 μm thickness with 60 V because of their resistivity which is 5 times larger than the LDRD-SOImager-2 prototype one. This implies the pixel pitch should be $\approx$ 30 μm to reject low-p_T tracks. Bump bonding of hybrid Pixel detectors puts a lower limit on the Pixel pitch to 50 μm, because of the soldering bump size, and the production of such a finely segmented hybrid pixel detector would be, even if possible, very costly. The only advantage in very high resistivity hybrid Pixels would be

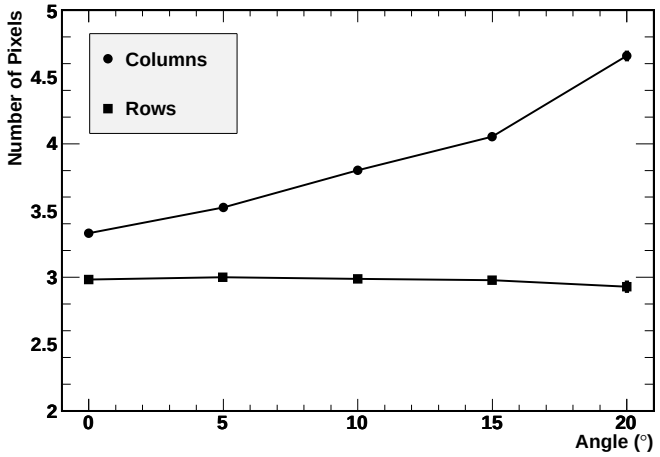

Figure 3.16: Cluster size in the LDRD-SOImager-2 prototype for different incidence angles of pion beam [74]. Courtesy of M. Battaglia, UCSC.

the large collected charge, compensating the efficiency loss due to recombination and trapping after Pixel degradation because of radiation damage, which is approximately 50 times larger in the current Pixel Detector position than at typical Outer Tracker distances.

On the other hand, the use of MAPS for triggering purposes could be effective in optimal conditions, such as those reported in the present Section, but the instrumentation of a very large surface with very-fine segmentation pixels or strips woult turn out into a huge amount of readout channels at large radii. Also this scenario is unaffordable because of the problems in handling data flow and because of the demanding power budget, which also implies difficulties in reducing the tracker material and in providing effective cooling.

The results presented in this Chapter put a significant milestone in the development of Phase 2 Tracker and Tracking Trigger, as they prove that the rejection of low-p_T tracks exploiting only information based on cluster width is a challenge still far from being overcome. Chapter 4 describes an alternative approach to low-p_T track rejection, based on pattern hit correlation in closely placed parallel sensors, which then could be the more realistic strategy to cope with the demanding requirements of very high luminosities at the Large Hadron Collider.

4. An Upgraded Tracker for Phase 2

After the description of the challenges associated with the luminosities envisaged for the LHC Phase 2 and the presentation of the concept of cluster-width Tracking Trigger, this Chapter describes a different approach, based on pattern hit correlation between two closely placed pixellated silicon sensors, called p_T-Modules. A detailed description of the principle behind these modules and of their implementation is here presented together with the concept Tracker used in the simulation studies analysed hereafter.

4.1 Requirements for a Phase 2 Tracker

At Phase 2 luminosities, the track and particle densities will be at least 10 times those expected for the LHC regime and a replacement Tracker will require higher bandwidth readout to handle the large amount of data. Moreover, as already stated in Section 2.3, the main challenge for a Tracker at Phase 2 luminosities is to feed a Level 1 Trigger together with Muon Detectors and Calorimeters. [75]. This challenge is a little different for each type of Trigger. For muons the goal is primarily to add tracking information to discriminate between different muon chamber hit combinations which appear to make valid muon trajectories. Reduction of fake muons and enhancement of momentum estimate reliability are fundamental too. For electrons a good association of Tracker hits to Calorimeter objects is needed to reject photon backgrounds. The present jet Trigger has a rate far higher than acceptable and improved isolation of tracks associated with τ jets appears, from HLT experience, to offer a means to reduce the raw Trigger rate. Vertexing capabilities of the Level 1 Trigger would be desirable too.

The tracking system has to be enhanced furthermore to have higher radiation resistance and higher readout granularity, to keep the channel occupancy at an adequate level. In addition, the new Tracker has to comply with constraints coming from the existing

CMS detector, services, infrastructures and available space in the underground caverns. It is currently foreseen to re-use the services (cables, fibers and pipes) running from the patch panel to the back end as they are interleaved with those of other subdetectors. This constraint translates to a limit in the total available cross section of conductors, cooling pipes, and number of optical channels. Such requirements and constraints drive a series of challenging developments:

- silicon sensors have to maintain adequate performance after accumulated radiation levels $\sim$ 10 times higher than the requirements of the present Tracker; higher granularity and thinner sensors are required everywhere, and radically different options may be useful for the innermost pixel layers
- more advanced ASIC technologies have to be used to cope with the high instantaneous rates in the inner pixel layers, to limit the power consumption with the higher granularity, and to implement the new trigger functionality
- novel powering schemes have to be employed to reduce the cross section of conductors inside the tracking volume and take full advantage of the lower operating voltage of the front-end ASICs, while remaining within the constraint of the existing supply cables
- more efficient cooling methods have to be used to reduce the mass of cooling pipes and heat exchangers, as well as the mass flow of the coolant, and to cope with the constraints from the existing pipes
- high-speed data links are required to handle the increased data volume generated by the increased granularity and by the trigger output, and still maintain compatibility with the installed optical fibers
- novel module concepts and electronics architectures need to be developed to implement on-detector data reduction, which allows the trigger functionality to be implemented while maintaining the bandwidth at an acceptable level

4.2 Tracker Information for a Level 1 Trigger

The current CMS Trigger exploits Tracking information only in the HLT [52]. Electron algorithms embedded with Tracking information can suppress neutral pion backgrounds

arising from minimum bias events and help distinguishing between electron and photon candidates. The τ-jet HLT is recalled at the beginning of Chapter 7 and employs tracking information to apply isolation criteria to the candidates built from Calorimeter.

One of the major constraints in a Level 1 Tracking Trigger does come from the latency time of the Level 1 buffers, which is currently 6.4 μs, three orders of magnitude shorter than the the time needed to produce Pixel tracks in HLT, and it is likely not to be extended by a large amount. Further challenges arise from the current approach to Tracker readout: signals are digitized, clustered and zero-suppressed off-detector in the FED and therefore cannot contribute to a Level 1 Trigger. Finally, the large occupancy at Phase 2 luminosities will strongly constrain the type of information that the Tracker can provide for Triggering purposes. With $\mathcal{L} = 10^{35}$ cm^{-2}s^{-1} and 40 MHz bunch crossing, an occupancy of $\sim$ 10 hits per cm^2 per bunch crossing is expected, from simulations, in a Pixel layer at 10 cm from the beam line. Assuming the same Pixel sixe as the current one of CMS Pixels and a 16 bit coding scheme, a data rate of $\sim$ 10 to 20 Gbcm^{-2}s^{-1} is expected. The current digital optical link technology envisaged for CMS Phase 2 upgrade has a maximum bandwidth of 10 Gb/s, meaning that the required link density and power consumption will be enormous.

The inclusion of one or more tracking layers with capability of discriminating hits based on the track p_T would help the achievement of such goals and the fulfillment of previous constraints. Two sensors could be placed in close radial proximity to share data and reject matching patterns consistent with a track p_T lower than few GeV/c, as the discussion on particle spectrum in minimum-bias events given in Section 3.3. This way, only selected information are passed from the Tracker to the Level 1 Trigger. These layers are referred to as "Stacked Modules", "p_T Modules" or "Trigger Layers" and their usage to reject low-p_T tracks is described starting from Chapter 5.

4.3 Stacked Modules for Low-p_T Track Rejection

A simple approach to p_T calculation of a charged track would rely on correlation of hits between sensors placed in close radial proximity. This distance should be $\sim$ 1 mm to keep the data exchange between the sensors practical. Another point to keep it so small is to keep the rate of fake combinatorics low [76, 77]. The benefit of matching hits

over minimally separated layers is that the high bandwidth requirements of transferring information for correlation takes places over a small distance and hence power consumption and material contribution to the tracker can be reduced significantly. From (3.3) one gets that, in the approximation of a perfectly cylindrical barrel ($d = 0$) with radius L, the crossing angle β depends on the bending radius R as

$$\cos\beta = \pm\sqrt{1 - \frac{L^2}{4R^2}} \tag{4.1}$$

which can be written in terms of the track p_T

$$\sin\beta = \pm\frac{L \cdot c \cdot B \cdot q \cdot 10^{-5}}{2 \cdot p_T} \tag{4.2}$$

where p_T is measured in GeV/c, R in cm, B in T, q in units of elementary charge and $c \simeq 299.792$ mm/ns is the speed of light. Assuming that $\sin\beta$ does not change from one sensor layer to the next one if they are close enough, it can be estimated by $\tan\beta = s/\Delta L$, where s is the transverse relative displacement of the hits and ΔL is the separation between sensor layers. Solving for s one gets

$$s = \frac{L \cdot c \cdot B \cdot q \cdot 10^{-5} \cdot \Delta L}{\sqrt{4p_T^2 - \left(L \cdot c \cdot B \cdot q \cdot 10^{-5}\right)^2}} \tag{4.3}$$

For $B = 4$ T, $L = 30$ cm, $\Delta L = 1$ mm and $p_T = 2$ GeV/c one gets $s \simeq 90$ μm, while $s \simeq 150$ μm at $L = 50$ cm. The current Pixel pitch of BPIX in the transverse plane is 100 μm. A stacked tracking layer using sensors with analogous Pixel/Strip pitch would therefore have sufficiently fine granularity to be able to discriminate on the transverse momentum of passing particles. This can be achieved by correctly matching the hits from each layer and calculating the track crossing angle relative to the surface of the sensor.

Stacked Modules can be seen as a Tracker structure of emerging complexity, as shown in Figure 4.1. The hierarchy of a Tracker based on Stacked Modules can be seen as:

- sensors, called *Stack Members*, with Pixels or Strips about 0.1 mm wide in the transverse plane

- two or more sensors, separated by a radial distance of about 1 mm, compose the fundamental unit to reject low p_T tracks, called *Stack*

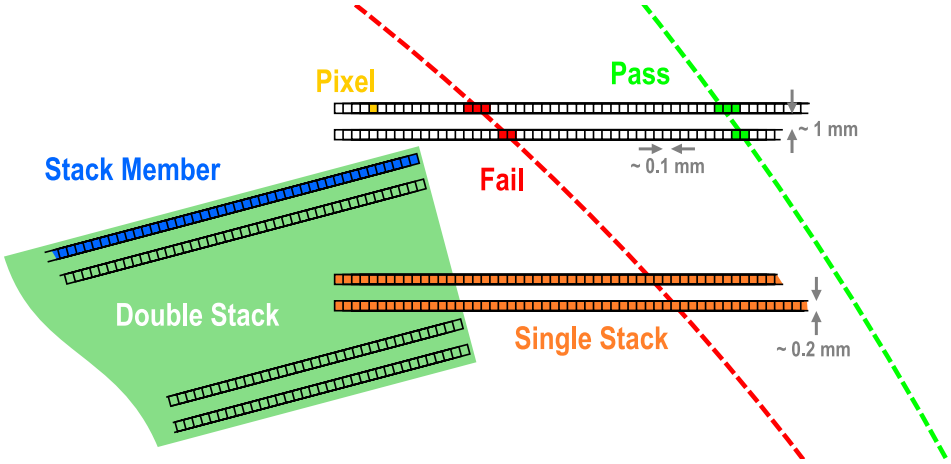

Figure 4.1: Trigger Layers hierarchy and operation principle: correlation of hits in two closely placed sensors can help in rejection of low-momentum tracks. The typical sizes, shown in the picture, allow for a sharp p_T threshold of ~ 2 GeV/c.

- pairs of Stacks separated by few cm in radial distance can be used to add further complexity to the Tracker structure and can be used in Level 1 Trigger, these pairs are called *Double Stacks*

This naming scheme can be enriched with further keywords and detail in case of a barrel-like layout:

- as Stacks are thought to be of effective use as closely paired sensors, the word "*Layer*" will mean barrels of Stacks, corresponding to two or more layers of sensitive elements
- if the Tracker Layout consists of Trigger Layers arranged in a way that allows data sharing between Layers, such as Double Stacks in particular configurations, the word "*Superlayer*" will group together the Layers involved
- within each Stack, the Stack Member which is closer to the origin of the global reference frame is called *lower Member* while the other one is called *upper Member*
- within each Double Stack, the Stack which is closer to the origin of the global reference frame is called *inner Stack* while the other one is called *outer Stack*
- Layers, Superlayers and Stack Members can be referenced to with a numbering scheme starting from 0 and increasing with distance from the origin of the global reference frame

4.4 Phase 2 Tracker Sensor, Read-Out and Cooling

The sensor R&D for a Phase 2 Tracker is currently planned in three main steps:

1. evaluation of different sensor technologies on both planar and 3D technologies with different substrates has already started and will go on for about one and a half years; this phase concentrates mainly on the issue of radiation hardness, but addresses already several geometry, design, connectivity and final testing strategy issue

2. submission of close-to-final designs to foundry

3. pre-series of the final design

Test structures in evaluation wafers will be subjected to neutron and proton irradiation to evaluate the materials in conditions which reproduce the hadron fluences at different radii. This procedure emphasizes the real operational conditions of the chips and has been developed together with RD50 representatives. Basically, all structures will be evaluated for Signal/Noise after the different irradiation and annealing steps.

Phase 2 luminosities, with proportional increases in occupancy and radiation levels, present severe challenges. For occupancy reasons the granularity will have to increase in all regions of the Tracker. The addition of Trigger capabilities brings another challenge for the on-detector readout which is power, both consumption and provision. Advanced CMOS technologies will help, but power savings per chip will depend on functionality, which may increase. At present, it is assumed that 130 nm CMOS technology will be used for Phase 2 upgrades. Since 130 nm chips operate at half the supply voltage of 0.25 mm, the supply current doubles even if the total Tracker power remains the same as at the LHC. The result is increased power dissipation and voltage drops in cables. Hence the need for a more advanced power distribution, and the choice to develop on-detector DC-DC conversion, which has implications for FE chip design. Front end specifications have been developed. A number of relevant issues are still open and are the subject of wider Tracker R&D.

The need for increased bandwidth to transfer the data from the front-end chips to the back-end electronics is addressed by the development of the GBT chipset [78]. In addition to the larger data rates, the Phase 2 environment imposes more severe requirements

in terms of radiation tolerance. The GigaBit Transceiver architecture allows the transmission of data simultaneously from the three systems (DAQ, Timing Trigger and Control, Slow Control) in the same link, aiming at a total bandwidth of $\sim$ 5 Gb/s in the version currently under development. As such requirements can be met using deep submicron CMOS commercial technologies, the GBT chipset is being designed and fabricated in 130 nm. The GBT architecture offers clear advantages in terms of development, production, installation and maintenance, since all functionalities are combined in a single system. It offers the possibility of a drastic reduction in the number of optical fibers, thanks to the large bandwidth. In addition, early modelling studies clearly show beneficial simplifications by using a single system, as compared to the current ring-architecture for the controls, which required a non-trivial matching of the granularity of control and readout as well as a rather complicated integration of the services.

The upgraded CMS Silicon Tracker will most likely dissipate at least as much power as the present one (if not more), while silicon sensor operation will require more stringent temperature control to limit the leakage current in the high radiation environment of Phase 2. CO_2 two-phase cooling appears to be a promising option to improve upon the present mono-phase fluorocarbon system, since it will achieve enhanced cooling performance with a lightweight system. Some of the main advantages of CO_2 cooling are:

- the high latent heat allows the use of small pipes, as well as large heat load per single channel, possibly reducing needs for manifolding
- the high heat transfer coefficient allows smaller heat-exchanger contacts
- CO_2 is a natural substance, which is more environmentally friendly and less expensive than fluorocarbons

The use of CO_2 cooling will contribute to an improved detector quality, while automatically ensuring compliance with the constraint of the cross section of the installed pipes.

4.5 Module Integration

Both the possibilities of developing Strip and Pixel Trigger Modules are being pursued with substantial efforts. Pixellated modules would also be suitable for use at interme-

diate radii and would provide tracking in the longitudinal view, possibly allowing for some primary vertex discrimination. However, the development of pixellated Trigger Modules is substantially more difficult, and requires the use of more advanced technologies. The challenge is the connectivity between the two sensors of the stack, which needs to be implemented through an "interposer" or "substrate". The high granularity and the complex connectivity naturally lead to higher mass and power consumption.

Two possible implementations of Pixel-based p_T-Modules are currently being investigated. In the first version, shown in Figure 4.2, each sensor is connected to the ASICs which are in turn connected to a substrate carrying power and signals. A foil of conductive material in the center of the assembly removes the heat. The substrates are connected together at one edge, while at the other edge they extend out of the sensor surface, and carry the auxiliary electronics. ASICs in one layer send data to ASICs in the other one, which operate the correlation logic and send trigger data out. A Pixel size of $\sim 0.1 \times 2$ mm^2 is envisaged, leading to an overall module size of $\sim 48 \times 48$ mm^2 (or larger, if the interconnection technology is proven to be reliable on large surfaces). The connections sensor-to-ASIC and ASIC-to-substrate could be done with direct oxide bonding and bump bonding, respectively; or both with bump bonding, with through silicon vias on the ASIC. Alternatively, low-height wirebonds could be used between ASIC and substrate, which would not require through silicon vias on the ASIC.

The readout ASIC for each column is assumed to be a 128 channel front-end element, with amplifier and other circuits in each pixel, plus an "assembler" at the periphery where the comparisons of patterns between the two layers takes place and the trigger data are temporarily stored. To minimize the interconnections on the module and take advantage of the higher density of metal lines possible at the chip level, the assembler is part of the ROC ASIC, not a separate chip. Probably several columns will be amalgamated into a single chip, perhaps with up to 8 adjacent channels.

At the edge of the module there is another ASIC, referred to as a "concentrator" which would be the interface to the GBT in both input (clock, trigger, control data) and output (data for the track-trigger) directions. Data should be stored on the pixel for full readout following a Level 1 Trigger. Given the likely number of layers in the future Tracker, it is probably desirable to read out all Level 1 data from Trigger Modules despite the low p_T threshold. This functionality would also be valuable for evaluation. It is estimated that

a binary pipeline in each Pixel would require too much space and an architecture similar to that used in the present pixel detector looks most promising.

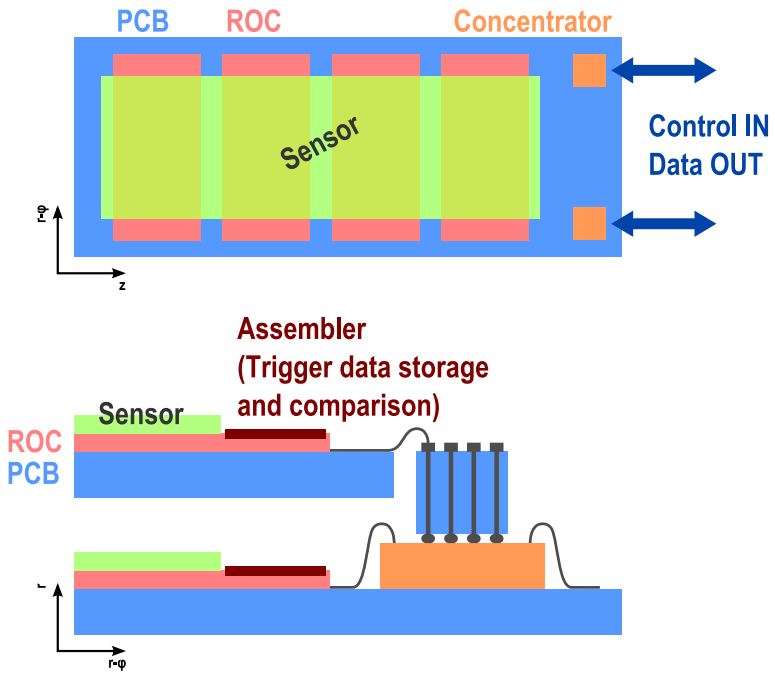

Figure 4.2: Implementation of Trigger Modules in case both lower and upper Stack Members feature same Pixel size: both top view and transverse cross section, not to scale, are shown.

Estimates of the power requirements have been made which suggest that a total consumption of 150-250 μW per channel might be achievable. Significant further contributions of about 2 W per channel comes from the GBT links. The GBT transceivers might be located outside the sensitive Tracker volume, probably in the region presently occupied by the TEC bulkhead, presenting even more challenges for the cooling system. The total power consumption for stacked layers with these pixel dimensions can be estimated to be about 9 kW for 40 million pixels at 25 cm radius, and 17 kW for 75 million pixels at 35 cm radius [79]. The total number of links required is 2900 and 5600 for the two cases and does not allow for full readout of the layers, only trigger data. These layers will therefore represent the major contribution to power consumption of a likely layout of a new Tracker and great care will be needed not to allow either power, material or numbers of links to increase significantly if the tracking performance is to be maintained.

The ROC logic should reject large clusters which could not be consistent with a high-

p_T track. For the Pixel dimensions considered, the occupancy is estimated, by simulations and extrapolations of values at 10^{34} cm^{-2}s^{-1} to be less than 0.5% at 10^{35} cm^{-2}s^{-1}. This is sufficiently low that most columns will be empty and one hit per column is the most likely case. Double hits in a column will occur but are most likely to be from charge sharing between pixels. A method which would allow to read out small numbers of hits in each 40 MHz clock cycle has been proposed so that the comparison logic can be placed at the periphery of the module. If this scheme proves not to be sufficiently robust at the maximum occupancy, alternatives will be studied, such as transferring data to the periphery at 80 MHz. This logic and module design allows the material to be minimized underneath the active region of the sensor, which has advantages in reducing secondary interactions and multiple scattering which would affect the efficiency of correlating hits from the two sensor layers. As the module design progresses it will be possible to evaluate more rigorously the total material and attempt to optimize it. At present, this concept also seems to be the most economical way of accessing the data by avoiding transferring data at high speed between Pixels in the two layers of the Stack.

However, since the logical design is at a very early stage and this is a new area, it is important to understand well the trade-offs in decision logic by comparing with alternative concepts. It is also possible that module assembly issues will prove to be important in manufacturing p_T Modules on a large scale. Therefore a second type of module design will also be developed in which data will be transferred through an intermediate substrate from one pixel layer to another. The aim is to maximally extend the dimensions of the basic building block and at the same time cover optimally the sensing area with a minimum of dead spaces. In addition, as in the previous case, this architecture is developed with the primary purpose of reducing the overall power consumption of the modules, and therefore tries to avoid moving data at high speed across chips whenever possible.

In this scenario, the modules are composed of a sandwich, as illustrated in Figure 4.3 and are assembled making use of a combination of standard technologies, such as wire-bonding and bump-bonding. The basic module consists of a matrix of ROCs called Tracker Front-End ASIC (TFEA). Each integrated circuit is itself an array of 4 by 160 identical channels, each of them corresponding to a different Pixel on the silicon sensor. These integrated circuits are connected with wire-bonding techniques on a double-sided substrate. The read-out chips are then sandwiched between two silicon sensor layers

connected to the chips using bump-bonding techniques. The architecture differs from the previous one, as it aims to perform all necessary functions on each front-end chip locally. No transfer of data to a correlator or assembler area on the chip is necessary as all front-end and triggering functions are performed in or close to each Pixel in the TFEA chip.

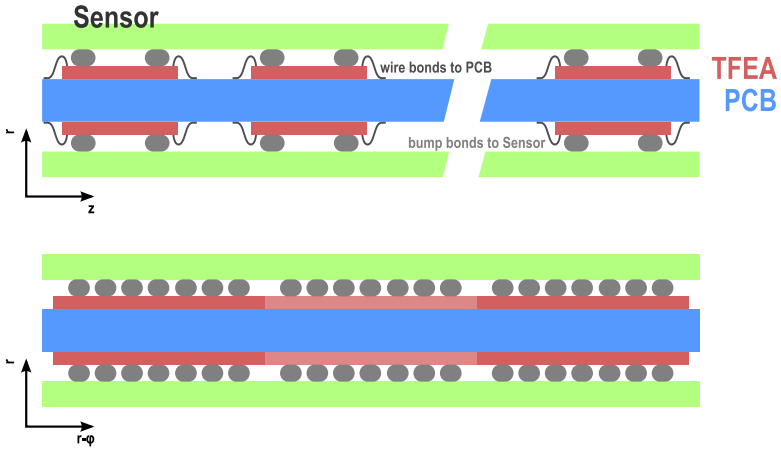

Figure 4.3: Alternative implementation of Trigger Modules in case both lower and upper Stack Members feature same Pixel size: both cross sections are shown; the picture is not to scale and without realistic number of channels for each TFEA.

In the second version of the Trigger Module implementation, there is only one layer of ASICs bonded onto a "master sensor" with finer granularity, such as $\sim 0.1 \times 1$ mm^2, with analog connections through an "interposer" to a "slave sensor" with longer channels, e.g $\sim 0.1 \times 5$ mm^2. Since the electronics are only on one side, the module could be cooled from the side of the master sensor. Options and issues for the interconnection sensor to ASIC and ASIC to interposer are similar to the first version. In addition to the design of an ASIC with a much higher level of complication, the development of these types of modules requires validating the chosen interconnection technologies on large surfaces, and addressing delicate system issues related to the high densities of interleaved analogue and digital lines.

4.6 Concept Layout for a Phase 2 Tracker

A simulation effort is going on within the CMS Collaboration, not only to help in the design of the Phase 2 Tracker modules, but also to understand their expected performance. One must remember that the Tracker is a tool for physics measurement and, particularly for Phase 2, must be helpful in triggering and rejecting background. Different layouts have been explored so far, with the common feature of including barrels of Stacked Modules. Modules, which comprise a pair of silicon sensors stacked above each other according to the description of Section 4.3, are arranged to form a single structure along z, called *Ladder*. Each barrel is the result of the replication of Ladders over $r - \phi$. A layout including also disks has not been described so far because of the difficulties it would bring in the correlation of hit patterns to reject low-p_T tracks.

Barrels of Stacked Modules have also the advantage of being highly customisable, through the so-called "strawman modules"[(1)], and can turn out into many layouts different from each other in terms of:

- number of Trigger Layers
- average radial distance of Trigger Layers from proton beams
- tilt angle of sensors in the transverse plane
- Pixel/Strip pitch
- Pixel/Strip length
- sensor thickness
- overlap of modules in the longitudinal direction
- overlap of modules in the transverse plane
- size and position of cooling, ASIC, cabling
- chosen materials

[(1)] "Strawman modules" are the basic cells used to model the Tracker: they include volumes and materials of sensitive elements, ROCs, ASICs, cooling, cabling and mechanics. Size and materials can be modified *à-la-carte*, while the basic structure remains unchanged.

This flexibility can also help in understanding the effects of module design in the overall material budget of the Tracker. A realistic estimate of the material budget is important to correctly simulate multiple scattering of hadrons, electron bremsstrahlung and photon conversion.

While the strawman module is essentially modeled on a pair of the BPIX modules used in the current CMS detector, the mechanics and cooling systems are modified so that they are shared between sensors. The cooling elements have been modified to simulate the usage of a low mass CO_2 cooling system designed to reduce the overall material budget. In fact, to obtain reliable results from simulations, one must take into account every relevant effect in the inner volumes, so that the track behaviour in Trigger Layers is correct. For this reason, the Phase 1 Pixel Detector is already included in the simulations of Phase 2 Tracker.

Previous simulation studies on the Tracker layout already dealt with many issues concerning advantages and disadvantages of specific choices for Ladder layout [80]. These studies focussed on a concept layout featuring only two Trigger Layers with average radius of 25 and 35 cm respectively, and including also a Silicon Strip Outer Tracker at larger radii. Some of the investigated options are:

- minimum Pixel length – track vertex z may turn out into parallax effects which are independent of η but are constrained by distance from the beamline and sensor separation; the Pixel length must be of the same size as the parallax displacement in order to keep the simplicity of the correlation algorithm
- effect of Lorentz drift – when using n^+ implants to collect charge, as in the envisaged sensors, electrons are the predominant carriers and each Pixel is sensirive to Lorentz drift which is compensated by either tilting the sensors, either by thinning them to ~ 100 μm with particular care to be adopted in order to keep high efficiency after irradiation
- overlap and offset of sensors within a module – overlap between modules is needed to guarantee hermetic coverage of the tracking volume; however, since the angle of incidence of tracks become slarger with increasing $|\eta|$, an offset is needed to avoid hit correlations between adjacent modules

The concept layout used in the work described herein is the so-called Long Barrel (LB) Layout. It consists, as illustrated in Figure 4.4, of 6 Layers of p_T Modules arranged

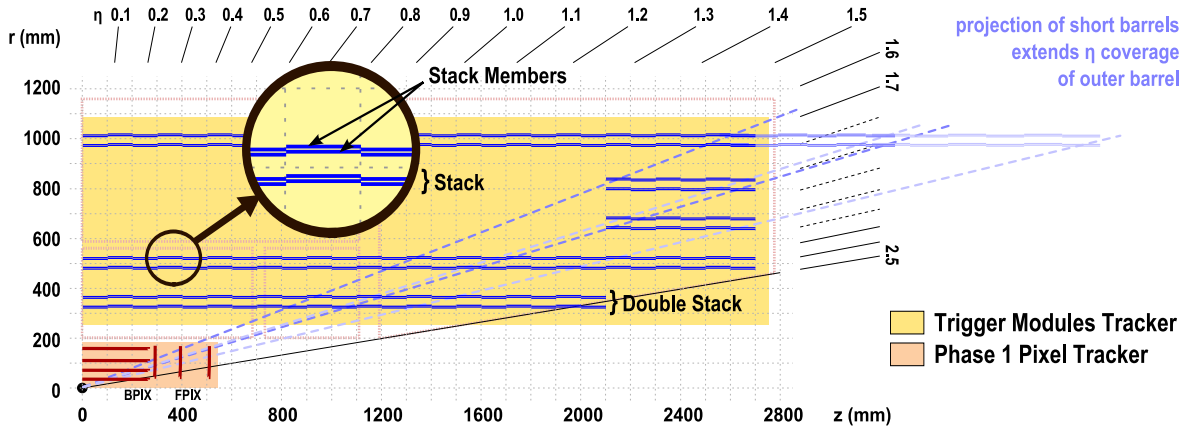

Figure 4.4: Concept layout of a Long Barrel Tracker for Phase 2.

in Double Stacks separated by ~ 4 cm. Two Superlayers cover the pseudorapidity range up to $|\eta| \sim$ 2.4-2.5, the same as the Pixel Detector, with Stacks at average radii of 32-36 cm and 48-52 cm respectively. The third Superlayer features Stacks at 98.5 and 102.5 cm and covers the pseudorapidity range up to $|\eta| \sim 1.7$. To extend the coverage of the third Superlayer, two additional short barrels are placed at radii of 64.3-68.3 cm and 80.3-84.3 cm respectively. The total lenght of the LB Tracker is ~ 540 cm, while short barrels are ~ 60 cm long on each side and the innermost Superlayer is ~ 420 cm long. All these lengths and radii can be modified according to the needs as well as the gap between the two sides of the short barrels. Further information is given in Table 4.1.

Superlayer	average radii (cm)	barrel $\|z\|$ range (cm)	Ladders	modules per Ladder	active surface (m^2)	ROCs
0	32-36	0-209.26	24	42	~ 19.5	20160
1	48-52	0-269.26	34	54	~ 35.5	36720
2	64.3-68.3	209.26-269.26	46	2×6	~ 10.7	11040
3	80.3-84.3	209.26-269.26	56	2×6	~ 13.0	13440
4	98.5-102.5	0-269.26	68	54	~ 70.9	73440

sensor				Pixel		
width (mm)	thickness (μm)	separation (mm)	tilt (°)	pitch (μm)	length (μm)	channels ($\times 10^9$)
100	200	1	0	98	989	3.096

Table 4.1: Summary of the Long Barrel concept layout features used in the present work.

Each p_T Module consists of Stack Members separated by 1 mm, Pixel modules are chosen instead of Strip ones. Each sensor is 10×10 cm^2 large and equipped with 10 ROCs

arranged in a 2×5 matrix in r-$\phi \times z$, with 500 rows and 20 columns, resulting in a Pixel pitch which is the same in all Trigger Layers: 0.1 mm width in the transverse plane and 1 mm along z. This choice does not reflect any of the proposed ones but allows particular effects due to Pixel length emerge, as described in Section 5.3.4, and it is mantained as the development of Trigger Modules design is still at an early stage.

One of the main features of the LB layout is the arrangement of Layers in Superlayers, according to the description of Tracking algorithms given in Appendix B. The distance between Stacks in each Superlayer is $\sim$ 4 cm, so that services and mechanics can be shared as well part of the back-end electronics. The $r - \phi$ arrangement of Ladders reflects a "hermetic design", in which both Layers in each Superlayer are composed by the very same number of Ladders, aimed at keeping the data flow local as much as achievable. Modules are vertically integrated in each Ladder, including all the elements needed to realize a Double Stack, which is obtained out of 4 parallel sensors. Further correlations between Trigger Primitives generated within each Stack are possible and add more flexibility to the Level 1 Trigger capabilities of this concept layout. A detailed transverse cross section of the first Superlayer is shown in Figure 4.5.

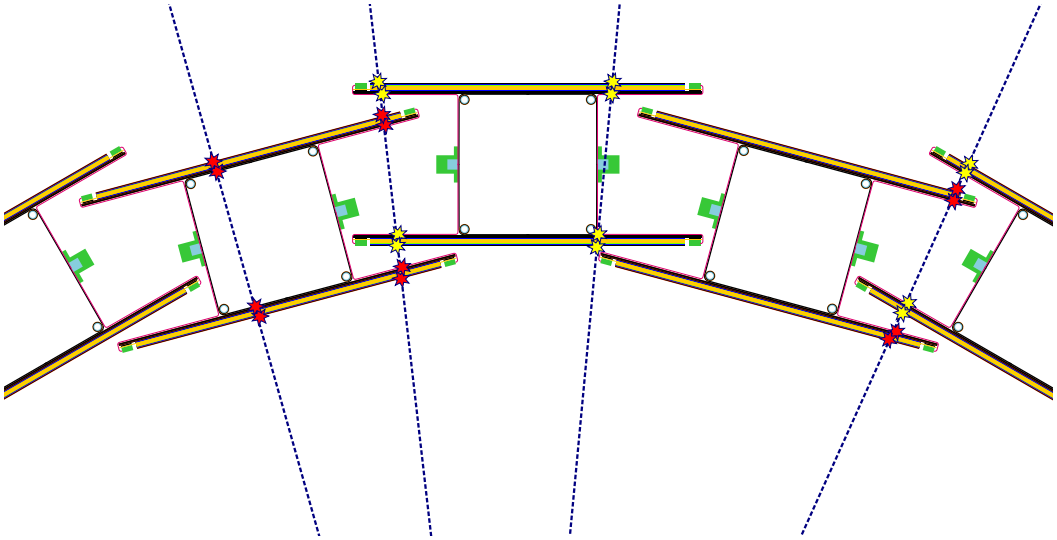

Figure 4.5: Example of hermetic design in ladder arrangement for Stacks at nominal radii of 32 and 36 cm. Each track with p_T above threshold is expected to intercep at least 4 sensor layers belonging to the same Ladder.

4.7 Trigger Modules with Silicon Strips

The Trigger Modules described so far, such as in Section 4.5, employ elongated Pixels. If the need for precise measurements along z at Level 1 is proven not to be necessary, the resolution can be relaxed leading to Strip p_T-Modules. The concept of Strip p_T-Modules is the same as Pixel ones, however the use of Strip-based stacked sensors is less challenging.

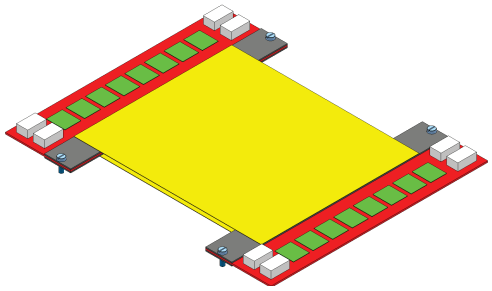

Figure 4.6: Schematic layout of a possible implementation of Strip p_T-Modules. All the ancillary electronics devoted to hit correlation between Stack Members is moved at the periphery resulting in a lighter and easier to cool module [81].

As sensor modules are envisaged to be $\sim$ 10 cm large, sensors can be wire-bonded to a single hybrid at the periphery, in order to access both sensors in the Stack, allowing 5 cm long Strips. Moreover, the strong reduction of all the needed electronics, associated to the high granularity of Pixels and to interconnectivity between Stack members, brings benefits in terms of a lower material budget and power consumption. These types of sensors could be suitable for the outer part of the Tracker, more than 40 cm from the beamline, due to the relatively long strips, which would cause too large an occupancy if placed in inner volumes. A schetch of one possible way to assemble Strip p_T-Modules is shown in Figure 4.6.

Corresponding strips on the two sensors can be bonded either to neighboring channels or to the same one on the readout ASIC, as pictured in Figure 4.7. Both options have been developed using spare sensors and ROCs from the current Tracker, resulting in a an effective pitch of 40 and 80 μm respectively, and tested with cosmic rays. The discrimination logic was implemented offline [82]. The tracking performance of stacked

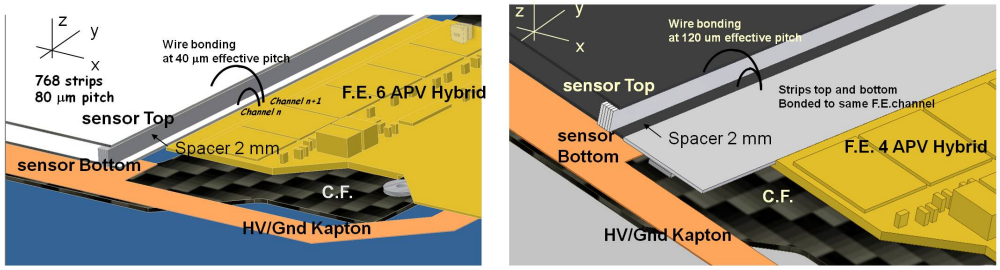

Figure 4.7: Schematic representation of the neighboring-channel (LEFT) and same-channel (RIGHT) bonding options for Strip p_T-Modules demonstrators [82].

modules prototype, has been evaluated with cosmic rays events. Figure 4.8 shows that, for both the bonding options, the distance between reconstructed clusters is linearly dependent on the incidence angle, if the latter is larger than 5°.

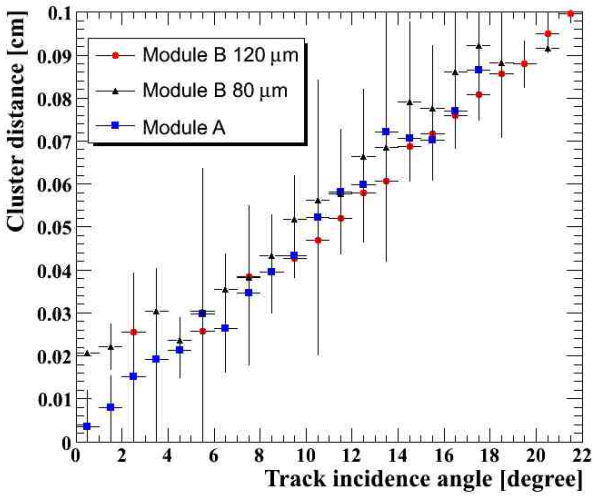

Figure 4.8: Measured distance between clusters as a function of the cosmic ray incidence direction, for different bonding options [82].

The performance of the discrimination logic has also been measured on LHC data, in collision runs at $\sqrt{s}$ = 7 TeV, from Tracker Outer Barrel stereo modules by using the tracking information to account for the stereo angle of those modules. In this configuration, sensors feature 0.120 mm Strip pitch and are separated by 2.45 mm. Hits from charged particles are reconstructed offline and their separation between Stack Members is reported in Figure 4.9 as a function of the track p_T. These studies represent the first validation of the p_T-module concept on real data.

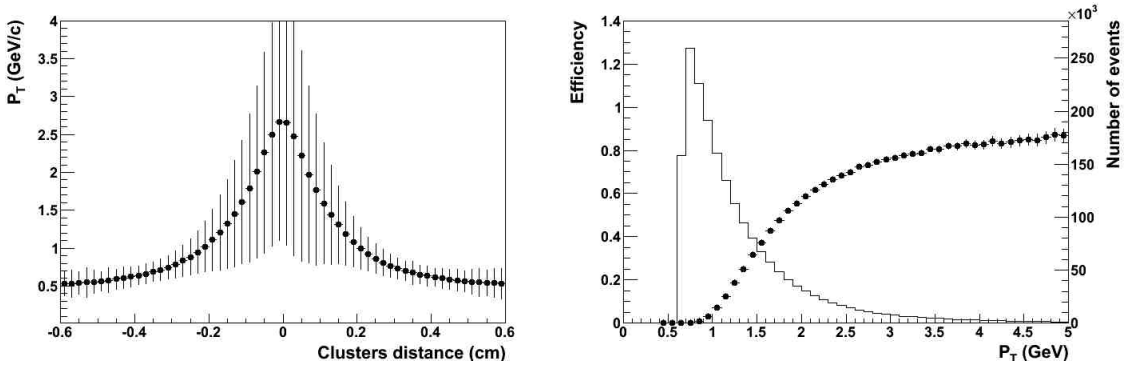

Figure 4.9: Cluster distance in double sided micro-strip detectors as a function of the track p_T in pp collisions at 7 (LEFT) and efficiency as a function of transverse momentum (RIGHT) [82].

The following Chapters describe the way a Phase 2 Tracker, such as the one described in Section 4.6, can be employed to feed the Level 1 Trigger with information relevant to distinguish background from bunch crossings useful for frontier physics measurements. Particular emphasis will be put on the state-of-the-art of Single Stack hit correlation and on the extension of Level 1 Tracking Trigger to more complex structures such as a Double Stack or a whole Long Barrel Tracker.

5. Tracking Trigger with the Concept Tracker

The concept Tracker layout described in Section 4.6 allows a deep study of Level 1 Trigger Objects which can be built at different levels of complexity in order to reduce collected data. Each of these levels can be associated to the Tracker elements corresponding to each sub-unit:

- Stack Member – reduce data within a single sensitive element
- Single Stack – reduce data within a single p_T Module
- Double Stack – reduce data within a Ladder
- whole Tracker – produce Level 1 Tracking objects to feed HLT

The state-of-the-art in Phase 2 Upgrade Tracking Trigger simulations is described both in the current Chapter and Chapter 6. Particular emphasis will be given in the description of the improvements of existing approaches and of the development of novel ideas. The effects of beam positioning and detector features are studied in this perspective.

If not otherwise stated, as in the major part of the present and next Chapters, all the results of simulation studies presented were obtained with CMS offline release `CMSSW_3_3_6` using `FastSimulation` [83]. As the power of `FastSimulation` consists in several simplifications, such as the approximation of detector geometry, the absence of delta-rays and of some nuclear interactions, the exclusion of forward regions and many other assumptions, important differences may arise with respect to a more detailed simulation based on `Geant4`. These were subject of previous works and are described throughout Sections 5.1 and 5.2. Further details on `FastSimulation` are given in Appendix A.

5.1 Clusters of Hits and Sensor Occupancy

Basic objects used in `CMSSW` simulations to identify hits are `SimHits` and `PixelDigis`:

- `SimHits` describe the exact entry and exit point of a particle in each detector element, the energy loss in the medium and all the physical processes included to simulate particle interaction with materials
- `PixelDigis`, on the other side, are built from `SimHits` taking into account detector response, including pixelization, charge sharing, noise and inefficiencies and the information they carry is limited to the coordinates in the Pixel matrix and the collected charge in units of ADC counts

Data rate reduction at large pile-up must deal with the expected high occupancy and begins with a proper association of hits to each other within the sensitive element [84]. Due to small size or track direction, a charged particle may release charge in more than one Pixel. Both data rate and combinatorial background reduction will benefit from association of hits into Clusters of `PixelDigis`. This operation must be completed before pattern hit correlation between Stack Members in order not to match an improper number of Trigger Primitives to each track. As such Primitives will be produced on-detector, also Clustering must be performed on-detector, even if it is still unclear what kind of degree of sophistication will be affordable. For this reason a few simple Clustering algorithms have been developed to this purpose. The trivial choice treats each Pixel as a different Cluster and should be taken into account when studying combinatorial backgrounds.

Broadside Clustering Algorithm The simplest available clustering algorithm is called `broadside`, and produces one-dimensional Clusters of Pixels grouped together along ϕ. Clusters built with the `broadside` algorithm contain Pixels labelled with the same column index and consecutive row index, since rows span the transverse direction. This algorithm features an optional cut which defines the maximum allowed Cluster size in number of Pixels. The default option is 3 Pixels. A sketch of `broadside` accepted or rejected Clusters is shown in Figure 5.1.

2D Clustering Algorithm Further complexity consists in adding Pixels in the longitudinal direction to the Cluster. The `2d` algorithm assumes that each Pixel can share information with its 8 immediate neighbours. Clusters which are wider or longer than 2

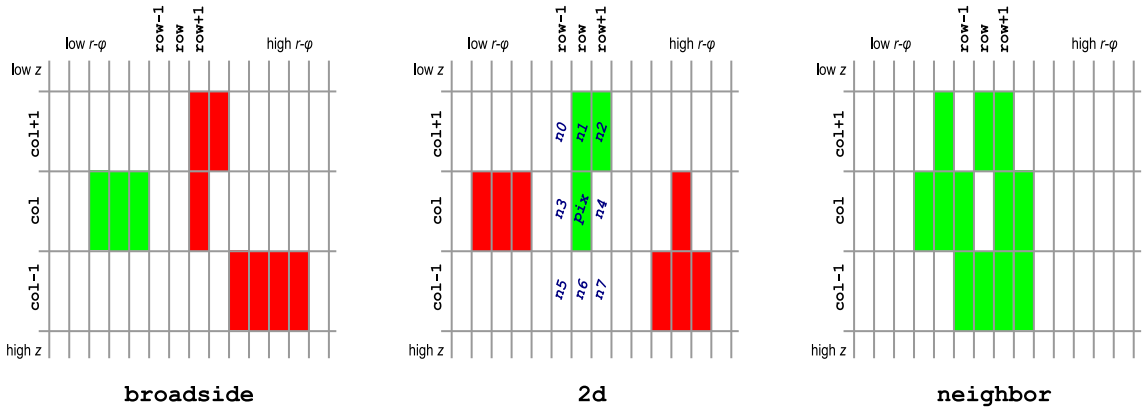

Figure 5.1: Comparison of different Clustering algorithms. Green rectangles represent Pixels in accepted Clusters, while red ones represent candidate Clusters that are rejected by the algorithm.

Pixels are vetoed. Both the interface to neighbour pixels and the vetoes ("kill bits") are handled through an 8-bit word. The procedure describede herein is repeated for each Pixel in a sensor. First of all, each Pixel *pix* and its neighbours are described according to the following matrix layout:

$$\begin{matrix} n_0 & n_1 & n_2 \\ n_3 & pix & n_4 \\ n_5 & n_6 & n_7 \end{matrix} = \begin{matrix} \text{increasing } z\text{, decreasing column:} & n_0 \rightarrow n_5 \\ \text{increasing } r\text{-}\phi\text{, increasing row:} & n_0 \rightarrow n_2 \end{matrix}$$

Each neighbour Pixel is associated to a specific bit in the 8-bit word: if position n_j corresponds to a Pixel over threshold, set to 1 the corresponding bit, if position n_j is out of sensor, let it be 0. The cluster is accepted or rejected according to some kill bits:

1. the first kill bit, k_1, prevents a Cluster to be larger than 2 Pixels in r-ϕ: if both columns $n_0 \rightarrow n_5$ and $n_2 \rightarrow n_7$ contain at least one Pixel over threshold each, this bit is set to 1, otherwise it is set to 0

2. the second kill bit, k_2, makes the Cluster to be built only if *pix* is in the leftmost-bottom position within the Cluster: if there is a Pixel over threshold either in column $n_0 \rightarrow n_5$ or in position n_6, this bit is set to 1, otherwise it is set to 0

3. if at least one of the Pixels, in $n_2 \rightarrow n_7$ column, fired and features its $k_1 = 1$, let a third kill bit k_3 be 1, otherwise set it to 0

4. if all the kill bits are set to 0, store a Cluster made of *pix* and all the n_j over threshold; note that k_3 prevents *pix* to report a Cluster when looking at its size out of the 3×3 Pixel window considered

Duplicates are removed at the end of bit check. This algorithm is still under test in order to understand the way a true Cluster is splitted into different reconstructed Clusters. Besides this open issue, this algorithm has performed reasonably well for most Tracking Trigger studies so far and it significantly reduces combinatorial backgrounds over the other available algorithms without affecting efficiencies. A sketch of `2d` accepted or rejected Clusters is shown in Figure 5.1.

Neighbour Clustering The third available clustering algorithm is called `neighbor` and works in 2 dimensions, as well as `2d`. It has been used to check Cluster sizes and set cuts in previously described algorithms, as shown in Figure 5.2. It groups together all the hits labelled with consecutive row and column index. This way, the Clusters are built as large as possible, but drawbacks of this approach at high pile-up have not been studied so far.

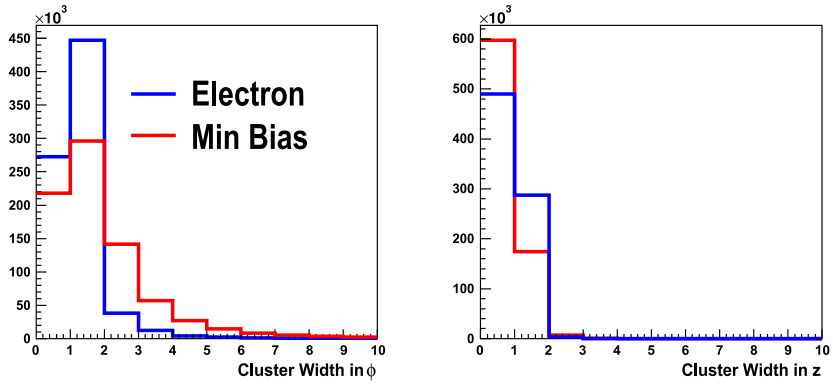

Figure 5.2: Cluster sizes in Stack at 32 cm, obtained using the `neighbor` clustering algorithm, in number of Pixels, for 10 GeV/c $< p_T <$ 50 GeV/c single electron gun events and for 200 pile-up purely minimum bias events. Pixel pitch is 0.1×1 mm^2 [84].

At this stage, simulation toolsshould be used for two main purposes: constrain detector features and study performance of different algorithms. As high pile-up environments do require long computing time to carry on a complete `Geant4` simulation(1), `CMSSW FastSimulation` is widely used despite its assumptions. For this reason, a com-

(1) Also called `FullSimulation`.

parison of `FastSimulation` to `Geant4` is needed.

The way `FastSimulation` reproduces rates and occupancies in superimposed minimum-bias events is particularly relevant for Phase 2 simulation studies. Figures 5.3 to 5.5 show the rates of `SimHits`, `PixelDigis` and Clusters, respectively [84]. The rates are shown as a function of module in z, for the Long Barrel concept tracker described in Section 4.6, which has 10 cm square modules. As the first two stacks are 420 cm long, there are 42 modules in z in these layers, while outermost stacks are 540 cm long, resulting in 54 modules. The center of the detector, corresponding to $\eta = 0$, occurs between the 21^{st} and 22^{nd} module in the first two stacks and between the 27^{th} and 28^{th} module in other stacks. The rates are given in MHz/cm^2 for the inner stack member of three of the ten stacks, and are obtained by calculating the average number of hits or Clusters per module per event, averaged over phi, normalized by the module area and multiplied by an assumed 40 MHz bunch crossing frequency in a scenario with 200 pile-up per bunch crossing. Since a major difference between the full and fast simulation is that the former includes out-of-time pile-up, also rates in the `FullSimulation`, when out-of-time pile-up hits are not included, are provided.

Each simulation is performed in two steps. First, minimum-bias events at $\sqrt{s} = 14$ TeV are generated[(2)], then they are superimposed to each other according to a Poissonian distribution with chosen average value, for each bunch crossing. The reported studies used a mean value of the Poisson distribution of 50 events per bunch crossing, then all the rates were simply multiplied by four to have estimates at 200 pile-up. Chosen clustering algorithm is `2d`.

The relevant discrepancies between `FullSimulation` and `FastSimulation` can be summarized as follows:

- there is a large difference between `SimHit` rates in the `FullSimulation` and in the `FastSimulation`, but this is mainly due to out-of-time pile-up; the `FullSimulation` includes the hits of up to five previous and three future bunch crossings, however, thanks to the fast response of the silicon detector, these are not associated to the wrong bunch crossing because of the timing information available after hit digitization

[(2)] `FullSimulation` minimum-bias events are provided by the group.

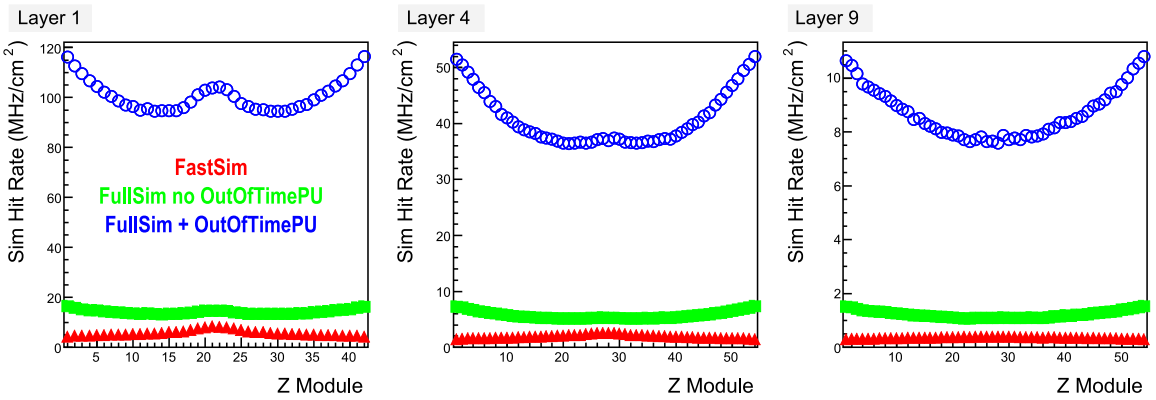

Figure 5.3: Comparison of `SimHit` rates in `FastSimulation` (red triangles) and in the `FullSimulation` with (blue circles) and without (green squares) out-of-time pile-up included. From LEFT to RIGHT are shown rates for Stack at 32, 52 and 98.5 cm [84].

- when out-of-time pile-up is removed, overall `SimHit` rates differ by approximately a factor two

- the shape of `SimHit` distributions versus module in z varies significantly between the two simulations; both of them show a peak in the central region, but the `FastSimulation` rates fall off quite rapidly at the outer edge; similar shape differences are observed in `PixelDigi` and Cluster rates as well

- `PixelDigi` rates are much lower for out-of-time pile-up events, reflecting the inclusion of timing information in the hit digitization; when removing the out-of-time hits, the `PixelDigi` rates tend to be slightly higher than the corresponding `SimHit` ones, indicating the possibility to have multiple `PixelDigis` for a given `SimHit`

5.2 Track Stubs with Trigger Modules

As already pointed out in Section 4.3, the main feature of Trigger Modules is the capability of performing pattern hit correlation between two closely piled sensors to identify candidate tracks with large p_T. Accepted pairs of Clusters in Stack Members belonging to the same p_T Module are called track stubs. This step may correspond to the Local Trigger in current Level 1 Trigger.

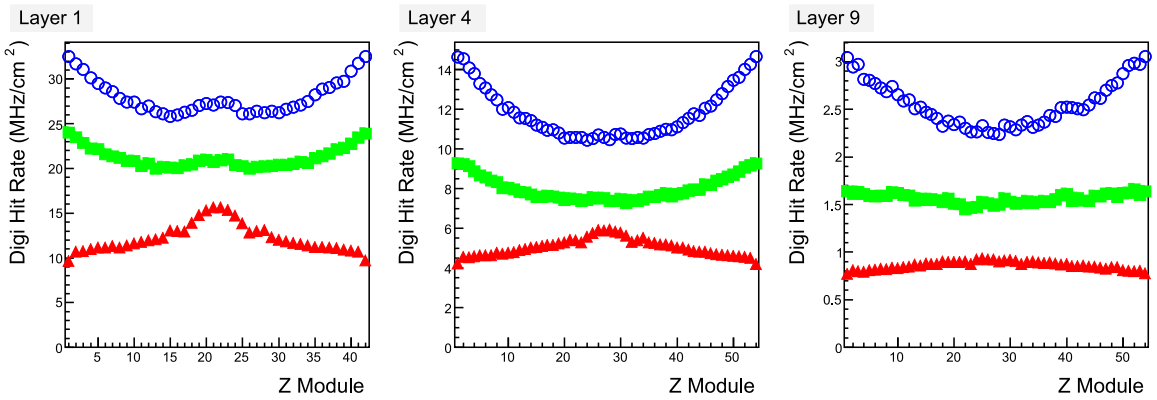

Figure 5.4: Comparison of `PixelDigi` rates in `FastSimulation` (red triangles) and in the `FullSimulation` with (blue circles) and without (green squares) out-of-time pile-up included. From LEFT to RIGHT are shown rates for Stack at 32, 52 and 98.5 cm [84].

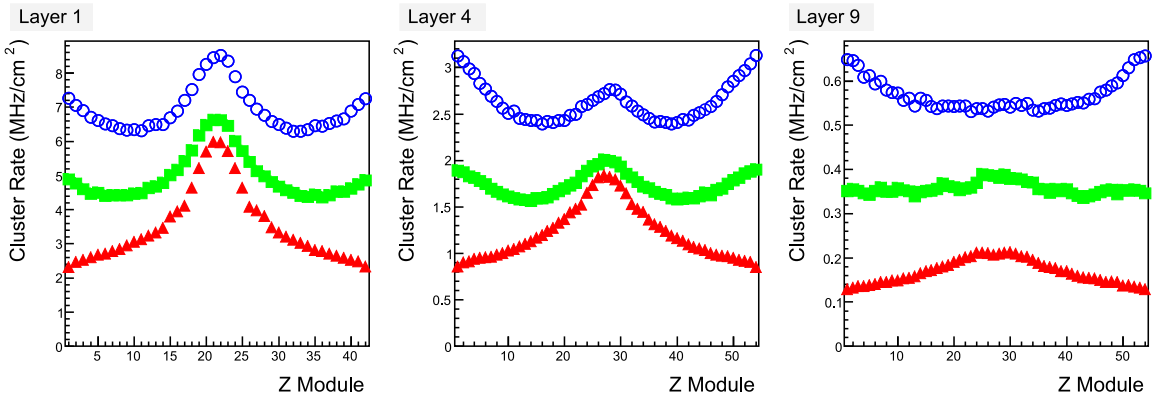

Figure 5.5: Comparison of rates of `2d` Clusters made from `PixelDigis` in `FastSimulation` (red triangles) and in the `FullSimulation` with (blue circles) and without (green squares) out-of-time pile-up included. From LEFT to RIGHT are shown rates for Stack at 32, 52 and 98.5 cm [84].

To preserve the local processing of data, only pairs of Clusters within the same module are taken into account by the Stub Builder. Different prescriptions are available to build stubs, inspired either by the search for physics performance or by the need of computation efficiency. All the hit matching algorithms described herein use `PixelDigi` Clusters as inputs. Stubs conceptually connect a global view of the Tracker to the local features of track interaction with sensitive elements and are therefore described by two kind of objects called `LocalStub` and `GlobalStub` according to which of the two aspects is emphasized.

Earlier studies explored matching criteria in order to understand advantages and

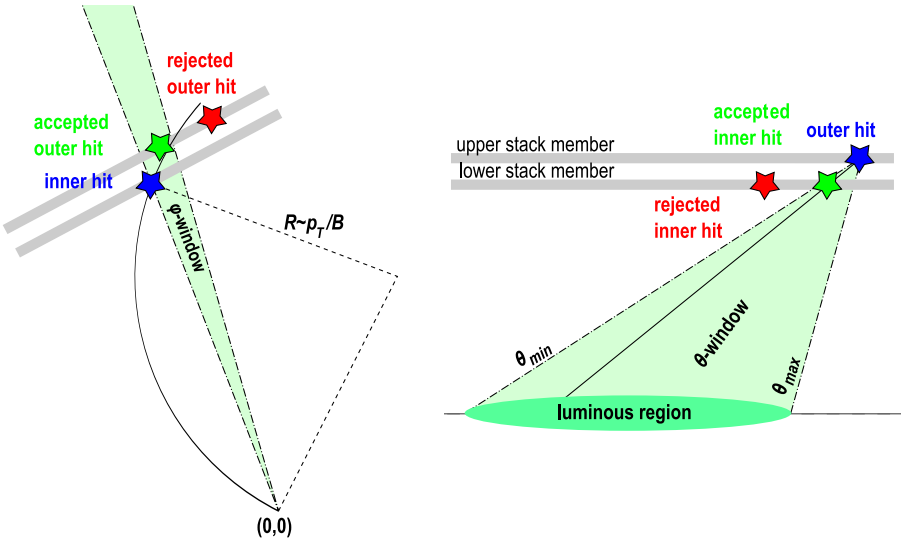

Figure 5.6: Global Geometry Hit Matching on transverse plane and longitudinal plane. The large size of pixels in z, which is of the order of 1 mm, like the gap between the two modules, does not allow precise z match. The value assigned to w_{IP} is, in fact, 2 m, while a reasonable size for a beam spot is 10 times smaller. The picture has been drawn showing the basic concept as it performs better when applied to tracklets. The ϕ_{win} angle has been drawn only on the same side as the track, while, in fact, the search window is open on both sides.

disadvantages of different approaches [80], including:

- correlation window size – an effective cut on the p_T of a crossing track, depending on sensor separation and Pixel pitch, can be applied by only selecting hits from each sensor that lie within a couple of Pixels in r-ϕ; in case of tilted sensors, an offset must be applied too

- effect of barrel approximation of a cylinder – also impact point on the sensors can affect window size, such as it affects track impact angle as in (3.3); the compromise between avoiding the cost of small sensor width and the bad performance of large correlation windows, a row correlation algorithm, should depend on the impact point itself

- effect of sensor separation – if correlation window size is fixed, increasing the sensor separation has the effect of increasing the p_T threshold for stub formation; this also affects the rate of combinatorial background; for each sensor separation, a new column correlation window must be applied in order to maintain efficiency

- effect of correlation window size – the row correlation window cut is another

method of controlling the p_T threshold; hit matching over the minimal number of pixels naturally leads to a lower power and simpler correlation implementation; however, if a low p_T cut is required and the sensor separation is fixed by construction constraints, it may be necessary to increase the correlation window; it was noticed that a stacked layer with a 2 mm sensor separation and a row correlation window of 5 can attain a similar performance as a layer with 1 mm sensor separation and row correlation window of 3, albeit with more fakes

- effect of Lorentz drift – tilting sensors eliminates electron drift due to the magnetic field within CMS, therefore reducing cluster size with important benefits for low power readout and correlation electronics; tilted sensors are still able to trigger on track p_T, but the threshold seems to be higher than in the untilted case, especially at larger sensor separations, and the stub rate seems to be lower if no clustering is performed; alternatively, larger clusters may be advantageous in improving the position resolution of hits in the layer if the full event information could be kept in buffers until a Level 1 accept

All these investigations contributed to the definition of the concept Tracker layout and drove to the development of the following algorithms for stub production.

Global Geometry Hit Matching The first algorithm, called `globalgeometry`, combines constraints on the p_T of the track generating the stub with the extrapolation of its vertex coordinates as shown in Figure 5.6. The main assumption is that the beamspot position on the transverse plane lays exactly at the center of the global reference frame, $x_{vtx} = y_{vtx} = 0$. Also the primary vertex of the event and the vertex of the track one may match to the candidate stub are assumed to have $x_{vtx} = y_{vtx} = 0$. This algorithm may be corrected for the actual beamspot position; however, as stubs should be built on-detector in the fastest way, this operation will need unpractical upload of information to the ASICs that produce stubs in each pair of Stacked Sensors.

The first request is made on the track p_T, to be larger than 2.0 GeV/c. A ϕ window is opened starting from the position[(3)] in the transverse plane $\rho = \sqrt{x^2 + y^2}$ of the inner and outer Cluster as:

$$\phi_{win} = (\rho_{\text{out}} - \rho_{\text{in}}) \times \frac{c \cdot B}{2 \cdot 10^7 \cdot p_T^{min}} \tag{5.1}$$

[(3)]The position of a Cluster is defined as the unweighted average of the positions of the Pixels composing the Cluster.

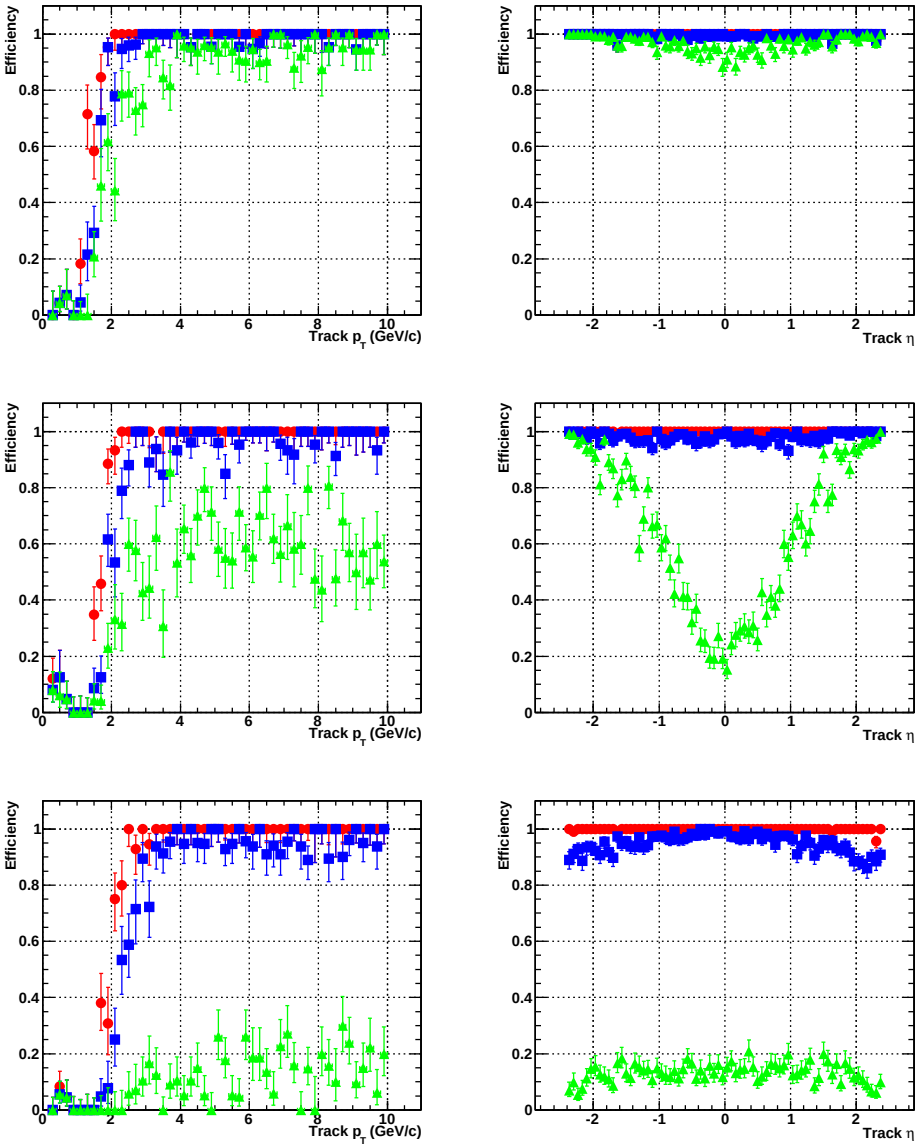

Figure 5.7: Loose tune stub production efficiency with `globalgeometry` in Stacks at 32 and 36 cm nominal radius for different clustering algorithms: no clustering (TOP), `broadside` (MIDDLE) and `2d` (BOTTOM). Efficiency is shown as a function of track p_T, for $0 < p_T < 10$ GeV/c, and track direction η, for $p_T > 20$ GeV/c. Efficiency to find at least one stub in the two Stacks is painted with red circular markers, efficiency to find at least two stubs is painted with blue square markers, and efficiency to find more than two stubs is painted with green triangular markers. The sample was composed of single μ^- with flat $0 < p_T < 100$ GeV/c distribution and flat distribution of track direction $|\eta| < 2.4$, using CMS offline `CMSSW_2_2_13`.

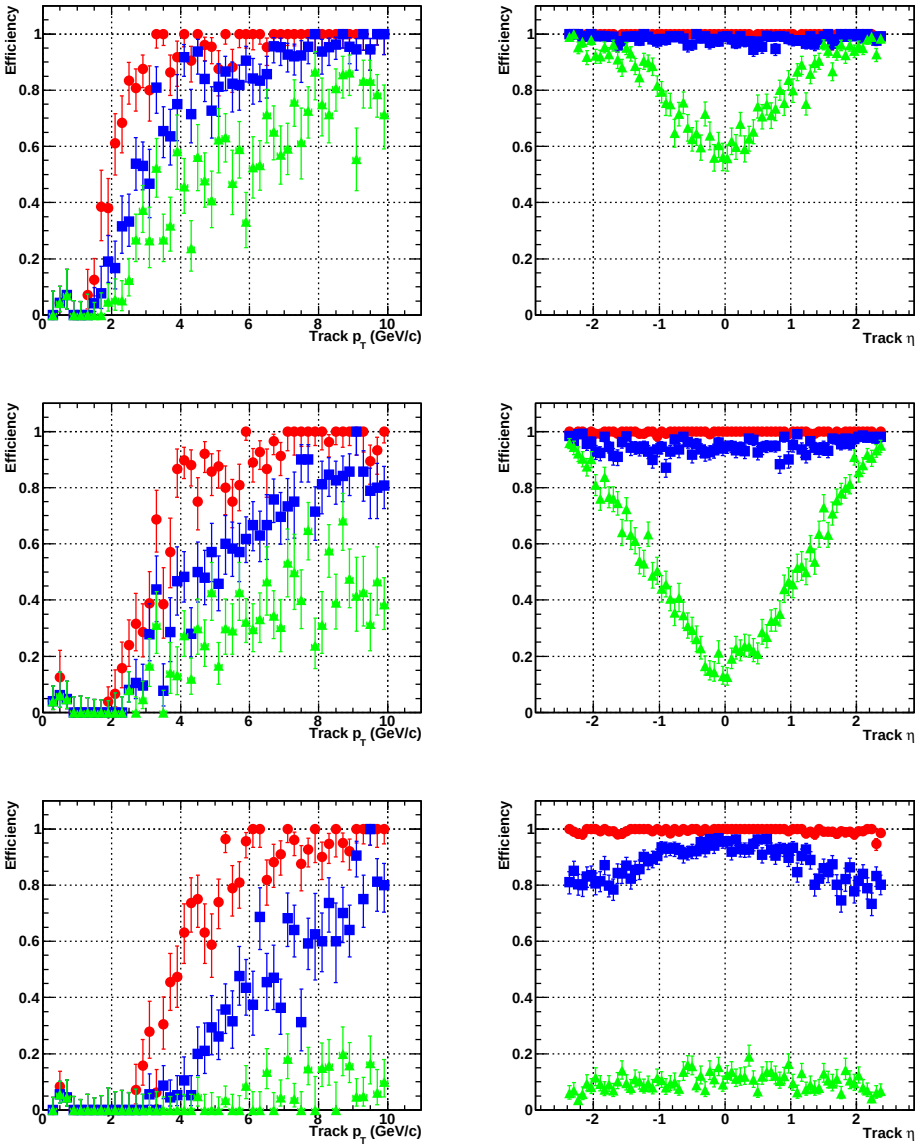

Figure 5.8: Tight tune stub production efficiency with `globalgeometry` in Stacks at 32 and 36 cm nominal radius for different clustering algorithms: no clustering (TOP), `broadside` (MIDDLE) and `2d` (BOTTOM). Efficiency is shown as a function of track p_T, for $0 < p_T < 10$ GeV$/c$, and track direction η, for $p_T > 20$ GeV$/c$. Efficiency to find at least one stub in the two Stacks is painted with red circular markers, efficiency to find at least two stubs is painted with blue square markers, and efficiency to find more than two stubs is painted with green triangular markers. The sample was composed of single μ^- with flat $0 < p_T < 100$ GeV$/c$ distribution and flat distribution of track direction $|\eta| < 2.4$, using CMS offline `CMSSW_2_2_13`.

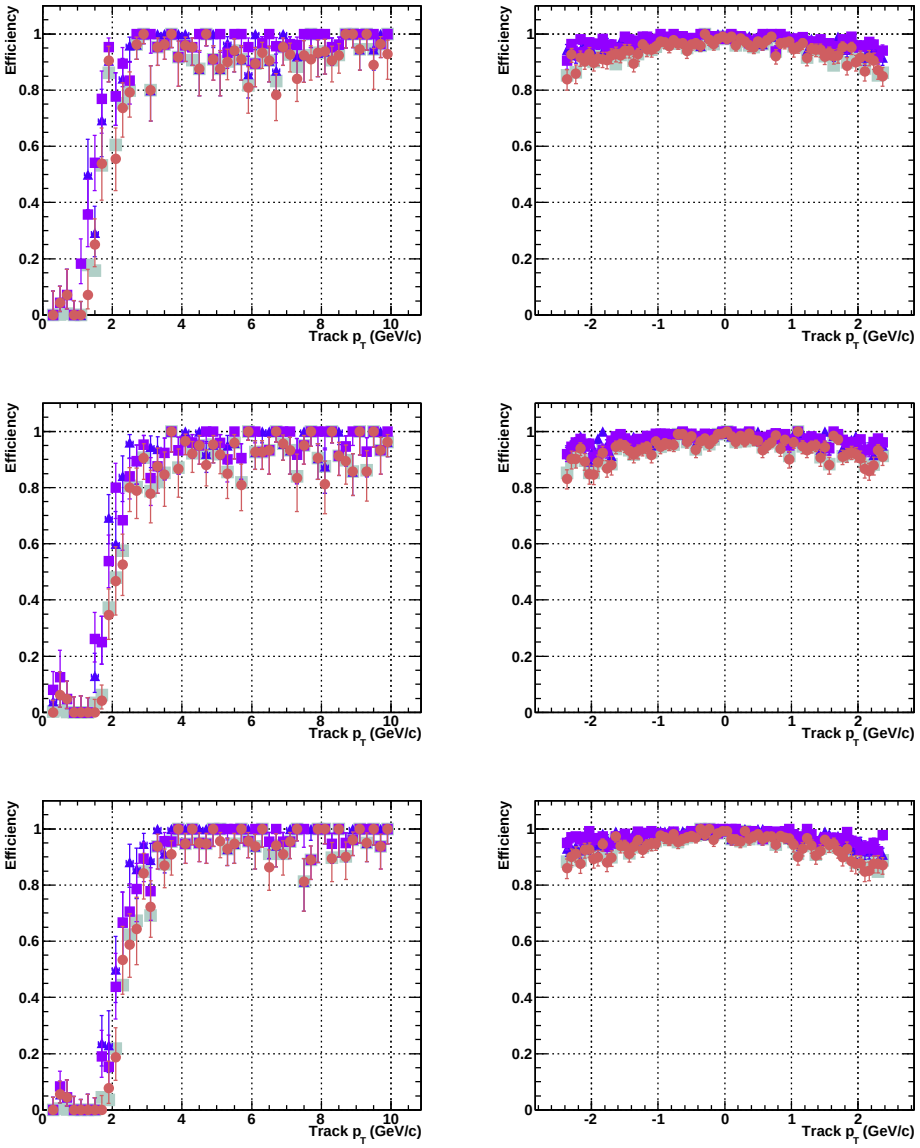

Figure 5.9: Loose tune stub production efficiency with `globalgeometry` in Stacks at 32 and 36 cm nominal radius for different clustering algorithms: no clustering (TOP), `broadside` (MIDDLE) and `2d` (BOTTOM). Efficiency is shown as a function of track p_T, for $0 < p_T < 10$ GeV/c, and track direction η, for $p_T > 20$ GeV/c. Efficiency to find at least one stub in the innermost Stack is painted with purple squares, the efficiency to find at least one stub in the outermost Stack is painted with navy blue triangles, their product is painted with grey squares while red brick circles represent the efficiency to find at least one stub in both Stacks within the same Ladder. The sample was composed of single μ^- with flat $0 < p_T < 100$ GeV/c distribution and flat distribution of track direction $|\eta| < 2.4$, using CMS offline `CMSSW_2_2_13`.

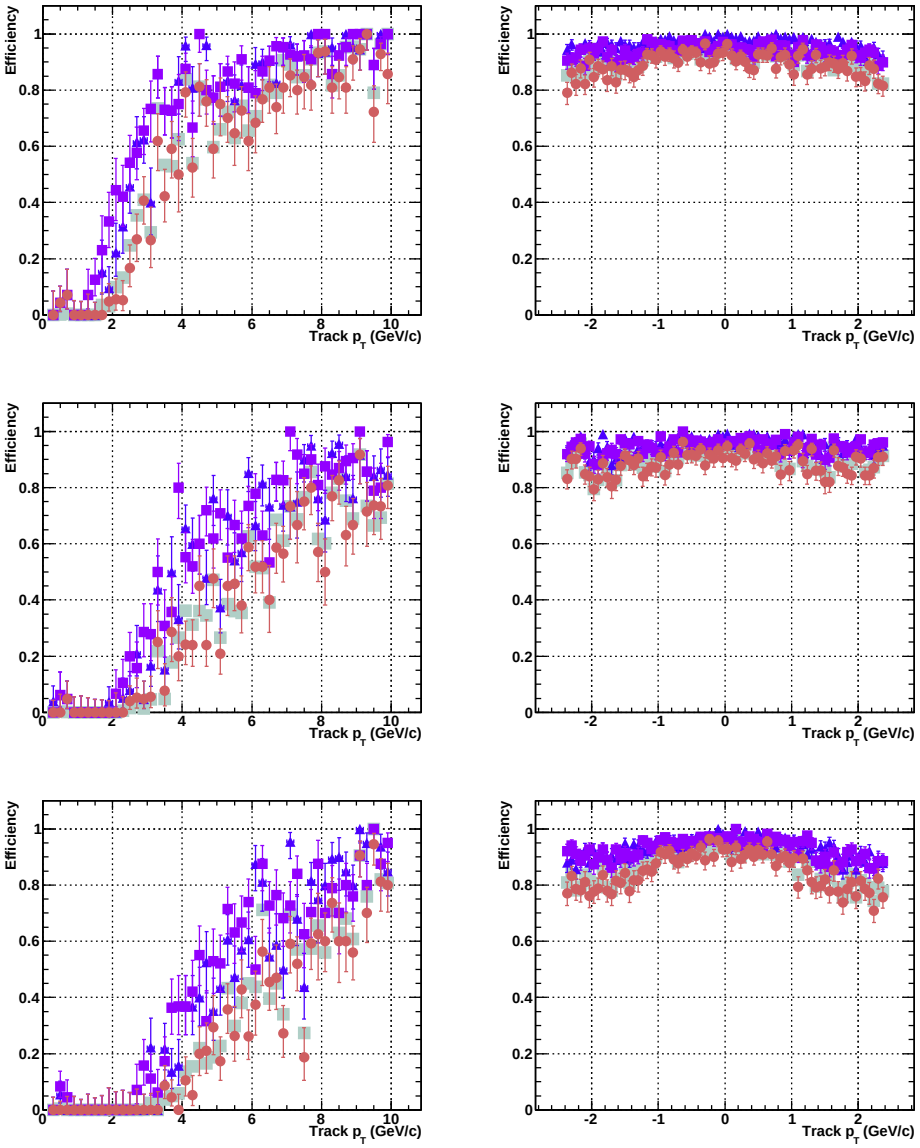

Figure 5.10: Tight tune stub production efficiency with `globalgeometry` in Stacks at 32 and 36 cm nominal radius for different clustering algorithms: no clustering (TOP), `broadside` (MIDDLE) and `2d` (BOTTOM). Efficiency is shown as a function of track p_T, for $0 < p_T < 10$ GeV/c, and track direction η, for $p_T > 20$ GeV/c. Efficiency to find at least one stub in the innermost Stack is painted with purple squares, the efficiency to find at least one stub in the outermost Stack is painted with navy blue triangles, their product is painted with grey squares while red brick circles represent the efficiency to find at least one stub in both Stacks within the same Ladder. The sample was composed of single μ^- with flat $0 < p_T < 100$ GeV/c distribution and flat distribution of track direction $|\eta| < 2.4$, using CMS offline `CMSSW_2_2_13`.

where c is the speed of light rounded to $3 \cdot 10^8$ m/s, B is the magnetic field at the origin of the detector reference frame rounded to 4 T, the distances are measured in cm and the p_T is measured in GeV/c. If the angle subtended by the two Clusters with respect to $(x, y) = (0, 0)$ is smaller than ϕ_{win}, the radius of the circle identified by this triangle is larger than the bending radius of a track with $p_T = p_T^{min}$.

The second step in `globalgeometry` is the compatibility cross-check with the size of luminous region in the longitudinal plane. The polar angle of a straight line connecting the two Clusters and pointing to $\rho = 0$ must be within the limits defined by the outer Cluster and the points $(\rho, z) = (0, +w_{IP})$ and $(\rho, z) = (0, -w_{IP})$. w_{IP} is the half-width of the luminous region, fixed to 200 cm after optimization studies. This constraint is easily translated into:

$$\left| \frac{z_{\text{in}}\rho_{\text{out}} - z_{\text{out}}\rho_{\text{in}}}{\rho_{\text{out}} - \rho_{\text{in}}} \right| < w_{IP} \tag{5.2}$$

The `globalgeometry` algorithm has then been modified in order to flag a stub if it is consistent with a $p_T > 5.0$ GeV/c threshold, with the same assumptions as for the default choice. A stub consistent with a 5.0 GeV/c threshold is called Tight, while an accepted stub in the 2.0 GeV/$c < p_T < 5.0$ GeV/c range is called Loose.

The efficiency to find stubs made with `globalgeometry` in Stacks at nominal radii of 32 and 36 cm, is shown in Figures 5.7 and 5.8 for different clustering algorithms and for both the Tight and Loose tunes. These results are obtained from a 10,000 single μ^- sample with flat $0 < p_T < 100$ GeV/c distribution, flat distribution of track direction $|\eta| < 2.4$ and Gaussian spread of vertex position with $\sigma_x = \sigma_y = 15$ μm and $\sigma_z = 5.3$ cm. The common denominator is the number of tracks per p_T bin or per η bin that release at least one `PixelDigi` in one of the Sensitive elements of the Stack.

A different approach in understanding stub production efficiency, making distinction and comparison between Inner and Outer Stacked Layer, is shown in Figures 5.9 and 5.10. The probability to create a stub in each Layers is compared to the probability to find a stub in both the Stacks within the same Ladder, according to the hermetic design philosophy.

Pixel-Ray Hit Matching An improved version of `globalgeometry`, called `pixelray`, tries to provide a better matching on the longitudinal plane. While the transverse matching is the same, the longitudinal one is done as follows:

1. the leftmost and rightmost Pixels are ordered according to ρ, to be sure that the Tracker layout does not affect the algorithm[4].

2. leftmost and rightmost Pixels of the outer Cluster are projected to the beam line:

$$z^{\text{proj}}_{\text{left}} = z^{\text{out}}_{\text{right}} + \left(z^{\text{in}}_{\text{left}} - z^{\text{out}}_{\text{right}}\right) \times \frac{\rho^{\text{out}}_{\text{left}}}{\rho^{\text{out}}_{\text{left}} - \rho^{\text{in}}_{\text{left}}} \tag{5.3}$$

$$z^{\text{proj}}_{\text{right}} = z^{\text{out}}_{\text{left}} + \left(z^{\text{in}}_{\text{right}} - z^{\text{out}}_{\text{left}}\right) \times \frac{\rho^{\text{out}}_{\text{left}}}{\rho^{\text{out}}_{\text{left}} - \rho^{\text{in}}_{\text{left}}} \tag{5.4}$$

3. a candidate stub is accepted if $z^{\text{proj}}_{\text{left}} < w_{IP}/2$ and $z^{\text{proj}}_{\text{right}} > -w_{IP}/2$

Also the `pixelray` algorithm has then been modified in order to flag a stub if it is Tight. The two main advantages of `pixelray` against `globalgeometry` are a comparable performance with a much smaller z window , $w_{IP} = 20$ cm, and a lower number of combinatorial fake stubs in high Pile-Up environment, as shown in Figure 5.15.

The efficiency to find stubs made with `pixelray` out of `2d` Clusters is shown in Figures 5.11 and 5.12 for different Double Stacks of the concept Tracker and for both the Tight and Loose tunes. These results are obtained from a 10,000 single μ^- sample with flat $0 < p_T < 100$ GeV/c distribution, flat distribution of track direction $|\eta| < 2.4$ and Gaussian spread of vertex position with $\sigma_x = \sigma_y = 15$ μm and $\sigma_z = 5.3$ cm. The common denominator is the number of tracks per p_T bin or per η bin that release at least one `PixelDigi` in one of the Sensitive elements of the Stack.

A different approach in understanding stub production efficiency, making distinction and comparison between Inner and Outer Stacked Layer, is shown in Figures 5.13 and 5.14. The probability to create a stub in each Layers is compared to the probability to find a stub in both the Stacks within the same Ladder, according to the hermetic design philosophy.

Window Hit Matching and Look-Up Tables The previously described algorithms make use of global coordinates of Clusters. As the goal is to keep the stub production on-detector, an approach based on local reference frame would be desirable. The `window`

[4] In some Geometries the outer Cluster may be found at a lower radius in transverse plane, e.g. if modules are tilted.

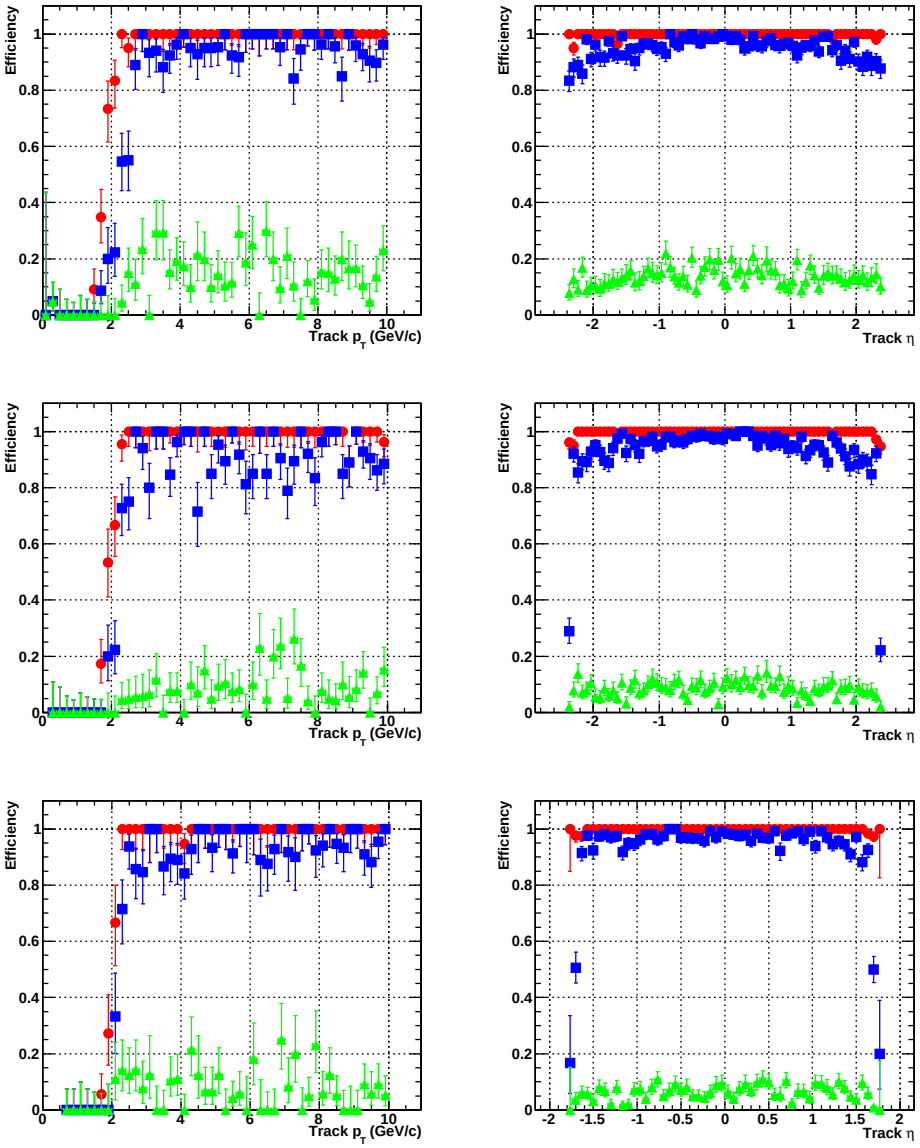

Figure 5.11: Loose tune stub production efficiency with `pixelray` applied on `2d` Clusters: 32 and 36 cm nominal radii of Stacks (TOP), 48 and 52 cm (MIDDLE) and 98.5 and 102.5 cm (BOTTOM). Efficiency is shown as a function of track p_T, for $0 < p_T < 10$ GeV/c, and track direction η, for $p_T > 20$ GeV/c. Efficiency to find at least one stub in the two Stacks is painted with red circular markers, efficiency to find at least two stubs is painted with blue square markers, and efficiency to find more than two stubs is painted with green triangular markers. The sample was composed of single μ^- with flat $0 < p_T < 100$ GeV/c distribution and flat distribution of track direction $|\eta| < 2.4$, using CMS offline `CMSSW_2_2_13`.

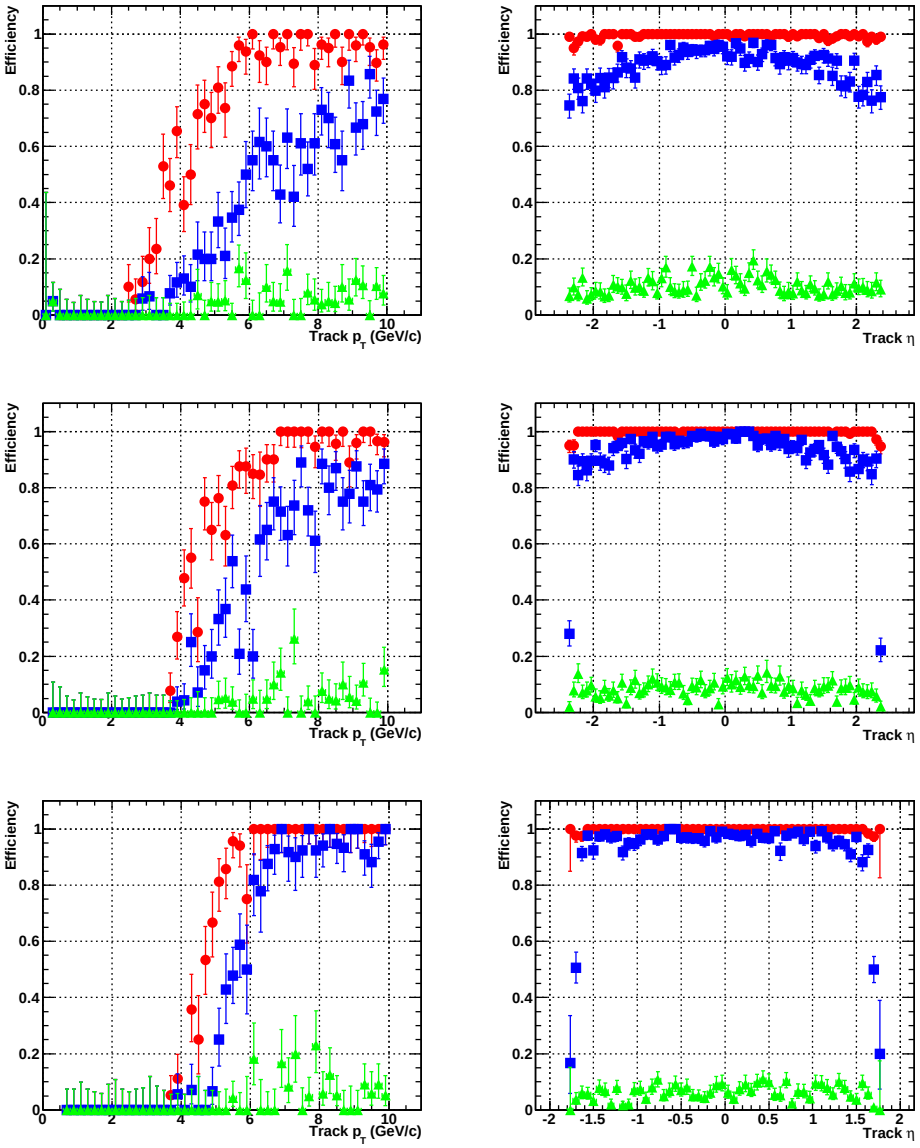

Figure 5.12: Tight tune stub production efficiency with `pixelray` applied on `2d` Clusters: 32 and 36 cm nominal radii of Stacks (TOP), 48 and 52 cm (MIDDLE) and 98.5 and 102.5 cm (BOTTOM). Efficiency is shown as a function of track p_T, for $0 < p_T < 10$ GeV/c, and track direction η, for $p_T > 20$ GeV/c. Efficiency to find at least one stub in the two Stacks is painted with red circular markers, efficiency to find at least two stubs is painted with blue square markers, and efficiency to find more than two stubs is painted with green triangular markers. The sample was composed of single μ^- with flat $0 < p_T < 100$ GeV/c distribution and flat distribution of track direction $|\eta| < 2.4$, using CMS offline `CMSSW_2_2_13`.

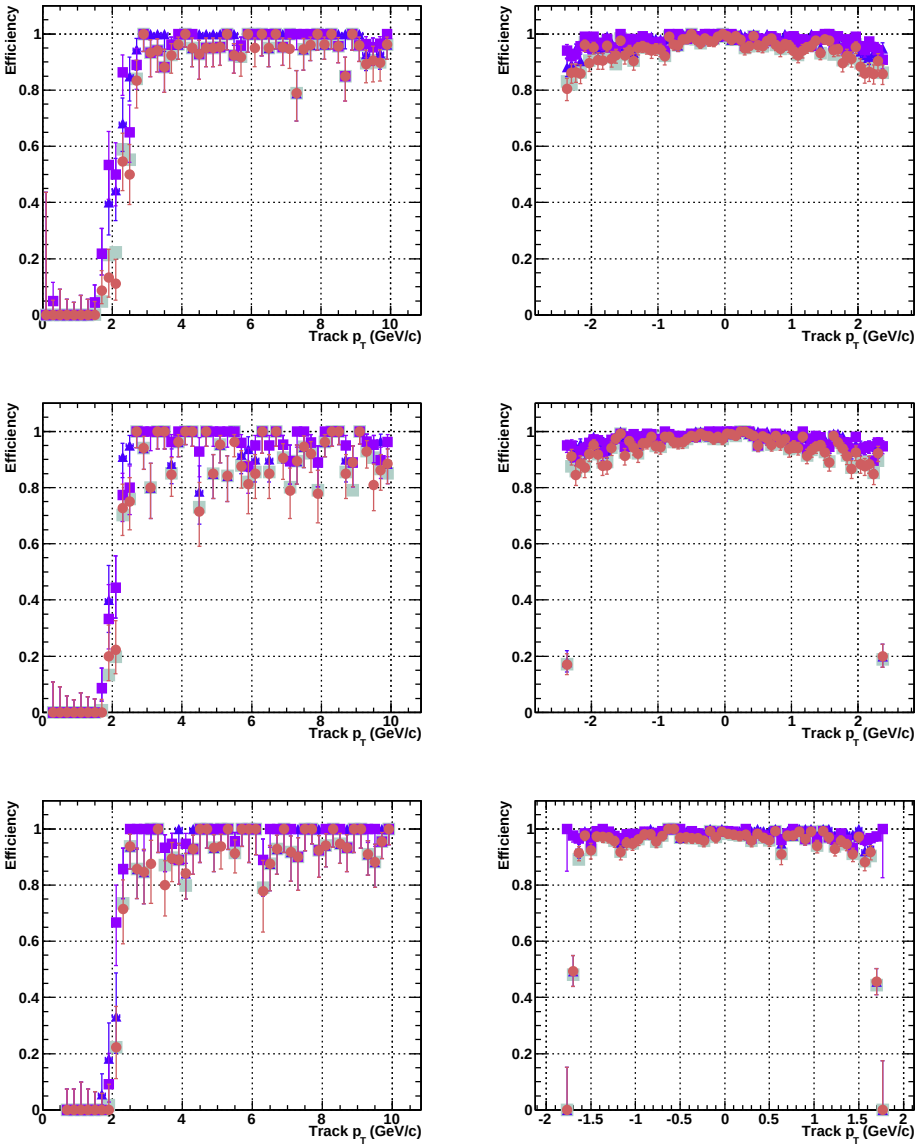

Figure 5.13: Loose tune stub production efficiency with `pixelray` applied on `2d` Clusters: 32 and 36 cm nominal radii of Stacks (TOP), 48 and 52 cm (MIDDLE) and 98.5 and 102.5 cm (BOTTOM). Efficiency is shown as a function of track p_T, for $0 < p_T < 10$ GeV$/c$, and track direction η, for $p_T > 20$ GeV$/c$. Efficiency to find at least one stub in the innermost Stack is painted with purple squares, the efficiency to find at least one stub in the outermost Stack is painted with navy blue triangles, their product is painted with grey squares while red brick circles represent the efficiency to find at least one stub in both Stacks within the same Ladder. The sample was composed of single μ^- with flat $0 < p_T < 100$ GeV$/c$ distribution and flat distribution of track direction $|\eta| < 2.4$, using CMS offline `CMSSW_2_2_13`.

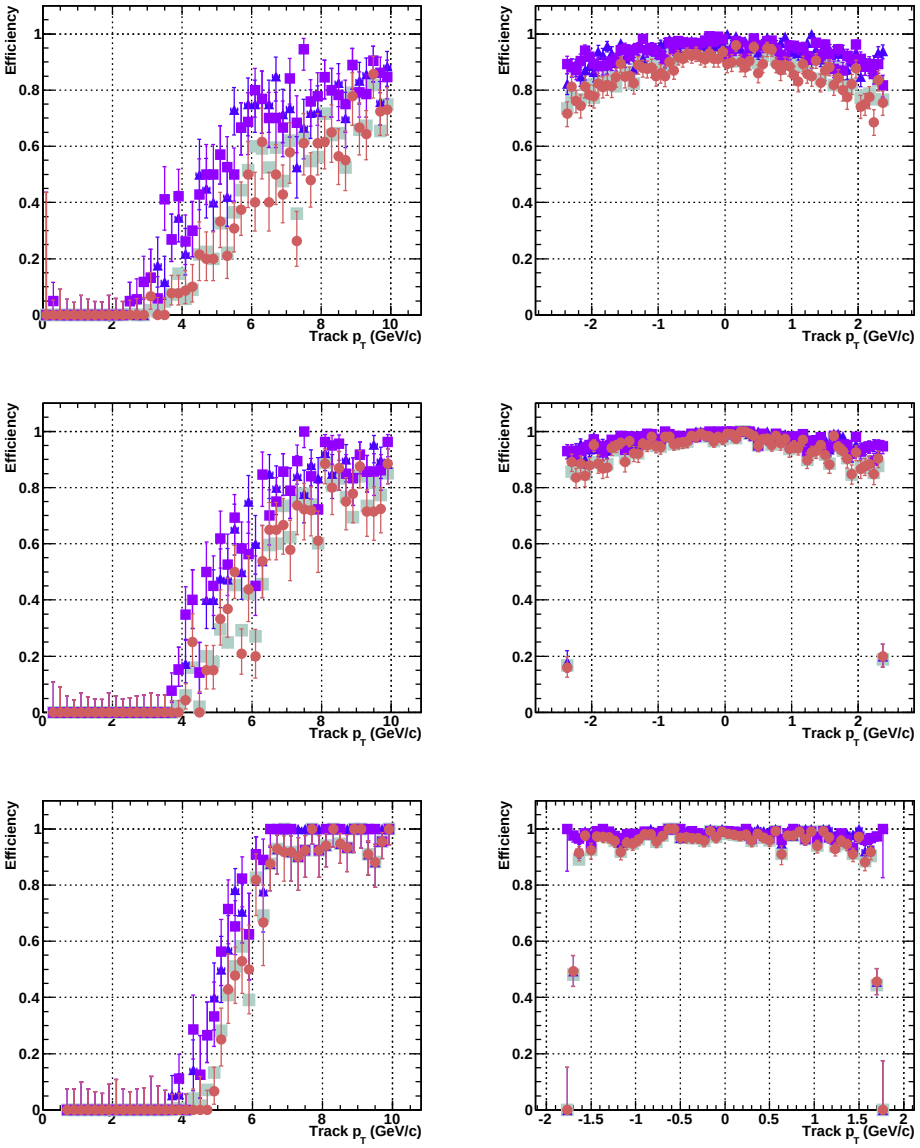

Figure 5.14: Tight tune stub production efficiency with `pixelray` applied on `2d` Clusters: 32 and 36 cm nominal radii of Stacks (TOP), 48 and 52 cm (MIDDLE) and 98.5 and 102.5 cm (BOTTOM). Efficiency is shown as a function of track p_T, for $0 < p_T < 10$ GeV/c, and track direction η, for $p_T > 20$ GeV/c. Efficiency to find at least one stub in the innermost Stack is painted with purple squares, the efficiency to find at least one stub in the outermost Stack is painted with navy blue triangles, their product is painted with grey squares while red brick circles represent the efficiency to find at least one stub in both Stacks within the same Ladder. The sample was composed of single μ^- with flat $0 < p_T < 100$ GeV/c distribution and flat distribution of track direction $|\eta| < 2.4$, using CMS offline `CMSSW_2_2_13`.

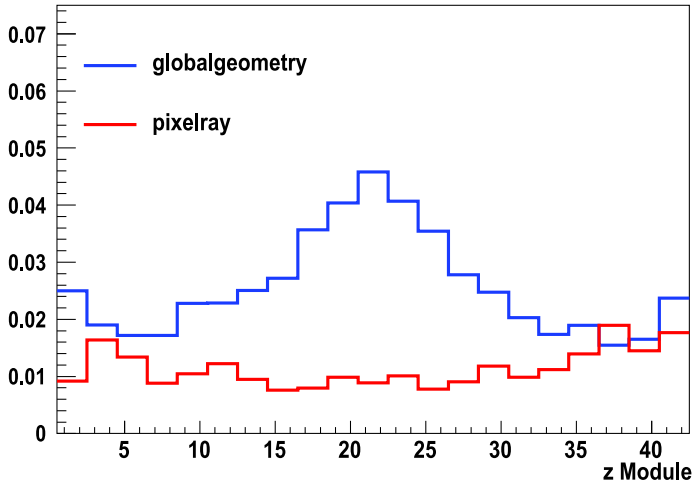

Figure 5.15: The fraction of stubs which are combinatorial (formed from the hits of two different particles) in the 32 cm radius Stack in 200 pile-up minimum bias events. The `pixelray` matching algorithm, a variation on the the `globalgeometry` algorithm, decreases the combinatorial stub rates. Pixel pitch is 0.1×1 mm^2 [84].

algorithm performs Cluster correlation using both local and global coordinates of Clusters in both Stack Members, as shown in Figure 5.16. The tangent line at Pixel bounds is allowed to have a maximum angle constrained by a scaling factor $SF \propto B/p_T$, as in `globalgeometry`:

$$\phi_{win} = \arcsin\left(SF \times \rho_{low}\right) \tag{5.5}$$

By making combined use of the position of both sensor and Pixel, one gets the angle between the sensor and the tangent to Pixel bounds:

$$\phi_{\text{Pix}} = \arccos\left(\sin\left(\phi_{\text{DET}} - \phi_{\text{low}}\right) \times \frac{\rho_{\text{DET}}}{x^{\text{local}}_{\text{low}}}\right) \tag{5.6}$$

where ϕ_{DET} and ρ_{DET} denote the position of the center of the lower sensor in the transverse plane and $x^{\text{local}}_{\text{low}}$ is the $\rho - \phi$ distance of the lower Cluster from the center of the lower sensor in the local frame. The deviation in the transverse plane is then easily found, given the separation s between the sensors, as:

$$\Delta x^{\pm} = s \times \tan\left(\phi_{\text{Pix}} \pm \phi_{win}\right) \tag{5.7}$$

The deviation in the longitudinal plane is calculated given the Pixel boundaries $x^{\pm}_{Pix}$ and

the luminous region limits $\pm w_{IP}$:

$$\Delta z^{\pm} = \left(z^{\pm}_{\text{Pix}} \pm w_{IP} \right) \times \frac{s}{\cos \phi_{\text{Pix}}} \frac{1}{\rho_{\text{low}}} \tag{5.8}$$

The deviations calculated so far are projected to the upper sensor reference frame and define the window after being translated into Pixel units. If the outer Cluster falls inside this window, the stub is accepted. One may note, as a remarkable difference with `globalgeometry`, that the `window` algorithm finds both the limits in z and $\rho - \phi$ starting from the lower Cluster and then looking at the position of the upper one. Also the `window` algorithm can be modified in order to flag Tight stubs.

Another approach, even more local than the previous one, and perhaps the most likely to be implemented on-detector once the final Tracker layout is designed, makes use of look-up tables. However, both this one and the `window` are still under developement and evaluation and are not taken into account in the present work.

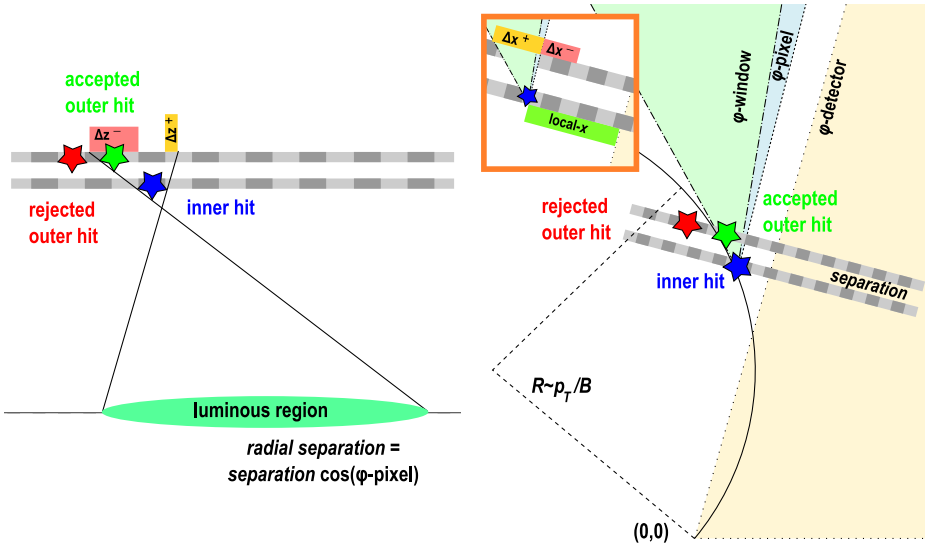

Figure 5.16: Window Hit Matching on transverse plane and longitudinal plane. Given the triangle defined in the transverse plane by the sensor center, (0, 0) and the lower Cluster, ϕ_{Pix} is calculated as the complementary angle to the one having the lower Cluster as vertex, using the Theorem of Sines. The same approach is used to calculate ϕ_{win} in a small angle approximation.

Also stub rates, using `2d+pixelray`, have been compared between `FullSimulation` and `FastSimulation`, as shown in Figure 5.17. Same settings are applied as for the

comparison of `SimHit`, `PixelDigi` and Cluster rates. Stub rates and shapes agree significantly better than hit rates. This indicates that a large portion of the effects causing discrepancies between the full and fast simulation are associated with tracks that do not form stubs because of their $p_T < 2.0$ GeV/c.

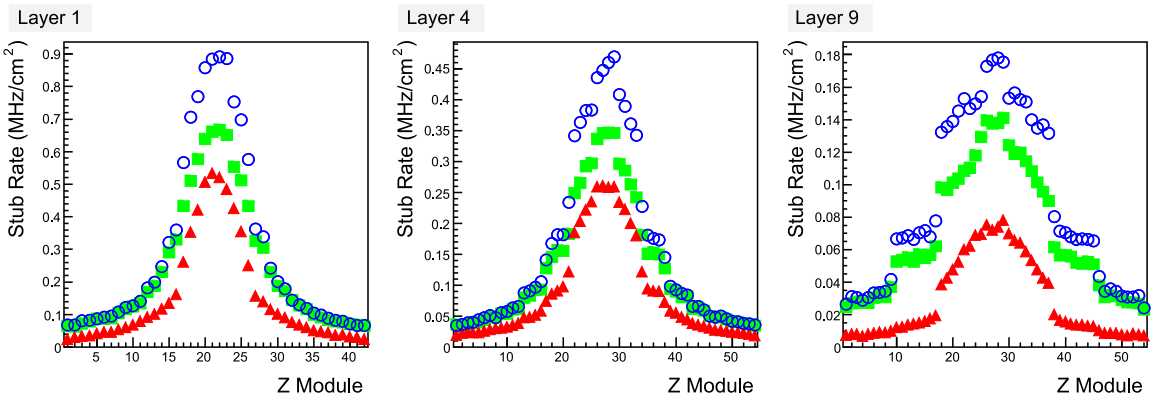

Figure 5.17: Comparison of rates of stubs from `PixelDigis`, using `2d+pixelray`, in `FastSimulation` (red triangles) and in the `FullSimulation` with (blue circles) and without (green squares) out-of-time pile-up included. From LEFT to RIGHT are shown rates for Stack at 32, 52 and 98.5 cm [84].

5.3 Tracklets within Double Stacks

Stubs can be looked at Tracker hits corresponding to tracks above threshold. For this reason they can be used to build higher complexity Trigger objects such as those built in Regional and Global Trigger. The natural step would be to associate stubs in different Layers to each other. To comply with the Long Barrel philosophy and with the hermetic design, only association of stubs to each other withn the same Double Stack will be allowed while crossing different Double Stack at this stage will be forbidden. Furthermore, every candidate pair of stubs must belong to the same Ladder to preserve the locality of data flow. Pairs of stubs associated to each other which pass matching criteria are called tracklets.

Correlation algorithm cannot rely on local coordinates as tracklets should be built out of information from different modules. For this reason candidate pairs of stubs are accepted or rejected according to a prescription analogous to `globalgeometry`:

- all pairs made of stubs in two consecutive Stacks are checked as candidate tracklets
- after a rough exclusion of pairs made of stubs clearly far-away from each other, the check for compatibility is the same as in `globalgeometry`, with threshold $p_T = 2.0$ GeV/c and $w_{IP} = 15.0$ cm
- Cluster coordinates are replaced by stub coordinates, which are the average coordinates of hits used to build the stub in the global reference frame
- each accepted tracklet can be fitted to extrapolate vertex and get momentum information

The already existing Tracklet Builder featured the pursuit for simplification: it did not accomplish the requirement of keeping the tracklet production within each Ladder and each Double Stack, it assumed the track to come from a non-displaced beamspot at $(x, y) = (0, 0)$ and it was embedded with a simple fit to get vertex and momentum information. Tracklet vertex is assumed in the transverse plane and found assuming a linear behaviour of ρ vs z, which is the same as a very small $\Delta\phi_{\text{out,in}}$[(5)] between stubs or large track p_T, as shown in Section 5.3.3:

$$z^{\mathbf{t}}_{\text{vtx}} = z_{\text{out}} - \rho_{\text{out}} \times \left(\frac{z_{\text{out}} - z_{\text{in}}}{\rho_{\text{out}} - \rho_{\text{in}}} \right) \tag{5.9}$$

Tracklet $p^{\mathbf{t}}_T$ is found by making use of elementary trigonometry, assuming unit charge and rounding B to 4 T and c to 300 mm/ns:

$$|\mathbf{r}_{\text{out}} - \mathbf{r}_{\text{in}}|^2_T = \rho^2_{\text{out}} + \rho^2_{\text{in}} - 2 \cdot \rho_{\text{out}} \cdot \rho_{\text{in}} \cdot \cos\left(\Delta\phi_{\text{out,in}}\right) \tag{5.10}$$

$$p^{\mathbf{t}}_T = c \cdot B \cdot 10^{-5} \cdot \frac{1}{2} \cdot \frac{|\mathbf{r}_{\text{out}} - \mathbf{r}_{\text{in}}|_T}{\sin\left|\Delta\phi_{\text{out,in}}\right|} \tag{5.11}$$

Tracklet direction can be estimated in a self-consistent way with $z^{\mathbf{t}}_{\text{vtx}}$:

$$\tan\theta^{\mathbf{t}} = \frac{\rho_{\text{out}} - \rho_{\text{in}}}{z_{\text{out}} - z_{\text{in}}} \tag{5.12}$$

which one can easily convert to $\eta^{\mathbf{t}} = -\ln\tan\theta^{\mathbf{t}}/2$, and find $p^{\mathbf{t}}_z = p^{\mathbf{t}}_T / \tan\theta^{\mathbf{t}}$.

[(5)] Subscripts refer to inner and outer stub of the pair candidate to be a tracklet.

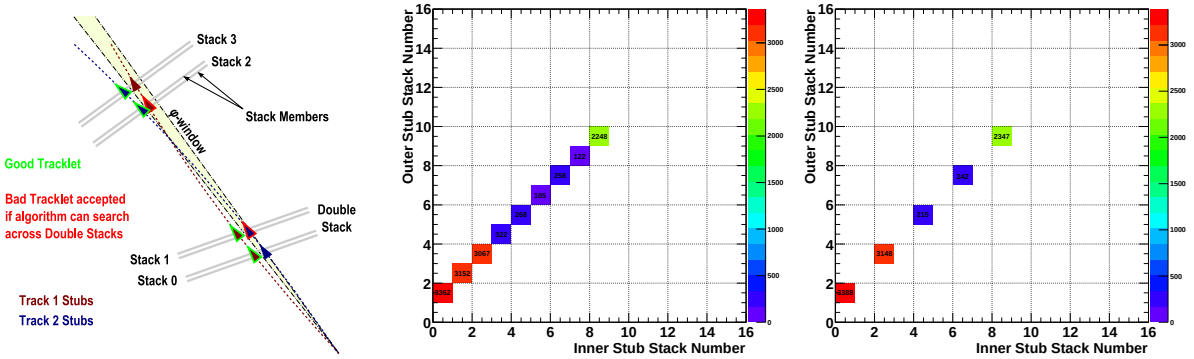

Figure 5.18: Undesirable tracklets may arise when looking at pairs of stubs which run across different Double Stacks if the ϕ-window is large enough (LEFT). The modified Tracklet Builder does not run across different Double Stacks (RIGHT) and it is compared to the standard Builder (MIDDLE). Used samples were made of 3000 μ^-, fixed p_T = 30 GeV/c, flat distribution of track direction $|\eta| < 2.4$, using `CMSSW_2_2_13`. Stubs are made with `pixelray` algorithm out of `2d` Clusters of hits. The inner/outer Stack number pair was included for all the tracklets built in the event, regardless of Hermetic Design.

5.3.1 Tracklets and Hermetic Design

The choice of keeping data flow local implies that not all consecutive pairs of Stacks can be seen as Superlayers in the Long Barrel layout. Tracklets therefore are being built only within the very same Double Stack. Another reason to introduce such a constraint is analogous to the one that drove the choice of keeping Stack Members separated by ~ 1 mm: the reduction of combinatorial background due to wrong association of stubs to each other, as shown in left side of Figure 5.18. In fact, if the same transverse displacement between stubs subtends an angle smaller than the threshold one, a pair of

	⟨position⟩ (mm)	σ (mm)	profile
x	0.5	0.0166	Gaus.
y	0.0	0.0166	Gaus.
z	0.0	53.0	Gaus.

xz crossing angle (mrad)	yz crossing angle (mrad)
140.0	0.0

β^* (cm)	transverse profile
55	circular

Table 5.1: Features of the beamspot used in the present work for simulations with `CMSSW_3_3_6`.

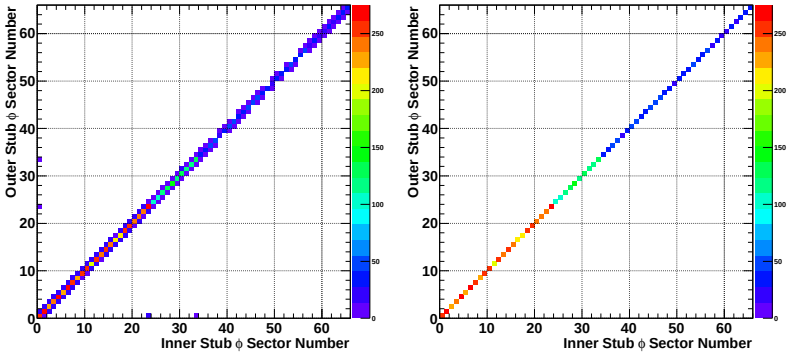

Figure 5.19: Test of the `hermetic` flag assignment in the modified Tracklet Builder: outermost stub ϕ-sector index is plotted vs the innermost stub one for all tracklets (LEFT) and for `hermetic=true` tracklets (RIGHT). Used sample was made of 3000 μ^-, fixed p_T = 30 GeV/c, flat distribution of track direction $|\eta| < 2.4$, using `CMSSW_2_2_13`.

stubs can be accepted even if they generated by different tracks. This improvement was tested on two samples of 3000 μ^- each, generated with the same features: fixed p_T = 30 GeV/c, flat distribution of track direction $|\eta| < 2.4$, vertex position with flat distribution within a 10^{-10} m sided cube. The first sample underwent standard procedure, while the second was processed rejecting tracklet candidates which run across different Double Stacks. In both the samples, `2d` and `pixelray` algorithms were used for Clustering and Hit Matching, respectively.

The second constraint given by hermetic design is that both stubs that form a candidate tracklet must belong to the same Ladder (also called "ϕ-sector"). To keep compatibility with other layouts, a candidate tracklet is flagged as `hermetic` or not without being deleted. This test was performed on the second of the two samples described in the previous paragraph about the use of consecutive Stacks and its result are shown in Figure 5.19.

5.3.2 Effect of a Displaced Beamspot Position

The standard definition of tracklet fits the position of the two stubs and of the vertex to a circumference. For this reason, a likely scenario for beamspot position and size has been used throughout the entire work with `CMSSW_3_3_6`, with the features listed in Table 5.1 which reflect a nominal LHC conditions.

The importance of this problem arose when looking for a strategy to correlate tracklets and stubs in different Double Stacks, as described in Section 6.1.2. To test these effects and check if an alternative definition of tracklet is possible, each candidate pair of stubs is checked twice: once with the standard vertex at $(0, 0, z)$, once assigning the transverse position of the beamspot used in the generation of events. This approach is not unrealistic as the current policies for powering the Inner Tracker do require stable beam. Therefore, its position in the transverse plane is known and can then be fed to the Tracklet Builder which is located off-detector and may have then this information loaded once per run.

To check the candidate tracklet with the second option, it is sufficient to subtract the beam spot transverse coordinates to the stub coordinates and check for compatibility this new candidate pair of stubs:

$$\begin{pmatrix} x^{\text{corr}}_{\text{stub}} \\ y^{\text{corr}}_{\text{stub}} \\ z^{\text{corr}}_{\text{stub}} \end{pmatrix} = \begin{pmatrix} x_{\text{stub}} \\ y_{\text{stub}} \\ z_{\text{stub}} \end{pmatrix} - \begin{pmatrix} x_{\text{beam}} \\ y_{\text{beam}} \\ 0 \end{pmatrix} \tag{5.13}$$

The extrapolation of the vertex coordinate $z^{\mathbf{t},\text{corr}}_{\text{vtx}}$ is done by substitution of stub coordinates with the new ones in (5.9) before calculation of ρ_{stub}. The extraction of the tracklet $p^{\mathbf{t}}_T$ is done as in (5.11) with angles and radii referred to the transverse position of the new vertex $(x_{\text{beam}}, y_{\text{beam}}, z^{\mathbf{t},\text{corr}}_{\text{vtx}})$. As the dominant effect in $x^{\mathbf{t}}_{\text{vtx}}$ reconstruction is the beamspot profile, whose size is order of magnitudes larger than the fraction of mm induced by the beamspot displacement, the only comparison that is worth being made is the one between $p^{\mathbf{t}}_T$.

This effect may also be reflected in the tracklet production efficiency curves, as the $p^{\mathbf{t}}_T$ fit is used to accept or reject a pair of candidate stubs. Figures 5.20 and 5.21 show there is no difference in tracklet production efficiency as they are not affected by this bias at low momenta. These results are obtained from a 20,000 single μ^- sample with flat $0 < p_T < 100\,\text{GeV}/c$ distribution, flat distribution of track direction $|\eta| < 2.4$ and beamspot defined as in Table 5.1. The common denominator in tracklet production efficiencies is the number of tracks per p_T bin or η bin that produced at least one valid stub in the Superlayer.

The behaviour at larger momenta has been checked too. Figures 5.22 and 5.23 show a

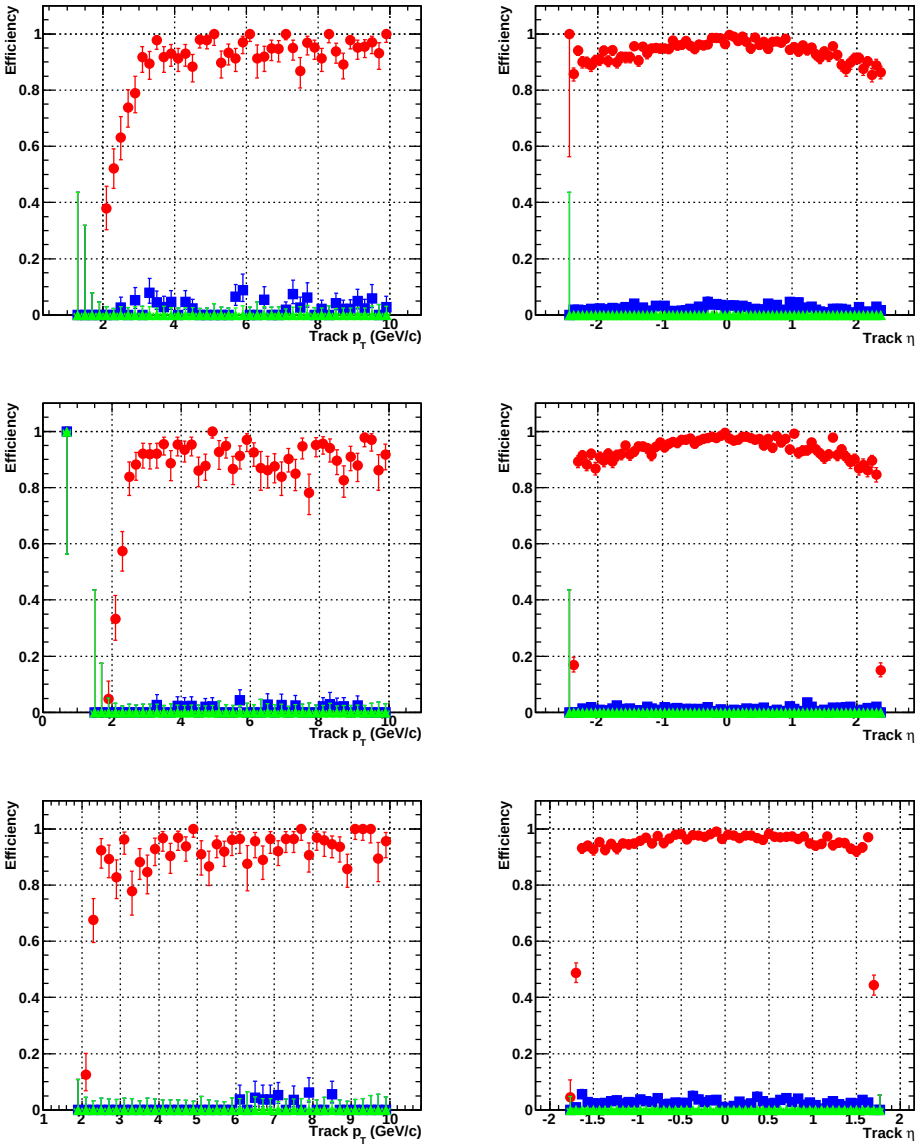

Figure 5.20: Tracklet production efficiency with `2d+pixelray` stubs and default choice for tracklet vertex in the transverse plane: 32 and 36 cm nominal radii of Stacks (TOP), 48 and 52 cm (MIDDLE) and 98.5 and 102.5 cm (BOTTOM). Efficiency is shown as a function of track p_T, for $0 < p_T < 10$ GeV$/c$, and track direction η, for $p_T > 20$ GeV$/c$. Efficiency to find at least one tracklet in the Double Stacks is painted with red circular markers, efficiency to find at least two tracklets is painted with blue square markers, and efficiency to find more than two tracklets is painted with green triangular markers. The sample was composed of single μ^- with flat $0 < p_T < 100$ GeV$/c$ distribution and flat distribution of track direction $|\eta| < 2.4$ and beamspot displaced 0.5 mm in the $+x$ direction.

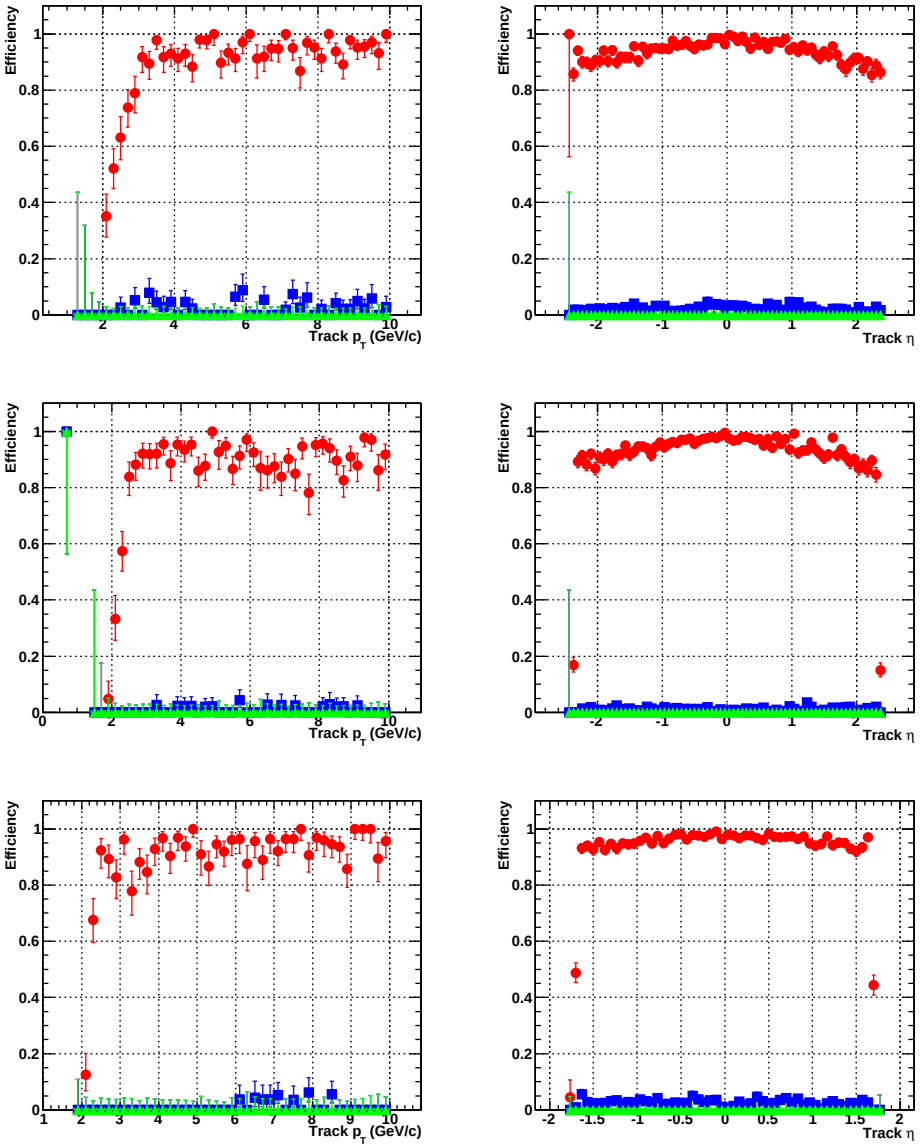

Figure 5.21: Tracklet production efficiency with `2d+pixelray` stubs and tracklet vertex in the transverse plane assumed to coincide with the true beamline: 32 and 36 cm nominal radii of Stacks (TOP), 48 and 52 cm (MIDDLE) and 98.5 and 102.5 cm (BOTTOM). Efficiency is shown as a function of track p_T, for $0 < p_T < 10$ GeV/c, and track direction η, for $p_T > 20$ GeV/c. Efficiency to find at least one tracklet in the Double Stacks is painted with red circular markers, efficiency to find at least two tracklets is painted with blue square markers, and efficiency to find more than two tracklets is painted with green triangular markers. The sample was composed of single μ^- with flat $0 < p_T < 100$ GeV/c distribution and flat distribution of track direction $|\eta| < 2.4$ and beamspot displaced 0.5 mm in the $+x$ direction.

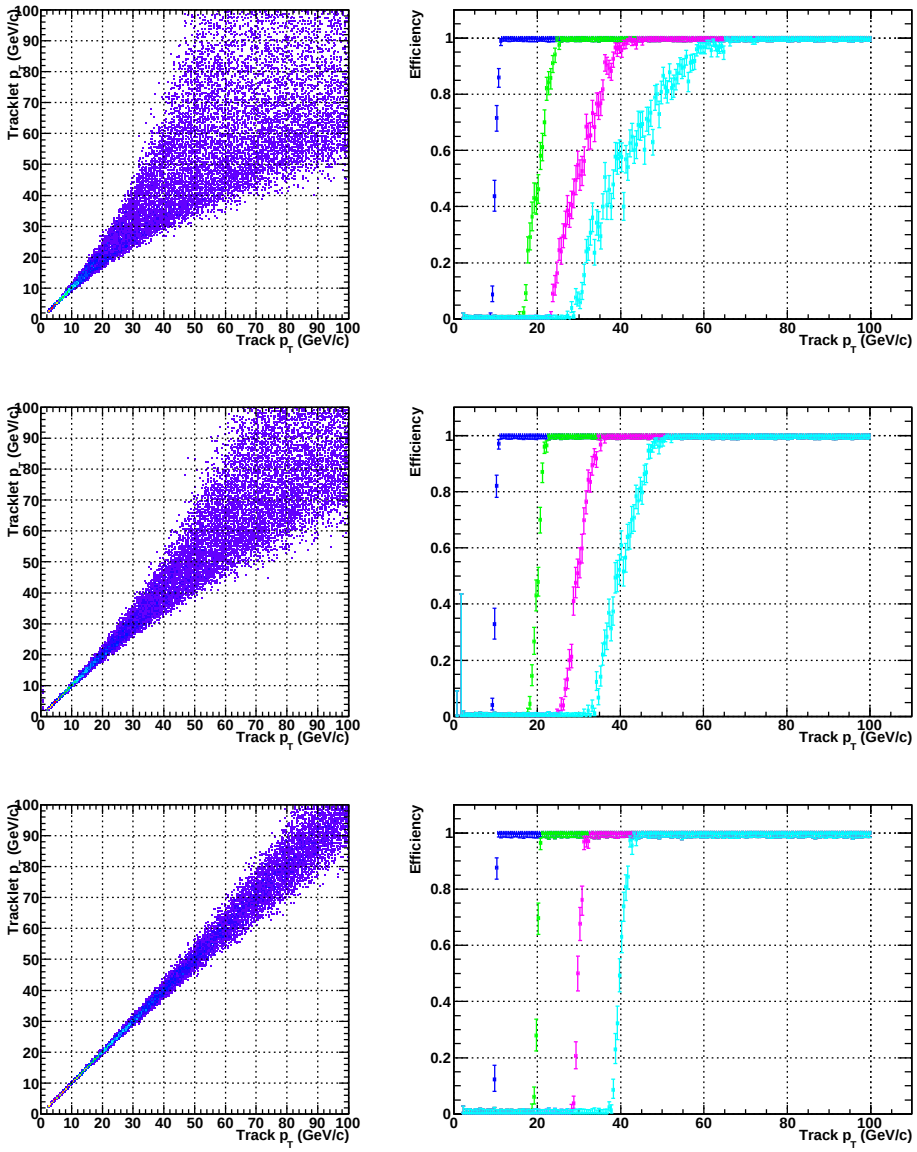

Figure 5.22: Correlation between tracklet p_T^{t} and track p_T for standard tracklets made out of `2d+pixelray` stubs (LEFT) and turn-on curves for different p_T thresholds for tracks which produced accepted tracklets (RIGHT). Blue markers refer to tracklet $p_T^{\mathrm{t}} > 10$ GeV$/c$, green ones to a 20 GeV$/c$ threshold, pink ones to a 30 GeV$/c$ threshold and light blue ones to a 40 GeV$/c$ threshold. Results are shown, from TOP to BOTTOM, for Stacks at nominal radii of 32-36 cm, 48-52 cm and 98.5-102.5 cm, respectively. The sample was composed of single μ^- with flat $0 < p_T < 100$ GeV$/c$ distribution and flat distribution of track direction $|\eta| < 2.4$ and beamspot displaced 0.5 mm in the $+x$ direction.

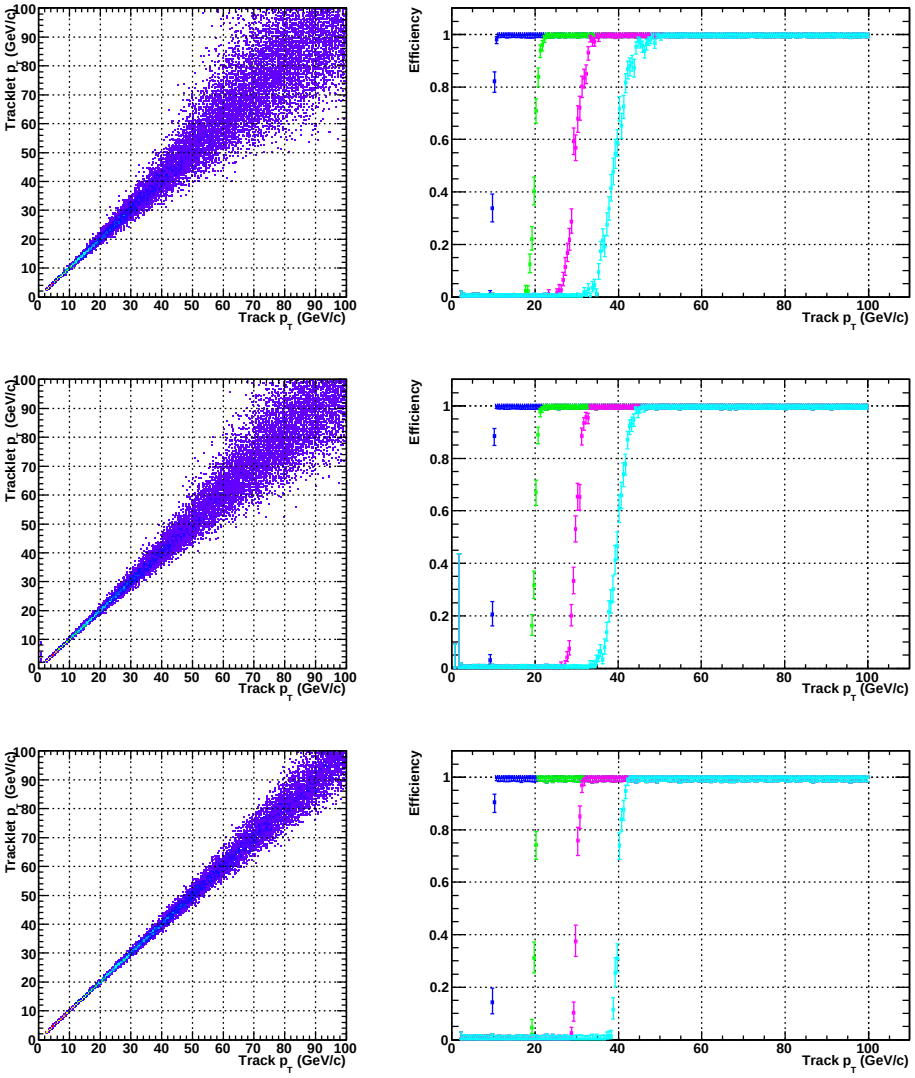

Figure 5.23: Correlation between tracklet $p_T^{\mathbf{t}}$ and track p_T for tracklets, after correction for the beamspot position, made out of `2d+pixelray` stubs (LEFT) and turn-on curves for different p_T thresholds for tracks which produced accepted tracklets (RIGHT). Blue markers refer to tracklet $p_T^{\mathbf{t}} > 10$ GeV/c, green ones to a 20 GeV/c threshold, pink ones to a 30 GeV/c threshold and light blue ones to a 40 GeV/c threshold. Results are shown, from TOP to BOTTOM, for Stacks at nominal radii of 32-36 cm, 48-52 cm and 98.5-102.5 cm, respectively. The sample was composed of single μ^- with flat $0 < p_T < 100$ GeV/c distribution and flat distribution of track direction $|\eta| < 2.4$ and beamspot displaced 0.5 mm in the $+x$ direction.

comparison of tracklet p_T^{t} to the corresponding track p_T together with turn-on curves for triggering on single tracklet at different p_T thresholds. These results are obtained from a 20,000 single μ^- sample with flat $0 < p_T < 100$ GeV/c distribution, flat distribution of track direction $|\eta| < 2.4$ and beamspot defined as in Table 5.1. The common denominator in the turn-on curves is the number of tracks per p_T bin that produced an accepted tracklet in the Superlayer. It is interesting to remark that the major benefits for the p_T^{t} measurement are found when the ratio between lever arms and distances of stubs from beamline is larger.

Another information that can be easily obtained and which depends on the tracklet vertex coordinates is the angular deviation of the outer stub with respect to the inner one. This information may also give a hint on the charge sign of the track:

$$\Delta\phi^N_{\mathrm{out,in}} = \begin{cases} \phi_{\mathrm{out}} - \phi_{\mathrm{in}} & \text{, if } \left|\phi_{\mathrm{out}} - \phi_{\mathrm{in}}\right| < \pi \\ \phi_{\mathrm{out}} - \phi_{\mathrm{in}} - 2\pi & \text{, if } \left|\phi_{\mathrm{out}} - \phi_{\mathrm{in}}\right| \geq \pi \textbf{ AND } \phi_{\mathrm{out}} - \phi_{\mathrm{in}} < 2\pi \\ 2\pi - \phi_{\mathrm{out}} - \phi_{\mathrm{in}} & \text{, otherwise} \end{cases} \tag{5.14}$$

where the angles are calculated with respect to the vertex used in the tracklet definition. The tracklet charge sign is then found as

$$q^{\mathrm{t}} = -\frac{\Delta\phi^N_{\mathrm{out,in}}}{\left|\Delta\phi^N_{\mathrm{out,in}}\right|} = \pm 1 \tag{5.15}$$

5.3.3 Effect of Small Angle Approximation of Vertex Extrapolation and Development of a Tracklet Helicoidal Fit

The trajectory of a charged particle in a uniform magnetic field, such as the CMS solenoidal field is supposed to be in the tracking volume, is a helix, which is a superimposition of a linear uniform motion along the field and a uniform circular motion in the plane transverse to the field. In particular, when looking at $\rho(t)$ agains $z(t)$, one finds that the linear approximation described by (5.12) is not always reliable. In fact, a helix trajectory is described by the following rule

$$z_2 - z_1 = \Delta\phi^c_{2,1} \cdot \frac{R}{p_T} \cdot p_z \tag{5.16}$$

for each pair of points $\mathbf{r}_1$ and $\mathbf{r}_2$ along the trajectory, where ϕ_1^c and ϕ_2^c are the angles measured with respect to the trajectory axis. One can therefore find the vertex and momentum of a tracklet as follows:

$$z_{\text{vtx}}^{\mathbf{t}} = z_{\text{in}} + \frac{\Delta\phi_{\text{vtx,in}}^{c}}{\Delta\phi_{\text{out,in}}^{c}} \cdot (z_{\text{out}} - z_{\text{in}}) \tag{5.17}$$

$$p_z^{\mathbf{t}} = (z_{\text{out}} - z_{\text{in}}) \cdot c \cdot B \cdot 10^{-5} \cdot \frac{1}{\Delta\phi_{\text{out,in}}^{c}} \tag{5.18}$$

with the usual units. The preliminary step consists in finding angles with respect to helix axis using the same approach as the one for calculating tracklet $p_T^{\mathbf{t}}$. In fact, given the result of (5.10) for $|\mathbf{r}_{\text{out}} - \mathbf{r}_{\text{in}}|_T$, and assuming the radius connecting each stub and the vertex to the helix axis has constant magnitude as calculated in (5.11), one easily gets:

$$\Delta\phi_{\text{out,in}}^{c} = \arccos\left(1 - \frac{|\mathbf{r}_{\text{out}} - \mathbf{r}_{\text{in}}|_T^2}{2 \cdot R^2}\right) = \arccos\left(1 - 2 \cdot \sin^2\left|\Delta\phi_{\text{out,in}}\right|\right) \tag{5.19}$$

Analogous procedure is used to get $\Delta\phi_{\text{vtx,in}}^{c}$. Transverse momentum is found as in (5.11) and tracklet direction comes from

$$\tan\theta^{\mathbf{t}} = \frac{p_T^{\mathbf{t}}}{p_z^{\mathbf{t}}} = \frac{1}{2} \cdot \frac{\Delta\phi_{\text{out,in}}^{c}}{z_{\text{out}} - z_{\text{in}}} \cdot \frac{|\mathbf{r}_{\text{out}} - \mathbf{r}_{\text{in}}|_T}{\sin\left|\Delta\phi_{\text{out,in}}\right|} \tag{5.20}$$

A comparison of (5.20) to (5.12) can be easly carried on by letting $\Delta\phi_{\text{out,in}}$ be very small. May that be the case, the following approximations hold:

- $\sin\left|\Delta\phi_{\text{out,in}}\right| \simeq \left|\Delta\phi_{\text{out,in}}\right|$
- $\cos\left(\Delta\phi_{\text{out,in}}\right) \simeq 1$
- $|\mathbf{r}_{\text{out}} - \mathbf{r}_{\text{in}}|_T \simeq \left|\rho_{\text{out}} - \rho_{\text{in}}\right|$
- $\Delta\phi_{\text{out,in}}^{c} \simeq 2\left|\Delta\phi_{\text{out,in}}\right|$

and it is clear that (5.12) is the limit of (5.20) when $\Delta\phi_{\text{out,in}} \ll 1$. This approximation holds when Stack radius is much larger than lever arm between Stacks or when bending radius is much larger than all other distances between stubs and vertex. Hence one may expect that tracklets generated by low p_T tracks, particularly in the outermost Double Stack, will benefit from an improved tracklet fit. The remaining parameter to be found

is the tracklet azimuth at vertex $\phi^{\mathbf{t}}$:

$$\phi^{\mathbf{t}} = \phi_{\text{out}} - q^{\mathbf{t}} \left(\arccos\left(\frac{1}{2} \cdot \frac{\rho_{\text{out}}}{R} \right) - \frac{\pi}{2} \right) \tag{5.21}$$

which is, if needed, adjusted by $\pm 2\pi$ to bring it back in the $(-\pi, \pi]$ range and does not depend on the particular choice for the fit of the longitudinal component.

The difference of the introduction of the helicoidal fit can be seen in Figures 5.24 and 5.25. A comparison of the results of the two methods is presented for different samples of 20,000 muons with fixed $p_T = 3$ or 20 GeV/c, flat distribution of track pseudorapidity in the $|\eta| < 2.4$ range and vertex generated according to the specifications of Table 5.1. The following quantities are pictured against track η:

- $\left(p_T^{\mathbf{t}} - p_T^{\text{track}} \right) / p_T^{\text{track}}$
- $\eta^{\mathbf{t}} - \eta^{\text{track}}$
- $\phi^{\mathbf{t}} - \phi^{\text{track}}$
- $z_{\text{vtx}}^{\mathbf{t}} - z_{\text{vtx}}^{\text{track}}$

Tracklets in different double Stack are separated from each other to emphasize the effect of the small angle approximation. There are a few comments which are worth being made:

- the approximated fit is remarkably affected for low momenta, while large momenta are safely treated
- if the pseudorapidity is underestimated, the tracklet will be more transverse than the real track and the extrapolated vertex will be found in a position displaced forwards, and vice-versa, as it could be easily predicted
- the introduction of the helicoidal fit brings back the average value of $z_{\text{vtx}}^{\mathbf{t}} - z_{\text{vtx}}^{\text{track}}$ and $\eta^{\mathbf{t}} - \eta^{\text{track}}$ to zero over the whole pseudorapidity range
- both $z_{\text{vtx}}^{\mathbf{t}} - z_{\text{vtx}}^{\text{track}}$ and $\eta^{\mathbf{t}} - \eta^{\text{track}}$ show periodic structures which are discussed in detail in Section 5.3.4
- the sign of the track charge becomes important at large η where the longitudinal momentum becomes important if compared to the transverse one, and this effect

remains unchanged from the standard fit to the helicoidal one, as the informationin the transverse plane is treated the same way

It is important to note that, at this stage of the development of Phase 2 Tracking Trigger tools, the acceptance of rejection of candidate tracklets does not make use of the helicoidal fit, but this feature could be introduced in the future.

5.3.4 Effect of Pixel Length

When looking at the way z^{t}_{vtz} and η^{t} depend on track pseudorapidity, the result shows a clear periodicity, such as a resonant behaviour. The reason of this is a periodic bias in measuring θ^{t} due to a combined effect of discrete Pixel coordinates and track direction. In fact stub coordinates suffer discretization, as they are calculated averaging the coordinates of `PixelDigis` that compose the stub. This is reflected into the extrapolation of tracklet vertex. The effect is larger when stub coordinates are closer to the real track trajectory and therefore the direction of the tracklet is closer to the track one, as shown in Figure 5.26. One could expect that a sample of purely transverse tracks would span uniformly Pixel length and therefore is likely not to show any region where z^{t}_{vtz} witdh shrinks.

To check this effect, a toy model was developed with `C++` based tools. Each Stack is described by the radii of its two members and by the length of the barrel. As an example, the second Stack in the Long Barrel layout features radii of 35.95 and 36.05 cm and a length of 2×210.0 cm. A high-p_T track is drawn as a straight line in the $\rho \times z$ plane and its pseudorapidity is chosen by a random number uniformly distributed in the $(-2.4, 2.4)$ range. The vertex of this track is placed at $\rho = 0$ and z chosen by a random number with Gaussian distribution centered at $z = 0$ and with $\sigma = 5.3$ cm.

Once this line is given, the coordinates at different radii ρ_i are computed as $z_i = z(\rho_i)$. For each pair of toy Stack Members a stub is calculated in terms of position and direction by averaging and subtracting the corresponding coordinates. This corresponds to a stub made of `SimHits`. The intersection coordinates of the toy track with toy Stack Members are rounded to the closest Pixel size. Moreover a Gaussian spread, centered on the Pixel and with $\sigma = 0.1$ times the lower Stack Member Pixel length, is added to mimic charge sharing among Pixels. These Pixel-like coordinates are used to compute stubs corresponding to those made out of `PixelDigis`.

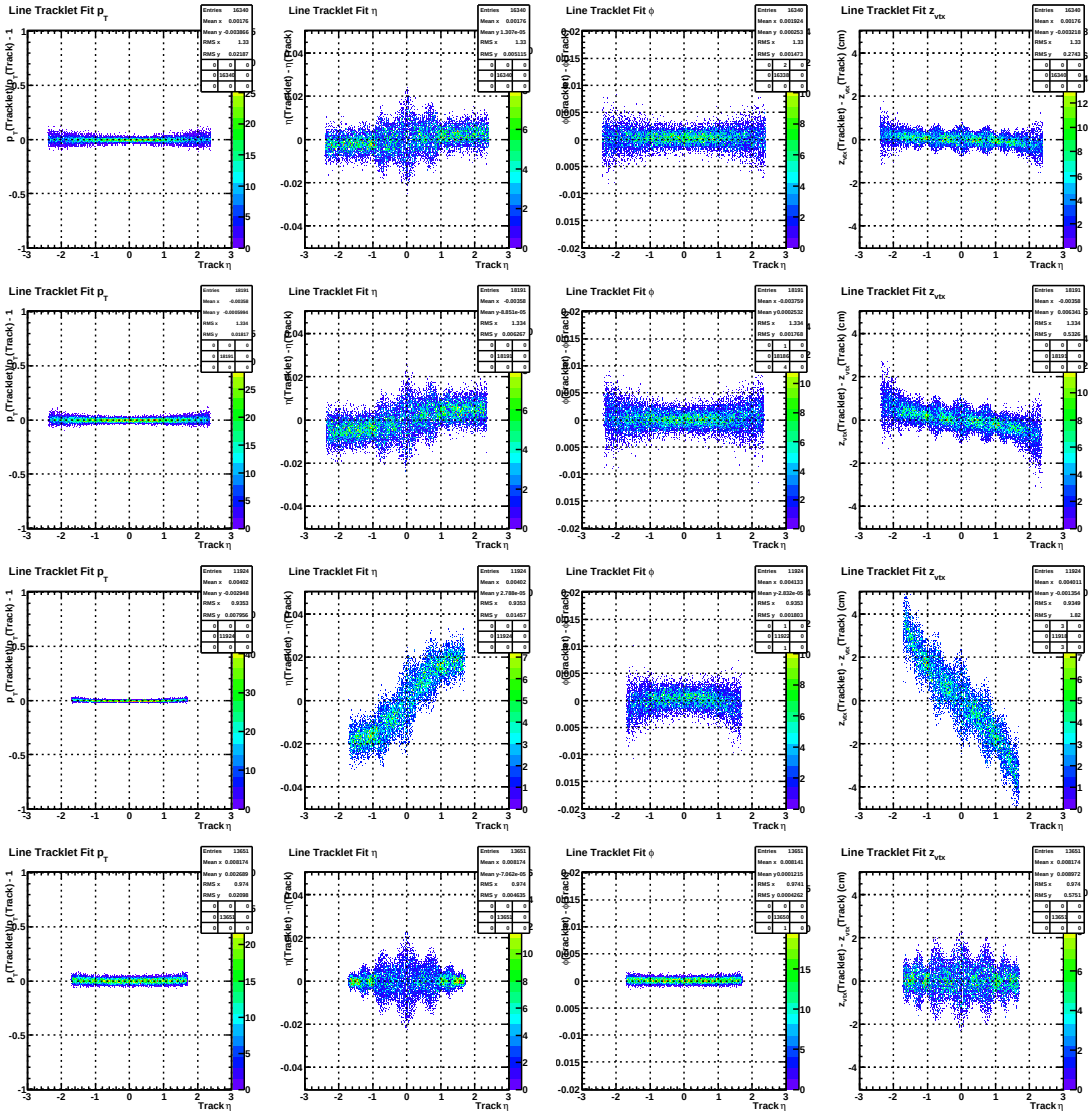

Figure 5.24: Standard fit of tracklets corrected for the beamspot displacement. A comparison of information from tracklet fit and the corresponding parameter of the simulated track is shown as a function of track η. From LEFT to RIGHT, columns show $\left(p_T^{\mathbf{t}} - p_T^{\text{track}}\right)/p_T^{\text{track}}$, $\eta^{\mathbf{t}} - \eta^{\text{track}}$, $\phi^{\mathbf{t}} - \phi^{\text{track}}$ and $z_{\text{vtx}}^{\mathbf{t}} - z_{\text{vtx}}^{\text{track}}$. From TOP to BOTTOM, rows show $p_T = 3$ GeV/c μ^+ tracklets in Superlayer 0, $p_T = 3$ GeV/c μ^- tracklets in Superlayer 1, $p_T = 3$ GeV/c μ^+ tracklets in Superlayer 4 and $p_T = 20$ GeV/c μ^- tracklets in Superlayer 4. Each sample was generated with flat pseudorapidity distribution in the $|\eta| < 2.4$ range.

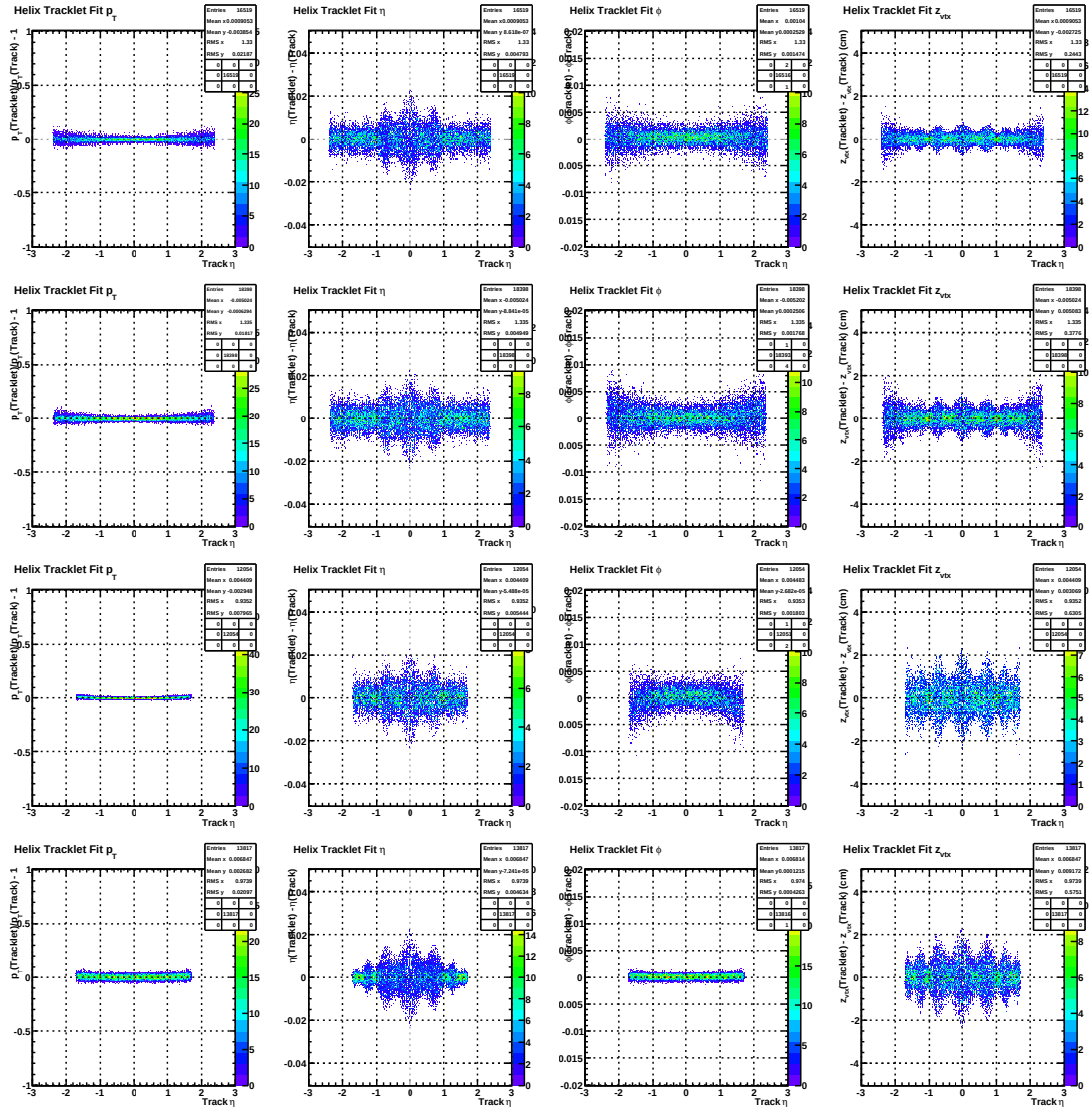

Figure 5.25: Helix fit of tracklets corrected for the beamspot displacement. A comparison of information from tracklet fit and the corresponding parameter of the simulated track is shown as a function of track η. From LEFT to RIGHT, columns show $\left(p_T^{\mathbf{t}} - p_T^{\text{track}}\right)/p_T^{\text{track}}$, $\eta^{\mathbf{t}} - \eta^{\text{track}}$, $\phi^{\mathbf{t}} - \phi^{\text{track}}$ and $z_{\text{vtx}}^{\mathbf{t}} - z_{\text{vtx}}^{\text{track}}$. From TOP to BOTTOM, rows show $p_T = 3$ GeV/c μ^+ tracklets in Superlayer 0, $p_T = 3$ GeV/c μ^- tracklets in Superlayer 1, $p_T = 3$ GeV/c μ^+ tracklets in Superlayer 4 and $p_T = 20$ GeV/c μ^- tracklets in Superlayer 4. Each sample was generated with flat pseudorapidity distribution in the $|\eta| < 2.4$ range.

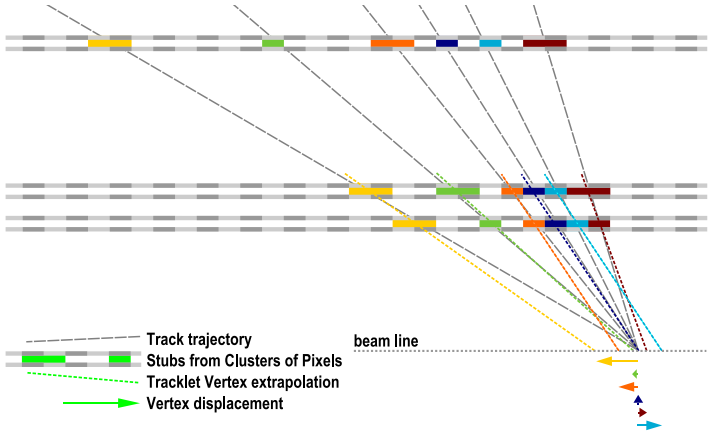

Figure 5.26: Conceptual representation of the effect of Pixel length and discretization on stub position and tracklet fit in the longitudinal plane.

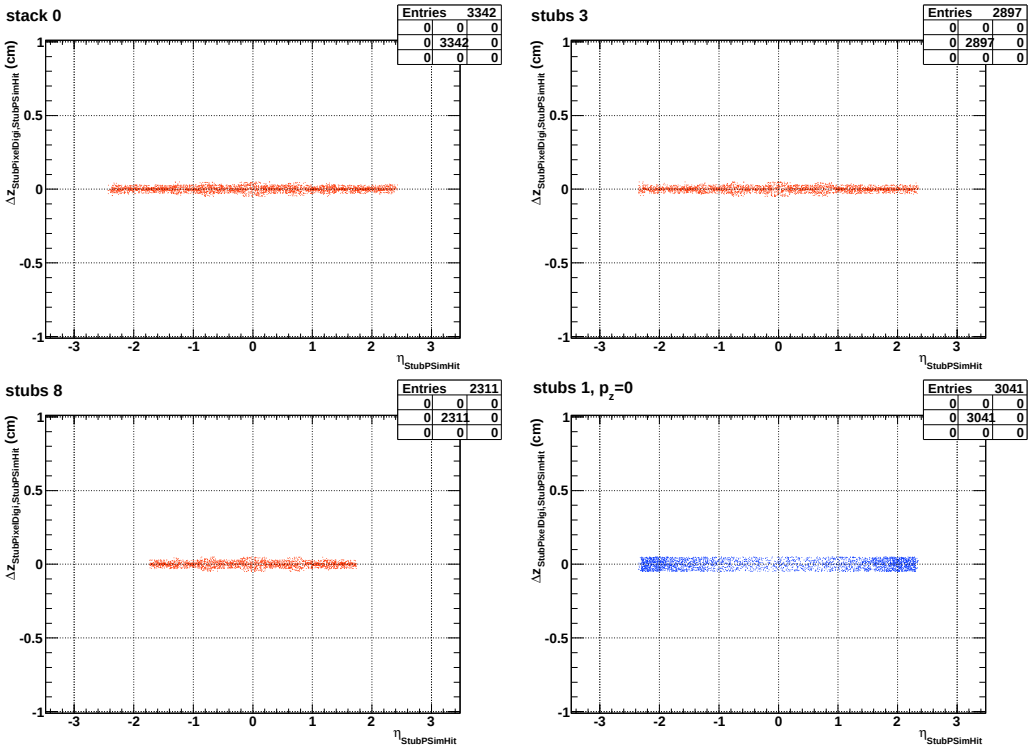

Figure 5.27: Comparison of the position of `2d+pixelray` stubs from `PixelDigis` to the crossing point of track trajectory at the median plane between two stacked sensors: correlation between difference in z and crossing point η. Used sample was made of 3,000 μ^- with fixed $p_T = 30$ GeV/c, flat distribution of track direction $|\eta| < 2.4$ and point-like distribution of vertex position, using `CMSSW_2_2_13`. Different Stacks are shown: 32 cm (TOP,LEFT), 52 cm (TOP,RIGHT), 98.5 cm (BOTTOM,LEFT) and 36 cm (BOTTOM,RIGHT). The latter one shows the results for a $p_z = 0$ sample with flat distribution of vertex position over $|z| < 180$ cm.

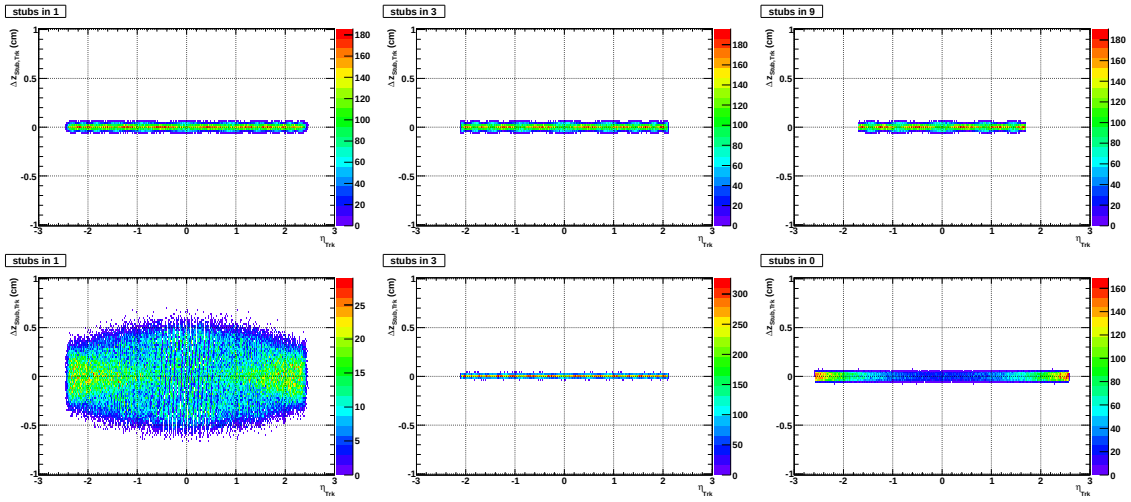

Figure 5.28: Results of toy model study of combined effects of track direction and Pixel length. TOP row shows the results for the concept Tracker Pixel size in Stacks at 36 cm (LEFT), 48 cm (MIDDLE) and 102.5 cm (LEFT). BOTTOM row shows some variations: behaviour at 36 cm with 10 mm long Pixels (LEFT), at 52 cm with 0.5 mm long Pixels (MIDDLE) and $p_Z \simeq 0$ with 1 mm long Pixels. η_{Trk} is the pseudorapidity of the crossing point of the toy track at the median layer between two Stack Members. The "attraction" of stub coordinates towards the crossing point when tracks are not transverse is relevant, as well as the uniform span of Pixel length in the $p_z \simeq 0$ test.

Then a pair of stubs of the second kind is connected by a straight line, to mimic a toy tracklet, which is then back-propagated to $\rho = 0$ to find the vertex coordinate. To check also the purely transverse track sample, toy track pseudorapidity is limited in the $(-0.001, 0.001)$ range and its vertex is chosen with a random number uniformly distributed in the $(-280.0, 280.0)$ cm range. Toy stubs are accepted only if they fall within barrel length. Each trial consists of 10^5 toy tracks.

A test of the toy model in terms of stub coordinates is mandatory. Figure 5.27 shows some examples of bias of stub coordinates due to the joint action of Pixel length and track direction. The coordinates of each stub are compared to those of the track calculated at the median plane between Stack members –crossing point– and the difference in z is drawn against the pseudorapidity of the crossing point. Also an example of a purely $p_Z = 0$ sample is included. The results of the toy model test are shown in Figure 5.28. The "attraction" of stub coordinates towards the crossing point when tracks are not transverse is relevant, as well as the uniform span of Pixel length in the $p_z \simeq 0$ test.

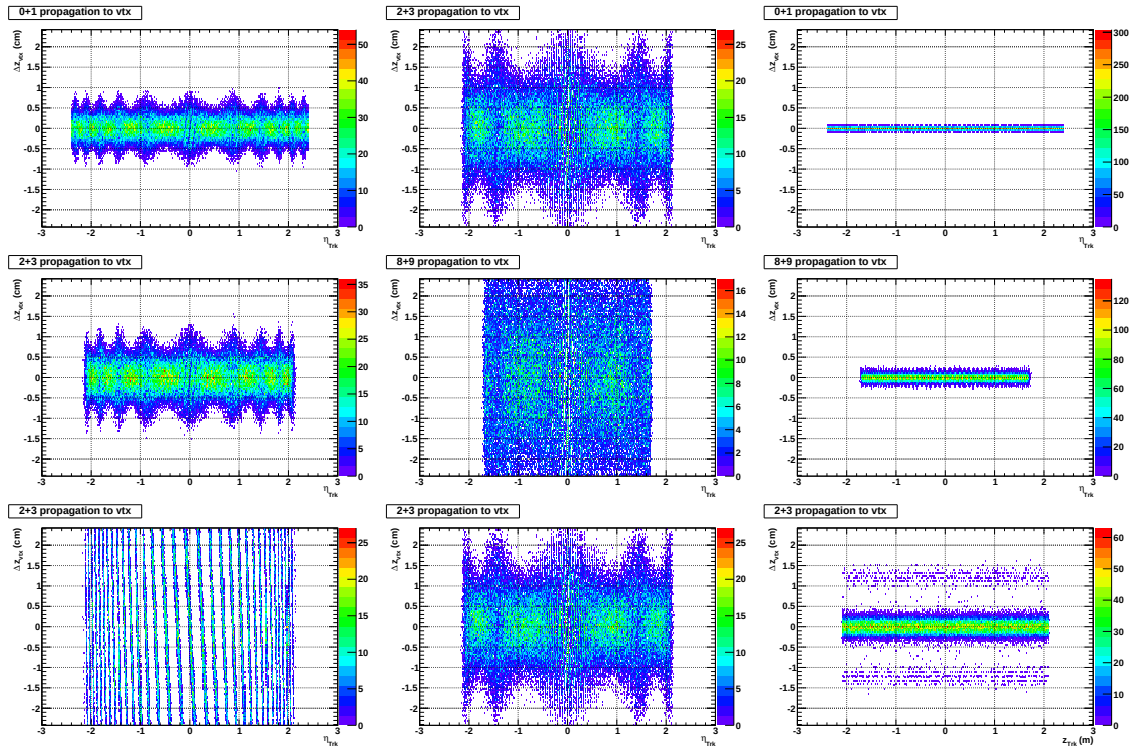

Figure 5.29: Results of toy model study of effect of Pixel length in longitudinal tracklet fit. All the pictures show the difference between track vertex z and the toy tracklet extrapolated z^{t}_{vtx}, drawn against toy track η. TOP row, from LEFT to RIGHT: 1 mm long Pixels with standard sample, using Superlayer 0; 2 mm long Pixels with standard sample, using Superlayer 1; 0.1 mm long Pixels with standard sample, using Superlayer 0. MIDDLE row, from LEFT to RIGHT: 1 mm long Pixels with standard sample, using Superlayer 1; 2 mm long Pixels with standard sample, using Superlayer 4; 0.1 mm long Pixels with standard sample, using Superlayer 4. BOTTOM row, from LEFT to RIGHT: 1 mm long Pixels in lower Stack Member and 10 mm long Pixels in upper Stack Member with standard sample, using Superlayer 1; 2 mm long Pixels shifted by half Pixel from lower to upper Stack member with standard sample, using Superlayer 1; 1 mm long Pixels with $\eta \sim 0$ toy tracks and uniform z_{vtx} distribution, using Superlayer 1 (in this case Δz_{vtx} is drawn against toy track z_{vtx}).

The results of vertex extrapolation are shown in Figure 5.29 and are worth a few comments. Toy models featuring same Pixel length as the concept Tracker show resonances at the same pseudorapidities as tracklet fit. Changing Pixel length moves the position of resonances and changes the width of Δz_{vtx} at the same time. The larger the distance of the Superlayer where the tracklet is, the larger the width of Δz_{vtx}. Choosing differen Pixel sizes for different Members in the same Stack introduces a different kind of resonant structure due to the additional bias in measuring stub position. Shifting Pixels by half

length does not change vertex extrapolation relevantly.

The effect described in the present Section must be taken into account when tracklets are matched to stubs in other Superlayers, as described in Chapter 6.

6. Global Objects for a Level 1 Tracking Trigger

Tracklets, in the fashion described in Chapter 5, already are exhaustive objects as they carry information on vertex coordinates, charge sign, momentum magnitude and direction. However, the use of only two Stacks may not be sufficient to guarantee a good enough momentum resolution and a background rate reduction suitable for Phase 2 luminosities, particularly if the Stacks are close to each other as in the concept layout used throughout this work. In this Chapter a first attempt at defining an object that extends the idea of Tracklet is presented. The construction of such an object, called Level 1 Track (or, briefly, `L1Track`), starts with the attempt to propagate the momentum vector of a Tracklet to any Tracker barrel and define a matching window to associate stubs to each other. The Chapter ends with the description of the performance of this object and with a Section dedicated to the genuinity of the Level 1 Trigger Primitives and objects described and developed so far.

6.1 Use of Tracklets as Seeds for Level 1 Tracks

Tracklets already contain basic information on momentum, vertex and direction. The natural choice for a `L1Track` would be a chain of stubs properly associated to each other. To define an algorithm suitable for this purpose, already existing tools available within `CMSSW` framework were explored. Among all, one of the simplest propagation tools, called `BaseParticlePropagator`, was chosen because of its linearity and because it was developed within `FastSimulation`, with which it is well integrated. `BaseParticlePropagator` does not include any energy loss or multiple scattering. This may be unphysical but it was developed as a geometric tool and therefore it was considered a proper starting point.

6.1.1 Propagation of Tracklets to Tracker Barrels

`BaseParticlePropagator` draws the helicoidal trajectory of a particle of given position, mass, charge and momentum, searching for any intersection of this helix with the surface of a chosen cylinder. These cylinders are centered together with the global CMS reference frame and their axis is parallel to z. The algorithm is briefly recalled herein only for charged particles.

From initial position $\mathbf{r}_0$ and momentum $\mathbf{p}_0$ of the particle, the trajectory radius ρ_{H} and axis are found, and a particle is actually propagated only if an intersection of the helix with a target cylinder can be found. The crossing angle at cylinder surface is found with elementary trigonometry and the result is corrected for 2π periodicity and to properly match the values of particle charge and magnetic field. A third-order Taylor development is used for large momenta. The calculated Track azimuth after propagation ϕ_{prop} is then used to find the remaining coordinates of position and momentum:

$$z_{\mathrm{prop}} = z_0 + \left(\phi_{\mathrm{prop}} - \phi_0\right) \cdot \frac{p_z \cdot \rho_{\mathrm{H}}}{p_T} \tag{6.1}$$

Both ϕ_{prop} and z_{prop} are then corrected if the particle trajectory crosses the cylinder on the endcaps. Another correction for the true speed of the particle and its lifetime is applied if needed.

One of the main drawbacks of this propagation procedure is that it does not reflect the true arrangement of flat Tracker modules. To take care of this and be able to compare the extrapolation of a Tracklet with the position of stubs in other Layers, a further step is needed. As described in Appendix A, the production of `SimHits` in `FastSimulation` shows the same problem. Therefore a similar solution is chosen, with strong simplifications. The updated trajectory state obtained after propagation is used to calculate the intersection point with the closest detector element described by a rectangular flat surface. The detector element is chosen so that it belongs to the first layer crossed by the helix during this last step of propagation. Forward and backward propagations are treated in a self-consistent way when using `BaseParticlePropagator` as well as when looking for the closest detector element[(1)]. A collection of impact points is then retireved.

[(1)] In fact, the distance of a detector element from the beamline may be either larger or smaller than the nominal Stack radius because of the in-out arrangement of Ladders.

To carry on a safe comparison with stubs, the position of these impact points, labelled herein as **IP**, must be compared with the position of Clusters in the target layer. When a Tracklet is propagated in the forward direction, the lower Stack member is chosen while the upper one is selected in case of backward propagation. At this stage, the original Tracklet fit, featuring the small angular displacement approximation, is still used. The new helicoidal fit will be introduced later to remark its importance at low transverse momenta.

6.1.2 Effects of a Displaced Beamspot Position and Pixel Length

As the goal is the definition of matching windows to associate stubs in target Layers to Seed Tracklets, the behaviour of $\Delta\phi_{\text{stub,IP}} = \phi_{\text{stub}} - \phi_{\text{IP}}$ and $\Delta z_{\text{stub,IP}} = z_{\text{stub}} - z_{\text{IP}}$ is analysed as a function of ϕ_{stub} and η_{stub}.

The very preliminary study, still carried on with `CMSSW_2_2_13` and a slightly different beamspot, however displaced along x by a fraction of mm, allowed first conclusions on the effects of detector arrangement and beamspot displacement. The sample was composed of 10,000 μ^- of fixed $p_T = 30$ GeV/c and flat distribution of track direction $|\eta| < 2.4$. Stubs are made with `pixelray` algorithm out of `2d` Clusters of hits. As shown in Figure 6.1, $\Delta\phi_{\text{stub,IP}}$ is remarkably affected by the assumption of tracklet vertex. The correction for the beamspot displacement is therefore needed to eliminate the sinusoidal modulation as a function of ϕ_{stub}. On the other hand, $\Delta z_{\text{stub,IP}}$ shows a main trend around $\Delta z_{\text{stub,IP}} \simeq 0$ with resonant structures analogous to those seen in Section 5.3.4. Two clear secondary correlations are also present.

Figure 6.2 shows the behaviour of $\Delta z_{\text{stub,IP}}$ with ϕ_{stub} for both standard and corrected $(x^{\text{t}}_{\text{vtx}}, y^{\text{t}}_{\text{vtx}})$. It suggests that the secondary tails in $\Delta z_{\text{stub,IP}}$ may be due to overlap regions between adjacent Ladders, where impact points are compared to stubs in the wrong Ladder. Secondary tails are therefore easily removed by requiring a self-consistent comparison of stubs with impact points within the same Ladder. Getting rid of these, and converting also the impact point coordinates into Pixel ones, the displacements of impact point with respect to existing stubs it the one pictured in Figure 6.3.

The remaining effect to be confirmed is the resonant behaviour of $\Delta z_{\text{stub,IP}}$ as a function

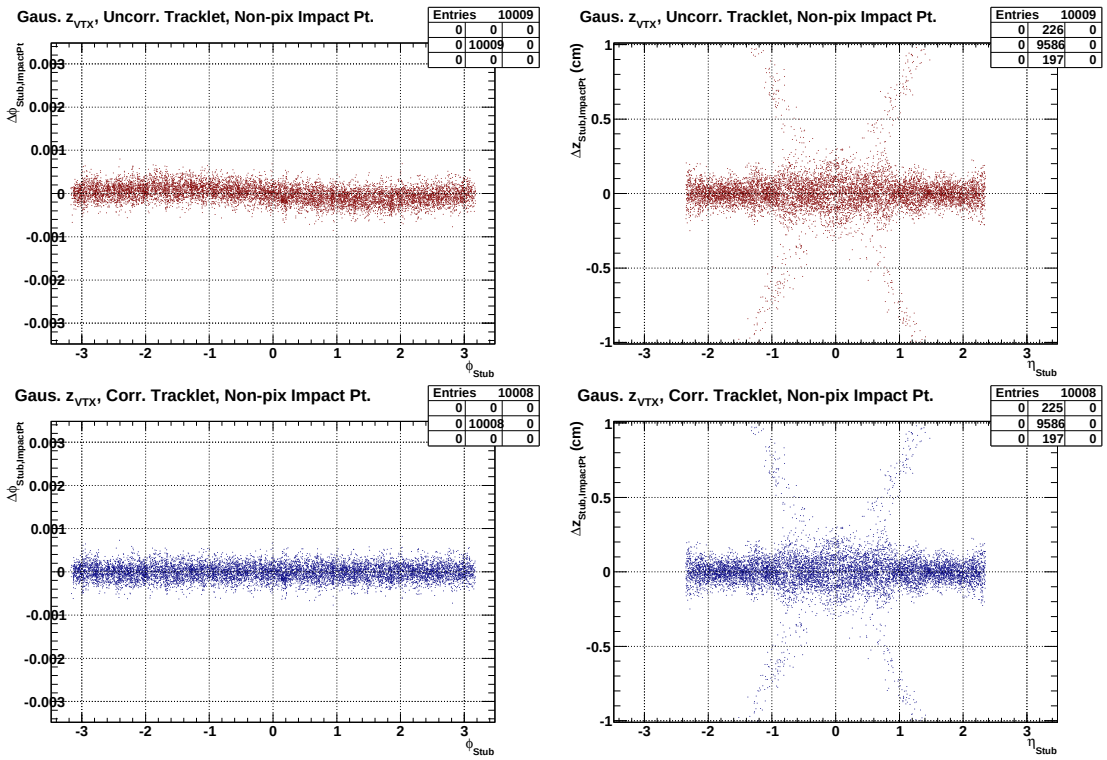

Figure 6.1: Raw result of the non-refined Tracklet propagation algorithm from Superlayer 0 to the lower sensor of the Stack at 48 cm radius. The impact point position is compared to the stub one: correlation between difference in azimuthal angle and stub ϕ (LEFT) and correlation between difference in z and stub z (RIGHT) are shown. Distinction is made between Tracklets making use of $(x^{\mathbf{t}}_{\text{vtx}}, y^{\mathbf{t}}_{\text{vtx}}) = (0, 0)$ (TOP) and corrected ones (BOTTOM). The sample was made of 10,000 μ^-, fixed $p_T = 30$ GeV/c, flat distribution of track direction $|\eta| < 2.4$, using `CMSSW_2_2_13`.

of η_{stub}. The best candidate explanation is the discretization of stub coordinates due to Pixel pitch, which already was demonstrated to reflect itself in the tracklet vertex and momentum fit. The same toy model as the one described in Section 5.3.4 was used, this time looking at the propagation of the toy tracklet towards different Stacks. Figure 6.5 shows some results of the toy model propagation to be compared with the `CMSSW_2_2_13` simulations shown in Figures 6.6 and 6.7, where a concept Tracker with different Pixel length was used. The toy model reflects also in this case the resonant stuctures except for the main modulation of the resonances, which keeps the tails shorter than in the model and makes them to decrease at large η. This is due to the extreme simplification of the model itself which spans over only two dimensions and does not include dead areas, and sensitive element overlaps and shifts between each other.

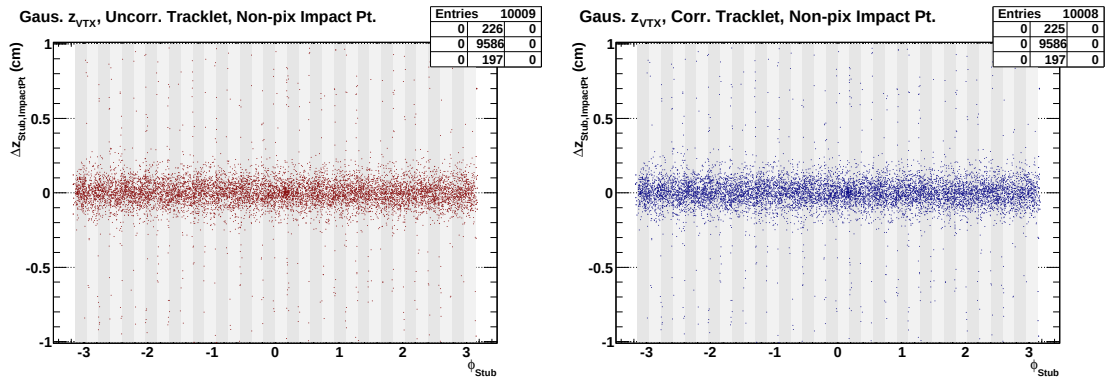

Figure 6.2: Raw result of the non-refined Tracklet propagation algorithm from Superlayer 0 to the lower sensor of the Stack at 48 cm radius. The impact point position is compared to the stub one: correlation between difference in z and stub ϕ is shown for standard Tracklets (LEFT) and for Tracklets corrected for the beamline displacement (RIGHT). The sample was made of 10,000 μ^-, fixed p_T = 30 GeV/c, flat distribution of track direction $|\eta| < 2.4$, using `CMSSW_2_2_13`. Shaded areas represent the 34 Ladders of the Stack. Large values of $\Delta z_{\text{stub,IP}}$, corresponding to secondary tails, clearly belong to overlap regions between adjacent Ladders.

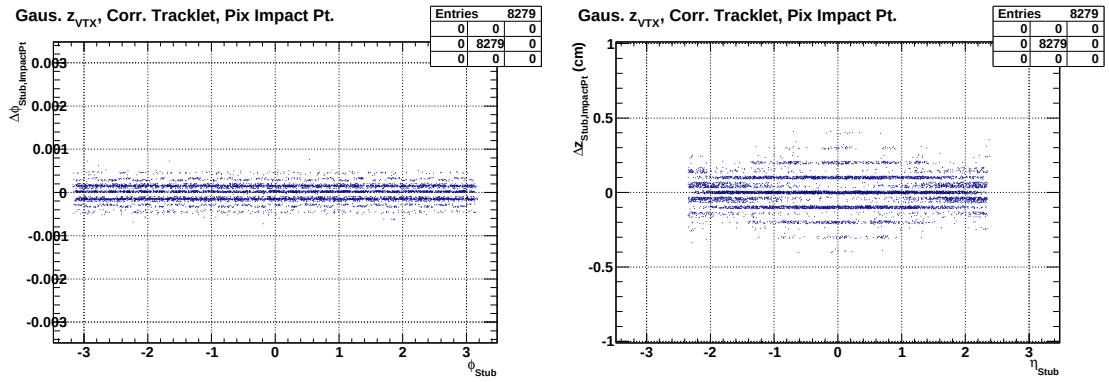

Figure 6.3: Result of the refined Tracklet propagation algorithm from Superlayer 1 to the upper sensor of the Stack at 32 cm radius. The pixellated impact point position is compared to the stub one within the same Ladder: correlation between difference in azimuthal angle and stub ϕ (LEFT) and correlation between difference in z and stub z (RIGHT) are shown. Only propagation of Tracklets corrected for the beamline is shown. The sample was made of 10,000 μ^-, fixed p_T = 30 GeV/c, flat distribution of track direction $|\eta| < 2.4$, using `CMSSW_2_2_13`.

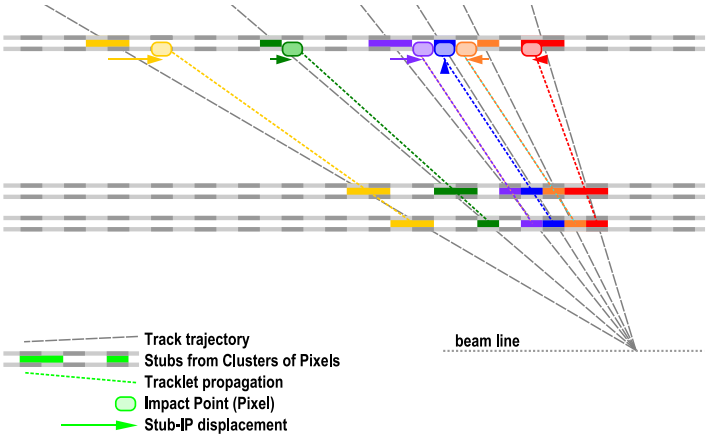

Figure 6.4: Conceptual representation of the effect of Pixel length and discretization on stub position and Tracklet propagation to different Superlayers.

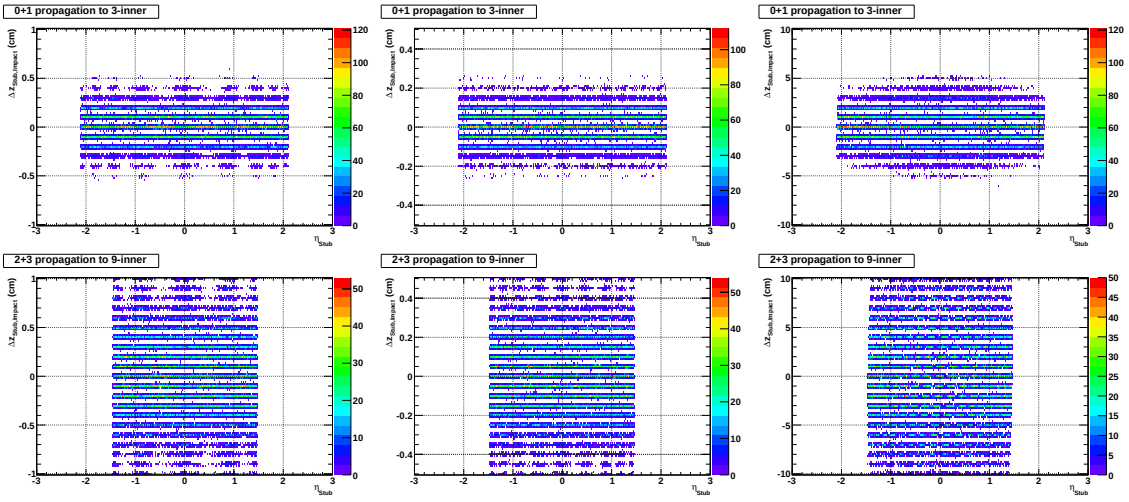

Figure 6.5: Results of toy model study of effect of Pixel length in longitudinal Tracklet fit. All the pictures show the difference between the stub coordinate z and the toy tracklet extrapolated one to another Layer, drawn against target Layer stub η. TOP row uses standard sample to propagate from Superlayer 0 to Layer 3, from LEFT to RIGHT: 1 mm long Pixels; 0.5 mm long Pixels; 10 mm long Pixels. BOTTOM row uses standard sample to propagate from Superlayer 2 to Layer 9, from LEFT to RIGHT: 1 mm long Pixels; 0.5 mm long Pixels; 10 mm long Pixels.

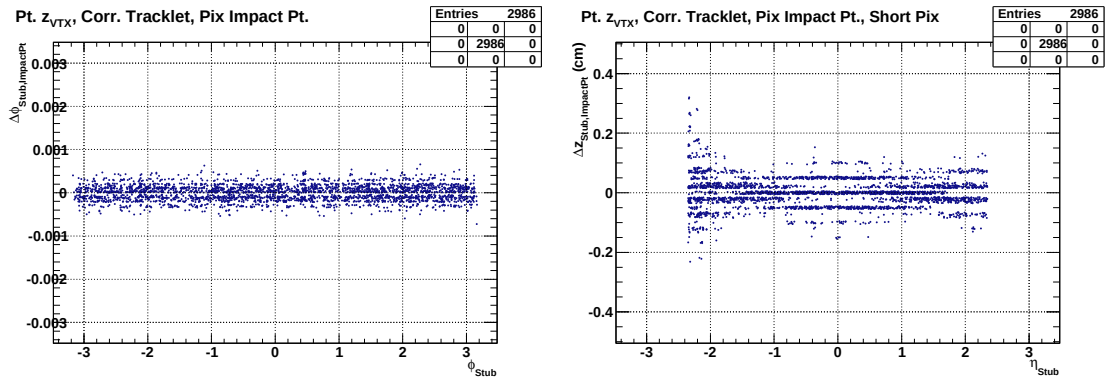

Figure 6.6: Effects of Pixel length in tracklet propagation algorithm from Superlayer 4 to the upper sensor of the Stack at 52 cm radius. Pixels are 0.5 mm long instead of 1 mm. The impact point position is compared to the stub one only within the same ladder and using the coordinates of the corresponding Pixel: correlation between difference in azimuthal angle and stub ϕ (LEFT) and correlation between difference in z and stub z (RIGHT) are shown. Only propagation of tracklets corrected for the beamline is shown. The sample was made of 10,000 μ^-, fixed p_T = 30 GeV/c, flat distribution of track direction $|\eta| < 2.4$, using `CMSSW_2_2_13`.

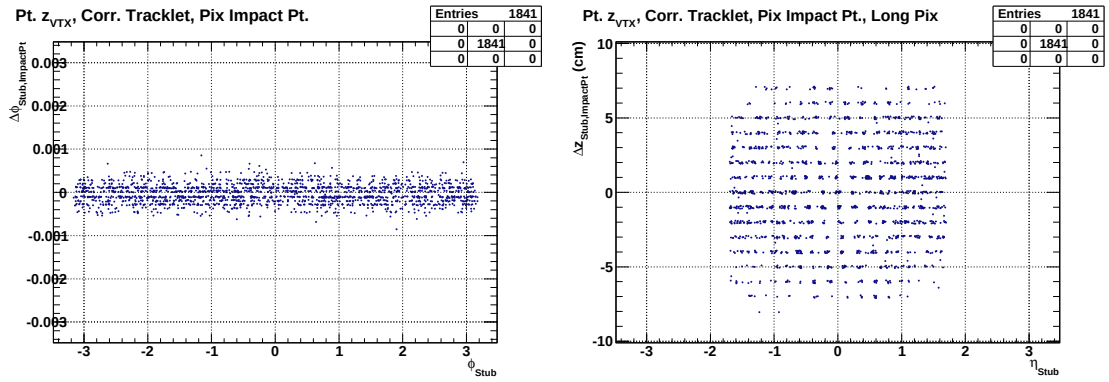

Figure 6.7: Effects of Pixel length in tracklet propagation algorithm from Superlayer 4 to the upper sensor of the Stack at 52 cm radius. Pixels are 10 mm long instead of 1 mm. The impact point position is compared to the stub one only within the same ladder and using the coordinates of the corresponding Pixel: correlation between difference in azimuthal angle and stub ϕ (LEFT) and correlation between difference in z and stub z (RIGHT) are shown. Only propagation of tracklets corrected for the beamline is shown. The sample was made of 10,000 μ^-, fixed p_T = 30 GeV/c, flat distribution of track direction $|\eta| < 2.4$, using `CMSSW_2_2_13`.

6.1.3 Effects of Small Angle Approximation and Definition of Matching Windows

The procedure described so far was tested with $p_T = 30$ GeV/c muons, which are well described by the approximated tracklet fit. The problems at low p_T, introduced by this approximation, were described in Section 5.3.3 and are relevant also when using tracklets as seeds for `L1Tracks`. To understand how much they are important, a comparison of the two approaches at low p_T is needed.

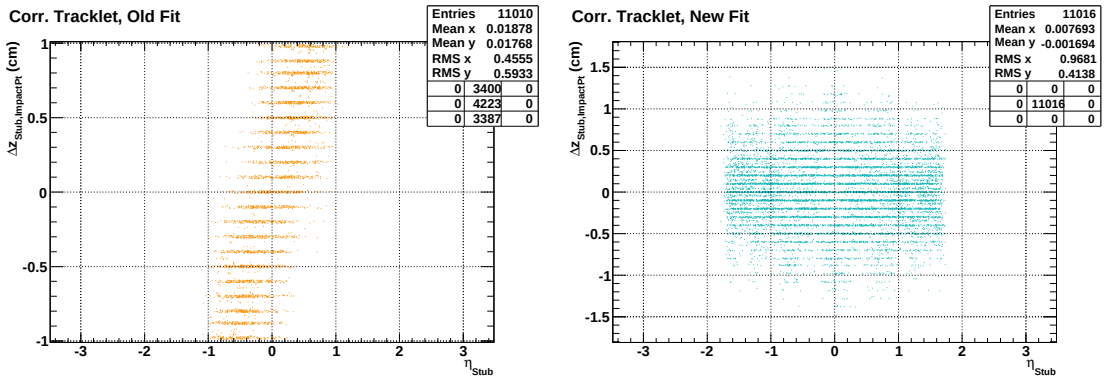

Figure 6.8: Effects of small angular displacement approximation in tracklet fit and propagation algorithm from Superlayer 4 to the upper sensor of the Stack at 32 cm radius. The impact point position is compared to the stub one only within the same ladder and using the coordinates of the corresponding Pixel: correlation between difference in z and stub z are shown for the standard fit (LEFT) and the helicoidal one (RIGHT). Only propagation of tracklets corrected for the beamline is shown. The sample was made of 20,000 μ^-, fixed $p_T = 3$ GeV/c, flat distribution of track direction $|\eta| < 2.4$. Note different scales between LEFT and RIGHT pictures.

A set of samples obtained with a single muon simulation were generated with the usual flat pseudorapidity distribution and with different transverse momenta: 3, 5, 7, 10, 20, and 30 GeV/c. When looking at the propagation of tracklets in the lowest p_T sample, the effect of the approximated fit becomes strongly evident, with an average value of $\Delta z_{\text{stub,IP}}$ which is different from zero on the whole η range and clearly depends on pseudorapidity. Figure 6.8 shows the strongest effect among all: tracklets from low p_T tracks in the outermost Double Stack. The bias introduced by the approximated fit in the estimate of tracklet direction shows a systematic increase with η of the average value of $\Delta z_{\text{stub,IP}}$, which turns out either in the definition of η-dependent matching windows, either in a very large size of the windows themselves. To mantain the matching algorithm

as simple as possible, all the following development of `L1Tracks` presented in this thesis will make use of both the correction for beamspot displacement and for helicoidal fit in tracklets.

Each fixed-p_T sample was used to explore average values and width of both $\Delta\phi_{\text{stub,IP}}$ and $\Delta z_{\text{stub,IP}}$ as a function of the track p_T, for each pair of tracklet Seed Superlayer and target stub Layer. All the $\Delta\phi_{\text{stub,IP}}$ and $\Delta z_{\text{stub,IP}}$ distributions were treated according to the following guidelines:

- each distribution was treated as symmetric around its average value
- only part of the integral of each distribution was "cleaned", by cutting symmetric tails on both sides; for example, to select the 90% of the integral, tails corresponding on 5% of the integral on each side were removed
- chosen fractions of the integral were 90%, 95%, 98%, and 99%, but only results for the 99% one, together with some relevant comparison, will be discussed
- upper and lower limits[(2)] of each "cleaned" distribution were used to find the average value and the width as

$$\left\langle \Delta\phi_{\text{stub,IP}} \right\rangle = \frac{\Delta\phi^{\text{UTE}}_{\text{stub,IP}} + \Delta\phi^{\text{LTE}}_{\text{stub,IP}}}{2} \qquad w_\phi = \left| \Delta\phi^{\text{UTE}}_{\text{stub,IP}} - \Delta\phi^{\text{LTE}}_{\text{stub,IP}} \right| \tag{6.2}$$

$$\left\langle \Delta z_{\text{stub,IP}} \right\rangle = \frac{\Delta z^{\text{UTE}}_{\text{stub,IP}} + \Delta z^{\text{LTE}}_{\text{stub,IP}}}{2} \qquad w_z = \left| \Delta z^{\text{UTE}}_{\text{stub,IP}} - \Delta z^{\text{LTE}}_{\text{stub,IP}} \right| \tag{6.3}$$

- the average value and size of each distribution define position and aperture of matching windows for each sample and each Seed Superlayer/target Layer pair; the average value may become important for the search in ϕ and it also may be sensitive to track charge
- position and aperture are then rounded or flattened to simplify the algorithm which will consitute the `L1Track` builder

This procedure is pictured in Figure 6.9, where shaded areas represent windows of different aperture. While there are no particular caveats about $\Delta\phi_{\text{stub,IP}}$, it is clear that this definition of matching windows, which is flat in η, will introduce inefficiencies where

[(2)] The notation used herein to label the limits of the distributions is UTE and LTE, standing for "upper tail edge" and "lower tail edge".

tails in $\Delta z_{\text{stub,IP}}$ are larger.

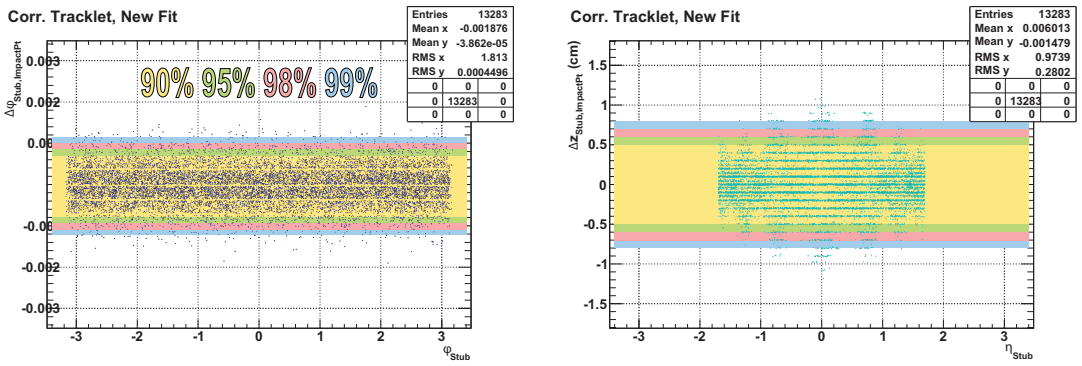

Figure 6.9: Definition of matching windows for propagation of tracklets from Superlayer 1 to Stack at 98.5 cm. The helicoidal tracklet fit is applied to tracklets corrected for the beamspot displacement. The propagated tracklet impact point position is compared to the stub one only within the same ladder and using the coordinates of the corresponding Pixel. Shaded areas represent the aperture of windows corresponding to 90%, 95%, 98%, and 99% of the integral, excluding symmetric tails. The sample was made of 20,000 μ^-, fixed $p_T = 10$ GeV/c, flat distribution of track direction $|\eta| < 2.4$. It is clear that this definition of matching windows, which is flat in η, will introduce inefficiencies where tails in $\Delta z_{\text{stub,IP}}$ are larger.

Tables 6.1 and 6.2 give an example of the matching windows opening and positioning obtained with the described procedure. These examples refer to propagation of seed tracklets in the innermost Double Stack towards the Stack at 48 cm. The use of these Tables in the `L1Track` Builder is described in Section 6.2.

6.2 Level 1 Tracks: Definition and Performance

The search for other stubs to be matched to already existing tracklets, as described so far, is not exhaustive of the construction of a `L1Track` from a seed tracklet and "brick" stubs. The production of a set of `L1Tracks` begins with the retrieval of all the tracklets in the event, divided by Superlayer, as well as all the stubs. Stubs are associated to a Superlayer if they belong to different ones. This will speed up the selection of candidate stubs to be associated to the seed by excluding stubs in the same Layers as those composing the seed itself. Then, for each tracklet, the following procedure is applied:

1. the momentum of the tracklet, which is being used as seed, is found with the

$\langle \Delta z_{\text{stub,IP}} \rangle$ (cm)						
	sample p_T (GeV/c)					
aperture	3	5	7	10	20	30
99%	0.00635	0.01319	0.00003	0.00030	0.00029	0.00029
98%	0.00004	0.00046	0.00008	0.00037	0.00010	0.00026
95%	0.00032	0.00020	0.00023	0.00056	0.00046	0.00020
90%	0.00091	0.00038	0.00121	0.00002	0.00006	0.00001

$w_z/2$ (cm)						
	sample p_T (GeV/c)					
aperture	3	5	7	10	20	30
99%	0.25444	0.22245	0.20922	0.20843	0.20826	0.20858
98%	0.20846	0.20625	0.20543	0.20464	0.20416	0.20454
95%	0.19908	0.19557	0.19405	0.19325	0.19188	0.19243
90%	0.14746	0.13760	0.13243	0.10988	0.10955	0.10958

Table 6.1: Average value of $\Delta z_{\text{stub,IP}}$ distribution (TOP) and window half-size $w_z/2$ (BOTTOM) for propagation of tracklets from Superlayer 0 to Stack at 48 cm. An average value of $\Delta z_{\text{stub,IP}} = 0$ is parsed to the `L1Track` Builder as well as the full $w_z/2$ matrix.

helicoidal fit, corrected for the beamspot position, and matching windows are calculated using linear interpolation

- tracklet $p_T^{\mathbf{t}}$ is used to select two of the tables built from fixed p_T samples, so that $p_T^{\text{table1}} \leqslant p_T^{\mathbf{t}} \leqslant p_T^{\text{table2}}$
- if $p_T^{\mathbf{t}} < 3$ GeV/c, use tables corresponding to $p_T^{\text{table1}} = 3$ GeV/c and $p_T^{\text{table2}} = 5$ GeV/c and allow linear interpolation outside of the interval
- if $p_T^{\mathbf{t}} > 30$ GeV/c, use table corresponding to $p_T = 30$ GeV/c
- calculate center and size of each window as an average of values of closest p_T tables, weighted on $p_T^{\mathbf{t}} - p_T^{\text{table1}}$ and $p_T^{\mathbf{t}} - p_T^{\text{table2}}$

2. the tracklet is propagated to each other Stack, according to the procedure described in Section 6.1 making use of `BaseParticlePropagator`
3. any stub falling within the matching window, corresponding to the right seed Superlayer/target Layer pair, is accepted and added to the chain
4. if more than one stub per Layer is added to the seed, the chain is duplicated until all the possible combinations, featuring only one stub per Layer, are produced
5. the procedure is repeated for each of the four apertures and a different set of `L1Tracks` is produced

$\langle \Delta\phi_{\text{stub,IP}} \rangle$ (radians)						
	sample p_T (GeV/c)					
aperture	3	5	7	10	20	30
99%	0.00023	0.00013	0.00012	0.00006	0.00001	0.00000
98%	0.00024	0.00018	0.00011	0.00005	0.00003	0.00000
95%	0.00024	0.00015	0.00011	0.00007	0.00003	0.00002
90%	0.00023	0.00014	0.00010	0.00005	0.00001	0.00001

$w_\phi/2$ (radians)						
	sample p_T (GeV/c)					
aperture	3	5	7	10	20	30
99%	0.00115	0.00081	0.00064	0.00056	0.00051	0.00051
98%	0.00096	0.00070	0.00060	0.00049	0.00046	0.00046
95%	0.00076	0.00057	0.00046	0.00041	0.00037	0.00037
90%	0.00064	0.00046	0.00040	0.00035	0.00032	0.00031

$w_{r\phi}/2$ (mm)						
	sample p_T (GeV/c)					
aperture	3	5	7	10	20	30
99%	0.58	0.41	0.32	0.27	0.24	0.24
98%	0.45	0.35	0.25	0.23	0.22	0.22
95%	0.38	0.29	0.23	0.20	0.18	0.18
90%	0.32	0.30	0.19	0.17	0.16	0.16

Table 6.2: Average value of $\Delta\phi_{\text{stub,IP}}$ distribution (TOP) and window half-size $w_\phi/2$ (BOTTOM) for propagation of tracklets from Superlayer 0 to Stack at 48 cm. An average value of $\Delta\phi_{\text{stub,IP}}$ =0.23, 0.15, 0.11, 0.05, 0.0, and 0.0 milliradians is parsed to the `L1Track` Builder for each p_T ranging from 3 to 30 GeV/c, as well as the full $w_\phi/2$ matrix. An approximated conversion into $r\phi$ displacement, useful to roughly convert the window width in Pixel units, is also given.

The same `L1Track` may be built from different seeds and the same seed may give multiple `L1Tracks`. The problem of duplicate removal will be described in Chapter 7, where the need of a clean sample will be relevant. In the present Chapter the focus will be put on efficiencies, as it is done for tracklets in Section 5.3.

The `L1Track` production efficiency is presented for two reference matching window apertures, 90% and 99%, divided by "chain length", i.e. the number of stubs that compose the `L1Track`. Efficiency is shown in Figures 6.10 and 6.11 as a function of both track p_T and η, where the latter is pictured only for tracks with $p_T > 10$ GeV/c. The sample is composed of 20,000 muon pairs with flat $0 < p_T < 50$ GeV/c distribution and flat distribution of track direction $|\eta| < 2.4$. The common denominator in efficiency plots is the number of tracks that produced a good tracklet which can be used as seed. The major

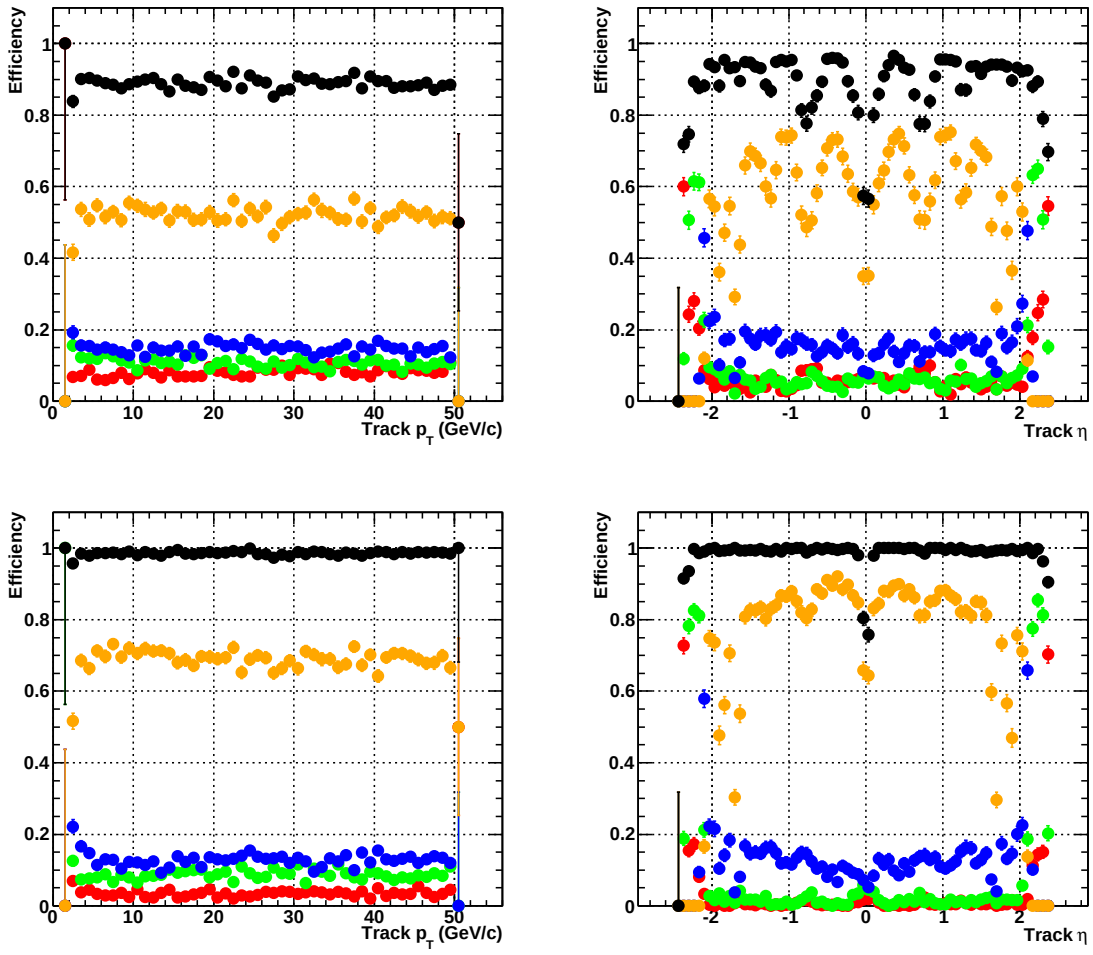

Figure 6.10: `L1Track` production efficiency with `2d+globalgeometry` stubs and tracklets. The seed is taken from Superlayer 0. Red points show the efficiency to build 3-stubs-long chains, green ones refer to 4-stubs-long chains, blue ones to 5-stubs-long chains and orange ones to 6-stubs-long chains. Black points show the cumulative efficiency to produce `L1Tracks` with at least 3 stubs. Both 90% (TOP) and 99% (BOTTOM) aperture windows are shown. The sample was composed of muon pairs with flat $0 < p_T < 50$ GeV$/c$ distribution and flat distribution of track direction $|\eta| < 2.4$.

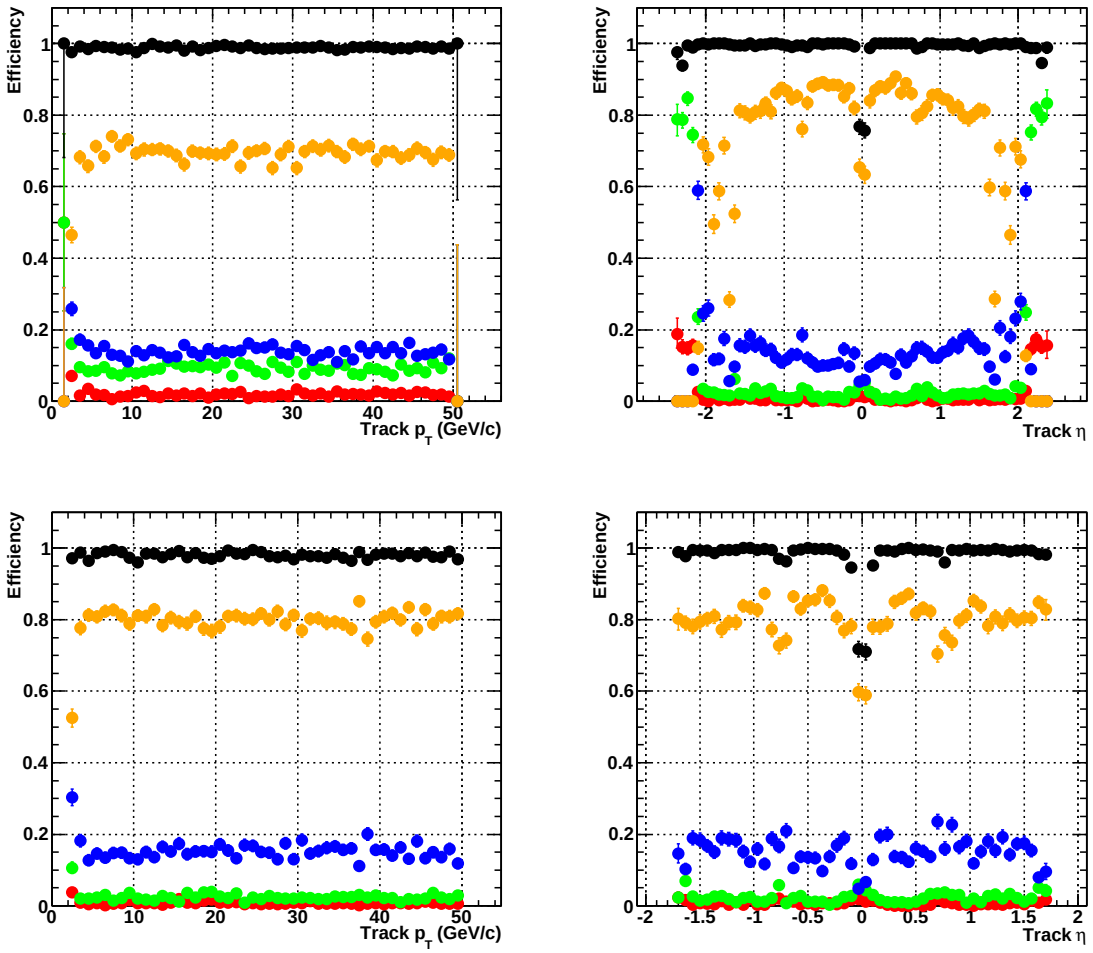

Figure 6.11: `L1Track` production efficiency with `2d+globalgeometry` stubs and tracklets. The seed is taken from Superlayer 1 (TOP) or 4 (BOTTOM). Red points show the efficiency to build 3-stubs-long chains, green ones refer to 4-stubs-long chains, blue ones to 5-stubs-long chains and orange ones to 6-stubs-long chains. Black points show the cumulative efficiency to produce `L1Tracks` with at least 3 stubs. Only 99% aperture windows are shown. The sample was composed of muon pairs with flat $0 < p_T < 50$ GeV$/c$ distribution and flat distribution of track direction $|\eta| < 2.4$.

feature that can be noticed was already predicted when the criteria to open matching windows were defined: the production inefficiency at pseudorapidities corresponding to large tails in $\Delta z_{\text{stub,IP}}$ distributions. In fact, as tails are remarkably cut by the small aperture window, the probability to associate a stub to the seed is obiously lower.

6.3 Level 1 Track Vertex and Momentum Fit

The next step in the definition of a `L1Track` is the extraction of basic information such as charge, vertex position, momentum magnitude and momentum direction. The fit is based on the tracklet one, for two main reasons. First of all, the development of `L1Tracks` is still at an early stage and a χ^2 approach cannot be reliable in terms of correct error handling and propagation. Then, any analytic fit exploiting techniques of minimization is unlikely to be implemented at a Level 1 Trigger. The tracklet fit is a more straightforward calculation than a real fit, as two points and a line in the 3D space are enough to fully constrain a helix. A Level 1 track is overconstrained by the number of its stubs: for this reason some manipulation is needed. The analytic fit is substituted by a rough estimate of track parameters from each doublet or triplet that can be found combining stubs in the `L1Track`, ordered with increasing ρ, and averaging the final result:

- the charge is found as in the tracklet fit (5.14) using the angular deviation between innermost and outermost stubs

$$q^{\text{L1T}} = -\frac{\Delta\phi^N_{\text{first,last}}}{\left|\Delta\phi^N_{\text{first,last}}\right|} = \pm 1 \tag{6.4}$$

- each triplet $\{i, j, k\}$ of stubs, with $\rho_i < \rho_j < \rho_k$, undergoes helicoidal tracklet fit as in (5.11) and (5.18), where stub i acts as tracklet vertex and all distances and angles are measured with respect to (x_i, y_i)

- the `L1Track` transverse momentum p_T^{L1T} is found by averaging the p_T estimated from each triplet $\{i, j, k\}$

$$p_T^{ijk} = c \cdot B \cdot 10^{-5} \cdot \frac{1}{2} \cdot \frac{\left|\mathbf{r}_k - \mathbf{r}_j\right|_T}{\sin\left|\Delta\phi_{\text{k,j}}\right|} \tag{6.5}$$

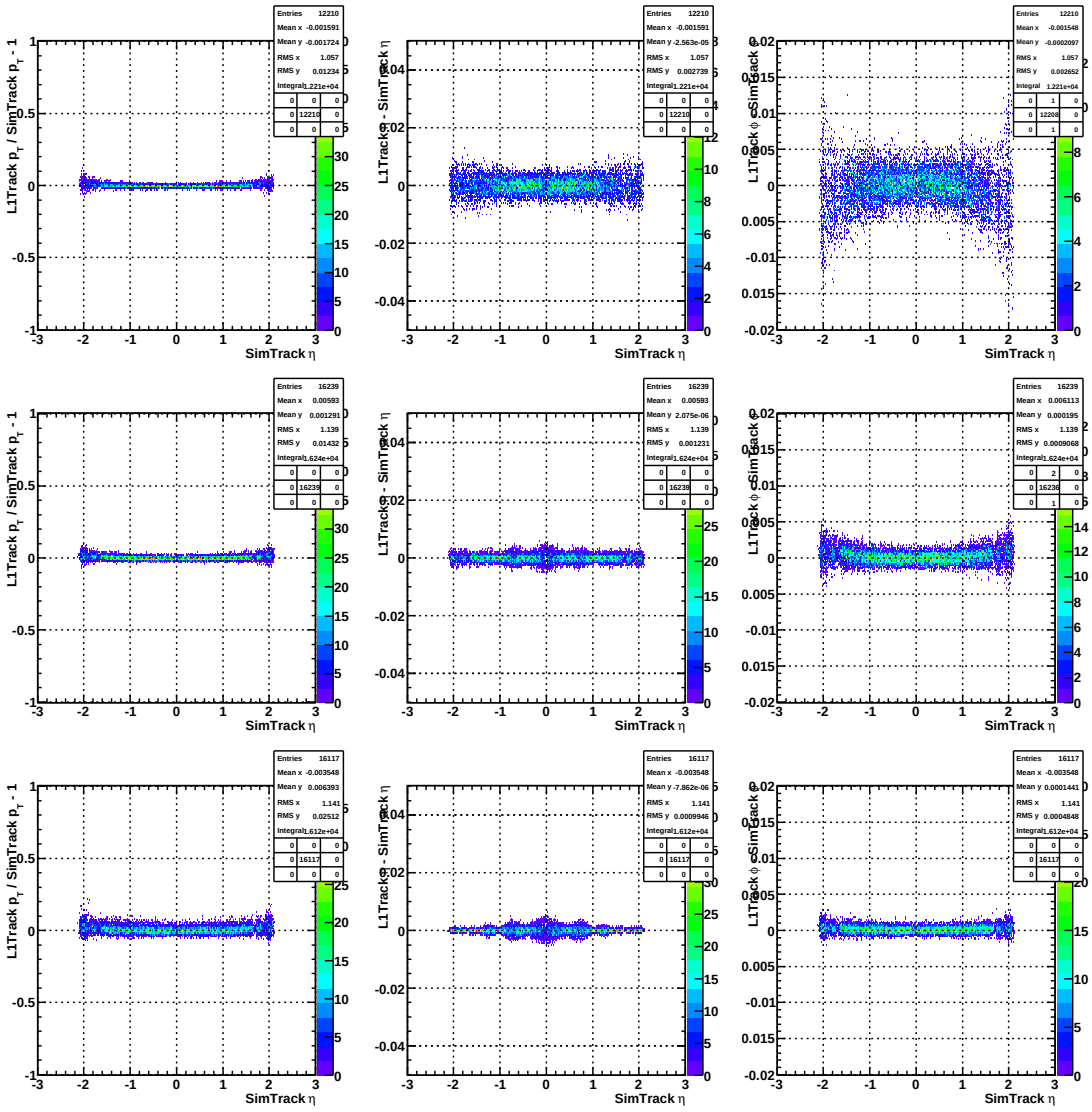

Figure 6.12: Momentum fit of Level 1 tracks. A comparison of information from the fit and the corresponding parameter of the simulated track is shown as a function of track η. From LEFT to RIGHT, columns show $\left(p_T^{\text{L1T}} - p_T^{\text{track}}\right)/p_T^{\text{track}}$, $\eta^{\text{L1T}} - \eta^{\text{track}}$ and $\phi^{\text{L1T}} - \phi^{\text{track}}$. From TOP to BOTTOM, rows show p_T = 3 GeV/c μ^+, p_T = 10 GeV/c μ^-, and p_T = 30 GeV/c μ^-. `L1Tracks` are built with the 99% aperture of matching windows from seeds in Superlayer 0. Only the subsample with `L1Tracks` composed of 6 stubs is shown. Each sample was generated with flat pseudorapidity distribution in the $|\eta| < 2.4$ range.

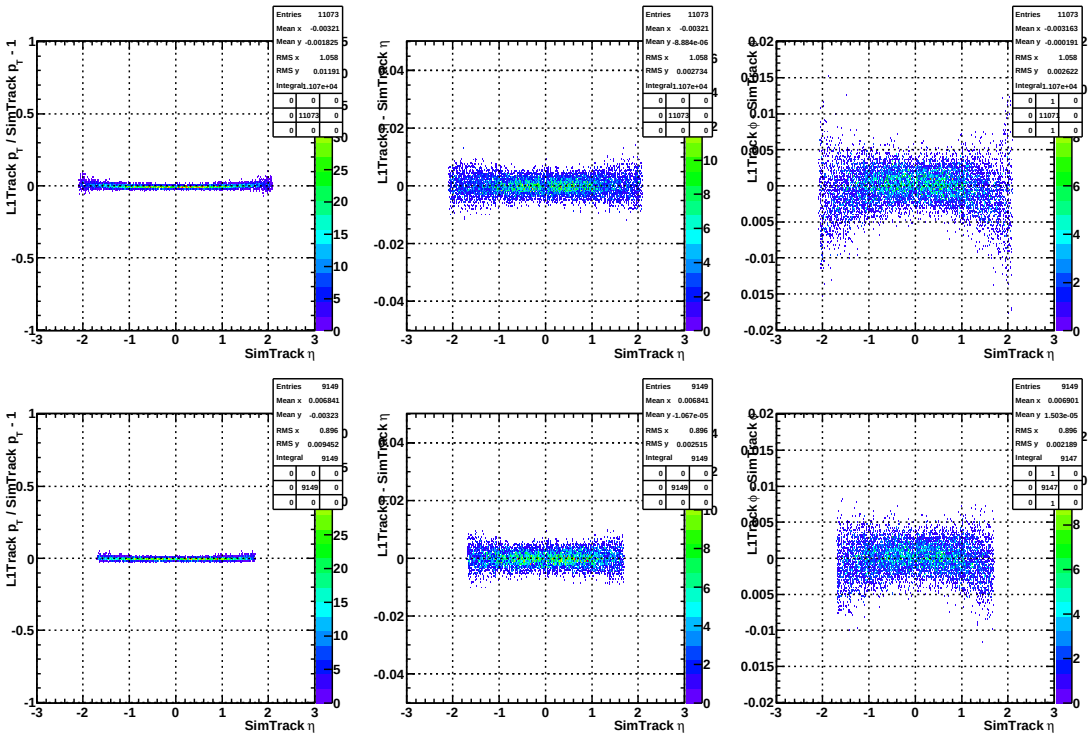

Figure 6.13: Momentum fit of Level 1 tracks. A comparison of information from the fit and the corresponding parameter of the simulated track is shown as a function of track η. From LEFT to RIGHT, columns show $\left(p_T^{\text{L1T}} - p_T^{\text{track}}\right)/p_T^{\text{track}}$, $\eta^{\text{L1T}} - \eta^{\text{track}}$ and $\phi^{\text{L1T}} - \phi^{\text{track}}$. `L1Tracks` are built with the 99% aperture of matching windows from seeds in Superlayer 1 (TOP) and 4 (BOTTOM). Only the subsample with `L1Tracks` composed of 6 stubs is shown. The sample consists of $p_T = 3$ GeV/c μ^+ generated with flat pseudorapidity distribution in the $|\eta| < 2.4$ range.

$$p_T^{\text{L1T}} = \frac{1}{\text{number of ordered triplets}} \sum_{i<j<k} p_T^{ijk} \tag{6.6}$$

- the `L1Track` longitudinal momentum p_z^{L1T} is found by averaging the p_z estimated from each triplet $\{i, j, k\}$, where the azimuth difference $\Delta\phi_{k,j}^{c}$ is measured with respect to the helix axis

$$p_z^{ijk} = \left(z_k - z_j\right) \cdot c \cdot B \cdot 10^{-5} \cdot \frac{1}{\Delta\phi_{k,j}^{c}} \tag{6.7}$$

$$p_z^{\text{L1T}} = \frac{1}{\text{number of ordered triplets}} \sum_{i<j<k} p_z^{ijk} \tag{6.8}$$

- for each triplet, the global (x, y) coordinates corresponding to the helix axis are

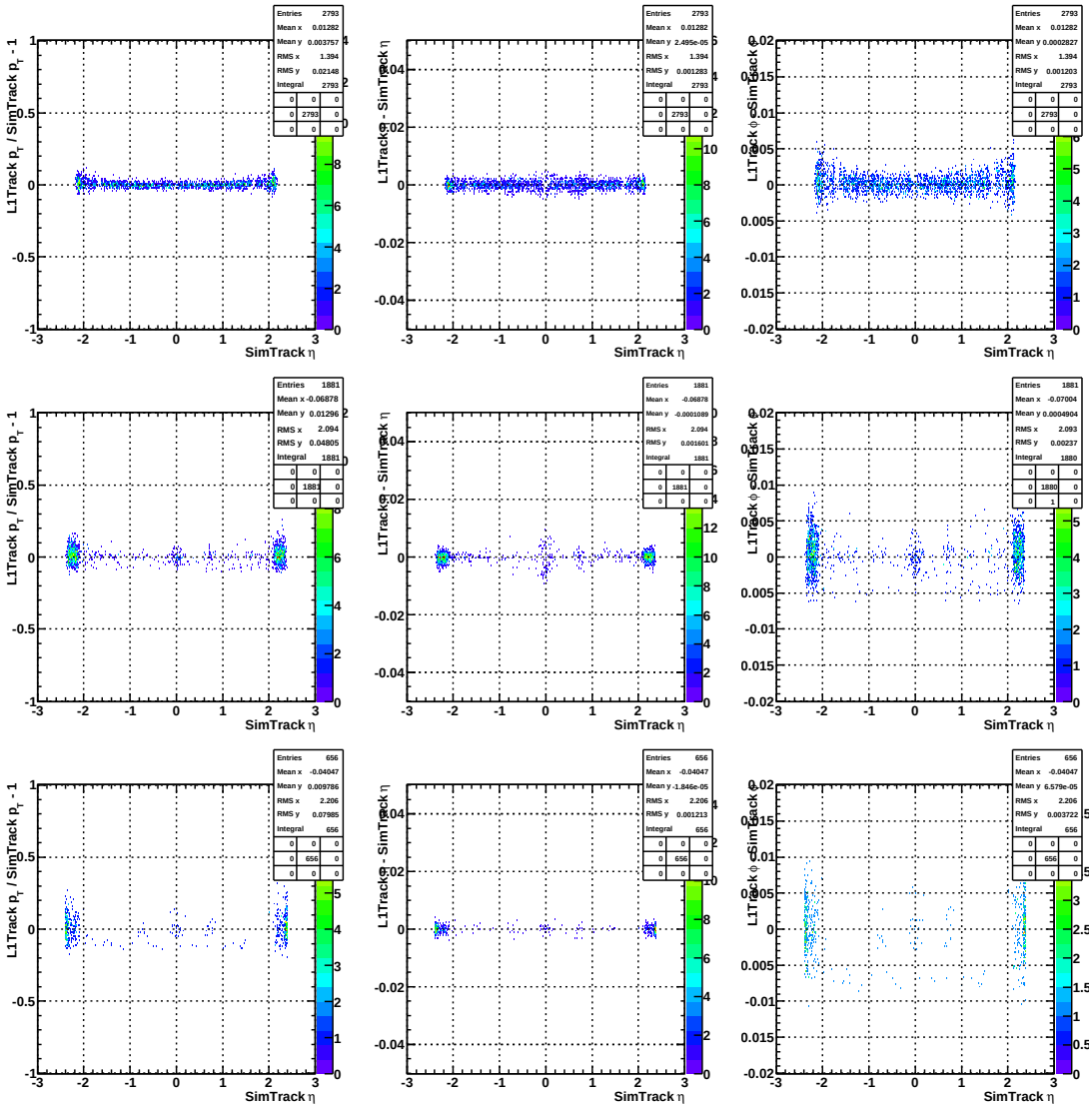

Figure 6.14: Momentum fit of Level 1 tracks. A comparison of information from the fit and the corresponding parameter of the simulated track is shown as a function of track η. From LEFT to RIGHT, columns show $\left(p_T^{\text{L1T}} - p_T^{\text{track}}\right)/p_T^{\text{track}}$, $\eta^{\text{L1T}} - \eta^{\text{track}}$ and $\phi^{\text{L1T}} - \phi^{\text{track}}$. `L1Tracks` are built with the 99% aperture of matching windows from seeds in Superlayer 0. The subsamples with `L1Tracks` composed of 5, 4, and 3 stubs are shown from TOP to BOTTOM. The sample consists of p_T = 10 GeV/c μ^- generated with flat pseudorapidity distribution in the $|\eta| < 2.4$ range.

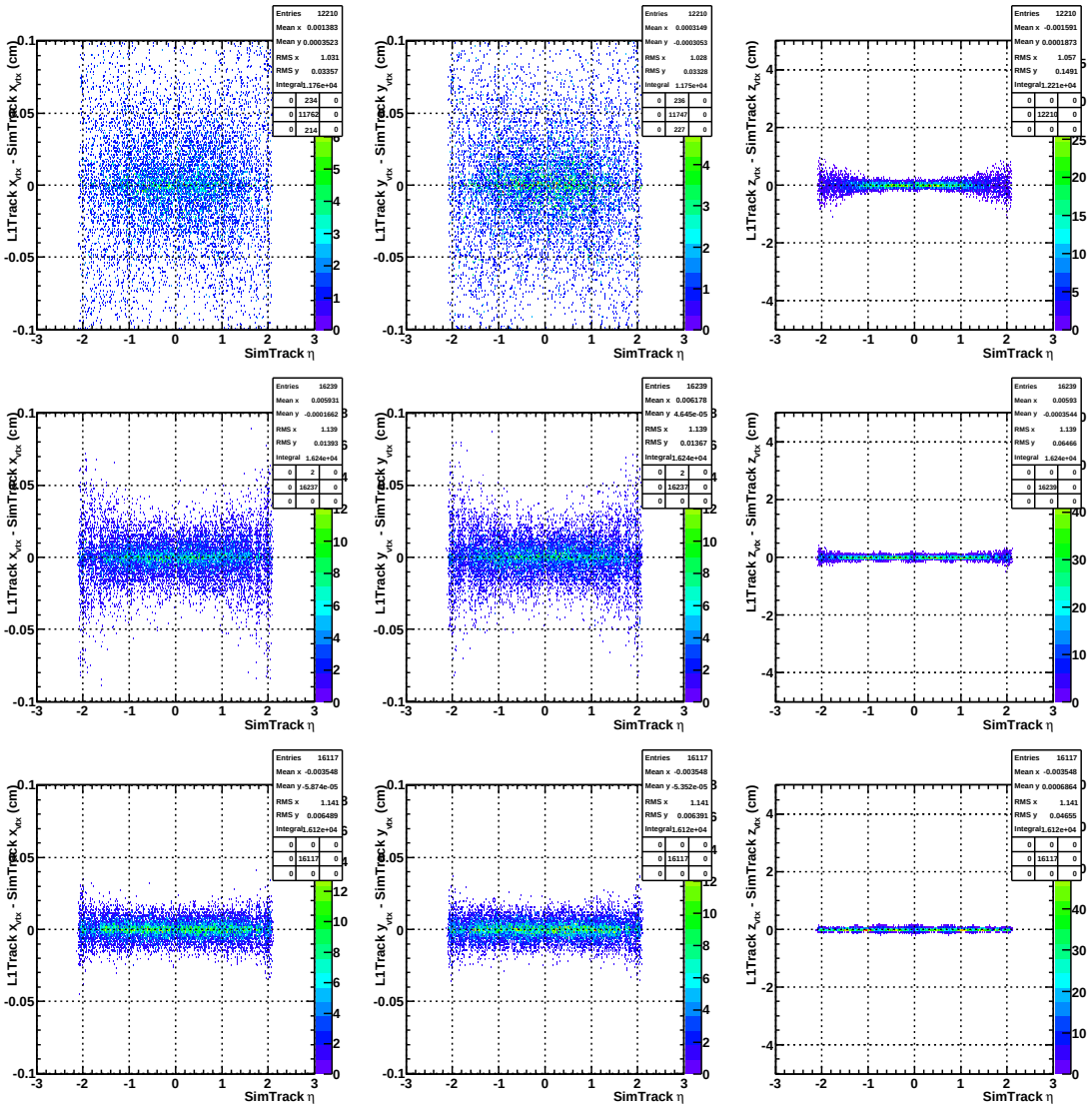

Figure 6.15: Vertex fit of Level 1 tracks. A comparison of information from the fit and the corresponding parameter of the simulated track is shown as a function of track η. From LEFT to RIGHT, columns show $x_{\text{vtx}}^{\text{L1T}} - x_{\text{vtx}}^{\text{track}}$, $y_{\text{vtx}}^{\text{L1T}} - y_{\text{vtx}}^{\text{track}}$ and $z_{\text{vtx}}^{\text{L1T}} - z_{\text{vtx}}^{\text{track}}$. From TOP to BOTTOM, rows show p_T = 3 GeV/c μ^+, p_T = 10 GeV/c μ^-, and p_T = 30 GeV/c μ^-. `L1Tracks` are built with the 99% aperture of matching windows from seeds in Superlayer 0. Only the subsample with `L1Tracks` composed of 6 stubs is shown. Each sample was generated with flat pseudorapidity distribution in the $|\eta| < 2.4$ range.

found

$$\begin{pmatrix} x_{\text{ax}}^{ijk} \\ y_{\text{ax}}^{ijk} \end{pmatrix} = \begin{pmatrix} x_i + R^{ijk} \cdot \cos\left(\phi_k - q^{\text{L1T}} \cdot \arccos\left(\frac{\rho_k}{2R^{ijk}}\right)\right) \\ y_i + R^{ijk} \cdot \sin\left(\phi_k - q^{\text{L1T}} \cdot \arccos\left(\frac{\rho_k}{2R^{ijk}}\right)\right) \end{pmatrix} \tag{6.9}$$

- the global (x, y) coordinates corresponding to the helix axis are averaged over the number of triplets and corrected for the beamline displacement in order to find the coordinates of minimum approach and the track direction at minimum approach

$$\tan\phi^{\text{L1T}} = \frac{q^{\text{L1T}} \cdot x_{\text{ax, corr}}^{\text{L1T}}}{-q^{\text{L1T}} \cdot y_{\text{ax, corr}}^{\text{L1T}}} \tag{6.10}$$

  where signs of numerator and denominator are important to solve ambiguities due to angle periodicity

- also the helix radius R^{L1T} is averaged over triplets of stubs

- the distance of minimum approach of the track to the beamline is

$$d_0^{\text{L1T}} = \rho_{\text{ax, corr}} - R^{\text{L1T}} \tag{6.11}$$

- the global coordinates of minimum approach, which are meant to be the transverse coordinates of the `L1Track` vertex, are then calculated from both the axis position and d_0^{L1T}

$$\begin{pmatrix} x_{\text{vtx}}^{\text{L1T}} \\ y_{\text{vtx}}^{\text{L1T}} \end{pmatrix} = \begin{pmatrix} x_{\text{beam}} + d_0^{\text{L1T}} \cdot \cos\phi_{\text{ax, corr}} \\ y_{\text{beam}} + d_0^{\text{L1T}} \cdot \sin\phi_{\text{ax, corr}} \end{pmatrix} \tag{6.12}$$

- the extraction of the longitudinal coordinate of the vertex $z_{\text{vtx}}^{\text{L1T}}$ cannot rely on triplets as the innermost stub is not on the beamline and, to be self-consistent, $z_{\text{vtx}}^{\text{L1T}}$ must be calculated as the longitudinal coordinate of the helix at the minimum approach: for this reason ordered doublets of stubs $\{j, k\}$ are treated as a tracklet with vertex on the line $(x, y) = (x_{\text{vtx}}^{\text{L1T}}, y_{\text{vtx}}^{\text{L1T}})$, and its third coordinate is calculated as in (5.17)

$$z_{\text{vtx}}^{jk} = z_{\text{j}} + \frac{\Delta\phi_{\text{vtx,j}}^{\text{c}}}{\Delta\phi_{\text{k,j}}^{\text{c}}} \cdot \left(z_{\text{k}} - z_{\text{j}}\right) \tag{6.13}$$

$$z_{\text{vtx}}^{\text{L1T}} = \frac{1}{\text{number of ordered doublets}} \sum_{j<k} z_{\text{vtx}}^{jk} \tag{6.14}$$

- also in this case the $c = 300$ mm/ns and $B = 4$ T approximations hold

Figures from 6.12 to 6.14 show the results of the momentum fit. In the first one p_T^{L1T}, η^{L1T}, and ϕ^{L1T} are shown for track p_T = 3, 10, and 30 GeV/c. In the second one, the effect of seed Superlayer is compared in the p_T = 3 GeV/c case. The third one shows the results for shorter `L1Tracks` in the p_T = 10 GeV/c case. The p_T estimate with this fit is better at lower transverse momenta. On the contrary, at larger track p_T, the direction is better calculated and also resonant effects due to Pixel size can be appreciated. The momentum fit could in principle depend on the Superlayer of the chosen seed, as the information on the seed tracklet vertex is used in every calculation requiring the position of the beamline in the transverse plane. However, this effect seems to be limited. The reduction of the chain length, besides remarking that shorter `L1Tracks` are mainly located at large η and in regions where the production efficiency is lower, shows that the distributions of residuals get wider if the stub chain is shorter.

Figure 6.15 shows the position of minimum approach compared to the track true vertex for different p_T. Following the considerations already made about the estimate of track direction at vertex, which makes use of coordinates of minimum approach to beamline, it is not surprising that the vertex is better calculated for larger p_T tracks. Resonant effects due to Pixel size become clear at large p_T also in the comparison of $z_{\mathrm{vtx}}^{\mathrm{L1T}}$ to track z_{vtx}.

All the results described so far do not make any attempt to include the vertex of the tracklet used as seed in the fit. Of course this is possibile but one must be careful not to use it in the doublets when fitting $z_{\mathrm{vtx}}^{\mathrm{L1T}}$. The improvements, in both momentum and vertex estimate, are pictured in Figures 6.16 and 6.17 for different values of track p_T.

It is interesting to note how the information extracted this way, in particular the p_T, can be used to trigger on a single track, compared to what can be done with tracklets, as shown in Figures 5.22 an 5.23. Figures 6.18 and 6.19 show, as examples, the turn-on curves for triggering on p_T^{L1Trk} in single muon events with flat p_T spectrum ranging from 0 to 50 GeV/c, generated with flat η distribution in the $[-2.4, 2.4]$ range. The first one displays the results of fit that does not include the seed vertex while the second one shows what happens if seed vertex is added. These pictures separate the turn-on curves, with p_T thresholds every 5 GeV/c up to p_T = 30 GeV/c, for different `L1Track` lengths. In particular, one could compare the curves relative to p_T thresholds of 10, 20, and 30 GeV/c. The striking aspect, with all the caveats due to low statistics in the shorter `L1Track` subsamples, is that tracklets still show sharper turn-on curves if stub radii are

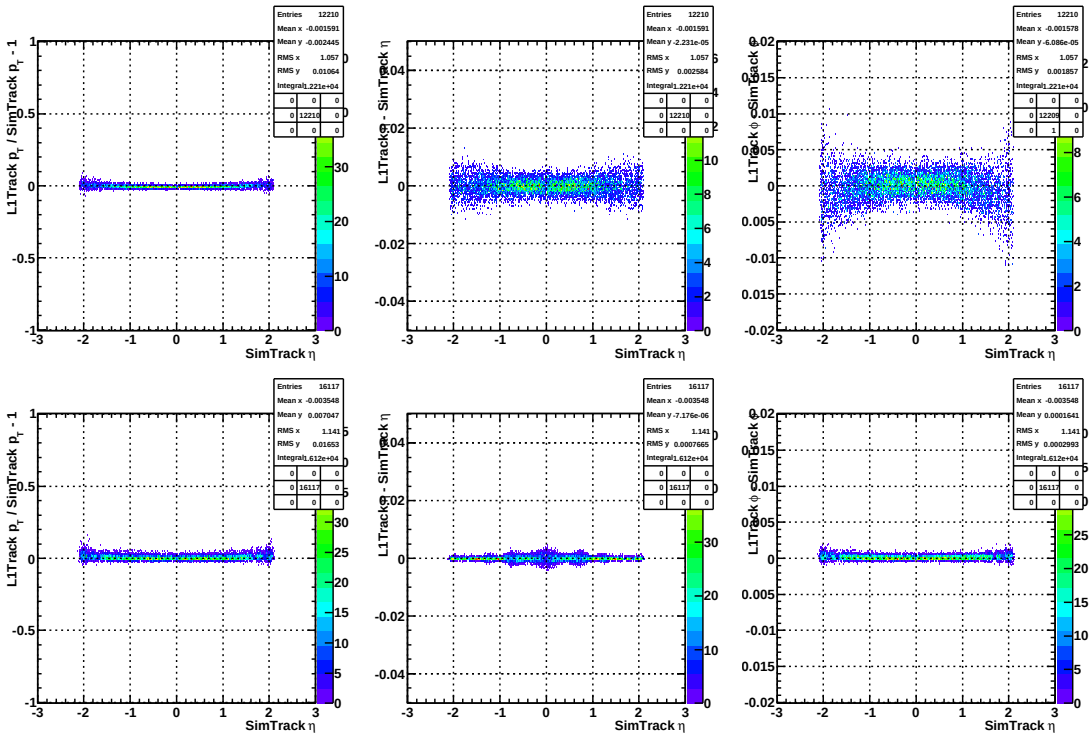

Figure 6.16: Momentum fit of Level 1 tracks. A comparison of information from the fit and the corresponding parameter of the simulated track is shown as a function of track η. From LEFT to RIGHT, columns show $\left(p_T^{\text{L1T}} - p_T^{\text{track}}\right)/p_T^{\text{track}}$, $\eta^{\text{L1T}} - \eta^{\text{track}}$ and $\phi^{\text{L1T}} - \phi^{\text{track}}$. Rows show results for p_T = 3 GeV/c μ^+ (TOP) and p_T = 30 GeV/c μ^- (BOTTOM). `L1Tracks` are built with the 99% aperture of matching windows from seeds in Superlayer 0. Only the subsample with `L1Tracks` composed of 6 stubs is shown. Each sample was generated with flat pseudorapidity distribution in the $|\eta| < 2.4$ range. Seed vertex is included in the fit procedure.

larger than 40 cm and if the seed vertex is not used in the fit. In fact, this is the case where ratios between lever arms are more similar to Superlayer 0 tracklets and the number of permutations is still small enough to keep the p_T resolution comparable. The inclusion of the seed vertex into the set of points used for the fit allows having longer lever arms and more triplets to average on, so that, particularly in the longer `L1Track` subsamples, the p_T threshold is sharp.

The problem of duplicate removal has already been introduced. To better cope with the necessity of reducing the number of `L1Tracks` when duplicates arise, discrimination criteria should be chosen. One kind of duplicates, as they were introduced, comes from overlap regions or seeding in different layers that may turn out in `L1Tracks` sharing part of their stubs. Discrimination criteria in such cases could be based on goodness of

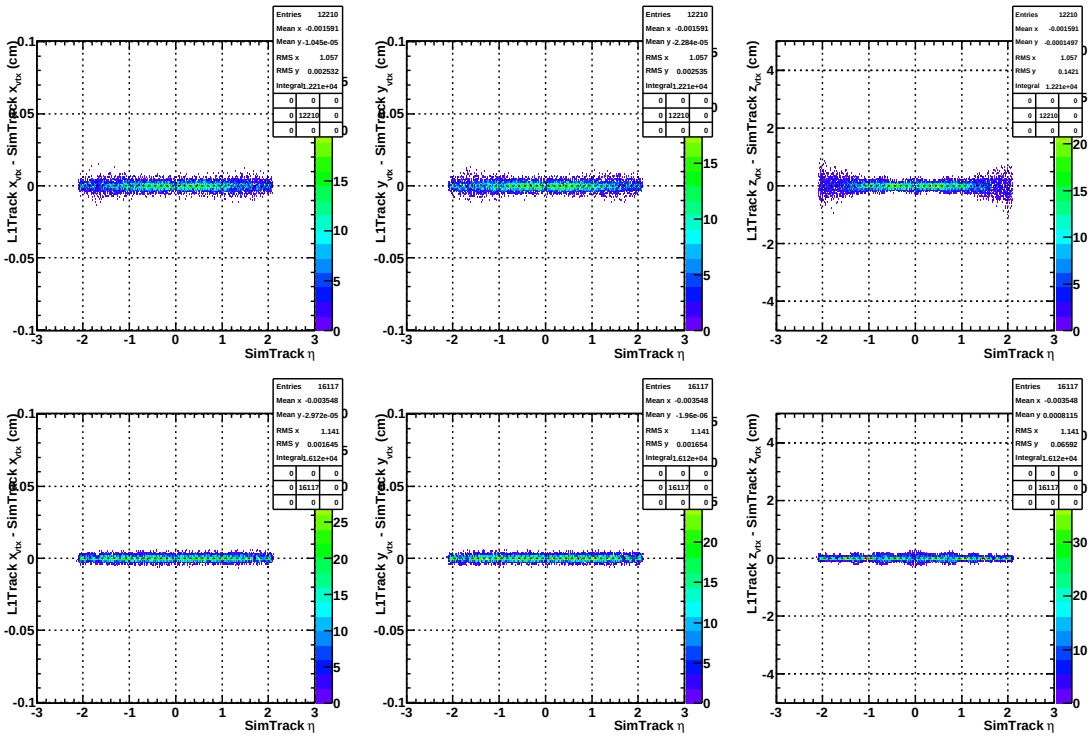

Figure 6.17: Vertex fit of Level 1 tracks. A comparison of information from the fit and the corresponding parameter of the simulated Track is shown as a function of Track η. From LEFT to RIGHT, columns show $x_{\text{vtx}}^{\text{L1T}} - x_{\text{vtx}}^{\text{track}}$, $y_{\text{vtx}}^{\text{L1T}} - y_{\text{vtx}}^{\text{track}}$, and $z_{\text{vtx}}^{\text{L1T}} - z_{\text{vtx}}^{\text{track}}$. Rows show results for $p_T = 3$ GeV/c μ^+ (TOP) and $p_T = 30$ GeV/c μ^- (BOTTOM). `L1Tracks` are built with the 99% aperture of matching windows from seeds in Superlayer 0. Only the subsample with `L1Tracks` composed of 6 stubs is shown. Each sample was generated with flat pseudorapidity distribution in the $|\eta| < 2.4$ range. Seed vertex is included in the fit procedure.

the momentum and vertex fit of `L1Tracks`. Since the decision of avoiding a fit based on minimization procedure was due to the absence of reliability in terms of correct error handling and propagation, a fit χ^2 cannot be calculated for the same reason. The goodness of the fit still can be estimated at this stage with the sum of squares of residuals. The sum of squares of residuals after a fit, still labelled as χ^2 throughout this document for sake of notation simplicity, is defined as

$$\chi^2 = \sum_{\text{points}} \left(\mathbf{r}_{\text{measured}} - \mathbf{r}(\text{fit parameters, independent variable})\right)^2 \tag{6.15}$$

As the helix is defined with the rule that difference in z between two any points is proportional to the difference in angle measured with respect to the trajectory axis, one

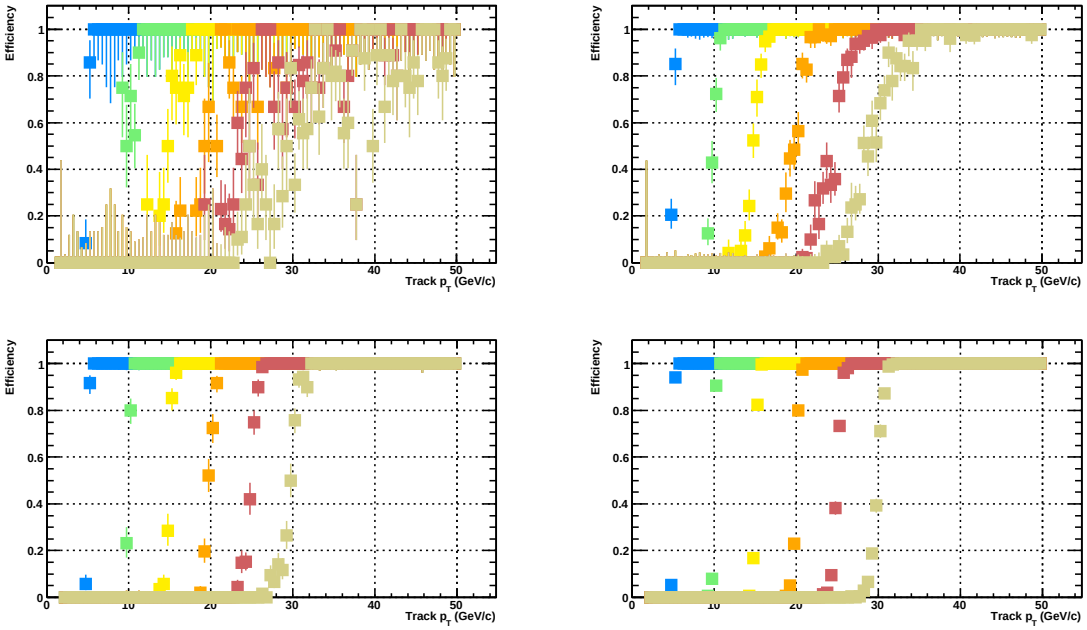

Figure 6.18: Turn-on curves with different p_T thresholds, for tracks which produced accepted `L1Tracks` seeded with tracklets in Superlayer 1 and built with 99% aperture of matching windows. Light blue markers represent $p_T^{\text{L1T}} > 5$ GeV/c, light green ones show $p_T^{\text{L1T}} > 10$ GeV/c, yellow ones show $p_T^{\text{L1T}} > 15$ GeV/c, orange ones show $p_T^{\text{L1T}} > 20$ GeV/c, brick red ones show $p_T^{\text{L1T}} > 25$ GeV/c, and sand brown ones show $p_T^{\text{L1T}} > 30$ GeV/c. TOP row shows subsamples of shorter `L1Tracks`, 3 stubs (LEFT) and 4 stubs (RIGHT) while BOTTOM row shows subsamples of longer `L1Tracks`, 5 stubs (LEFT) and 6 stubs (RIGHT). The sample was composed of muons with flat $0 < p_T < 50$ GeV/c distribution and flat distribution of track direction $|\eta| < 2.4$ and beamspot displaced 0.5 mm in the $+x$ direction. The seed vertex is not included in the fit procedure.

can describe it as

$$\mathbf{r}\left(\phi^{\text{c}}\right) = \begin{pmatrix} x_{\text{ax}}^{\text{L1T}} + R^{\text{L1T}} \cos\left(\phi^{\text{c}}\right) \\ y_{\text{ax}}^{\text{L1T}} + R^{\text{L1T}} \sin\left(\phi^{\text{c}}\right) \\ z_{\text{offset}}^{\text{L1T}} + \phi^{\text{c}} \cdot H_{\text{prop}}^{\text{L1T}} \end{pmatrix} \tag{6.16}$$

where all angles ϕ^{c} are measured with respect to $(x_{\text{ax}}^{\text{L1T}}, y_{\text{ax}}^{\text{L1T}})$ and $z_{\text{offset}}^{\text{L1T}}$ and $H_{\text{prop}}^{\text{L1T}}$ are the average over doublets of points used in the fit of

$$z_{\text{offset}}^{jk} = z_j - \phi_j^{\text{c}} \cdot \frac{z_k - z_j}{\Delta\phi_{k,j}^{\text{c}}} \tag{6.17}$$

$$H_{\text{prop}}^{jk} = \frac{z_k - z_j}{\Delta\phi_{k,j}^{\text{c}}} \tag{6.18}$$

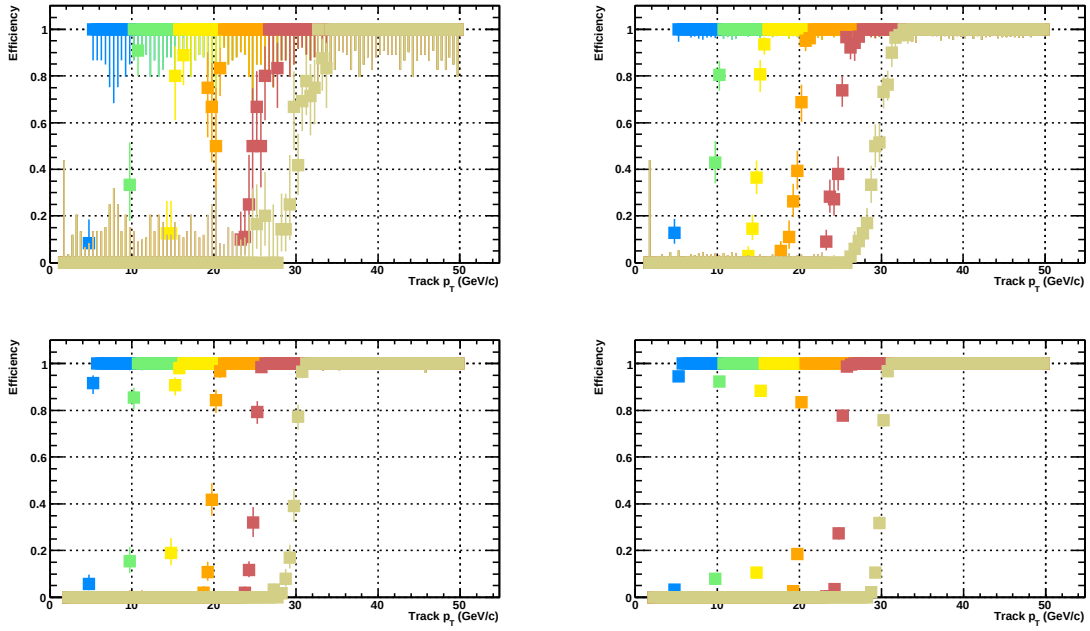

Figure 6.19: Turn-on curves with different p_T thresholds, for tracks which produced accepted `L1Tracks` seeded with tracklets in Superlayer 1 and built with 99% aperture of matching windows. Light blue markers represent $p_T^{\text{L1T}} > 5$ GeV/c, light green ones show $p_T^{\text{L1T}} > 10$ GeV/c, yellow ones show $p_T^{\text{L1T}} > 15$ GeV/c, orange ones show $p_T^{\text{L1T}} > 20$ GeV/c, brick red ones show $p_T^{\text{L1T}} > 25$ GeV/c, and sand brown ones show $p_T^{\text{L1T}} > 30$ GeV/c. TOP row shows subsamples of shorter `L1Tracks`, 3 stubs (LEFT) and 4 stubs (RIGHT) while BOTTOM row shows subsamples of longer `L1Tracks`, 5 stubs (LEFT) and 6 stubs (RIGHT). The sample was composed of muons with flat $0 < p_T < 50$ GeV/c distribution and flat distribution of track direction $|\eta| < 2.4$ and beamspot displaced 0.5 mm in the $+x$ direction. The seed vertex is included in the fit procedure.

The χ^2 is calculated separating the transverse component from the longitudinal one:

$$\chi^2_T = \sum_k \left(x_k - x^{\text{L1T}}_{\text{ax}} - R^{\text{L1T}} \cos\left(\phi^{\text{c}}_k\right)\right)^2 + \left(y_k - y^{\text{L1T}}_{\text{ax}} - R^{\text{L1T}} \sin\left(\phi^{\text{c}}_k\right)\right)^2 \tag{6.19}$$

$$\chi^2_L = \sum_k \left(z_k - z^{\text{L1T}}_{\text{offset}} - \phi^{\text{c}}_k \cdot H^{\text{L1T}}_{\text{prop}}\right)^2 \tag{6.20}$$

Each χ^2 is called "normalized" after being divided by the number of points used in the fit, i.e. the number of stubs of the `L1Track` plus the seed vertex, if employed.

Figures 6.20 and 6.21 show the behaviour of χ^2_T and χ^2_L, as well as the normalized ones, as a function of track η and p_T. The first evident comment that can be made is that

χ^2_L is definitely larger than χ^2_T, perfectly consistent with the different precision in position measurement one has along z and in the transverse plane with the concept Tracker. Moreover, the inclusion of the seed vertex in the fit allows both the normalized χ^2_L and χ^2_T to be lower, confirming the better estimate of track parameters that can be obtained with the inclusion of a further point close to the true track vertex.

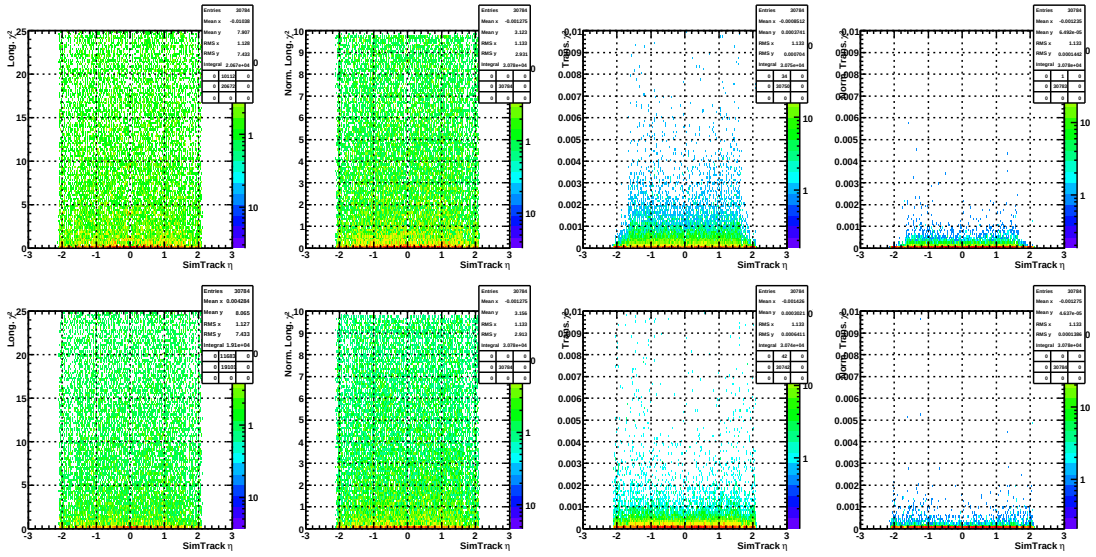

Figure 6.20: Helicoidal fit of Level 1 tracks: goodness-of-fit estimate. The sum of squares of residuals, still labelled χ^2 to simplify notations, of stub positions (measured as a function of the angle measured with respect to the trajectory axis) is shown against η^{L1T}. From LEFT to RIGHT: χ^2_L, renormalized χ^2_L, χ^2_T, and renormalized χ^2_T. TOP row shows the godness-of-fit without including seed vertex while BOTTOM row shows the result in case seed vertex is included in the fit procedure. `L1Tracks` are built with the 99% aperture of matching windows from seeds in Superlayer 0. Only the subsample with `L1Tracks` composed of 6 stubs is shown. The used sample was composed of muon pairs with flat p_T distribution ranging from 0 to 50 GeV/c and flat pseudorapidity distribution in the $|\eta| < 2.4$ range.

6.4 Fake Rates of Level 1 Tracking Trigger Objects

One important aspect of all the Level 1 Tracking Objects described so far, from stubs to Level 1 tracks, is the true track content they deliver. As all of them come out from opportunely combined Tracker hits, at high luminosity they may be composed of hits released by different tracks. `PixelDigis` can be compared to the simulated track through an *ad-hoc* linker to check if all the `PixelDigis` composing the Level 1 Tracking Object are

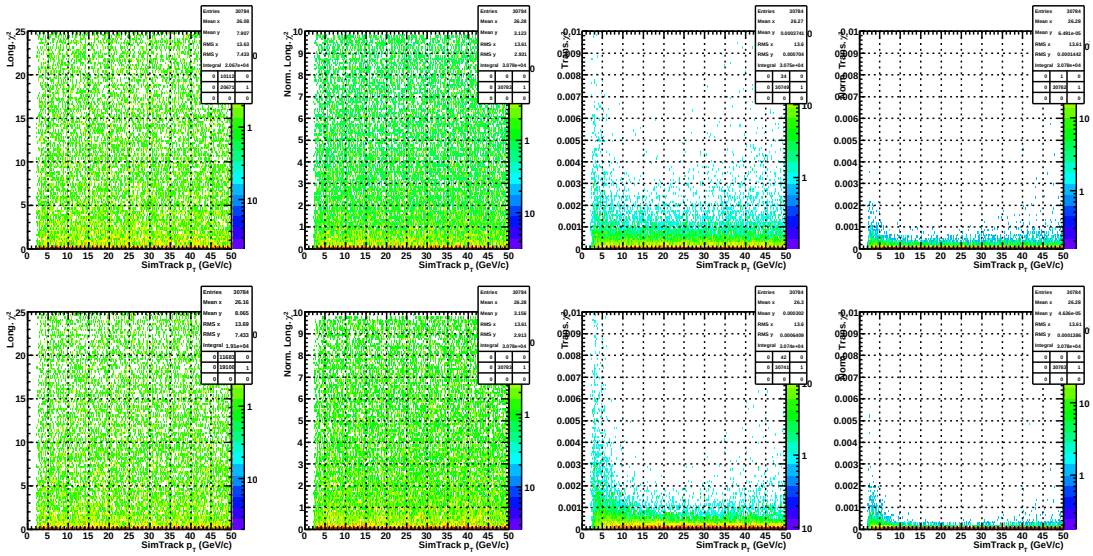

Figure 6.21: Helicoidal fit of Level 1 tracks: goodness-of-fit estimate. The sum of squares of residuals, still labelled χ^2 to simplify notations, of stub positions (measured as a function of the angle measured with respect to the trajectory axis) is shown against p_T^{L1T}. From LEFT to RIGHT: χ^2_L, renormalized χ^2_L, χ^2_T, and renormalized χ^2_T. TOP row shows the godness-of-fit without including seed vertex while BOTTOM row shows the result in case seed vertex is included in the fit procedure. `L1Tracks` are built with the 99% aperture of matching windows from seeds in Superlayer 0. Only the subsample with `L1Tracks` composed of 6 stubs is shown. The used sample was composed of muon pairs with flat p_T distribution ranging from 0 to 50 GeV/c and flat pseudorapidity distribution in the $|\eta| < 2.4$ range.

really generated by the same track. As the large majority of particles in minimum-bias events are pions, one must also take into account the results obtained with single pion events reported in Appendix C.

6.4.1 Stubs

Studies on the stub fake rate were already performed in the past [80], based on the request that the hits paired into a stub are associated or not to the same track in simulation. Based on this simple definition, sets of minimum-bias events, at different pile-up, were generated, and the fake rate was measured as the fraction of stubs, with `2d` clustering and `pixelray` matching, produced by more than one track in each Stack. Results are shown in Figure 6.22 for both the standard threshold at 2 GeVc and a higher one at 5 GeV/c.

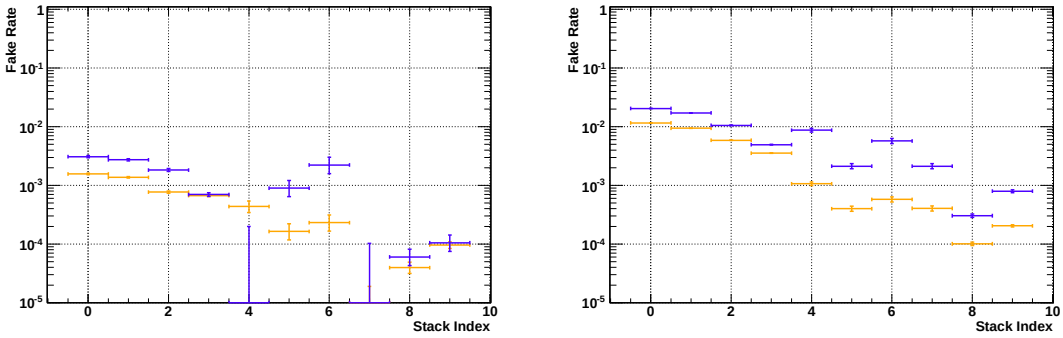

Figure 6.22: Stub fake rate in different Stacks of the Long Barrel layout at LHC nominal luminosity (LEFT)and 200 superimposed collisons per bunch crossing (RIGHT). Stubs are made out of `2d` clustering and `pixelray` matching and fake rates are provided for both the standard threshold (dark yellow markers) and a higher one at 5 GeV/c (navy blue markers).

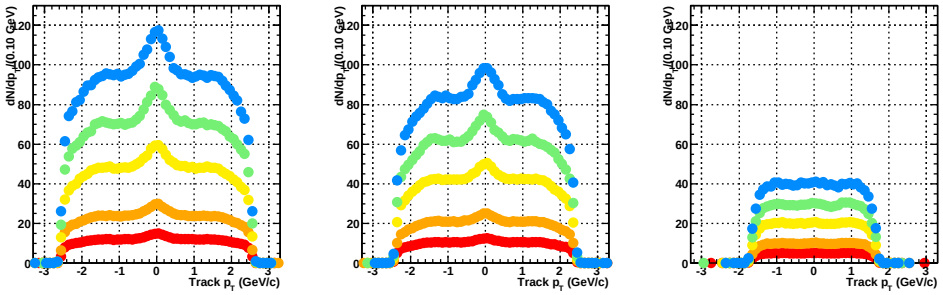

Figure 6.23: Pseudorapidity distribution of charged particles in minimum-bias events with `FastSimulation`, averaged per bunch crossing, leaving at least one hit in sensor layers placed at 32 (LEFT), 48 (MIDDLE) and 98.5 cm from the beamline (RIGHT). Different colours correspond to different pile-up values, ranging from 25 to 200 superimposed events per bunch crossing.

The fake rate for the 5 GeV/c p_T threshold is higher mainly because of the rapidly decreasing spectrum of charged particles in minimum-bias events (see Figure 3.14) and the production efficiency, as shown in Figures 5.11 to 5.14, which make the denominator smaller. As cluster size is larger at larger pseudorapidities, it may be interesting to check how the fake rate depends on pseudorapidity. Figure 6.24 displays the results for Stacks at radii of 32 and 48 cm at Phase 2 luminosities with 200 superimposed events per bunch crossing. The fake rate is larger at larger pseudorapidities, particularly for the higher threshold subsample. As the pseudorapidity distribution of charged particles leaving hits in Stack Members is the one shown in Figure 6.23, the larger fake rate is mainly due to larger clusters which include contributions from different tracks. The behaviour is similar to the one of Figure 5.15, however the overall rates are normalized using different

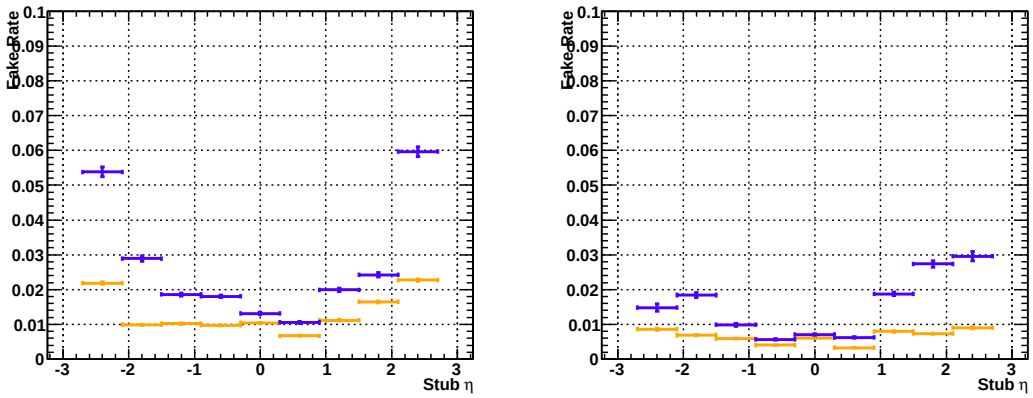

Figure 6.24: Stub fake rate in Stacks at 32 (LEFT) and 48 cm (RIGHT) at 200 superimposed collisons per bunch crossing, averaged per pseudorapidity bin. Stubs are made out of `2d` clustering and `pixelray` matching and fake rates are provided for both the standard threshold (dark yellow markers) and a higher one at 5 GeV/c (navy blue markers).

coordinates.

6.4.2 Tracklets

The tracklet fake rate can be described analogously to the stub one, with one more detail. In fact, it may be useful to distinguish between tracklets containing a fake stub and tracklets whose fakeness is due to combinatoric effect in matching genuine stubs to each other. The same samples used to get the stub fake rate are taken into account for tracklets. Figure 6.25 displays the tracklet fake rate at different pile-up and in different Superlayers of the Long Barrel concept Tracker.

It is interesting to note also the results of momentum fit for tracklets contributing to the fake rate, as displayed in Figures 6.26 and 6.27. Almost all the fake rate is due to combinatorics in stub matching and it is larger in the central region, as it can be inferred from Figure 6.23, which shows that the particle density is larger at $|\eta| < 1$. On the transverse momentum side, the fake rate increases with p_T^t up to 10 GeV/c, and shows a nearly random behaviour at larger momenta.

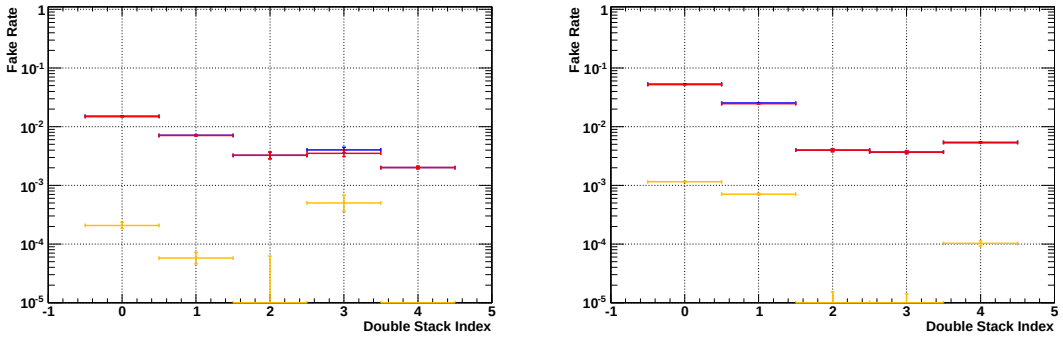

Figure 6.25: Tracklet fake rate in different Double Stacks of the Long Barrel layout at LHC nominal luminosity (LEFT)and 200 superimposed collisons per bunch crossing (RIGHT). Stubs are made out of `2d` clustering and `pixelray` matching. Red markers show the combinatoric fake rate and yellow ones the contribution of fake stubs to the overall tracklet fake rate, which is shown by blue markers when not hidden by red ones.

6.4.3 Level 1 Tracks

The Level 1 track fake rate is calculated as the tracklet one. In fact, both tracklets and Level 1 tracks are built out of stubs and therefore also Level 1 tracks may contain either fake stubs either genuine ones produced by different charged particles. Figure 6.28 displays the Level 1 tracklet fake rate at different pile-up as a function of the seed Superlayer. Only Level 1 tracks containing 6 stubs and built using 99% matching windows are shown.

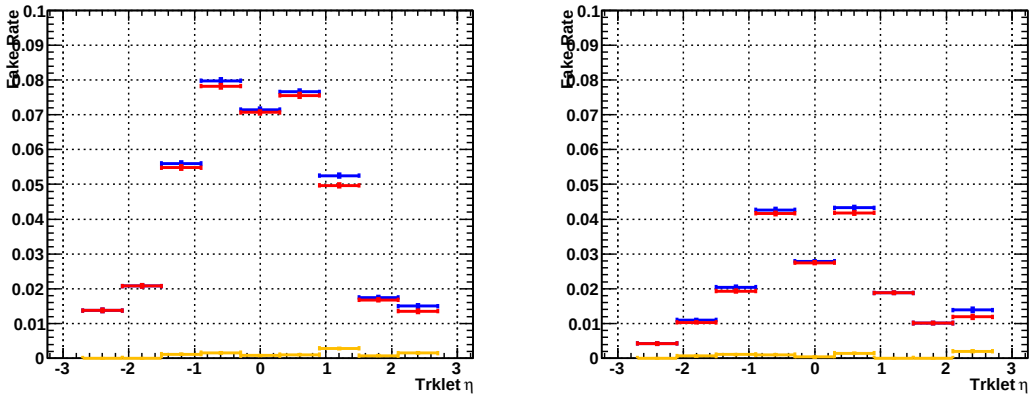

Figure 6.26: Tracklet fake rate in Superlayers 0 (LEFT) and 1 (RIGHT) of the Long Barrel concept Tracker at 200 superimposed collisons per bunch crossing, as a function of η^{t}, averaged per pseudorapidity bin. Stubs are made out of `2d` clustering and `pixelray` matching. Red markers show the combinatoric fake rate and yellow ones the contribution of fake stubs to the overall tracklet fake rate, which is shown by blue markers when not hidden by red ones.

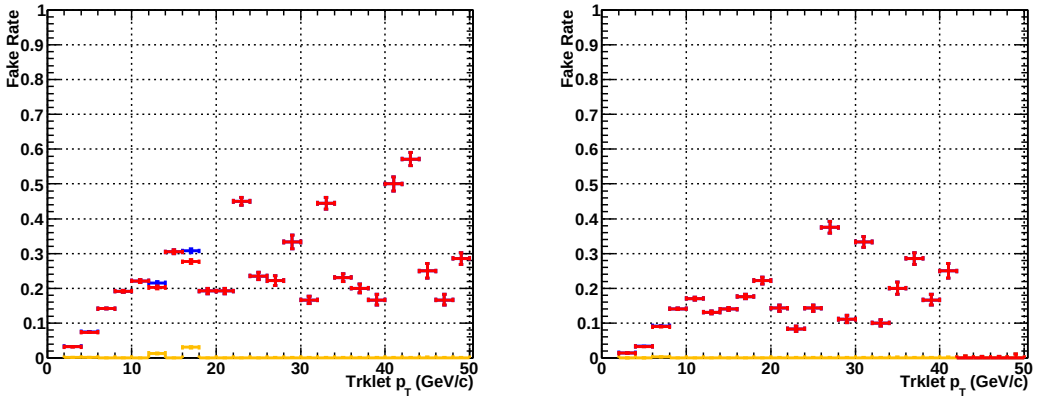

Figure 6.27: Tracklet fake rate in Superlayers 0 (LEFT) and 1 (RIGHT) of the Long Barrel concept Tracker at 200 superimposed collisons per bunch crossing, as a function of p_T^{t}, averaged per p_T bin. Stubs are made out of `2d` clustering and `pixelray` matching. Red markers show the combinatoric fake rate and yellow ones the contribution of fake stubs to the overall tracklet fake rate, which is shown by blue markers when not hidden by red ones.

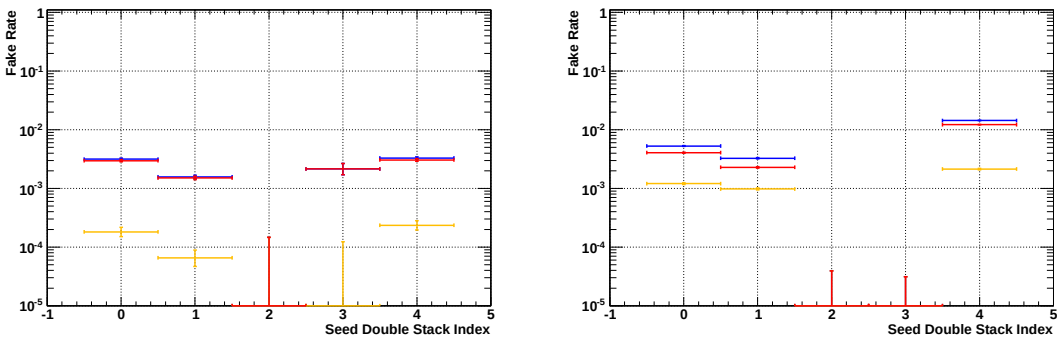

Figure 6.28: Level 1 track fake rate in the Long Barrel concept Tracker at LHC nominal luminosity (LEFT)and 200 superimposed collisons per bunch crossing (RIGHT), as a function of the seed Superlayer. Stubs are made out of `2d` clustering and `pixelray` matching. Red markers show the combinatoric fake rate and yellow ones the contribution of fake stubs to the overall Level 1 track fake rate, which is shown by blue markers when not hidden by red ones. Only 6-stubs Level 1 tracks built with the 99% aperture of matching windows are taken into account.

7. Application of L1 Tracking Trigger to τ Final States

After describing the state-of-the-art in Level 1 Tracking Trigger simulations from the point of view of available, improved and brand new tools, this Chapter describes an example of they can be employed in triggering final states containing τ leptons decaying to hadrons. In fact, τ-jets are very narrow and current Trigger employs calorimeters to identify narrow energy deposits but, as shown in Section 2.3, also this kind of Trigger is expected to exceed the bandwidth limits at Phase 2 luminosities. For this reason, improved Calorimetry Trigger, which exploit the finer Calorimeter segmentation which will be available with Phase 1 upgrades, are currently under evaluation. This Chapter describes one possible approach to introduct Level 1 Tracking Trigger within this effort.

7.1 Current τ Trigger at CMS

Calorimetric Level 1 Trigger was already introduced in Section 1.2.5. Narrow jets in the Calorimeters are identified as candidate τ leptons. The jet Trigger employs the sum of transverse energies measured in ECAL and HCAL regions (square arrays of 16 towers each). The complete Calorimeter is spanned with a 3×3 region window to identify jets: candidates are selected once the central region E_T is higher than the one measured in the eight neighbor regions, as shown in Figure 7.1. For each Calorimeter region, a τ-veto bit is set true if there are more than two active ECAL or HCAL towers in the region. If none of the regions in the 3×3 towers window reports the τ-veto bit, the jet is defined as a τ-jet. Level 1 τ-jets are not taken into account if there is a candidate electron in the same region.

As many of the interesting processes involving τ leptons in the final state are characterized by two τ's, only the two-jet HLT algorithm is recalled herein as an example

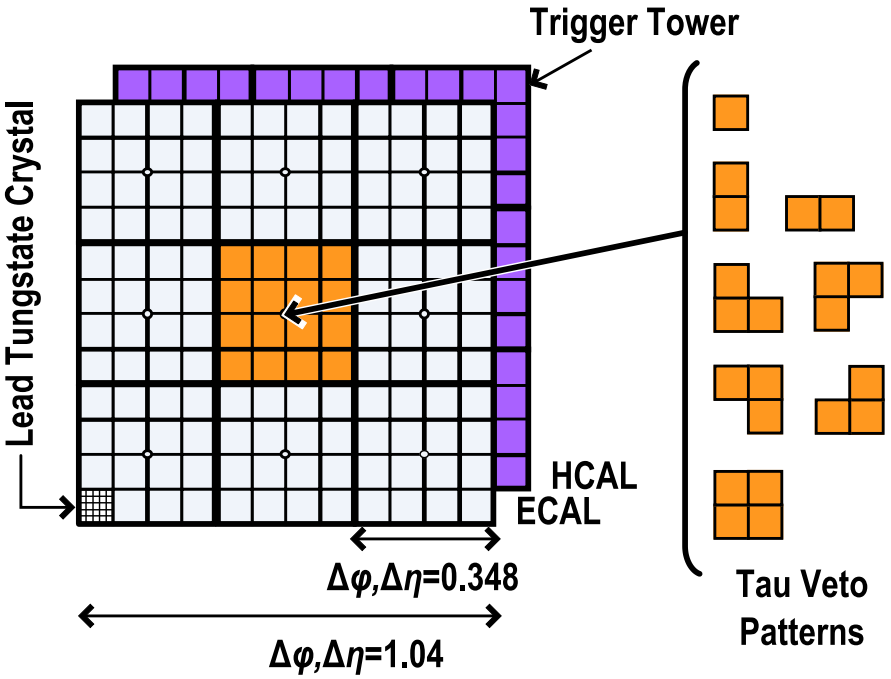

Figure 7.1: Level 1 τ jet allowed patterns for active towers.

[85, 86]. Two candidate τ-jets from the Level 1 stream are chosen according to jet energy and are reconstructed in a restricted region. These are identified as Level 2 jets and undergo isolation test, either by calorimetric isolation followed by Pixel Detector isolation, either using full tracker isolation criteria which do not take calorimetric information into account.

Electromagnetic isolation is defined from the scalar sum of E_T measured in a ring around the τ-jet, whose size can be tuned as a function of the luminosity. A τ-jet is defined as isolated if this sum of transverse energies in the isolation ring does not exceed a chosen fraction of the τ-jet E_T. Tracker isolation exploits track reconstruction inside the jet cones.

The isolation-based tagging compares the number of tracks with $p_T > 1\,\mathrm{GeV}/c$ within a "signal cone" of radius R_S to the trakcs within an an "isolation cone" of radius R_I [86]. Signal cone is defined around the direction of the largest p_T track inside a "matching cone" of radius R_M around the calorimetric jet direction. The isolation cone is defined around the jet direction for the Pixel Detector case, while it is around the leading track

direction for the Silicon Strip Tracker case. The trigger selection requires zero good tracks in the ring $R_S < R < R_I$. Also these radii are tunable [87], typical sizes are $R_S = 0.07$, $R_M = 0.1$, and $0.2 < R_I < 0.45$. The idea behind these isolation criteria is pictured in Figure 7.2.

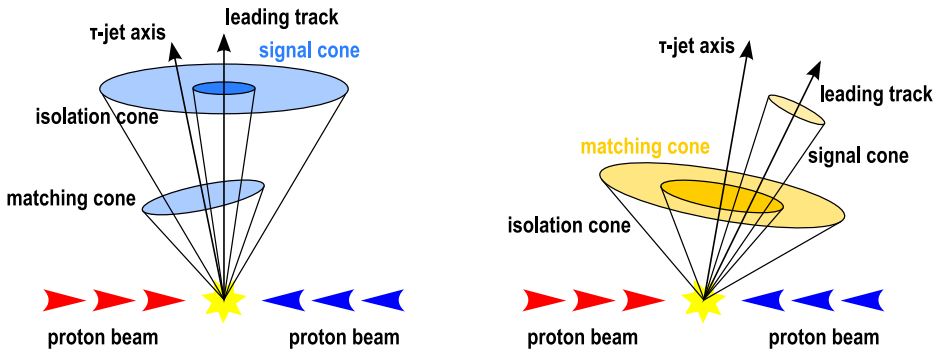

Figure 7.2: Schematic representation of τ-jet isolation criteria in CMS HLT using full tracking information (LEFT) and Pixel Detector track seeds (RIGHT).

7.2 A Possible Level 1 Calorimeter Trigger for Luminosity Upgrades

There are already ongoing studies for Level 1 Calorimeter Triggers at Phase 1 and Phase 2 luminosities **[FONTE]** . As these works are still in progress, the latest version ensuring compatibility with the simulation studies reported herein will be briefly recalled:

- **Particle Cluster Finder:** local primitives from the Calorimeter TPG are taken from each tower; each clustering block takes four towers as input; ECAL and HCAL activity thresholds are applied on towers and for each tower a 2×2 tower Cluster is created; Cluster pattern is compared to predefined ones and accepted or rejected according to comparison satisfaction; e/γ discrimination is performed computing the ECAL E_T fraction

- **Cluster Overlap Filter:** each Cluster is compared to its 8 neighbors which share at least one tower with the central one; if central cluster E_T is lower than the neighbor

one, overlapping towers are removed from the central one; if towers are not pruned, the cluster is marked as "central"

- **Cluster Isolation and Particle ID:** an 8×8 square of towers around each cluster is checked for absolute and relative energy deposits, and an isolation bit is set if luminosity criteria are satisfied; clusters of 2×3 towers (wider in ϕ) are also checked as τ candidates; e/γ candidates require to be "central" cluster and the e/γ bit, τ candidates require to be "central" cluster and 2×3 isolation, as shown in Figure 7.3

- **Jet Reconstruction:** jets are reconstructed by summing energy around a local maximum cluster in a 8×8 towers region, only filtered clusters are taken into account

- **Final Operations:** particles are sorted and only the most energetic ones are returned, final calculations of H_T and $\not{E}_T$ are performed

Activity thresholds are very low, of few GeV, and still need tuning for very high luminosity. However, the standard settings for the algorithm will be used as the main goal is to test the improvements that can be brought by the introduction of Tracking information in the Level 1 Trigger and not to set performance benchmarks on Level 1 τ Trigger.

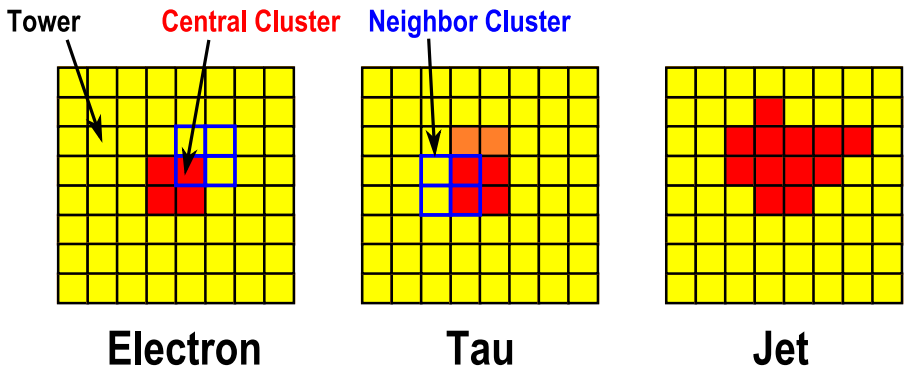

Figure 7.3: Schematic representation of upgraded Level 1 Calorimeter Trigger particles.

7.3 A Candidate Level 1 Tracking Trigger τ

The most straightforward strategy to include Level 1 Tracking Trigger in the on-line selection of τ leptons would follow the current HLT τ selection. The very first step in the definition of a τ Tracker candidate is the understanding of the kind of Level 1 tracks that are generated by a τ lepton decaying to hadrons.

7.3.1 Removal of Duplicates of Level 1 Tracks

Starting from the tools developed in Chapter 6, the first open point to solve before moving to study τ leptons is the removal of duplicates arising either from seeding from different Superlayers, either from stubs in overlap regions between adjacent Ladders. The following criteria have been chosen to remove duplicate `L1Tracks`:

- each pair of `L1Tracks` is compared stub by stub to find the number of shared ones
- if the number of shared stubs is at least two, the two `L1Tracks` are assumed to be the same and undergo the discrimination procedure
- the minimum number of shared stubs has not been optimized yet but comes from reasonable assumptions; first of all, a `L1Track` is composed of at least three stubs, so setting the minimum number to allows the comparison and rejection of short tracks in forward regions; then, a pair of stubs always points to the same direction and vertex if fitted as a tracklet, independently of any other stub included in the `L1Track` and independently of the Layer containing each stub, and therefore their sharing is a good indicator of the point occupied by the track in phase space
- the `L1Track` with the largest renormalized sum of squares of residuals in the transverse plane χ^2_T is pruned; `L1Tracks` are fitted including the seed vertex because of the improved resolution in vertex and momentum measurement; transverse χ^2_T is preferred to the longitudinal and to the total ones because χ^2_L is dominated by the Tracker resolution along z and the effect of including the seed vertex in the fit cannot be appreciated as much as for χ^2_T
- if the two `L1Tracks` are composed by the very same stubs and cannot be discriminated according to χ^2_T, the one with the seed closer to the beamline is chosen

The procedure was tested in a PYTHIA6 sample of Standard Model Z production in pp collisions at $\sqrt{s} = 14$ TeV, without added pile-up. The Z boson is forced to decay to τ pairs and each τ is prevented from decaying to electron or muon plus neutrinos. Figure 7.4 shows the τ four-momentum features relevant for triggering[(1)]. Figure 7.5, on the other hand, shows the relevant distributions of momentum magnitude and direction of charged decay products in τ lepton final states. Approximately 40% of the τ charged decay products are out of Tracker acceptance and their p_T is pulled towards low values.

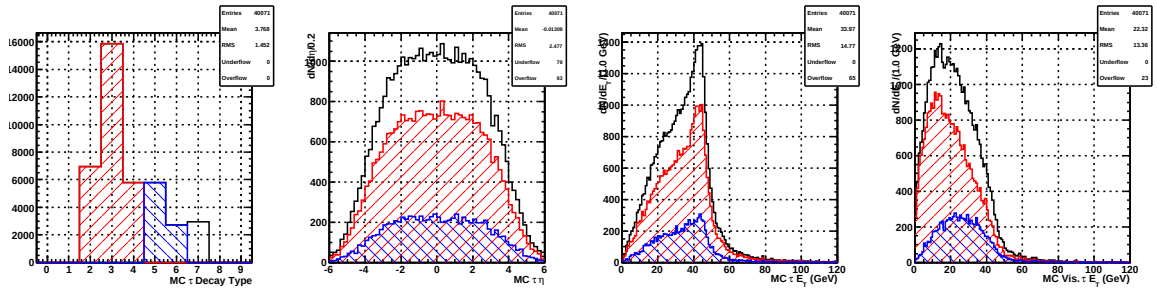

Figure 7.4: PYTHIA6 sample of Standard Model $Z \rightarrow \tau^+\tau^- \rightarrow$ hadrons in pp collisions at $\sqrt{s} = 14$ TeV. From LEFT to RIGHT: τ decay channel, τ pseudorapidity, τ transverse energy and τ visible transverse energy. τ decay channels: 0 and 1 are the leptonic modes suppressed in the present study; 2 to 4 are 1-prong hadronic final states including a number of neutral pions ranging from 0 to 2; 5 and 6 are 3-prongs hadronic final states including 0 or 1 neutral pion; 7 cumulates all other final states. Red distributions describe 1-prong final states, blue distributions describe 3-prongs final states while black ones inculde all hadronic final states.

The number of tracklets per Superlayer[(2)] is compared to the number of L1Tracks before and after the duplicate removal in Figure 7.6. The described procedure to remove duplicates is able to bring back to 1 the number of L1Tracks associated to 1-prong decays and also to reduce the effect of Ladder overlap which is clear for those 1-prong decays with two tracklets in a Superlayer. Moreover, the procedure is able to keep to 3 the maximum number of L1Tracks in 3-prongs decays, as it is for tracklet multiplicity, despite the slight difference in relative population of bins 2 and 3.

[(1)] "Visible" four-momentum of a τ lepton is the vector sum of all four-momenta of its decay products excluding neutrinos.

[(2)] For the purpose of understanding Tracking Trigger objects in τ decays, the outermost Superlayer is grouped to the two short barrels that extend its pseudorapidity coverage, as illustrated in Figure 4.4.

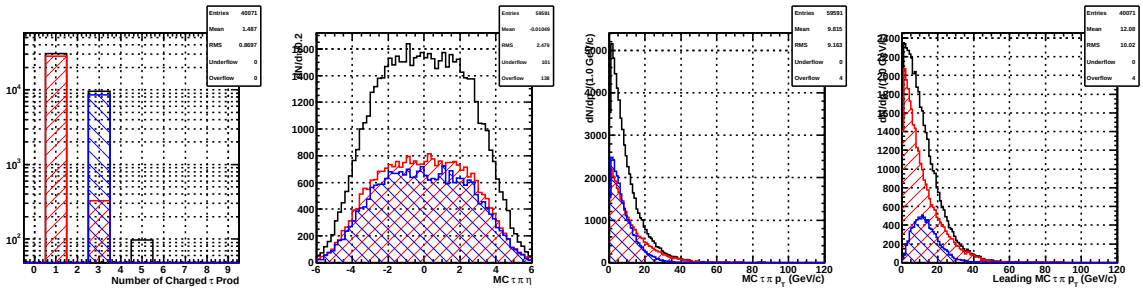

Figure 7.5: Charged decay products in PYTHIA6 sample of Standard Model $Z \rightarrow \tau^+\tau^- \rightarrow$ hadrons in pp collisions at $\sqrt{s}$ = 14 TeV. From LEFT to RIGHT: number of charged decay products, particle pseudorapidity, particle p_T and p_T of the largest-p_T particle in the decay. Red distributions describe 1-prong final states, blue distributions describe 3-prongs final states while black ones inculde all hadronic final states.

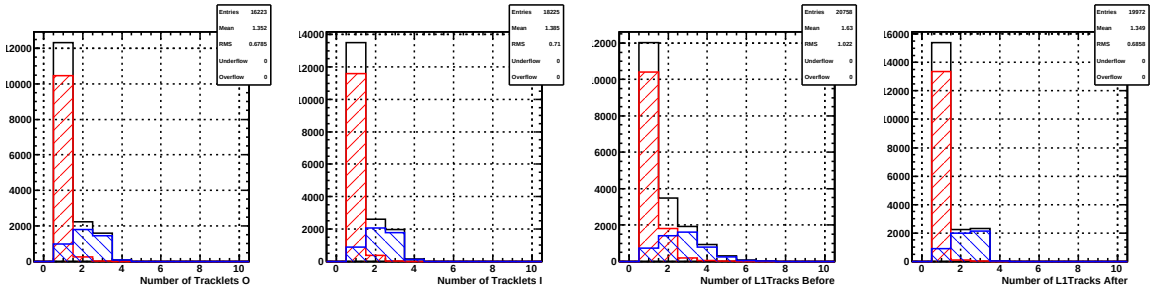

Figure 7.6: Number of tracklets and L1Tracks in PYTHIA6 sample of Standard Model $Z \rightarrow \tau^+\tau^- \rightarrow$ hadrons in pp collisions at $\sqrt{s}$ = 14 TeV. From LEFT to RIGHT: number of tracklets in the outermost Superlayer including short barrels, number of tracklets in the innermost Superlayer, number of raw L1Tracks returned by the builder and number of L1Tracks after duplicate pruning. Red distributions describe 1-prong final states, blue distributions describe 3-prongs final states while black ones inculde all hadronic final states.

7.3.2 Definition of the Candidate Level 1 Tracker τ

The next step in understanding L1Tracks from τ decay products is the comparison of distributions relative to momentum and vertex. Figure 7.7 displays two subsamples of L1Tracks mutually exclusive: the first one comes from τ's which produced only one L1Tracks after duplicate removal, while the second one contains multiple L1Tracks produced by the same τ. As expected from Figures 7.5 and 7.6, the first subsample is mainly associated to 1-prong decays and the second one to 3-prongs decays. Moreover, the tail of the p_T^{L1T} distribution dominated by 1-prong decays extends to higher values. Vertexing in the transverse plane shows that all L1Track vertexes are contained within few tenths

of mm from the beamline.

A candidate Level 1 Tracker τ can therefore be descibed by a cluster of `L1Tracks` very close in phase space, i.e. pointing to the same direction and being close in vertex. For this reason, the subsample composed of more than one `L1Track` per τ needs further manipulation to understand the clustering criteria to group `L1Tracks` together to form a candidate Level 1 Tracker τ. Figure 7.8 shows that difference in p_T^{L1T} cannot be a clustering criterion as spans over a wide range. On the other side, `L1Track` azimuth ϕ^{L1T} and pseudorapidity η^{L1T} can be used to associate `L1Tracks` to each other as they are contained within a reasonable cone size ≈ 0.2. The HLT signal cone radius used as reference is $R_S = 0.07$. Such a value applied to $\Delta\eta^{\mathrm{L1T}}$ and $\Delta\phi^{\mathrm{L1T}}$ distributions contains approximately the 75% of all pairs of `L1Tracks` generated by the same τ in 3-prongs decays, while 1-prong decays are almost exclusively reproduced by a single `L1Track`.

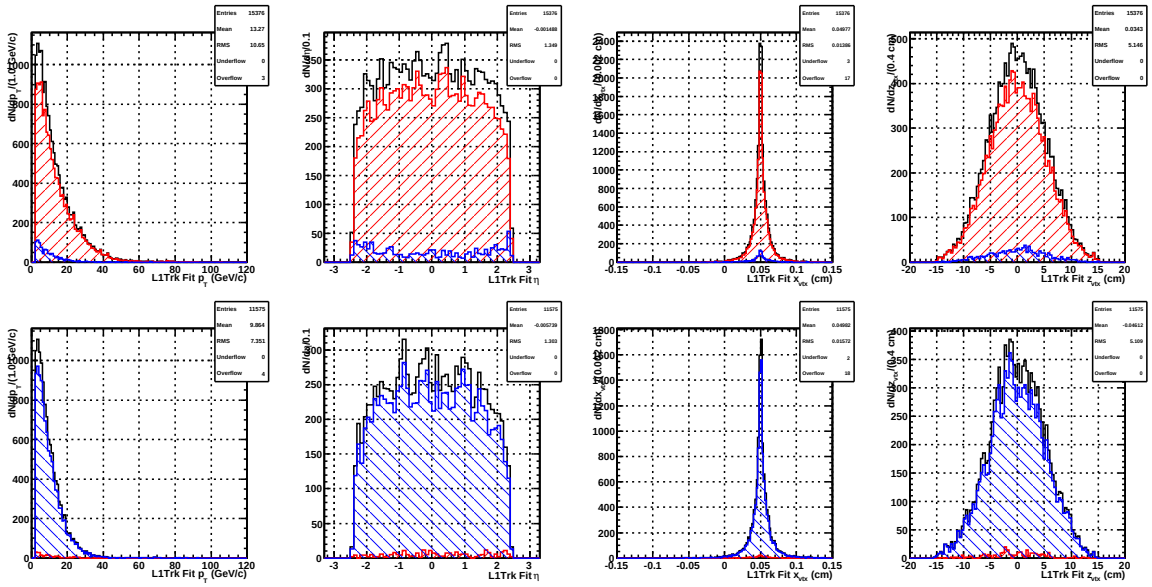

Figure 7.7: Vertex and momentum fit of `L1Tracks` in `PYTHIA6` sample of Standard Model $Z \rightarrow \tau^+\tau^- \rightarrow$ hadrons in pp collisions at $\sqrt{s} = 14$ TeV. From LEFT to RIGHT: p_T^{L1T}, η^{L1T}, $x_{\mathrm{vtx}}^{\mathrm{L1T}}$, and $z_{\mathrm{vtx}}^{\mathrm{L1T}}$. TOP row shows subsample where only one `L1Track` per τ is left after duplicate removal, while BOTTOM row shows its complement. Red distributions describe 1-prong final states, blue distributions describe 3-prongs final states while black ones inculde all hadronic final states.

The same approach was used on `PYTHIA6` samples of Standard Model $H \rightarrow \tau^+\tau^- \rightarrow$ hadrons in pp collisions at $\sqrt{s} = 14$ TeV, with $m_H = 100$ and $m_H = 120\,\mathrm{GeV}/c$. Besides the p_T and E_T spectra, the only remarkable difference with $Z \rightarrow \tau^+\tau^-$ is the pseudorapidity

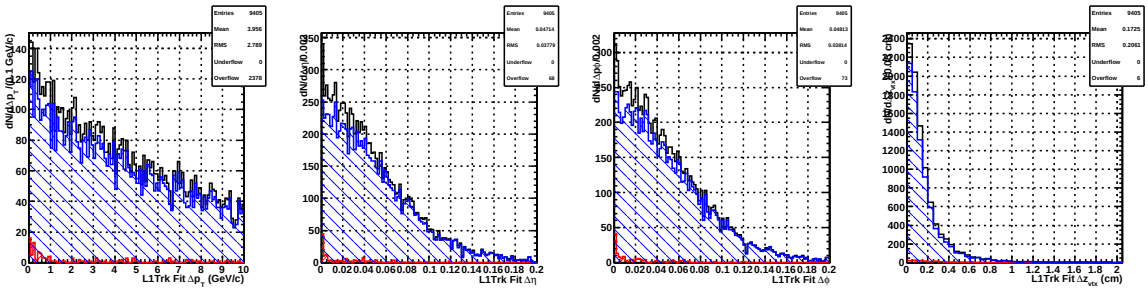

Figure 7.8: Vertex and momentum fit of `L1Tracks` in `PYTHIA6` sample of Standard Model $Z \rightarrow \tau^+\tau^- \rightarrow$ hadrons in pp collisions at $\sqrt{s} = 14$ TeV. From LEFT to RIGHT difference between measured p_T^{L1T}, η^{L1T}, ϕ^{L1T}, and $z_{\mathrm{vtx}}^{\mathrm{L1T}}$ in pairs of `L1Tracks` generated by the same τ and left after duplicate removal. Red distributions describe 1-prong final states, blue distributions describe 3-prongs final states while black ones inculde all hadronic final states.

distribution which is narrower and can keep more than 80% of charged particles within Tracking volume.

For the purpose of the study presented in this Chapter, iterative clustering was used to create at most five clusters of `L1Tracks` matched to the largest-p_T^{L1T} one within $\Delta R < 0.2$. No selection on $z_{\mathrm{vtx}}^{\mathrm{L1T}}$ was applied as isolation from vertexing information is an interesting option to be studied separately. Once a cluster is completed, the procedure is repeated starting from the largest-p_T^{L1T} `L1Track` remaining among the non-clustered ones until either all `L1Tracks` are put into a cluster, either the maximum amount of allowed clusters is built. Moreover, one cluster may be composed of a single `L1Track` if it is the largest-p_T^{L1T} and it is not associated to any other `L1Track` within $\Delta R < 0.2$. Lower cone apertures will be discussed in Section 7.3.3, together with isolation criteria.

After describing the clustering criteria, they must be used "blindfold", without any prior cross check on the τ nature of the employed `L1Tracks`. Figure 7.9 shows the vertex and momentum distributions for the leading `L1Track` in each Tracker τ candidate, analogous tho those pictured in Figure 7.7. Distinction is made between purely underlying-event clusters and clusters with at least one `L1Track` from τ decay and the constraint on the maximum number of clusters to be produced is relaxed. Figure 7.10 includes all the `L1Tracks` for each cluster.

It is interesting to note that the resolution in measurement of `L1Track` vertex in the transverse plane is comparable to the one shown in Figure 7.7 for clusters of `L1Tracks`

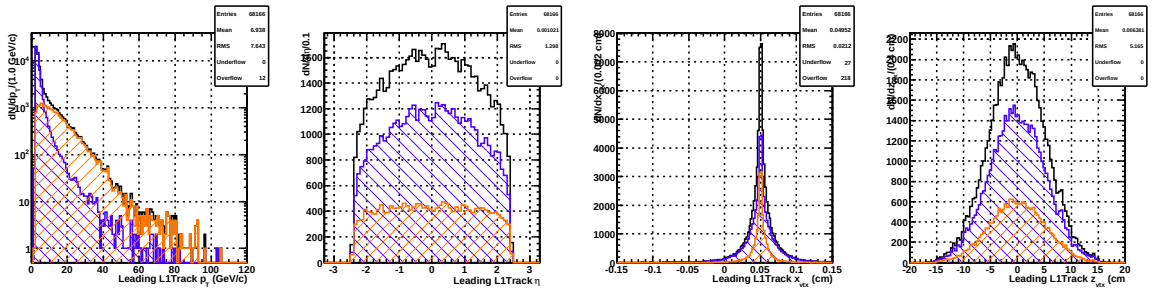

Figure 7.9: Vertex and momentum fit of the largest-p_T^{L1T} `L1Track` in candidate τ clusters in `PYTHIA6` sample of Standard Model $Z \rightarrow \tau^+\tau^- \rightarrow$ hadrons in pp collisions at $\sqrt{s} = 14$ TeV. From LEFT to RIGHT: p_T^{L1T}, η^{L1T}, $x_{\mathrm{vtx}}^{\mathrm{L1T}}$, and $z_{\mathrm{vtx}}^{\mathrm{L1T}}$. Orange distributions describe clusters with a certified τ content in simulations, while navy blue distributions describe underlying event.

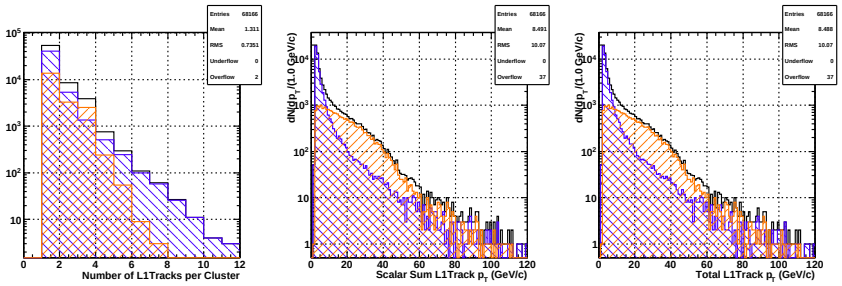

Figure 7.10: Total momentum of candidate τ clusters in `PYTHIA6` sample of Standard Model $Z \rightarrow \tau^+\tau^- \rightarrow$ hadrons in pp collisions at $\sqrt{s} = 14$ TeV. From LEFT to RIGHT: number of `L1Tracks` per candidate τ cluster, scalar sum of transverse momenta of all `L1Tracks` in each candidate, vector sum of transverse momenta of all `L1Tracks` in each candidate. Orange distributions describe clusters with a certified τ content in simulations, while navy blue distributions describe underlying event.

with a certified τ content in simulations. The number of `L1Tracks` included in each cluster is not always limited to three, as tracks from underlying event are selected by the procedure: the fraction of clusters with such a feature is nevertheless negligible with respect to the total sample. If the total momentum of the cluster is measured, there are no remarkable differences between performing a vector sum or a scalar sum of transverse momenta, meaning that all `L1Tracks` inside the cluster are very close in phase space. For this reason, the scalar sum may be preferred as it is easier to compute.

7.3.3 Definition of Isolation Criteria

As already pointed out at the beginning of Section 7.3, the simplest way to include Tracking information in Level 1 Trigger would be to confirm Calorimeter Level 1 Triggers or provide isolation information. To better understand what kind of information is more effective in providing isolation, some test were carried. Each candidate Level 1 Tracker τ is associated to the closest Level 1 Calorimeter τ if their directions, defined respectively by the leading `L1Track` vector and by the Calorimeter Cluster position, are closer in (η, ϕ) than a matching cone radius $\Delta R < R_M$. This defines the Tracker confirmation.

Then, a signal cone of radius R_S and an isolation cone of radius R_I are defined around the Level 1 Tracker τ leading `L1Track`, as in current HLT with full Tracker isolation. The "isolation ring" is the volume defined by the difference between the two cones. Only `L1Tracks` with $p_T^{\mathrm{L1T}} > 2.0$ GeV/c are taken into account in both the signal and isolation cones. Further subsamples may be obtained by selecting only `L1Tracks` whose vertex is closer than 0.5 mm in the transverse plane and/or 5 mm in z to the leading `L1Track` one. These reference distances are obtained from Figures 7.7 and 7.8.

Different combinations of R_M, R_S, and R_I have been tested in order to define some isolation cuts. Figures 7.11 to 7.13 show the scalar sum of transverse momenta of `L1Tracks` included in the signal cone and in the isolation ring of candidate τ's in events of Standard Model Higgs boson production, via gluon fusion in pp collisions at $\sqrt{s} = 14$ TeV, with $m_H = 120$ GeV/c^2, at luminosities corresponding to 100 superimposed minimum-bias events per bunch crossing. A straightforward comparison of p_T^{L1T} scalar sum, with different restriction on the vertexes of the selected `L1Tracks`, shows that nearly all the signal is preserved if distance in the transverse plane from the leading `L1Track` vertex is required to be less than 0.5 mm, or distance along z is required to be less than 5 mm. On the other hand, the contribution of tracks within the isolation ring is strongly reduced by a selection on $z_{\mathrm{vtx}}^{\mathrm{L1T}}$. Moreover, a sharp peak at 4 GeV/c appears in the scalar sum of p_T^{L1T} within the isolation ring, corresponding to the inclusion of a second `L1Track` in the isolation ring.

Two main options have been chosen to define isolation criteria, on the basis of the previous observations:

- **vertex isolation** – as the strong track rejection in the isolation ring comes from z association, the number of `L1Tracks` in the isolation ring with $z_{\mathrm{vtx}}^{\mathrm{L1T}}$ closer than 5 mm

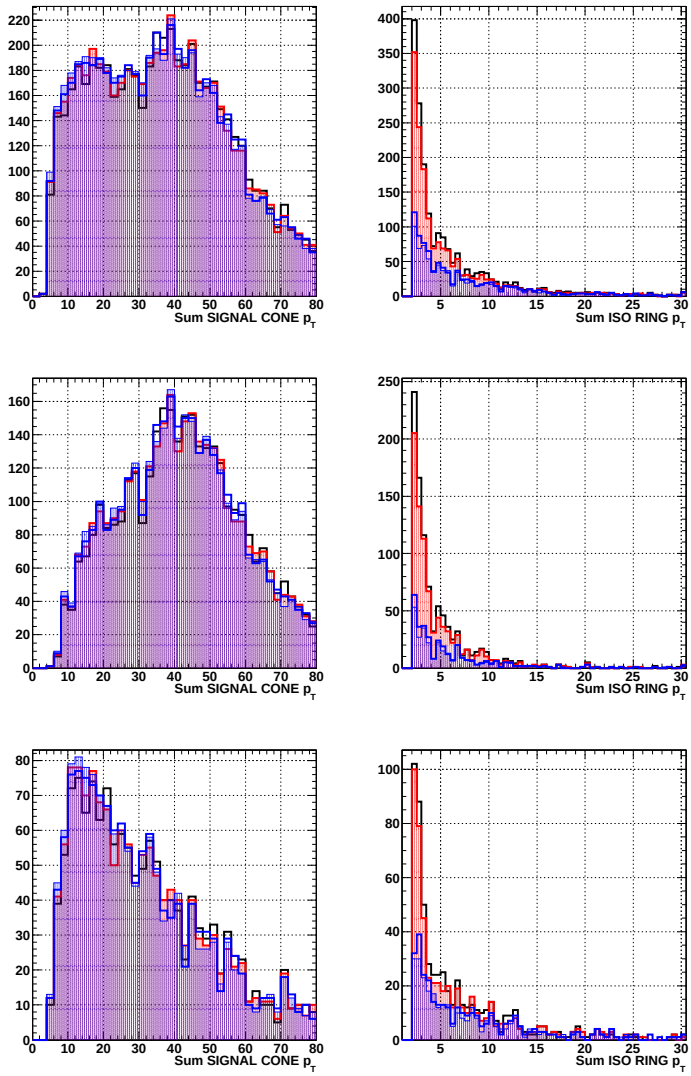

Figure 7.11: Comparison of `L1Track` contribution to the signal cone and to the isolation cone in events of Standard Model Higgs boson production, via gluon fusion in pp collisions at $\sqrt{s}$ = 14 TeV, with m_H = 120 GeV/c^2, at luminosities corresponding to 100 superimposed minimum-bias events per bunch crossing: scalar sum of `L1Track` transverse momenta in the signal cone (LEFT) and in the isolation ring (RIGHT), with R_M = 0.16, R_S = 0.10, and R_I = 0.20. Black histogram includes all the selected `L1Tracks`, red thick histogram is produced with the subsample of `L1Tracks` whose vertex is closer than 0.5 mm to the leading `L1Track` one in the transverse plane, blue thick histogram is produced with the subsample of `L1Tracks` whose vertex is closer than 5 mm in z to the leading `L1Track`, and blue-filled histogram combines the two selections on `L1Track` vertex. TOP row includes all the candidates, MIDDLE row includes only the candidates with the largest leading `L1Track` p_T, BOTTOM row includes only the candidates with the second largest leading `L1Track` p_T.

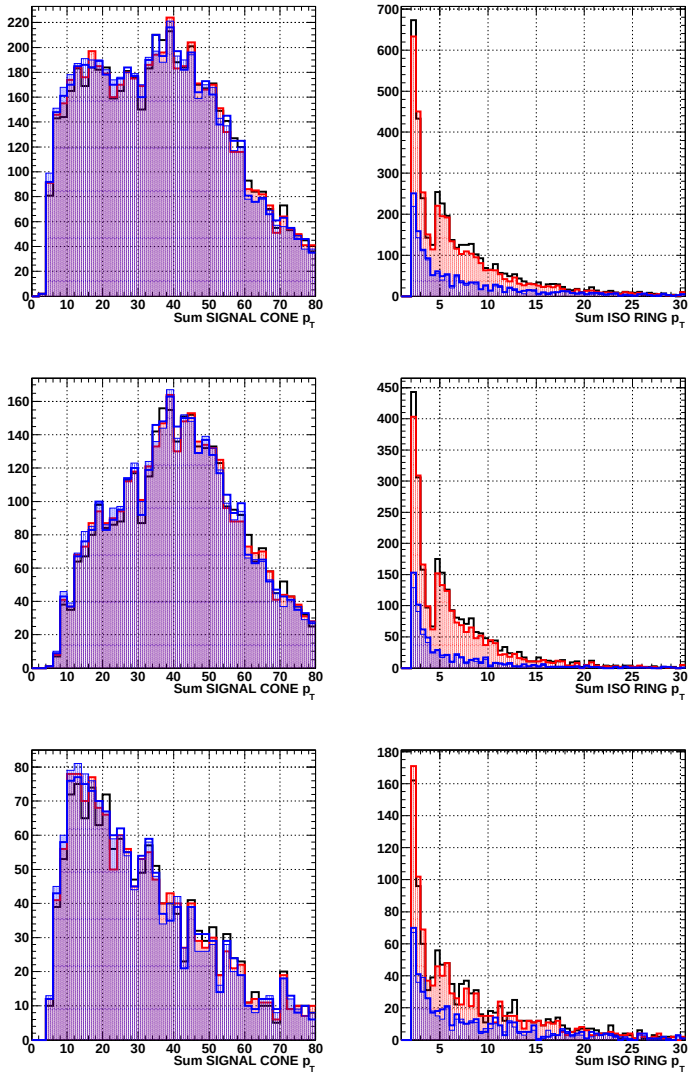

Figure 7.12: Comparison of `L1Track` contribution to the signal cone and to the isolation cone in events of Standard Model Higgs boson production, via gluon fusion in pp collisions at $\sqrt{s}$ = 14 TeV, with m_H = 120 GeV/c^2, at luminosities corresponding to 100 superimposed minimum-bias events per bunch crossing: scalar sum of `L1Track` transverse momenta in the signal cone (LEFT) and in the isolation ring (RIGHT), with R_M = 0.16, R_S = 0.10, and R_I = 0.40. Black histogram includes all the selected `L1Tracks`, red thick histogram is produced with the subsample of `L1Tracks` whose vertex is closer than 0.5 mm to the leading `L1Track` one in the transverse plane, blue thick histogram is produced with the subsample of `L1Tracks` whose vertex is closer than 5 mm in z to the leading `L1Track`, and blue-filled histogram combines the two selections on `L1Track` vertex. TOP row includes all the candidates, MIDDLE row includes only the candidates with the largest leading `L1Track` p_T, BOTTOM row includes only the candidates with the second largest leading `L1Track` p_T.

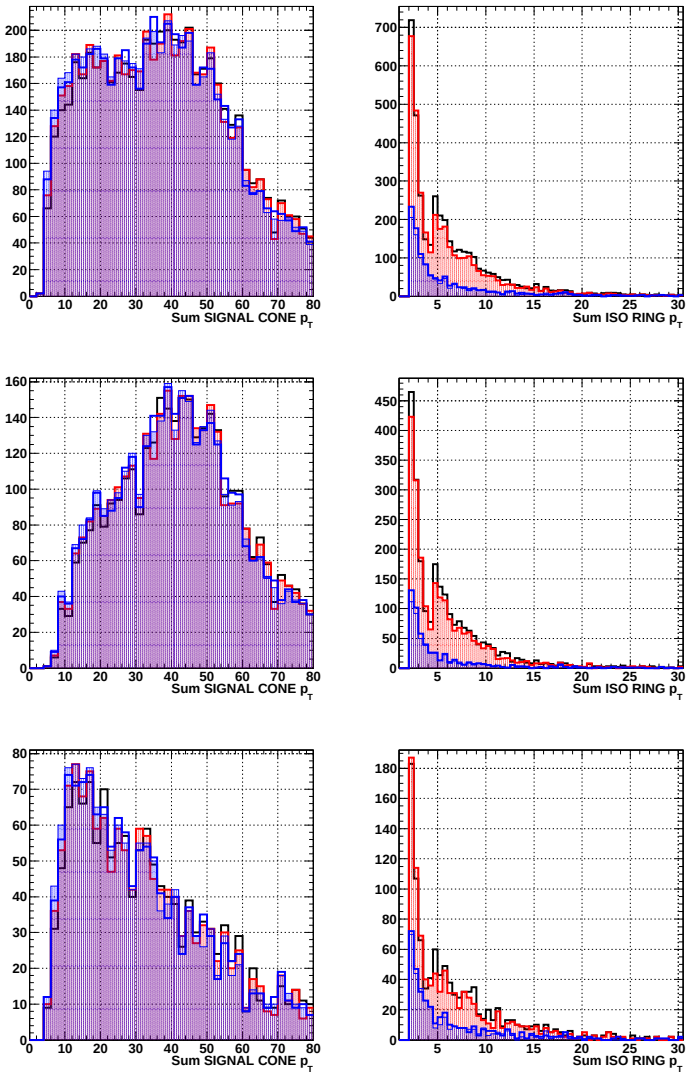

Figure 7.13: Comparison of `L1Track` contribution to the signal cone and to the isolation cone in events of Standard Model Higgs boson production, via gluon fusion in pp collisions at $\sqrt{s}$ = 14 TeV, with m_H = 120 GeV/c^2, at luminosities corresponding to 100 superimposed minimum-bias events per bunch crossing: scalar sum of `L1Track` transverse momenta in the signal cone (LEFT) and in the isolation ring (RIGHT), with R_M = 0.16, R_S = 0.16, and R_I = 0.40. Black histogram includes all the selected `L1Tracks`, red thick histogram is produced with the subsample of `L1Tracks` whose vertex is closer than 0.5 mm to the leading `L1Track` one in the transverse plane, blue thick histogram is produced with the subsample of `L1Tracks` whose vertex is closer than 5 mm in z to the leading `L1Track`, and blue-filled histogram combines the two selections on `L1Track` vertex. TOP row includes all the candidates, MIDDLE row includes only the candidates with the largest leading `L1Track` p_T, BOTTOM row includes only the candidates with the second largest leading `L1Track` p_T.

to the vertex of the leading `L1Track` is required to be zero

- **momentum isolation** – the scalar sum of transverse momenta in the isolation ring should be less than 4 GeV/c to exclude any contribution of a second `L1Track` in the isolation ring

7.3.4 Efficiency on Signal and Background Rate

The effects of the introduction of Tracker confirmation and isolation on background rate have been studied in samples corresponding to different luminosities at 40 MHz bunch crossing and 0.8 fill rate. LHC luminosity, namely 25 pile-up, is compared to Phase 1 luminosity, namely 50 pile-up, and a plausible value of Phase 2 luminosity, up to 150 pile-up, corresponding to $\mathcal{L} \approx 7 \cdot 10^{34}$ cm^{-2}s^{-1}.

The best combination of R_M, R_S, and R_I should be chosen according to the best background rate reduction achievable. In fact, a larger value of R_M implies a larger background rate after Tracker confirmation of Calorimeter candidate. Moreover, both the ratio between R_S and R_I and their values do contribute to the achievement of isolation criteria. It is worth to take into account some examples of these effects, and Phase 1 luminosities are presented as main reference.

Figure 7.14 shows the effect of R_M: the larger value of R_M allows a larger rate of Tracker-confirmed Calorimeter candidates at low transverse energies. As any threshold would be set at E_T values larger than 10 GeV, the value of R_M may affect only efficiency on signal.

The effect of R_S and R_I cannot be separated, as isolation is defined with respect to the difference between the two cones. Figure 7.15 shows the combined effect of signal and isolation cone: the largest values of R_I of course would reduce the background rate, as both the requirements of vertex-isolation and momentum-isolation must be satisfied on a larger volume. Another interesting observation can be made on the relative size of the two radii. In fact, the isolation volume is defined as the difference between isolation and signal cones: a larger signal cone would result into a smaller isolation ring if the size of the latter is unchanged. The best reduction rate is achieved with a small signal cone and a large isolation cone.

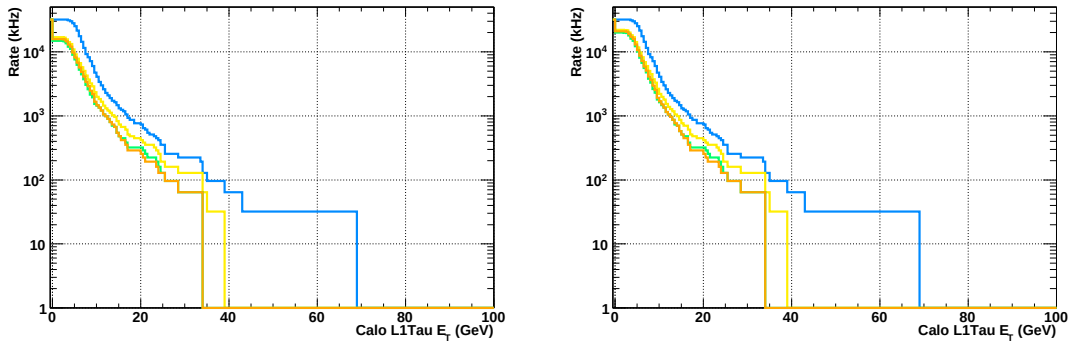

Figure 7.14: Effect of R_M on background rate at Phase 1 luminosities, in terms of accepted bunch crossing per second at Level 1, as a function of Calorimeter Level 1 candidate τ's E_T. Blue line represents the background rate if only Calorimeter Level 1 object are used, dark yellow line includes confirmation with a candidate from Tracker, green line includes confirmation with a vertex-isolated Tracker candidate, and orange line includes confirmation with a momentum-isolated Tracker candidate. LEFT side makes use of $R_M = 0.16$, $R_S = 0.10$, and $R_I = 0.20$, while RIGHT one makes use of $R_M = 0.20$, $R_S = 0.10$, and $R_I = 0.20$.

Tables 7.1 to 7.4 report the approximated E_T threshold that should be applied to Calorimeter Level 1 candidate τ's in order to keep the background rate at 100 kHz for different combinations of R_M, R_S, and R_I, different luminosities, and different integrations of Tracker with Calorimeter information to select candidate τ's. The best data rate reduction, which corresponds to lower thresholds, is the one that can be achieved with $R_S = 0.10$ and $R_I = 0.40$ for most of the studied luminosities.

			100 kHz E_T threshold (GeV)			
R_M	R_S	R_I	CAL	+TRK	+TRK+z-ISO	+TRK+p_T-ISO
0.16	0.10	0.20	35	30	16	19
0.20	0.10	0.20	35	30	16	19
0.16	0.16	0.20	35	30	20	30
0.20	0.16	0.20	35	30	16	19
0.16	0.10	0.40	35	30	14	16
0.20	0.10	0.40	35	30	14	16
0.16	0.16	0.40	35	30	18	30
0.20	0.16	0.40	35	30	18	30

Table 7.1: Comparison of approximate thresholds on Calorimeter Level 1 τ candidate E_T corresponding to background rate of 100 kHz in the scenario with 25 superimposed events per bunch crossing.

The other important feature of any trigger, besides background rate, is the efficiency

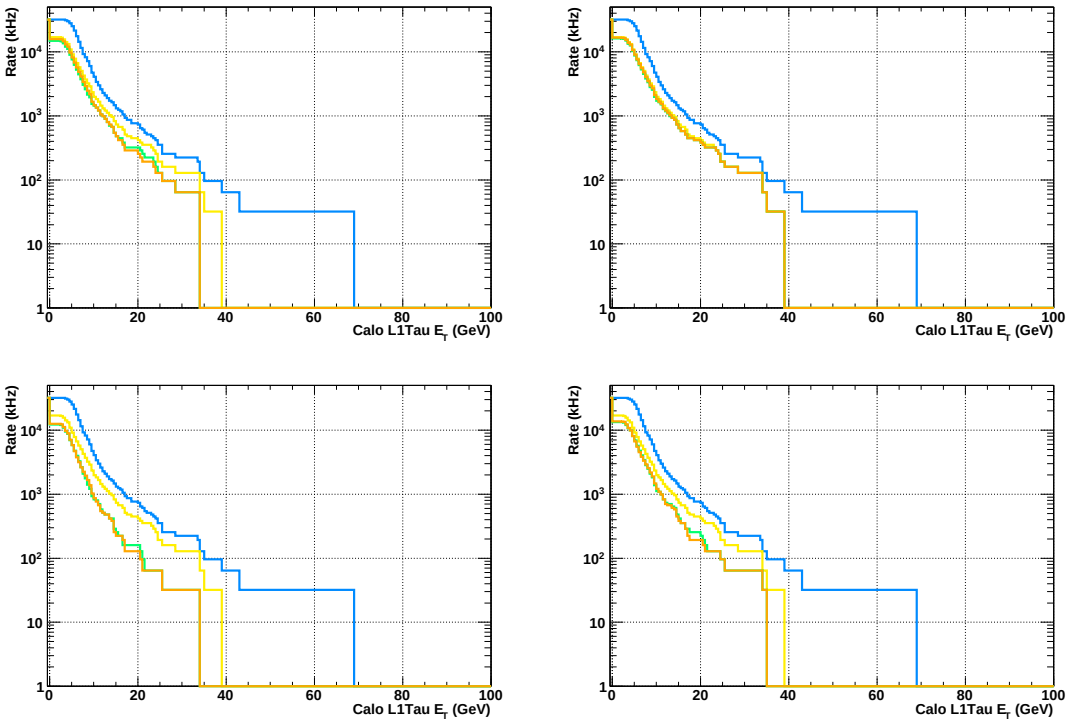

Figure 7.15: Effect of R_S and R_I on background rate at Phase 1 luminosities, in terms of accepted bunch crossing per second at Level 1, as a function of Calorimeter Level 1 candidate τ's E_T. Blue line represents the background rate if only Calorimeter Level 1 object are used, dark yellow line includes confirmation with a candidate from Tracker, green line includes confirmation with a vertex-isolated Tracker candidate, and orange line includes confirmation with a momentum-isolated Tracker candidate. TOP row: LEFT side makes use of $R_M = 0.16$, $R_S = 0.10$, and $R_I = 0.20$, while RIGHT one makes use of $R_M = 0.16$, $R_S = 0.16$, and $R_I = 0.20$. BOTTOM row: LEFT side makes use of $R_M = 0.16$, $R_S = 0.10$, and $R_I = 0.40$, while RIGHT one makes use of $R_M = 0.16$, $R_S = 0.16$, and $R_I = 0.40$.

on the kind of signal it is supposed to select. For this purpose, different `PYTHIA6` samples of Standard Model Higgs boson production, via gluon fusion in pp collisions at $\sqrt{s} = 14$ TeV, were simulated and superimposed to minimum-bias events according to different luminosities. Higgs boson mass is set to $m_H = 120\,\mathrm{GeV}/c^2$. For each luminosity, a threshold close to the one corresponding to 100 kHz background rate is imposed to the candidate τ. The procedure is repeated for each Calorimeter/Tracker combination taken into account, using $R_M = 0.16$, $R_S = 0.10$, and $R_I = 0.40$. The proper threshold is imposed for each Calorimeter/Tracker combination. Efficiencies are shown in Figures **[VERIFICA]** . All simulated τ's within acceptance contribute to the denominator, while those matched within $\Delta R < 0.3$ to the Calorimeter candidate are used in the numerators.

			100 kHz E_T threshold (GeV)			
R_M	R_S	R_I	CAL	+TRK	+TRK+z-ISO	+TRK+p_T-ISO
0.16	0.10	0.20	40	35	25	25
0.20	0.10	0.20	40	35	25	25
0.16	0.16	0.20	40	35	35	35
0.20	0.16	0.20	40	35	35	35
0.16	0.10	0.40	40	35	21	21
0.20	0.10	0.40	40	35	21	21
0.16	0.16	0.40	40	35	25	25
0.20	0.16	0.40	40	35	25	25

Table 7.2: Comparison of approximate thresholds on Calorimeter Level 1 τ candidate E_T corresponding to background rate of 100 kHz in the scenario with 50 superimposed events per bunch crossing.

			100 kHz E_T threshold (GeV)			
R_M	R_S	R_I	CAL	+TRK	+TRK+z-ISO	+TRK+p_T-ISO
0.16	0.10	0.20	45	45	38	38
0.20	0.10	0.20	45	45	38	38
0.16	0.16	0.20	45	45	38	45
0.20	0.16	0.20	45	45	38	45
0.16	0.10	0.40	45	45	35	20
0.20	0.10	0.40	45	45	35	25
0.16	0.16	0.40	45	45	38	28
0.20	0.16	0.40	45	45	38	30

Table 7.3: Comparison of approximate thresholds on Calorimeter Level 1 τ candidate E_T corresponding to background rate of 100 kHz in the scenario with 100 superimposed events per bunch crossing.

The presented background rates and Trigger efficiencies are the very first result of the integration of a Tracking Trigger with the Calorimeter Trigger, at Level 1, that makes use of more complex objects than stubs. The background rate reduction that can be achieved with `L1Track`-based isolation criteria is encouraging, particularly at lower Phase 2 luminosities $\mathcal{L} \approx 5 \cdot 10^{34}$ cm^{-2}s^{-1}. The stronger reduction can be obtained with momentum-based isolation, however this kind of isolation shows a drawback in terms of a loss of efficiency on the signal of about 30%. Therefore a vertex-based isolation is recommended as it allows lower thresholds than purely Calorimeter candidates do, with a signal efficiency raising up to 80%.

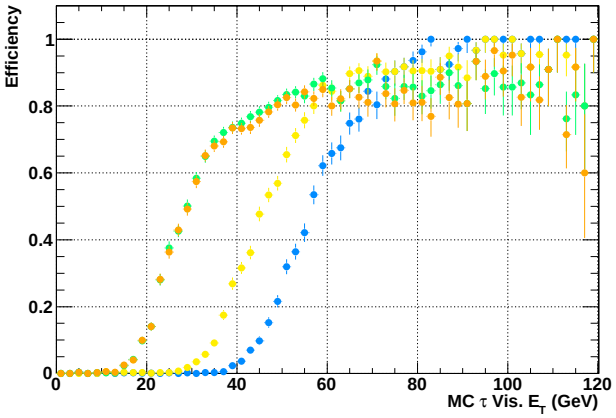

Figure 7.16: Efficiency of τ triggering in a PYTHIA6 sample of Standard Model Higgs boson production, via gluon fusion in pp collisions at $\sqrt{s}$ = 14 TeV, with m_H = 120 GeV/c^2, at luminosities corresponding to 25 superimposed minimum-bias events per bunch crossing. Blue points represent selection based only on Calorimeter Level 1 objects with E_T^{Cal} = 40 GeV, dark yellow points include confirmation with a candidate from Tracker with E_T^{Cal} = 30 GeV, green points include confirmation with a vertex-isolated Tracker candidate with E_T^{Cal} = 15 GeV, and orange points include confirmation with a momentum-isolated Tracker candidate with E_T^{Cal} = 15 GeV. Radii of cones used in the algorithm are R_M = 0.16, R_S = 0.10, and R_I = 0.40.

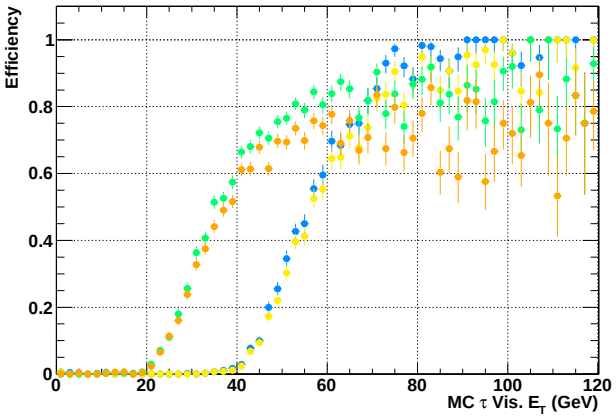

Figure 7.17: Efficiency of τ triggering in a PYTHIA6 sample of Standard Model Higgs boson production, via gluon fusion in pp collisions at $\sqrt{s}$ = 14 TeV, with m_H = 120 GeV/c^2, at luminosities corresponding to 50 superimposed minimum-bias events per bunch crossing. Blue points represent selection based only on Calorimeter Level 1 objects with E_T^{Cal} = 40 GeV, dark yellow points include confirmation with a candidate from Tracker with E_T^{Cal} = 40 GeV, green points include confirmation with a vertex-isolated Tracker candidate with E_T^{Cal} = 20 GeV, and orange points include confirmation with a momentum-isolated Tracker candidate with E_T^{Cal} = 20 GeV. Radii of cones used in the algorithm are R_M = 0.16, R_S = 0.10, and R_I = 0.40.

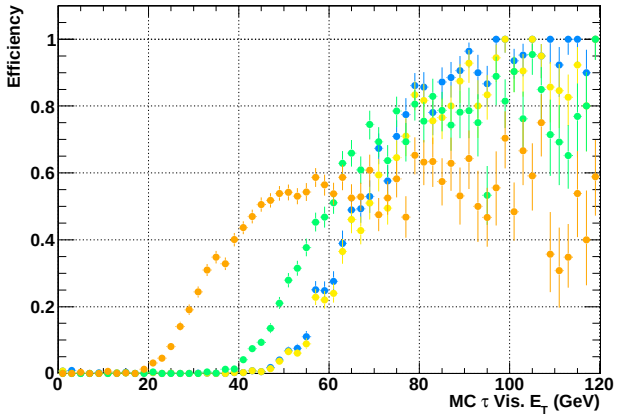

Figure 7.18: Efficiency of τ triggering in a PYTHIA6 sample of Standard Model Higgs boson production, via gluon fusion in pp collisions at $\sqrt{s}$ = 14 TeV, with m_H = 120 GeV/c^2, at luminosities corresponding to 100 superimposed minimum-bias events per bunch crossing. Blue points represent selection based only on Calorimeter Level 1 objects with E_T^{Cal} = 50 GeV, dark yellow points include confirmation with a candidate from Tracker with E_T^{Cal} = 50 GeV, green points include confirmation with a vertex-isolated Tracker candidate with E_T^{Cal} = 40 GeV, and orange points include confirmation with a momentum-isolated Tracker candidate with E_T^{Cal} = 20 GeV. Radii of cones used in the algorithm are R_M = 0.16, R_S = 0.10, and R_I = 0.40.

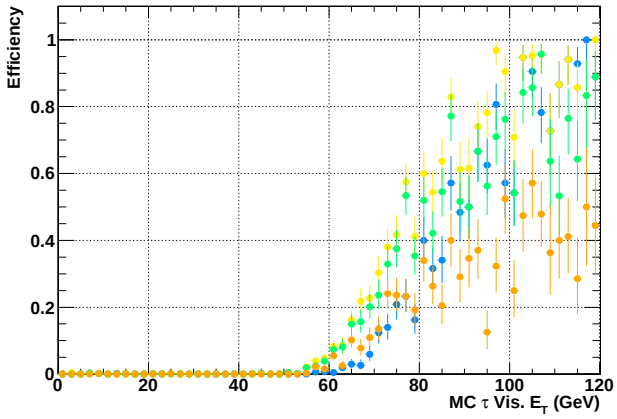

Figure 7.19: Efficiency of τ triggering in a PYTHIA6 sample of Standard Model Higgs boson production, via gluon fusion in pp collisions at $\sqrt{s}$ = 14 TeV, with m_H = 120 GeV/c^2, at luminosities corresponding to 150 superimposed minimum-bias events per bunch crossing. Blue points represent selection based only on Calorimeter Level 1 objects with E_T^{Cal} = 70 GeV, dark yellow points include confirmation with a candidate from Tracker with E_T^{Cal} = 60 GeV, green points include confirmation with a vertex-isolated Tracker candidate with E_T^{Cal} = 60 GeV, and orange points include confirmation with a momentum-isolated Tracker candidate with E_T^{Cal} = 60 GeV. Radii of cones used in the algorithm are R_M = 0.16, R_S = 0.10, and R_I = 0.40.

			100 kHz E_T threshold (GeV)			
R_M	R_S	R_I	CAL	+TRK	+TRK+z-ISO	+TRK+p_T-ISO
0.16	0.10	0.20	70	60	60	60
0.20	0.10	0.20	70	60	60	60
0.16	0.16	0.20	70	60	60	60
0.20	0.16	0.20	70	60	60	60
0.16	0.10	0.40	70	60	55	60
0.20	0.10	0.40	70	60	55	60
0.16	0.16	0.40	70	60	55	60
0.20	0.16	0.40	70	60	55	60

Table 7.4: Comparison of approximate thresholds on Calorimeter Level 1 τ candidate E_T corresponding to background rate of 100 kHz in the scenario with 150 superimposed events per bunch crossing.

Concluding Remarks and Outlook

The forthcoming decade of the operations of the CERN Large Hadron Collider will bring exciting challenges to the particle physics community. The LHC scientific program will be enhanced by the increase in available energy, from the current $\sqrt{s} = 7$ TeV to the designed $\sqrt{s} = 14$ TeV. This will allow us to achieve a confident awareness of the experimental apparatus and, hopefully, to reach also a deeper understanding of the behavior of Nature. This period will be crucial in setting up for the further challenge represented by the breaking of the luminosity frontier with the planned upgrades of the LHC injection chain and LHC strong focussing optics.

A luminosity increase of about one order of magnitude puts some major constraints on the performance of the Compact Muon Solenoid detector, in particular on its Tracking system. The current CMS Silicon Pixel Detector and Silicon Strip Tracker should be replaced by novel detectors to cope with the strict requirements that arise by just doubling the design luminosity. These requirements can be expressed in terms of radiation tolerance at short distances from the beamline, where the hadron fluence is larger, as well as vertexing capabilities to ensure highly efficient track seeding. When the LHC is be pushed to even higher luminosities, the current Level 1 Trigger strategies could not withstand the enormous data rate unless thresholds are increased to such high values that all interesting processes are rejected by the Trigger system. The most attractive alternative is to include Tracking information at Level 1 in order to ensure that data rate can be easily handled.

Two possible approaches for the introduction of Tracking information at Level 1 Trigger, and reject low-p_T tracks, have been described. The first one, based on the measurement of the width of charge deposition in a silicon sensor by tracks with large impact angle, was proven to be, thanks to measurements performed on novel prototypes of Monolithic Arrays of Pixel Sensors, beyond powering, computing and financial re-

sources of the experiment.

The second approach is based on pattern correlation between hits in closely separated sensors, which allows a rough measurement of track direction and p_T. These Trigger Modules are currently envisaged to be the best candidates for Tracking Trigger in the future at CMS. The Long Barrel concept Tracker layout has been described, as well as the Trigger primitives, called stubs, that can be obtained from pattern hit correlation in Trigger Modules. These stubs can be combined into tracklets that can be furtherly expanded to longer chains of stubs that compose Level 1 Trigger tracks. The ongoing project to implement these objects in a real hardware Trigger system have been described as well as corresponding simulation tools within the CMS framework.

In particular, the effects of Tracker geometry, of single hit resolution along z, and of beam positioning in the transverse plane have been investigated and turned out to be relevant for low-p_T tracks. The chosen approach is the one that best fits any track and it has been used to produce a first definition and construction of Level 1 tracks at simulation level. Also these Level 1 tracks have been treated without the strong assumptions of straight line trajectory approximation. Even if the chosen strategy may be not be managed by a hardware implementation of Level 1 Tracking, the described approach is capable to put emphasis on the major problems that may arise, after further simplifications, in terms of Tracking efficiency or fake rate.

The tools developed and described in this thesis have then been succesfully tested in simulations of a Level 1 Trigger aiming at the selection of τ leptons. The proposed integration of Tracking Trigger to Level 1 Calorimeter Trigger was inspired by the current τ Trigger and preliminary tests, on simulated events at high luminosity, showed that the benefits brought by the integration of Tracker and Calorimeter at Level 1 are remarkable and encouraging. This work will be hopefully expanded in the future, together with the improvements in the design of the new Tracker layout.

The main results presented in this thesis, the experimental proof of the unlikely feasability of low-p_T track rejection with cluster width, and the progress in simulation studies for Level 1 Tracking and it applications to final states with τ leptons, can be truly seen as a milestone in the path towards the design and production of a new Tracker, for the CMS experiment, with Trigger capabilities already at Level 1.

A. Fast Simulation of the CMS Tracker

In order to make sense of the data and search for new physics phenomena, accurate and precise MonteCarlo simulations of the detector are needed. Two different types of simulation are used by the CMS collaboration: a `Geant4` simulation, known as the "Full" Simulation, and a detector model which uses simplified geometry, response evaluation and pattern recognition to decrease the processing time per event, the "Fast" Simulation [83]. `FastSimulation` and Tracking inside its framework are briefly described herein.

With complex events taking minutes to simulate, the `FullSimulation` cannot keep up with the data rate. At 100-1000 times faster per event, the `FastSimulation` is the only way to produce large statistic data sets necessary for studying background processes and systematic errors. Using intuitive detector parameters as inputs, either data-driven or derived from the `FullSimulation`, the `FastSimulation` can quickly and easily be tuned to reproduce the data. Not to be underestimated, this feature will allowed the data to be understood more quickly during the start up.

`FastSimulation` is only a simulation of the CMS detector and not of the physics during the collision, therefore simulated particle decays produced by event generators such as `PYTHIA` are used as inputs. The resulting particles are then propagated through the detector and all physically relevant material effects are included in the `FastSimulation`. As one of the main goals of the `FastSimulation` is to produce analysis-grade simulated data, the output is designed to be completely accessible to CMS users, containing objects with the same format as the standard offline reconstruction. Additional realism is brought by in-time pile-up, emulations of the Level 1 and High Level Triggers, and mis-calibration and misalignment of the detector.

The propagation of the particles through the layers of the tracker is modeled taking into account five different material effects: bremsstrahlung, photon conversions, multi-

ple Coulomb scattering, energy loss through ionization and nuclear interactions. All of the effects except for nuclear interactions are calculated analytically. Nuclear interactions are simulated calculating their probabilities from cross section tables. The kinematics of the resulting daughter particles are derived from single particle collisions using a particle gun. To save time simulating the material effects, the Tracker uses a simplified geometry of nested cylindrical layers, as shown in Figures A.1 and A.2 for the current CMS Tracker and the Long Barrel concept Tracker. The thicknesses of the different layers are tuned to create the same amount of material interactions as in the `FullSimulation`.

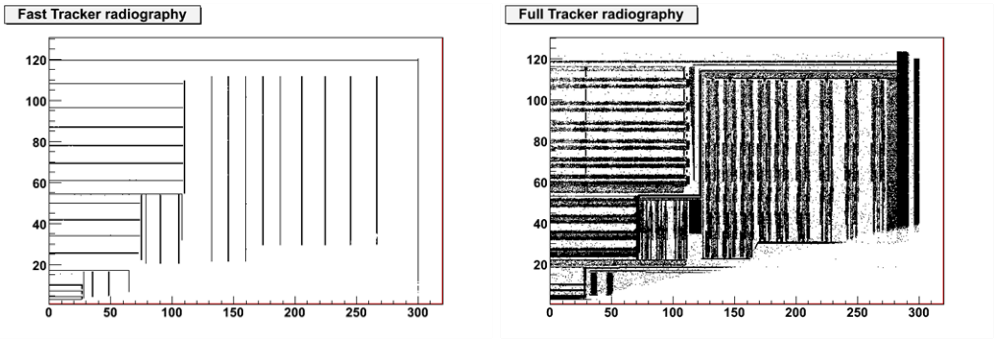

Figure A.1: Radiography of the CMS Tracker with photon pair conversions from electrons with `FastSimulation` (LEFT) and `FullSimulation` (RIGHT) [88].

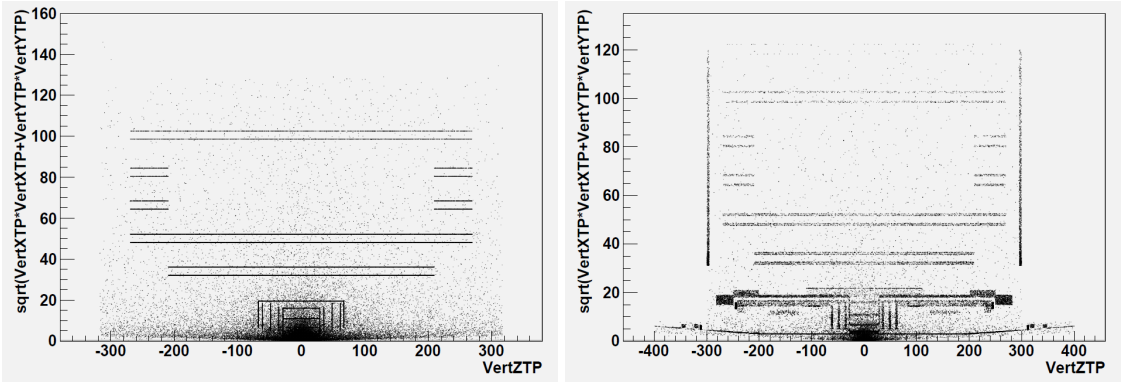

Figure A.2: Radiography of the Long Barrel concept Tracker with pion production vertexes in minimum-bias events with `FastSimulation` (LEFT) and `FullSimulation` (RIGHT) [89]. Courtesy of E. Salvati, Cornell University.

The base of the tracking simulation is the reconstructed hits. The local position resolution and efficiencies of the hits are currently parameterized with input from the `FullSimulation`, and in the future they will be parameterized to match data. For the

silicon strip tracker, the local positions are smeared according to a gaussian. The parameterization for the pixel detectors is more complicated, and depends on histograms derived from the `FullSimulation`, which make use of both the angle of incidence and the multiplicity of the pixel clusters. To make tracks, the `FastSimulation` emulates the different steps of the standard iterative tracking sequence, using only the hits from the simulated tracks to make track candidates. Therefore, each reconstructed track corresponds to a simulated track. For the seeding emulation, only seeds that pass the standard seeding criteria are included. The standard pattern recognition algorithms are too time consuming for the `FastSimulation`. Like the standard pattern recognition tracking, the `FastSimulation` removes hits that give large contributions to the track χ^2 from the tracks. The final tracking step uses the same fitting algorithms as the standard reconstruction sequence. High occupancy events may have fake tracks, which are not produced by the `FastSimulation`. Hit sharing between different tracks is also not included in the `FastSimulation`. For specialized studies, a translation algorithm allow the reconstructed hits made with the `FastSimulation` to be input into the full pattern recognition chain.

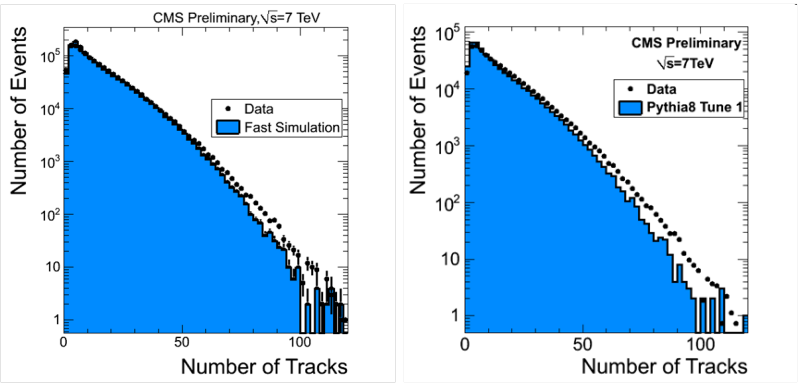

Figure A.3: Comparison of `FastSimulation` tracking performance to data collected at $\sqrt{s} = 7$ number of reconstructed tracks in data to `FastSimulation` (LEFT) and `FullSimulation` (RIGHT). All track distributions are normalized by the number of tracks and overflows (underflows) are included in the last (first) bins [90].

Figures A.3 to A.5 show a comparison of `FastSimulation` tracking performance, obtained with the current CMS Tracker on 10^7 minimum bias events at $\sqrt{s} = 7$ TeV and including realistic detector conditions for alignment and calibrations, to data collected during 2010 at the same center-of-mass energy. Only high purity tracks with $p_T > 5$ GeV/c and $\Delta p_T/p_T < 0.05$ are taken into account. All track distributions are normalized

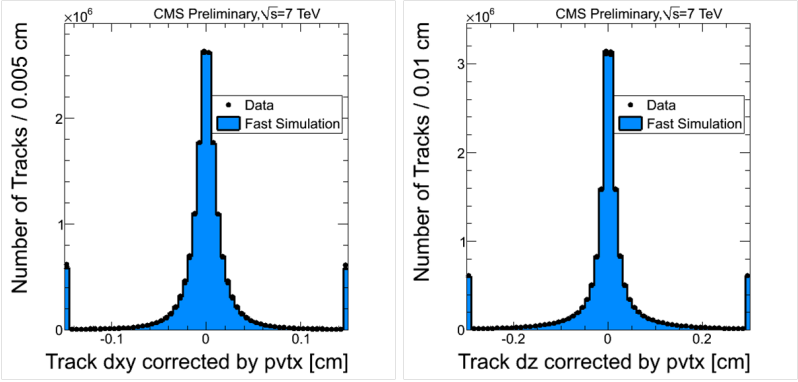

Figure A.4: Comparison of `FastSimulation` tracking performance to data collected at $\sqrt{s} = 7$: vertexing in transverse plane (LEFT) and along z (RIGHT). All track distributions are normalized by the number of tracks and overflows (underflows) are included in the last (first) bins [90].

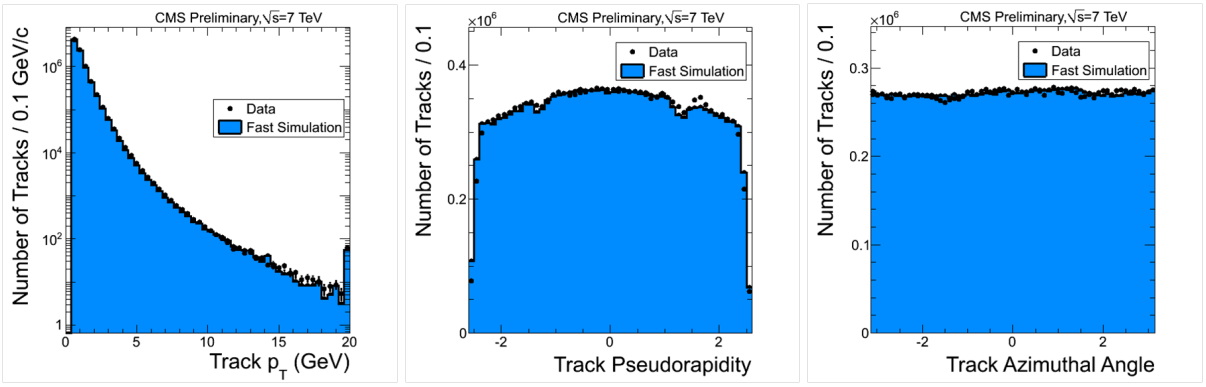

Figure A.5: Comparison of `FastSimulation` tracking performance to data collected at $\sqrt{s} = 7$: from LEFT to RIGHT, momentum reconstruction in terms of p_T, η and ϕ. All track distributions are normalized by the number of tracks and overflows (underflows) are included in the last (first) bins [90].

by the number of tracks and overflows (underflows) are included in the last (first) bins.

In order to understand the differences between the two simulations, for the purpose of high luminosity studies, it is useful to focus on single particle events, in particular charged pions whuch are produced copiously in minimum bias interactions [84]. Studies with a small sample of 1000 pions with $p_T = 500$ MeV/c within the Tracking volume allowed to understand the source of the difference in `SimHit` rate between `FastSimulation` and `FullSimulation`, already described in Section 5.1. Table A.1 shows the number of `SimHits` produced in the inner Stack Member of the first Stack of the Long Barrel concept Tracker, for both `FastSimulation` and `FullSimulation`.

	$\|\eta\| < 2.5$		$\|\eta\| > 2.5$	
particle	FullSim	FastSim	FullSim	FastSim
inclusive	5781	2779	892	27
π^+	2565	2133	212	19
e^-	1769	1	327	0
μ^+	864	641	13	0
p	305	1	115	5
e^-	141	3	103	0
π^-	77	0	65	3
μ^-	25	0	42	0
γ	33	0	0	0
n	2	0	1	0

Table A.1: Number of SimHits registered in the inner Stack Member of the innermost Stack of the Long Barrel concept Tracker for both FullSimulation and FastSimulation from samples of 1000 single pion events. The first row is the total number of SimHits, whereas the following rows are the numbers of SimHits generated by different particles. The second and third columns are obtained with pions generated in the region $|\eta| < 2.5$; the last two columns are from pions generated in the region $2.5 < |\eta| < 5.5$. All pions are generated with $p_T = 500$ MeV/c [84].

The difference in SimHits number is consistent with the effect already described in Section 5.1. It is clear that there are some effects not present in the FastSimulation. The main difference is due to electrons – which constitute about 30% of SimHits in the FullSimulation – which have only one SimHit in the reported study with the FastSimulation. The number of positron SimHits is much smaller than the electron one, indicating the presence of δ-rays in the FullSimulation. The second highest contribution is that of pions and protons, which indicate that the FastSimulation does not properly take into account some nuclear interactions. Another possible explanation to this deficiency of hits is that the entire tracker material is replaced by a cylinder such that the material effects are overall correctly simulated. With such an approximation, the actual geometrical location of active material is not taken into account, which might lead to missing SimHits in the FastSimulation. These results have been confirmed by other studies with single particles, including electrons, muons, neutrons, and photons.

B. Hardware Implementation of Level 1 Tracking Trigger

The work described in this thesis makes a wide use of the Long Barrel concept Tracker which is the baseline of a joint effort between Fermilab and Brown University aiming at designing a strategy to match stubs to each other [91]. The described design includes the ability to read out events at the same time as gathering the trigger data. The proposed Tracking system is based on Superlayers 0, 1 and 4 of the Long Barrel Tracker and employs 24 sectors arranged as projective towers. Each sector, 15° wide, has a readout organized to avoid information being split across sector boundaries and consists in one Ladder for the innermost Double Stack, two Ladders in the intermediate one and four in the outermost one. With a maximum radius of 1.1 m, the minimum p_T that can be evaluated within a 15° opening angle is 2.4 GeV/c, which is reasonably similar to the threshold used throughout this thesis.

Data from Stacks are sent to an optical transceiver and to off-detector processing electronics which assembles stubs into tracklets. Tracklet vectors are then used to project the track to the remaining four Layers to search for other stubs and compare with allowed patterns. Resulting Level 1 tracks are sent to the Level 1 Trigger for further processing and use. The design is based on Field Programmable Gate Arrays (FPGAs) as they can be programmed to evaluate several combinations at the same time. Another option would be the use of Content Addressable Memories (CAMs), which made great progress in the last few years, but are more difficult to program. The major limit to this design is the number of hits that can be simultaneously evaluated and compared by a single FPGA. As commercially available FPGAs feature approximately half a million logic cells, and the number of combinations to be compared is likely to be much larger, the proposed design divides each 15° sector into independent subsections.

Much of the front end electronics will be located between two sensors, emphasising capacitive effects between Stacks. For this reason it is very important to minimize the high frequency signals in the front end chips. This design is based on self clocking micro pipelines so the only clock going to the chips is the bunch crossing one. The trigger is embedded in this clock by a single phase reversal similar to the one currently used in CMS. All timing signals are derived from this clock. All circuits operate asynchronously after being triggered.

B.1 Transfer Hits and Stub Formation

Simulation studies, making use of clustering algorithms similar to the `broadside` one described in Section 5.1, showed that the expected number of Clusters per sensor per bunch crossing is approximately 50, while the one of stubs above the 2.4 GeV/c p_T threshold is about 6. Each chip must process, on average, only 1/30 of them as there are 30 chips per sensor in the proposed design. Fast asynchronous pipelines are needed to move data between chips and the design must be robust so that a single failure will not affect other chips than the one which failed. A candidate design, the MOUSETRAP pipeline, consisting of transparent latches and and exlusive NOR gate, has already been identified [92]. Each step in the pipeline is 25 ns long.

Data must be sent between chips in order to measure the transverse momentum because of bending induced by the magnetic field. Edge channels must be sent to neighboring chips because of charge spread. The pipeline simply ignores non existent chips. Position informatino must be transferred in both directions to allow p_T determination. The transfer mechanism consists of a MOUSETRAP pipeline that transfers a total of 50 bits in 5 stages. The MOUSETRAP pipeline is asynchronous and the pipeline steps are synchronous so there is a synchronous to asynchronous transitions at both the beginning and end of the operation. This is done by using two separate buffers at both ends in a "ping pong" configuration. During one crossing one set of buffers is transferring data between the chips. At the same time the sending chip fills the other set of buffers. At the next clock event (bunch crossing) the chip pads are connected to the new data set and the data transferred to the neighboring chip. This technique eliminates the need to join 2 data sets into an asynchronous pipeline. The main challenge in this design is to make certain that there is enough time to connect the chip pads to the new buffer and transfer

the data in one crossing interval. As the maximum allowed number of Pixels/Strips per cluster is 3, the Clustering can be implemented with simple boolean operations between adjacent units, up to a maximum of 5. Stubs are formed by simply comparing Cluster centroids in the two Stack Members, using the z information to address the stub and up to 3 bits to store momentum.

MOUSETRAP pipelines and dual buffers are used also to gather the data from several chips and send it off detector via a fiber optic link. Both stub data for triggers and cluster (or hit data) for the event readout need to be sent. The amount of event data is much larger than the trigger data one, but the readout rate is more than 100 times less. Minimizing detector mass is a major goal of this design and one way of achieving this goal is to minimize the number of components also in the readout. This design exploits the different readout rate requirements to combine trigger data and event data into one data stream and separate them off detector.

signal bits	number of bits	cluster readout	stub readout
0-10	11	address of cluster hit	address of stub hit
11-15	5	chip address	chip address
16-17	2	layer in stack	z address
18-20	3	event tag	p_T and particle sign
21	1	data/trigger flag	data/trigger flag
22	1	cluster readout token	not used
23-26	4	MOUSETRAP control	MOUSETRAP control
27-29	3	broadcast of event tag	not used

Table B.1: Bit assignment of the readout and control bus [91].

pipeline step	operation
1	send boundary hits across chip boundary to the right
2	form ϕ clusters
3	send z data at boundaries
4	form stubs for trigger
5	encode hit addresses
6	compress data into short pipeline to transmit data off chip
7	send data to chips at the end of the pipeline
8	send data to the fiber optic driver

Table B.2: Pipeline stages in the trigger readout [91].

B.2 Off-Detector Level 1 Tracking Objects

For each 15° sector, in order to find all the tracks, one must also include adjacent sectors, as shown in Figure B.1, at least for the intermediate and the outermost Superlayers. Taking into account the Pixel/Strip pitch, all possible combinations of track hits to be checked need 5 to 7 million logic equations, depending on the fraction of adjiacent sector that is included in the search. Therefore a realistic number of FPGAs needed to process each sector is around 20. Routing a large number of multi gigabit lines to multiple destinations is a complex task but it is certainly possible. However, the use of tracklets allows data segmentation so that multiple destinations are not required. One can use this information to project the track onto the other Superlayers.

Each layer is divided into sections so that all the equations for tracks passing through one of them can fit into a single FPGA. Tracklets are projected from the innermost and the intermediate Superlayers to the appropriate section of the outer one, where the FPGA matches the input tracklets against all possible valid stubs and sends out the four-vectors of matched tracks. Assuming 4 FPGAs are needed to process one Ladder, then each of them would have around 6 optical fibers in and 36 fibers out. The segment processing FPGA would have 4 fibers from each of the 3 Superlayers and 3 adjacent segments (36 total) and one output fiber to a data gathering module for this Trigger segment. Current FPGAs have a maximum of 48 fibers but both FPGA size and number of communication links are growing with time.

Tracklets are built by taking hits from the two Stacks and checking if the displacement is less than or equal to the minimum for a 2.4 GeV/c track. It then, the procedure determines which section to send the track to in the destination Superlayer and puts the stub pair onto an appropriate queue for transmission. The tangential displacement of a track with a p_T = 2.4 GeV/c is about 16 mm in the outermost Layer and is translated into discrete units for easier comparison with stub positions. To allow for easier data processing, each Ladder contains all the information needed to build tracklets, as shown in Figure 4.5. Matching along z is done as described in Section 5.3. The finite length of the interaction region means that stubs in an inner layer chip can be associated with a range of chips in the outer layer, resulting in an offset on both ends of a chip which must be handled with particular care, as shown in Figure B.2.

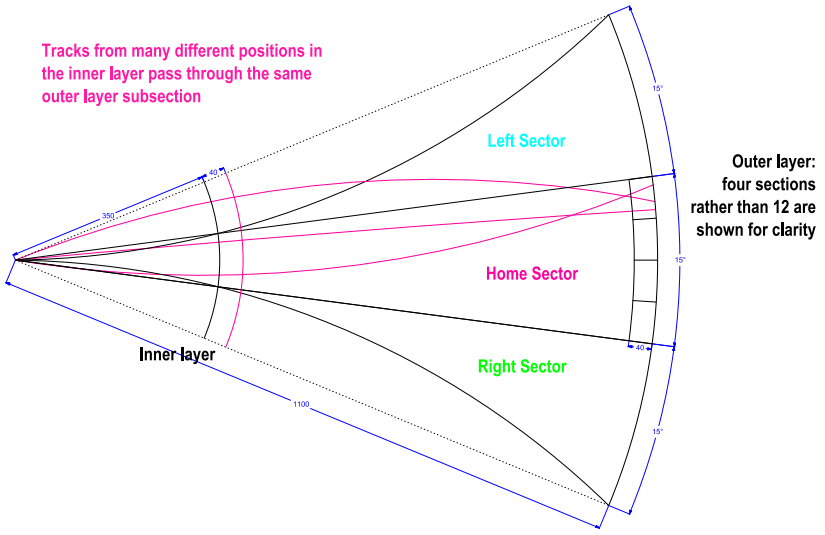

Figure B.1: Example of a 15 degree home sector with its two neighboring sectors. By using both p_T and position in the inner layer, one can sort the tracklets according to their position in the outer layer [91].

Two input registers are envisaged for each row of chips in each Ladder. Each row in the inner Layer is associated to 5 rows in the outer one. Simultaneous feeding of cell data into subtraction units allow to test the difference in hit coordinates for both the transverse and longitudinal match.

The projection of a tracklet onto other Layers is performed with straight line approximations. These projections have errors, as demonstrated in Chapters 5 and 6, so one must project the tracklet to a range of positions that can be determined by a simple table look up. The range is based on the Layer, $\Delta\phi$ and Δz in the original rod, with the same concept as described for the `L1Track` Builder used in the simulation studies presented in this thesis.

Taking into account all the segmentations of target sectors, the number of remote Superlayers and the segmentation of the one containing the seed, the total amount of possible locations to send projected vector is 84. The tracklet rate is about a factor of 2 less than the stub rate, but if one integrates over an entire Ladder, the average rate is about a factor of 5 less than the peak stub one. This results in less than one tracklet per transfer line. Once all the stub information is in an FPGA, all that is required is to see if the stub hits match one of the precomputed equations. If it is, the track vector is the one

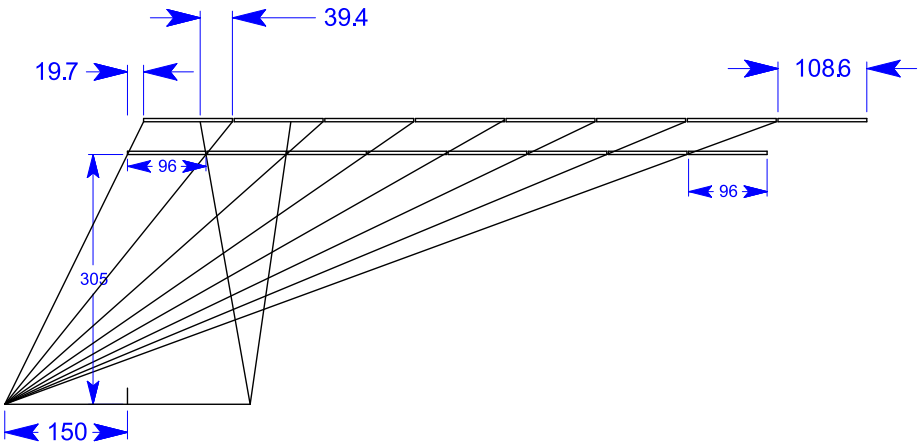

Figure B.2: Effect of a finite interaction region: the overlap is less than one sensor length [91].

associated with the precomputed equation.

What described in the present Appendix is only a conceptual summary of the possible implemetation of the Tracklet and Level 1 Track Builders in terms of real hardware tools processing data online. The presented design does not exceed the capacity of current commercial parts, except for power consumption and radiation tolerance, and has a fair potential of being able to implement all the relevant aspects of Tracking Trigger objects that have been emphasized in this document.

C. Studies with Single Pions

The present Appendix reports examples of relevant efficiency plots obtained in studies with single charged pions, to be compared to those produced with single muon events already reported in Chapters 5 and 6. As many secondary particles are produced when charged pions interact with the Tracker material, only tracks with vertex in the beamspot volume have been taken into account. A brief summary of the preliminary results reported herein is included, with references to the corresponding ones in single muon events.

- Figure C.1 shows the loose tune stub production efficiency with `pixelray` applied on `2d` Clusters; to be compared to Figure 5.11
- Figure C.2 shows the loose tune stub production efficiency with `pixelray` applied on `2d` Clusters, and compares the production efficiency in each Stack to the efficiency of finding a pair of stubs in the same Ladder; to be compared to Figure 5.13
- Figure C.3 shows the tracklet production efficiency if no correction for the beamspot is applied; to be compared to Figure 5.20
- Figures C.4 and C.5 show the tracklet transverse momentum fit; to be compared to Figures 5.22 and 5.23
- Figure C.6 shows the Level 1 track production efficiency when the seed is taken from Superlayer 0, for two different apertures of matching windows; to be compared to Figure 6.10

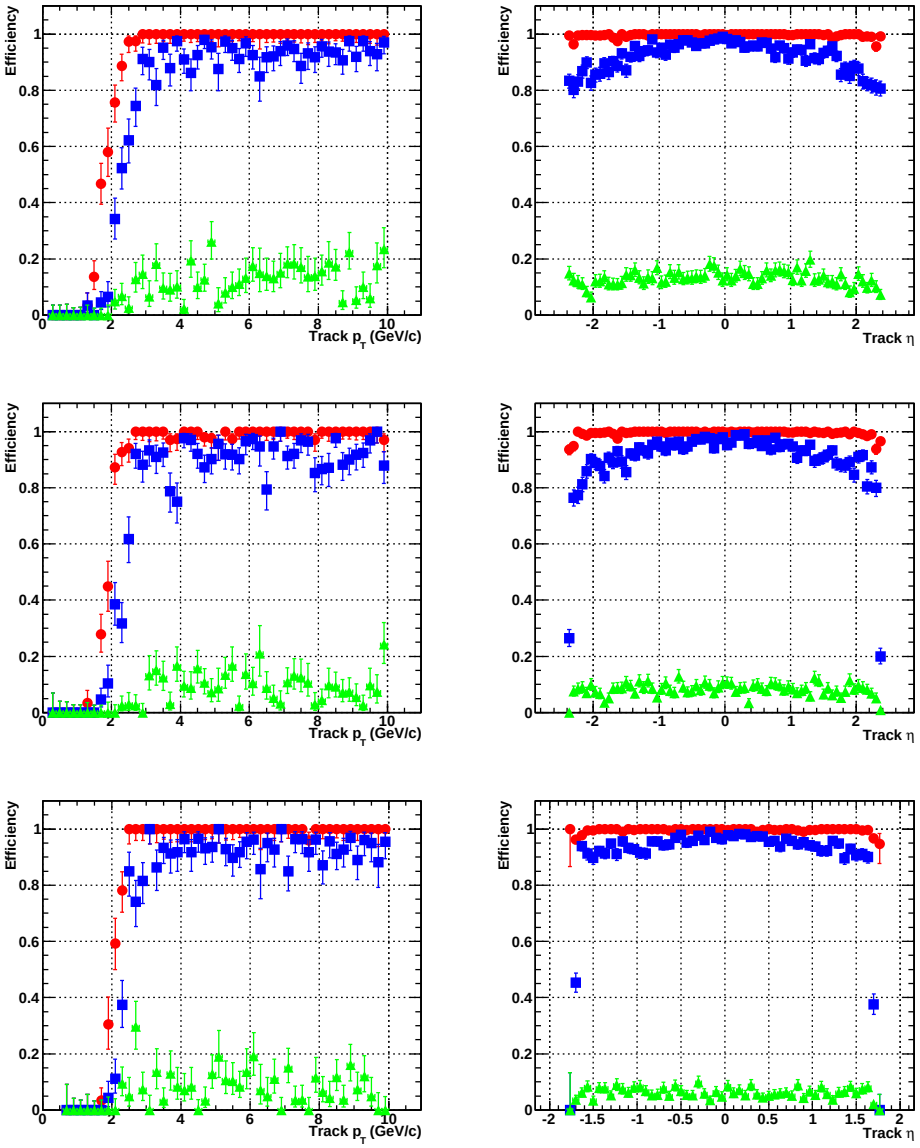

Figure C.1: Loose tune stub production efficiency with `pixelray` applied on `2d` Clusters: 32 and 36 cm nominal radii of Stacks (TOP), 48 and 52 cm (MIDDLE) and 98.5 and 102.5 cm (BOTTOM). Efficiency is shown as a function of track p_T, for $0 < p_T < 10$ GeV$/c$, and track direction η, for $p_T > 20$ GeV$/c$. Efficiency to find at least one stub in the two Stacks is painted with red circular markers, efficiency to find at least two stubs is painted with blue square markers, and efficiency to find more than two stubs is painted with green triangular markers. The sample was composed of single π^+ with flat $0 < p_T < 100$ GeV$/c$ distribution and flat distribution of track direction $|\eta| < 2.4$.

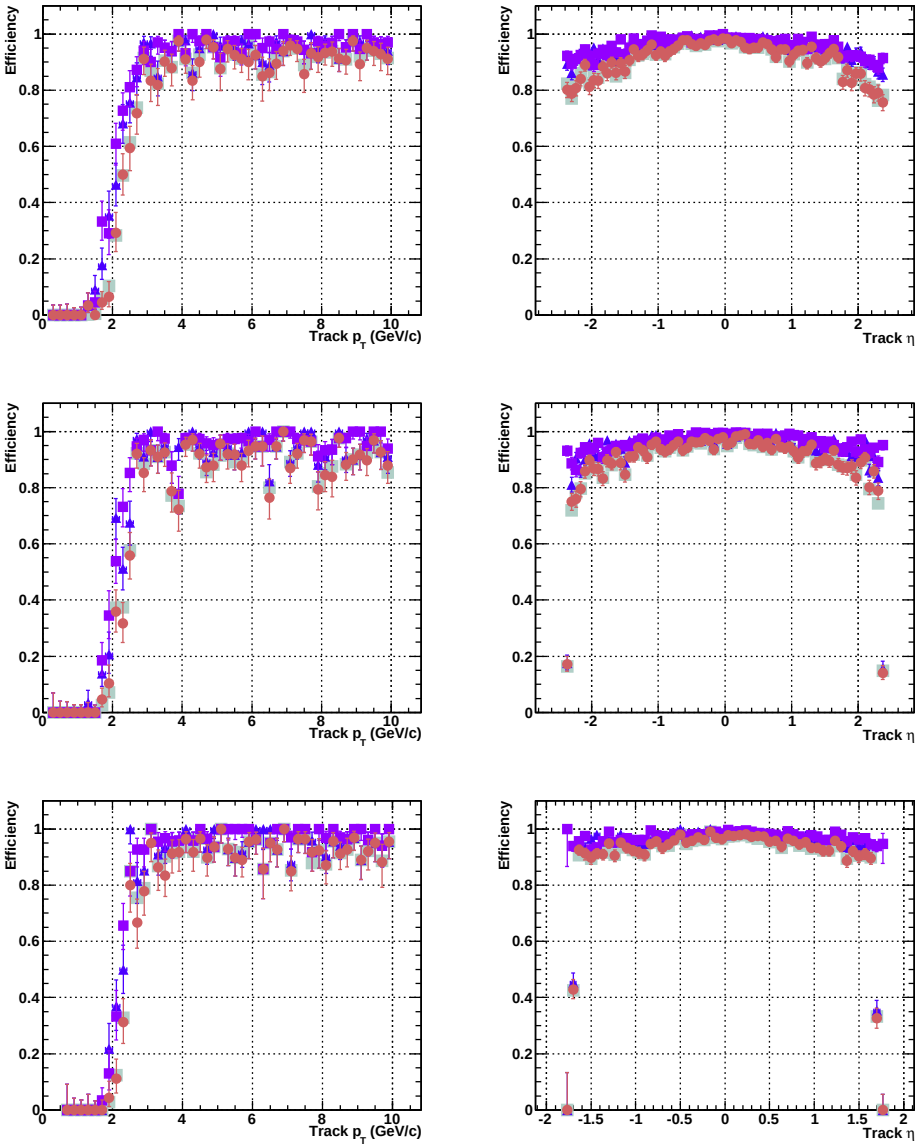

Figure C.2: Loose tune stub production efficiency with `pixelray` applied on `2d` Clusters: 32 and 36 cm nominal radii of Stacks (TOP), 48 and 52 cm (MIDDLE) and 98.5 and 102.5 cm (BOTTOM). Efficiency is shown as a function of track p_T, for $0 < p_T < 10$ GeV$/c$, and track direction η, for $p_T > 20$ GeV$/c$. Efficiency to find at least one stub in the innermost Stack is painted with purple squares, the efficiency to find at least one stub in the outermost Stack is painted with navy blue triangles, their product is painted with grey squares while red brick circles represent the efficiency to find at least one stub in both Stacks within the same Ladder. The sample was composed of single π^+ with flat $0 < p_T < 100$ GeV$/c$ distribution and flat distribution of track direction $|\eta| < 2.4$.

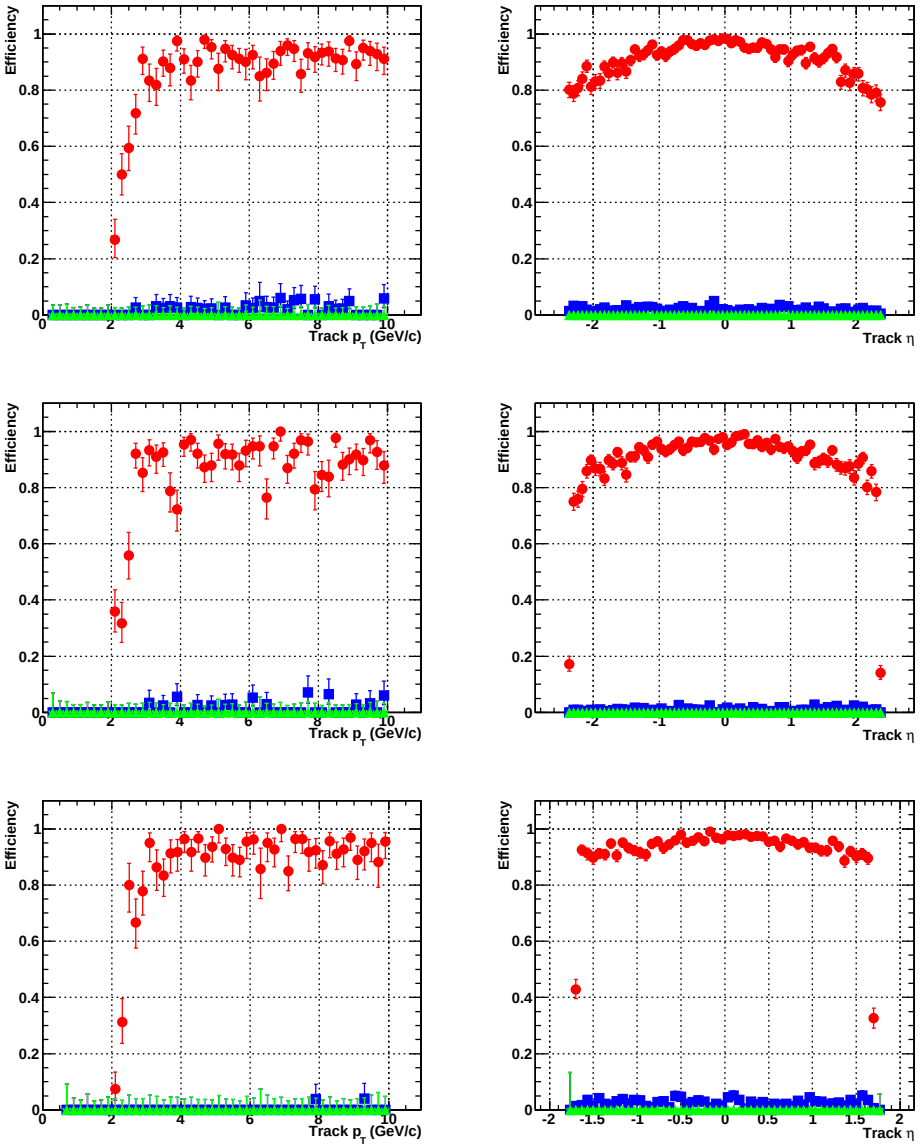

Figure C.3: Tracklet production efficiency with `2d+pixelray` stubs and default choice for tracklet vertex in the transverse plane: 32 and 36 cm nominal radii of Stacks (TOP), 48 and 52 cm (MIDDLE) and 98.5 and 102.5 cm (BOTTOM). Efficiency is shown as a function of track p_T, for $0 < p_T < 10$ GeV/c, and track direction η, for $p_T > 20$ GeV/c. Efficiency to find at least one tracklet in the Double Stacks is painted with red circular markers, efficiency to find at least two tracklets is painted with blue square markers, and efficiency to find more than two tracklets is painted with green triangular markers. The sample was composed of single π^+ with flat $0 < p_T < 100$ GeV/c distribution and flat distribution of track direction $|\eta| < 2.4$ and beamspot displaced 0.5 mm in the $+x$ direction.

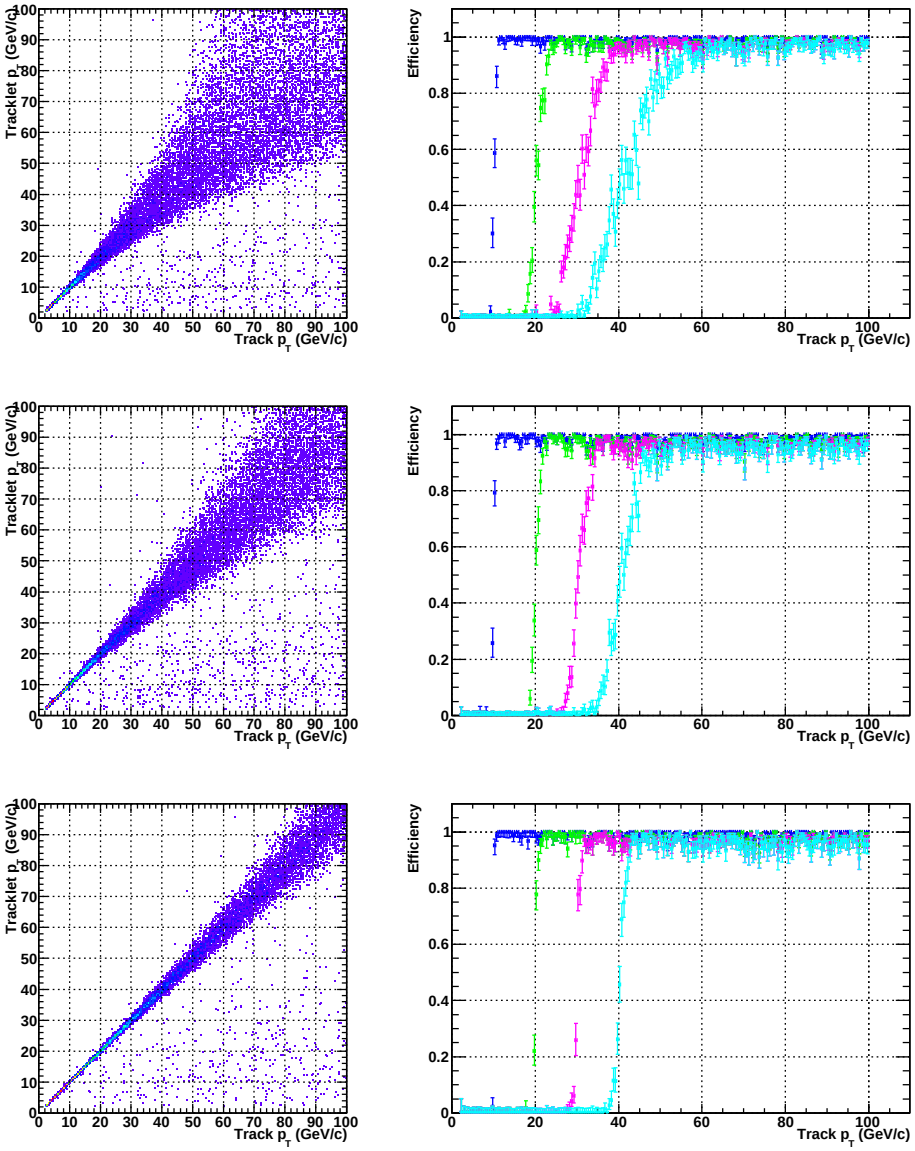

Figure C.4: Correlation between tracklet p_T^{t} and track p_T for standard tracklets made out of `2d+pixelray` stubs (LEFT) and turn-on curves for different p_T thresholds for tracks which produced accepted tracklets (RIGHT). Blue markers refer to tracklet $p_T^{\mathrm{t}} > 10$ GeV$/c$, green ones to a 20 GeV$/c$ threshold, pink ones to a 30 GeV$/c$ threshold and light blue ones to a 40 GeV$/c$ threshold. Results are shown, from TOP to BOTTOM, for Stacks at nominal radii of 32-36 cm, 48-52 cm and 98.5-102.5 cm, respectively. The sample was composed of single π^+ with flat $0 < p_T < 100$ GeV$/c$ distribution and flat distribution of track direction $|\eta| < 2.4$ and beamspot displaced 0.5 mm in the $+x$ direction.

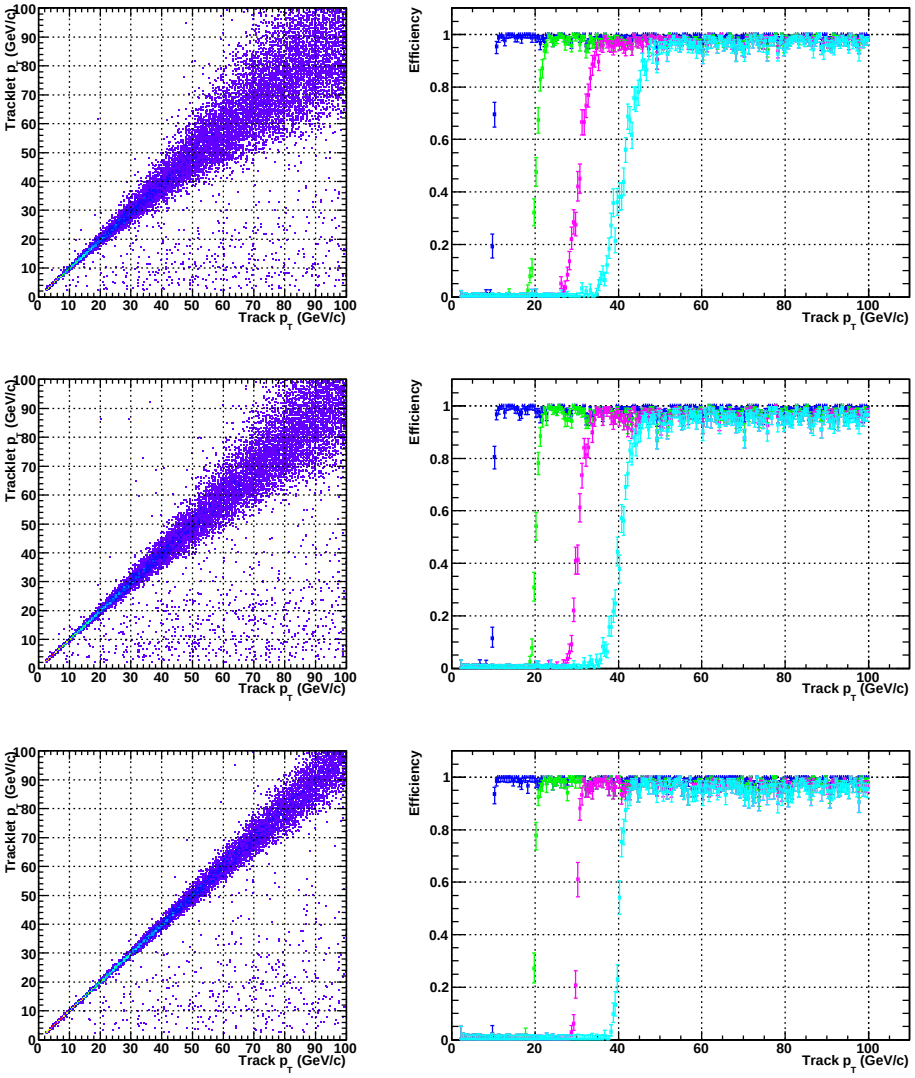

Figure C.5: Correlation between tracklet p_T^{t} and track p_T for tracklets, after correction for the beamspot position, made out of `2d+pixelray` stubs (LEFT) and turn-on curves for different p_T thresholds for tracks which produced accepted tracklets (RIGHT). Blue markers refer to tracklet $p_T^{\mathrm{t}} > 10$ GeV/c, green ones to a 20 GeV/c threshold, pink ones to a 30 GeV/c threshold and light blue ones to a 40 GeV/c threshold. Results are shown, from TOP to BOTTOM, for Stacks at nominal radii of 32-36 cm, 48-52 cm and 98.5-102.5 cm, respectively. The sample was composed of single π^+ with flat $0 < p_T < 100$ GeV/c distribution and flat distribution of track direction $|\eta| < 2.4$ and beamspot displaced 0.5 mm in the $+x$ direction.

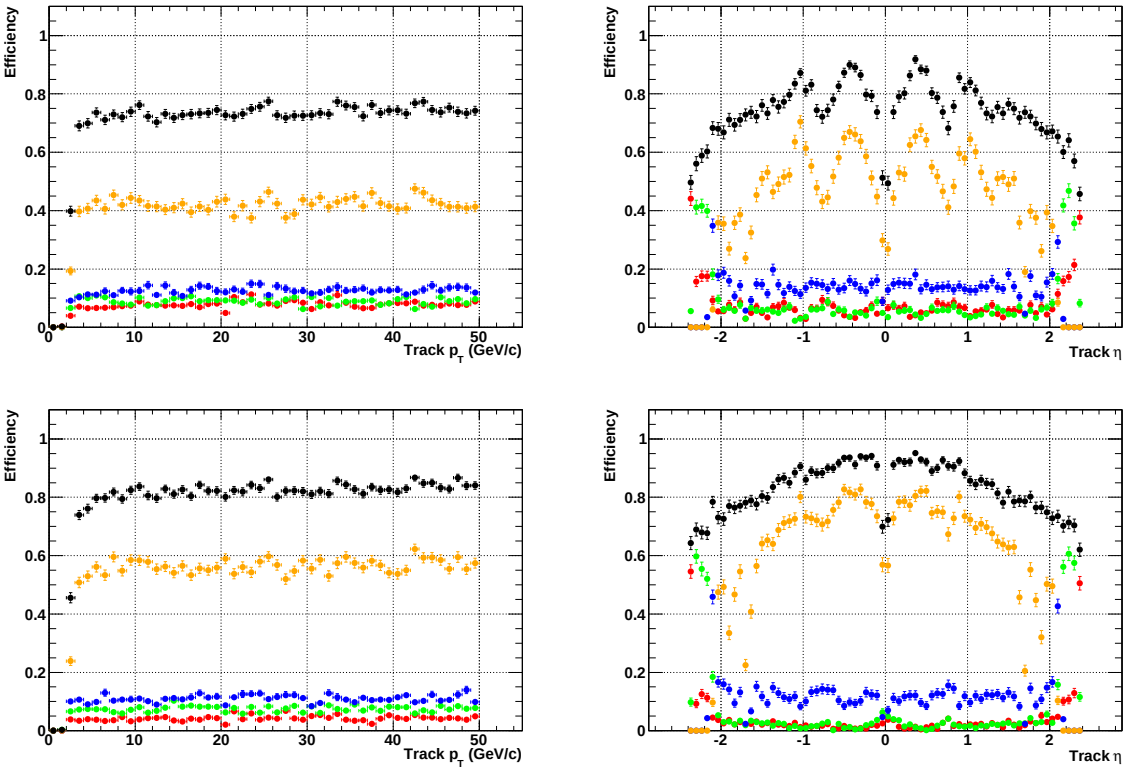

Figure C.6: `L1Track` production efficiency with `2d+globalgeometry` stubs and tracklets. The seed is taken from Superlayer 0. Red points show the efficiency to build 3-stubs-long chains, green ones refer to 4-stubs-long chains, blue ones to 5-stubs-long chains and orange ones to 6-stubs-long chains. Black points show the cumulative efficiency to produce `L1Tracks` with at least 3 stubs. Both 90% (TOP) and 99% (BOTTOM) aperture windows are shown. The sample was composed of pion pairs with flat $0 < p_T < 50$ GeV$/c$ distribution and flat distribution of track direction $|\eta| < 2.4$.

Bibliography

[1] S. L. Glashow, *Partial Symmetries of Weak Interactions*, *Nucl. Phys.* **22** (1961) 579.

[2] J. Goldstone, A. Salam, and S. Weimberg, *Broken Symmetries*, *Phys. Rev.* **127** (1962) 965.

[3] S. Weimberg, *A Model of Leptons*, *Phys. Rev. Lett.* **19** (1967) 1264.

[4] S. L. Glashow, J. Iliopoulos, and L. Maiani, *Weak Interactions with lepton-hadron Symmetry*, *Phys. Rev. D* **2** (1970) 1985.

[5] P. W. Higgs, *Broken Symmetries, Massless Particles and Gauge Fields*, *Phys. Lett.* **12** (1964) 132.

[6] P. W. Higgs, *Broken Symmetries and the Masses of Gauge Bosons*, *Phys. Rev. Lett.* **13** (1964) 508.

[7] P. W. Higgs, *Spontaneous Symmetry Breakdown Without Massless Bosons*, *Phys. Rev.* **145** (1966) 1156.

[8] Gargamelle Neutrino Collaboration, *Observation of Neutrino Like Interactions Without Muon Or Electron in the Gargamelle Neutrino Experiment*, *Phys. Lett. B* **46** (1973) 138.

[9] UA1 Collaboration, *Experimental observation of isolated large transverse energy electrons with associated missing energy at* $\sqrt{s} = 540$ *GeV*, *Phys. Lett. B* **122** (1983) 103.

[10] UA1 Collaboration, *Experimental observation of lepton pairs of invariant mass around 95 GeV/*c^2 *at the CERN SPS collider*, *Phys. Lett. B* **126** (1983) 398.

[11] UA2 Collaboration, *Observation of single isolated electrons of high transverse momentum in events with missing transverse energy at the CERN* $\bar{p}p$ *collider*, *Phys. Lett. B* **122** (1983) 476.

[12] UA2 Collaboration, *Evidence for $Z^0 \to e^+e^-$ at the CERN $\bar{p}p$ collider*, *Phys. Lett. B* **129** (1983) 130.

[13] ALEPH, DELPHI, L3, OPAL Collaborations and LEP Electroweak Working Group, *A Combination of Preliminary Electroweak Measurements and Constraints on the Standard Model*. CERN-PH-EP/2006-042.

[14] Tevatron Electroweak Working Group, *Updated Combination of CDF and D0 Results for the Mass of the W Boson*. FERMILAB-TM-2439-E.

[15] E821: Muon (g-2) Collaboration, *Measurement of the Negative Muon Anomalous Magnetic Moment to 0.7 ppm*, *Phys. Rev. Lett.* **92** (2004) 161802.

[16] ALEPH, DELPHI, L3, OPAL, SLD Collaborations, LEP Electroweak Working Group and SLD Electroweak, Heavy Flavour groups, *Precision Electroweak Measurements on the Z Resonance*, *Phys. Rept.* **427** (2006) 257.

[17] CDF Collaboration, *Observation of Top Quark Production in $\bar{p}p$ Collisions with the Collider Detector at Fermilab*, *Phys. Rev. Lett.* **74** (1995) 2626.

[18] D0 Collaboration, *Observation of the Top Quark*, *Phys. Rev. Lett.* **74** (1995) 2632.

[19] Tevatron Electroweak Working Group, *Combination of CDF and D0 Results on the Mass of the Top Quark*. FERMILAB-TM-2427-E.

[20] A. Djouadi, *The anatomy of electroweak symmetry breaking: Tome I: The Higgs boson in the Standard Model*, *Phys. Rept.* **457** (2007) 1.

[21] A. Djouadi, *The anatomy of electroweak symmetry breaking: Tome I: The Higgs boson in the Standard Model*, *Phys. Rept.* **459** (2007) 1.

[22] Particle Data Group, *Review of Particle Physics*, *J. Phys. G* **37** (2010) 075021.

[23] ALEPH, CDF, D0, DELPHI, L3, OPAL, SLD Collaborations, LEP Electroweak Working Group, Tevatron Electroweak Working Group and SLD Electroweak, Heavy Flavour groups, *Precision Electroweak Measurements and Constraints on the Standard Model*. CERN-PH-EP/2010-095.

[24] SNO Collaboration, *Measurement of the Rate of $\nu_e + d \to p + p + e^-$ Interactions Produced by ^8B Solar Neutrinos at the Sudbury Neutrino Observatory*, *Phys. Rev. Lett.* **87** (2001) 071301.

[25] Super-Kamiokande Collaboration, *Constraints on Neutrino Oscillations Using 1258 Days of Super-Kamiokande Solar Neutrino Data*, *Phys. Rev. Lett.* **86** (2001) 5656.

[26] E. Komatsu *et. al.*, *Five-Year Wilkinson Microwave Anisotropy Probe (WMAP) Observations: Cosmological Interpretation*, *Astrophys.J.Suppl.* **180** (2009) 330.

[27] S. P. Martin, *A Supersymmetry Primer*. `hep-ph/9709356v5`, 2008.

[28] CMS Collaboration, *CMS Physics Technical Design Report Volume I: Detector Performance and Software*. Technical Design Report CMS Series. CERN, Geneva, CMS-TDR-008-1, 2006.

[29] CMS Collaboration, *CMS physics Technical Design Report, Volume II: Physics Performance*. Technical Design Report CMS Series. CERN, Geneva, CMS-TDR-008-2, 2006.

[30] L. Evans, P. Bryant, *et. al.*, *LHC Machine*, *JINST* **3** (2008) S08001.

[31] *Design study of the Large Hadron Collider (LHC): a multiparticle collider in the LEP tunnel*. CERN, CERN-91-03, 1991.

[32] T. S. Pettersson and P. Lefèvre, *The Large Hadron Collider: conceptual design.* Geneva, CERN-AC-95-05 LHC, 1995.

[33] A. Buenaventura, C. Hauviller, and B. Skoczen, *Mechanical Behaviour of the LHC Cryodipoles*. EPAC 2000, 2001.

[34] J.-P. Guillaud and A. Sobol, *Simulation of diffractive and non-diffractive processes at the LHC energy with the PYTHIA and PHOJET MC event generators*. Annecy-le-Vieux, LAPP-EXP 2004-06, 2004.

[35] A. Moraes, C. Buttar, and I. Dawson, *Prediction for minimum bias and the underlying event at LHC energies*, *Eur. Phys. J. C* **50** (2007) 435.

[36] ATLAS Collaboration, *The ATLAS Experiment at the CERN Large Hadron Collider*, *JINST* **3** (2008) S08003.

[37] CMS Collaboration, *The CMS Experiment at the CERN LHC*, *JINST* **3** (2008) S08004.

[38] The LHCb Collaboration, *The LHCb Detector at the CERN LHC*, *JINST* **3** (2008) S08005.

[39] The TOTEM Collaboration, *The TOTEM Experiment at the CERN Large Hadron Collider*, *JINST* **3** (2008) S08007.

[40] The LHCf Collaboration, *The LHCf Detector at the CERN Large Hadron Collider*, *JINST* **3** (2008) S08006.

[41] ALICE Collaboration, *The ALICE Experiment at the CERN LHC*, *JINST* **3** (2008) S08002.

[42] K. Schindl, *The injector chain for the LHC*. CERN-OPEN-99-052, 1999.

[43] CMS Collaboration, *The CMS Magnet Project: Technical Design Report*. Technical Design Report CMS Series. CERN, CMS-TDR-001, 1997.

[44] CERN, *Document Server Photo Archive*.

[45] CMS Collaboration, *The Muon Project: Technical Design Report*. Technical Design Report CMS Series. CERN, CMS-TDR-003, 1997.

[46] CMS Collaboration, *The Electromagnetic Calorimeter Project: Technical Design Report*. Technical Design Report CMS Series. CERN, CMS-TDR-004, 1997.

[47] CMS Collaboration, *The Hadron Calorimeter Project: Technical Design Report*. Technical Design Report CMS Series. CERN, CMS-TDR-002, 1997.

[48] CMS Collaboration, *The Tracker Project: Technical Design Report*. Technical Design Report CMS Series. CERN, CMS-TDR-005, 1998.

[49] CMS Collaboration, *Addendum to the Tracker Technical Design Report*. Technical Design Report CMS Series. CERN, CMS-TDR-005 Addendum 1, 2000.

[50] N. Wermes, *Pixel detectors for tracking and their spin-off in imaging applications*, *Nucl. Inst. Meth. A* **541** (2005) 150.

[51] CMS Collaboration, *The TriDAS Project: Technical Design Report, Volume 1 – The Trigger System*. Technical Design Report CMS Series. CERN, CMS-TDR-006-1, 2000.

[52] CMS Collaboration, *The TriDAS Project: Technical Design Report, Volume 2 – Data Aquisition and High Level Trigger*. Technical Design Report CMS Series. CERN, CMS-TDR-006-2, 2002.

[53] F. Gianotti, M. L. Mangano, T. Virdee, *et. al.*, *Physics potential and experimental challenges of the LHC luminosity upgrade*, *Eur. Phys. J. C* **39** (2005) 293.

[54] F. Zimmermann, *CERN Upgrade Plans for the LHC and its Injectors*, *PoS* **EPS-HEP2009** (2009) 140.

[55] W. Scandale and F. Zimmermann, *Scenarios for sLHC and vLHC*, *Nucl. Phys. B (Proc. Suppl.)* **177-178** (2008) 207.

[56] CMS Collaboration, *Technical Proposal for the Upgrade of the CMS Detector Through 2020*. **DRAFT**. CERN, CMS-DOC-2717, v.12, 2010.

[57] P. Giubilato *et. al.*, *Tests of monolithic pixel detectors in SOI technology with depleted substrate*, *Nucl. Inst. Meth. A* **in press**.

[58] N. Wermes, *Trends in Pixel Detectors: Tracking and Imaging*, *IEEE Trans. Nucl. Sci.* **51** (2004) 1006.

[59] R. Turchetta *et. al.*, *A monolithic active pixel sensor for charged particle tracking and imaging using standard VLSI CMOS technology*, *Nucl. Inst. Meth. A* **458** (2001) 677.

[60] J. Kemmer and G. Lutz, *New Semiconductor Detector Concepts*, *Nucl. Inst. Meth. A* **253** (1987) 356.

[61] M. Battaglia *et. al.*, *study of monolithic CMOS pixel sensors back-thinning and their application for a pixel beam telescope*, *Nucl. Inst. Meth. A* **579** (2007) 675.

[62] G. Rizzo, *Recent development on CMOS monolithic active pixel sensors*, *Nucl. Inst. Meth. A* **576** (2007) 103.

[63] J. Marczewski *et. al.*, *Monolithic silicon pixel detectors in SOI technology*, *Nucl. Inst. Meth. A* **549** (2005) 112.

[64] Y. Arai *et. al.*, *Development of SOI pixel process technology*, *Nucl. Inst. Meth. A* **in press**.

[65] G. C. Keller and S. Cristoloveanu, *Frontiers of silicon-on-insulator*, *J. Appl. Phys.* **93** (2003) 4955.

[66] G. Celler and M. Wolf, *SmartCut: a guide to the technology, the process, the products*. SOITEC, 2003.

[67] Synopsys, *TCAD Process and Device Simulation Tools*. `http://www.synopsys.com/tools/tcad/Pages/default.aspx`.

[68] M. Battaglia *et. al.*, *Monolithic pixel sensors in deep-submicron SOI technology with analog and digital pixels*, *Nucl. Inst. Meth. A* **604** (2009) 380.

[69] S. Mattiazzo, *Private communications*.

[70] S. Mattiazzo *et. al.*, *Total dose effects on a FD-SOI technology for Monolithic Pixel Sensors*, *IEEE Trans. Nucl. Sci.* **57** (2010) 2135.

[71] P. E. Dodd *et. al.*, *SEU-sensitive volumes in bulk and SOI SRAMs from first-principles calculations and experiments*, *IEEE Trans. Nucl. Sci.* **48** (2001) 1893.

[72] P. Giubilato, *Private communications*.

[73] P. Giubilato *et. al.*, *A DAQ system for pixel detectors R&D*, *Nucl. Inst. Meth. A* **511** (2009) 105.

[74] M. Battaglia, *Private communications*.

[75] L. Feld *et. al.*, *Prototyping stacked modules for the L1 track trigger*, *Proposal to the CMS Upgrade Management Board* (2009).

[76] J. Jones *et. al.*, *A Pixel Detector for Level-1 Triggering at SLHC*, *LECC Workshop* **CERN-2005-011** (2005) 130.

[77] J. Jones *et. al.*, *A Study for a Tracking Trigger at First Level for CMS at SLHC*. `physics/0510227`, 2005.

[78] P. Moreira *et. al.*, *The GBT, a proposed architecture for multi-Gbps data transmission in high energy physics*. TWEPP-07, 2007.

[79] G. Hall, *A Study for a Tracking Trigger at First Level for CMS at SLHC*, *CMS Upgrade Workshop*.

[80] M. Pesaresi, *Development of a New Silicon Tracker at CMS for Super-LHC*. PhD thesis, Imperial College, London, 2009.

[81] D. Abbaneo, *Private communications*.

[82] J. Bernardini *et. al.*, *Design and development of micro-strip stacked module prototypes for tracking at S-LHC*, *JINST* **5** (2010) C11018.

[83] D. Orbaker, *Fast Simulation of the CMS Detector*, *CMS Conference Report* **CR-2009-074** (2009).

[84] A. Ryd, L. Fields, and E. Salvati, *Simulations Studies of Stacked Track Trigger Modules*, *CMS Internal Note* **DRAFT**.

[85] D. Acosta *et. al.*, *CMS High Level Trigger*, *CMS Analysis Note* **AN2007/009** (2009).

[86] S. Gennai, *Tau identification in CMS*, *CMS Conference Report* **CR2005/018** (2005).

[87] J. Conway *et. al.*, *Size of signal cones and isolation rings in the CMS tau identification algorithm*, *CMS Analysis Note* **AN2008/026** (2008).

[88] P. Azzi, *Private communications*.

[89] E. Salvati, *Private communications*.

[90] CMS Collaboration, *Comparison of the Fast Simulation of CMS with the first LHC data*, *CMS Detector Performance Summary* **DP-2010-074** (2010).

[91] J. Hoff *et. al.*, *CMS Track Trigger Study*, *CMS Internal Note* **DRAFT**.

[92] M. Singh and S. Nowick, *MOUSETRAP: High-Speed Transition-Signaling Asynchronous Pipelines*, *IEEE Trans. VLSI Syst.* **15** (2007) 684.